UNIVERSITAT
POLITÈCNICA
DE VALÈNCIA

Departamento de Máquinas y Motores Térmicos

DOCTORAL THESIS:

"Flow capacity and efficiency modelling of twin-entry radial turbines under unequal admission conditions through CFD analysis and experiments"

Presented by: D. Nicolás Medina Tomás
Supervised by: Dr. D. Luis Miguel García-Cuevas González
Dr. D. José Galindo Lucas

in fulfillment of the requisites for the degree of

Doctor of Philosophy

Valencia, June 2022

Flow capacity and efficiency modelling of twin-entry radial turbines under unequal admission conditions through CFD analysis and experiments

Nicolás Medina Tomás

Abstract

The current work focuses on the flow capacity and efficiency analysis and modelling of twin-entry radial turbines under unequal admission conditions. These conditions are the most common in real operation, so they must be properly assessed. A thorough analysis of the flow patterns within twin-entry turbines and the main sources of losses have been carried out by means of computational fluid dynamics (CFD) simulations and experimental campaigns, identifying and quantifying the most important phenomena under different admission conditions.

The CFD analysis and the laser Doppler anemometry experimental campaign have shown that the flow from each branch does not fully mix within the rotor. It means that twin-entry turbines could be studied as two single-entry turbines working in parallel in one-dimensional models. Moreover, the rotor inlet and outlet areas corresponding to each branch depend linearly on the mass flow ratio (*MFR*).

The main phenomena producing losses in twin-entry turbines have been identified. Well-known sources of losses have been quantified, such as passage losses in volutes, interspace and rotor, incidence losses or tip leakage losses. However, additional sources of losses have been found that explain the behaviour of twin-entry turbines under unequal admission conditions. There is a sudden expansion downstream of the junction of the volutes that produces losses in the branch with higher pressure. Although the flow from each branch does not fully mix within the rotor, there is a momentum exchange between branches produced in the contact region between branches. The branch with higher momentum transmits some of it to the branch with lower momentum. This phenomenon produces losses in the branch with higher momentum within the interspace and the rotor, but it also produces gains in the branch with lower momentum. This momentum exchange between branches is an essential phenomenon to properly understand the behaviour of twin-entry turbines under unequal admission conditions. Finally, since the full mixing of both flows is produced in the outlet region, the mixing losses are only computed in the outlet region.

The flow behaviour information extracted from the CFD simulations and experimental campaigns has been used to develop effective area and efficiency models. The effective area model is used to extrapolate the flow capacity map. The model has been validated with experimental data. Its capability of extrapolating towards other *MFR* values has been proven, obtaining an error lower than 3% in each branch when only partial and full admission maps are provided to feed the model.

The efficiency model is used to extrapolate the efficiency map. This model has also been validated with experimental data. Its capability of extrapolating towards other *MFR* values is also reliable, obtaining a combined error between both branches lower than 7%. Moreover, the predictions of this loss-based efficiency model have been compared to empirical and commercial models, obtaining more accurate predictions under

unequal admission conditions. Since unequal admission conditions are the most common in real operation, the performance of twin-entry turbines could be better predicted most of the time. This improvement in the performance prediction could help to work in optimum operational points most of the time, which could lead to higher internal combustion engine efficiency and a reduction in fuel consumption and pollutant emissions.

Additionally, a twin-entry turbine with a considerably different geometry has been analysed, finding the same flow behaviour. The models developed have been applied to this geometry, giving good results. These results corroborate that these models provide a reasonable physical description of the behaviour of the twin-entry turbines under unequal admission conditions.

Resumen

El presente trabajo está centrado en analizar el flujo y la eficiencia de turbinas de doble entrada, así como desarrollar modelos de capacidad de flujo y eficiencia que sean capaces de predecir su comportamiento en condiciones de admisión desiguales. Dichas condiciones son las más comunes en funcionamiento real, por lo que deben ser evaluadas adecuadamente. Se ha realizado un análisis profundo de los patrones de flujo y de las principales fuentes de pérdidas en turbinas de doble entrada mediante simulaciones CFD y campañas experimentales, identificando y cuantificando los fenómenos más importantes en distintas condiciones de admisión.

El análisis CFD y la campaña experimental con la técnica LDA han mostrado que el flujo de cada rama no se mezcla completamente con el otro dentro del rotor. Esto significa que las turbinas de doble entrada podrían estudiarse como dos turbinas de entrada simple trabajando en paralelo en modelos unidimensionales. Además, las áreas de entrada y salida del rotor correspondientes a cada rama dependen linealmente de la relación de gastos másicos (*MFR*).

Los principales fenómenos de pérdidas en turbinas de doble entrada han sido identificados. Fenómenos ya conocidos como las pérdidas por fricción en las volutas, interespacio y rotor, las pérdidas por incidencia o las pérdidas en punta de álabe se han cuantificado. Sin embargo, se han encontrado fuentes de pérdidas adicionales que ayudan a explicar el comportamiento de las turbinas de doble entrada en condiciones de admisión desiguales. Se ha encontrado una expansión brusca aguas abajo de la unión de las volutas que produce pérdidas en la rama con más presión. Aunque el flujo de cada rama no se mezcla completamente dentro del rotor, hay un intercambio de momento entre ramas producido en la región de contacto entre ramas. La rama con mayor momento transmite parte de este a la rama con menor momento. Este fenómeno produce pérdidas en la rama con mayor momento en el interespacio y el rotor, pero también produce ganancias en la rama con menor momento. Este intercambio de momento entre ramas es un fenómeno esencial para entender correctamente el funcionamiento de las turbinas radiales de doble entrada en condiciones de admisión desiguales. Finalmente, como la mezcla completa de los flujos de cada rama se produce en la región de salida, es en esta región donde se computan las pérdidas por mezcla.

La información sobre el comportamiento del flujo extraída de las simulaciones CFD y las campañas experimentales se ha usado para desarrollar modelos de área efectiva y eficiencia. El modelo de área efectiva se utiliza para extrapolar en el mapa de capacidad flujo. Este modelo se ha validado con medidas experimentales. Su capacidad de extrapolación hacia otras condiciones de admisión se ha demostrado fidedigna, obteniendo un error menor del 3% en cada rama cuando solo se proporcionan al modelo los mapas de condiciones de admisión completa y parcial.

El modelo de eficiencia se utiliza para extrapolar en el mapa de eficiencia. Este modelo también se ha validado con medidas experimentales.

Su capacidad de extrapolación hacia otros valores de *MFR* también se ha demostrado fidedigna, obteniendo un error combinado de las dos ramas menor del 7%. Además, las predicciones de este modelo de eficiencia basado en pérdidas se han comparado con modelos empíricos y comerciales, obteniendo predicciones más precisas en condiciones de admisión desiguales. Como las condiciones de admisión desiguales son las más comunes en funcionamiento real, el comportamiento de las turbinas de doble entrada estará mejor predicho la mayor parte del tiempo de operación. Esta mejora en las predicciones de las prestaciones puede ayudar a trabajar en condiciones de operación óptimas la mayor parte del tiempo, lo que puede significar una eficiencia del motor de combustión interna mayor y su correspondiente reducción en consumo de combustible y emisión de gases contaminantes.

Adicionalmente, otra turbina de doble entrada con una geometría considerablemente distinta se ha analizado, encontrado un comportamiento muy similar. Los modelos desarrollados se han aplicado a esta geometría con buenos resultados. Estos resultados corroboran que dichos modelos proporcionan una descripción física razonable del comportamiento de las turbinas de doble entrada bajo condiciones de admisión desiguales.

Resum

El present treball està centrat en analitzar el flux i l'eficiència de turbines de doble entrada, així com desenvolupar models de capacitat de flux i eficiència que siguen capaços de predir el seu comportament en condicions d'admissió desiguals. Aquestes condicions són les més comunes en funcionament real, per la qual cosa s'han d'avaluar adequadament. S'ha realitzat una anàlisi profunda dels patrons de flux i de les principals fonts de pèrdues en turbines de doble entrada mitjançant simulacions CFD i campanyes experimentals, identificant i quantificant els fenòmens més importants en distintes condicions d'admissió.

L'ànalisi CFD i la campanya experimental amb la tècnica LDA han mostrat que el flux de cada rama no es mescla completament amb l'altre dins del rotor. Açò significa que les turbines de doble entrada podrien estudiar-se com dues turbines d'entrada simple treballant en paral·lel en models unidimensionals. A més, les àrees d'entrada i eixida del rotor corresponents a cada rama depenen linealment de la relació de gastos màssics (*MFR*).

Els principals fenòmens de pèrdues en turbines de doble entrada han estat identificats. Fenòmens ja coneguts com les pèrdues per fricció en les volutes, interespai i rotor, les pèrdues per incidència o les pèrdues en punta de pala s'han quantificat. Tanmateix, s'han trobat fonts de pèrdues addicionals que ajuden a explicar el comportament de les turbines de doble entrada en condicions d'admissió desiguals. S'ha trobat una expansió brusca aigües avall de la unió de les volutes que produeixen pèrdues en la rama amb més pressió. Encara que el flux de cada rama no es mescla completament dins del rotor, hi ha un intercanvi de moment entre rames produit en la regió de contacte entre rames. La rama amb més moment transmet part d'aquest a la rama amb menor moment. Aquest fenomen produeix pèrdues en la rama amb major moment en l'interespai i el rotor, però també produeix guanys en la rama amb menor moment. Aquest intercanvi de moment entre rames es un fenomen essencial per a entendre correctament el funcionament de les turbines radials de doble entrada en condicions d'admissió desiguals. Finalment, com la mescla completa dels fluxos de cada rama es produeix en la regió d'eixida, és en aquesta regió on es computen les pèrdues per mescla.

La informació sobre el comportament del flux extreta de les simulacions CFD i de les campanyes experimentals s'ha utilitzat per desenvolupar models d'àrea efectiva i eficiencia. El model d'àrea efectiva s'utilitza per a extrapolar en el mapa de capacitat de flux. Aquest model s'ha validat amb mesures experimentals. La seua capacitat d'extrapolació cap a altres condicions d'admissió s'ha demostrat fidedigna, obtenint un error menor del 3% en cada rama quan sols es proporciona al model els mapes de condicions d'admissió completa i parcial.

El model d'eficiència s'utilitza per a extrapolar en el mapa d'eficiència. Aquest model també s'ha validat amb mesures experimentals. La seua capacitat d'extrapolació cap a altres valors d'*MFR* també s'ha demostrat

fidedigna, obtenint un error combinat de les dues rames menor del 7%. A més, les prediccions que ofereixen els nous models basats en pèrdues han estat comparades amb models empírics i comercials, aconseguint prediccions més precises en condicions d'admissió desiguals. Com les condicions d'admissió desiguals són les més comunes en funcionament real, el comportament de les turbines de doble entrada estaran millor predites la major part del temps d'operació. Aquesta millora en les prediccions de les prestacions pot ajudar a treballar en condicions d'operació òptimes la major part del temps, el qual pot significar una major eficiència del motor de combustió interna i la seua corresponent reducció en consum de combustible i emissió de gasos contaminants.

Addicionalment, una altra turbina de doble entrada amb una geometria considerablement diferent s'ha analitzat, trobant un comportament molt similar. Els models desenvolupats s'han aplicat a aquesta geometria amb bons resultats. Aquests resultats corroboren que els models proporcionen una descripció física raonable del comportament de les turbines de doble entrada baix condicions d'admissió desiguals.

List of publications

The papers presented here are the basis of this thesis:

- "Experimental and computational analysis of the flow passing through each branch of a twin-entry turbine", in *14th International Conference on Turbochargers and Turbocharging* (2020) by Galindo, Serrano, García-Cuevas and Medina [1].

- "Using a CFD analysis of the flow capacity in a twin-entry turbine to develop a simplified physics-based model", in *Aerospace Science and Technology* (2021) by Galindo, Serrano, García-Cuevas and Medina [2].

- "Twin-entry turbine losses: an analysis using CFD data", in *International Journal of Engine Research* (2021) by Galindo, Serrano, García-Cuevas and Medina [3].

- "Experimental assessment of the rotor outlet flow in a twin-entry radial turbine by means of Laser Doppler Anemometry", in *International Journal of Engine Research* (2021) by Galindo, Tiseira, García-Cuevas and Medina [4].

- "Assessment of a twin-entry turbine efficiency model including momentum exchange between branches", Under Review in *International Journal of Heat and Fluid Flow* (2022) by Galindo, Serrano, García-Cuevas and Medina [5].

Division of work between authors

The mentioned publications have been done in cooperation with other researchers from the CMT - Motores Térmicos. The author signatures of these publications are in order of seniority. The author carried out the LDA experimental measurements and the 3D CFD simulations. Then, he post-processed the results and developed the models described here. The results discussions were done mainly in collaboration with his supervisors, Assist. Prof. García-Cuevas and Prof. Galindo. The rest of co-authors also helped in the results discussions.

Funding acknowledgements

Acknowledgements

"Nothing in life is to be feared, it is only to be understood."

Marie Curie

Contents

List of Figures

List of Tables

Nomenclature

Abbreviations

1D	One-dimensional
2D	Bi-dimensional
3D	Three-dimensional
CAD	Computer-aided design
CFD	Computational fluid dynamics
CO_2	Carbon dioxide
DNS	Direct numerical simulation
DOC	Diesel oxidation catalyst
DPF	Diesel particulate filters
EGR	Exhaust gas recirculation
GCI	Global convergence index
GOA	Global order of accuracy
GPF	Gasoline particulate filters
ICE	Internal combustion engines
LDA	Laser Doppler anemometry
LES	Large eddy simulation
MFP	Mass flow parameter
MFR	Mass flow ratio

MRF	Multiple reference frame
NO_x	Nitrogen oxides
ORC	Organic Rankine cycle
RANS	Reynolds-averaged Navier-Stokes
RMSE	Root mean square error
RTD	Resistance temperature detector
SCR	Selective catalytic reduction catalysts
SMM	Sliding mesh model
SPC	Shroud particle concentration
SST	Shear stress transport
TWC	Three-way catalysts
URANS	Unsteady Reynolds-averaged Navier-Stokes
VEMOD	Virtual engine model
VGT	Variable geometry turbine

Greek Symbols

α	Absolute flow angle
β	Relative flow angle

β^*	Turbulent model coefficient
ϵ	Turbulent dissipation, error
η	Efficiency
γ	Heat capacities ratio
μ	Dynamic viscosity
ω	Angular velocity, specific dissipation rate
π	Pressure ratio
ρ	Density
σ	Blade speed ratio

Roman symbols

A	Area
a	Calibration coefficient
AG	Geometrical parameter
b	Calibration coefficient
c	Calibration coefficient, absolute velocity
C	Compressor
CC	Combustion chamber
CD	Discharge coefficient
C_p	Specific heat capacity at constant pressure
CS	Coolant system
D	Diameter
d	Calibration coefficient
e	Calibration coefficient

Exp	Experimental
f	Calibration coefficient
h	Height, specific enthalpy
i	Difference between the stator inlet flow angle and the stator vane angle
K	Fitting parameter
k	Turbulent kinetic energy, coefficient, parameter
L	Characteristic length
LS	Lubricant system
M	Mach, Torque
$\dot{m}$	Mass flow rate
N	Rotational speed
n	Number
p	Pressure
P_c	Control parameter
R	Gas constant, radius
R^2	Coefficient of determination
r	radius
s	Entropy
T	Temperature, turbine
T1	Turbine 1
T2	Turbine 2
u	Tangential velocity, Uncertainty
v	Absolute velocity

Vbp1	Backpressure valve 1		blade	Rotor blade
Vbp2	Backpressure valve 2		CA	Contact area
VBs	Bleeding valves		Exp	Experimental
Vbypass	Bypass valve		exp	Expansion
VCC	Combustion chamber valve		geom	Geometric
VCS	Cold air valve		h	Hub branch
VG1	General valve 1		i	Intermediate radius
VG2	General valve 2		inc	Incidence
VIC	Discharge valve		in	Inlet
VT1	Turbine inlet valve 1		inner	Inner radius
VT2	Turbine inlet valve 2		int	Interspace
$\dot{W}$	Power		is	Isentropic state
w	Relative velocity		loss	Losses
Y^+	Non-dimensional distance to the centroid of the first layer of cells close to the walls		max	Maximum
			ME	Momentum exchange
			metal	Metal
Z	Fitting parameter		mix	Mixing
z	Parameter		M	Mach

Subscripts and superscripts

			m	Meridional
+	Pressure-driven tip leakage flow		mod	Modelled
			ND	Non-dimensional
-	Friction-driven tip leakage flow		Neq	Equivalent nozzle
			nut	Rotor nut
$0, 1, \dots$	Stations, coefficient number		opt	Optimum
app	Apparent		other	Other branch
ax	Axial component			

outer   Outer radius

out   Outlet

pass   Passage

PS   Pressure side

red   Reduced

rot   Rotor

r   Radial component

samples Samples

sh   Shroud branch

s   Static state

SS   Suction side

stat   Stator

SudExp Sudden expansion

tan   Tangential component

θ Tangential component

tip   Tip clearance

t   Total state, turbulent

turb   Turbine

vol   Volute

Introduction

Contents

1.1 Background

ALFRED Büchi patented turbochargers in 1905. The turbochargers were first implemented in aircraft engines to reduce the effect of the low air density at elevated altitudes. They did not completely eliminate the power losses at elevated altitudes. However, their performance was improved, achieving higher altitudes. Moreover, it allowed reducing the engine size and weight for a power target. It led to a lower frontal area and lower drag. The turbochargers were rapidly implemented in several applications in the 1920s. They were employed in naval transportation or trains.

In the 1930s, Saurer implemented the turbochargers in diesel engines for the automotive industry, and during the 1950s, they were extendedly employed in trucks. However, there were reliability problems introducing them in cars, as experienced by the Chevrolet Corvair Monza and the Oldsmobile Jetfire launched in 1962. Another problem that needed to be reduced was the turbo lag, the time spent between the moment an increased power is demanded and the moment the turbocharger provides that increased power.

The 1970s oil crisis and the first emissions regulations increased the turbocharger research since its correct implementation would reduce fuel consumption and emissions. Some turbocharged diesel passenger cars were introduced in 1978, such as the Mercedes Benz 300SD or the Peugeot 604. They were also implemented in motorsports such as Formula 1 or World Rally Championships, achieving better performances than the naturally aspirated vehicles. The turbochargers became generally employed for all diesel engines in the 1990s, and they are also used in gasoline engines nowadays.

However, the economic growth of several countries such as China, India, or the South-American countries has exponentially increased the demand for transportation and, therefore, pollutant emissions. This increasing demand and the limited quantity of oil reserves have made the oil price increase continually. Moreover, the pollutant emissions produced by the combustion of the engine exacerbate global warming and deteriorate the air quality in urban areas.

Therefore, oil consumption and pollutant emissions must be reduced by developing more efficient vehicles to not aggravate the world's and humanity's health. Countries worldwide have been concerned about these issues, and they are imposing increasingly stringent emissions regulations to limit the emissions of greenhouse (i.e. CO_2) and pollutant gases (i.e. NO_x, unburnt hydrocarbons or particulate matter). The Euro 6 in the European Union [6], the Tier 3 in the United States of America [7], the China 5 and 6 in China [8] or the Bharat Stage 6 in India [9] are examples of current regulations applied in different countries to the light-duty vehicles.

This concern is not restricted to the automotive sector. Agencies and regulators worldwide are preparing new pollutant emission standards and regulations

for aero-engines, as described in categories 1.A.3 and 1.A.5 of the European Environment Agency Report No 13/2019 [10] or in the International Civil Aviation Organization Resolution A40-18 [11].

Alternative technologies such as electric vehicles or fuel cells could be the solution to these pollutant emissions and oil demand. However, these technologies are still in development, and they are not accessible for most transportation needs. Therefore, it is still essential to reduce the pollutant emissions and fuel consumption of the internal combustion engines (ICE).

There are two primary approaches for reducing these problems. One is to reduce pollutant emissions with an after-treatment system capable of reducing the emissions produced by the combustion system. Typical technologies employed in the after-treatment system are the diesel oxidation catalyst (DOC), diesel particulate filters (DPF), NO_x adsorbers, selective catalytic reduction catalysts (SCR), three-way catalysts (TWC) or gasoline particulate filters (GPF).

The other primary approach is to reduce the emissions generated in the combustion system itself. The fuel injection system, the combustion concepts, the exhaust gas recirculation (EGR) or turbocharging are typically investigated to increase the engine efficiency and reduce fuel consumption and pollutant emissions.

Particularly, turbochargers are implemented to increase the cylinder inlet pressure. This higher pressure benefits the combustion and injection processes. However, the most significant effect is that it allows reducing the engine size obtaining the same effective power and overall engine performance. This engine downsizing means lower fuel consumption and lower greenhouse and pollutant gases.

The turbine configuration typically employed was the single-entry turbine. This configuration presents some issues when connected to a multiple cylinder engine since the pulsating flow coming from cylinders of adjacent firing order create interferences [12]. These interferences produced by the pressure wave returning from the turbine increase engine backflows that damage the cylinder scavenging process. The pressure at exhaust valve increases due to these interferences, which worsen the capability of the cylinder of evacuating the air. Therefore, the volumetric efficiency of the engine is reduced due to these interferences. Therefore, multiple-entry turbines could reduce these interferences connecting each entry to different cylinders. A typical and straightforward configuration adopted has been the twin-entry turbine. It consists of two meridionally separated entries that discharge the air at different rotor blade heights. Half the cylinders are connected to each entry, ensuring that the cylinders of adjacent firing order are connected to different entries.

Turbochargers can be characterised by measuring them experimentally or with computational fluid dynamics (CFD) simulations. However, there is greater interest in developing reliable one-dimensional models to obtain accurate

turbocharger behaviour predictions instantly. Then, these models can be coupled with whole engine simulation codes to predict the overall performance of the engine.

The research institute where the current thesis has been done, CMT-Motores Térmicos, has thoroughly investigated turbochargers and has developed increasingly accurate models. The first approach to this topic was carried out in the PhD thesis of F. Payri [13]. Turbocharger modelling in transient loads was further investigated by J.R. Serrano [14] and A. Rodríguez [15] in their PhD thesis. The one-dimensional modelling has been improved considering other physical phenomena in different PhD theses. M.A. Reyes included heat flows and improved the pulsating performance in the turbocharger modelling [16], M.A. López modelled the turbocharger rotor dynamics [17], and A. Dombrovsky synthesised the effect of the turbocharger modelling on the engine performance [18]. The modelling of the turbocharger compressor and turbine has also been improved separately, taking into account other effects. C. Cervelló modelled variable geometry turbines in her PhD thesis [19], P. Fajardo characterised radial turbines under pulsating flow [20], L.M. García-Cuevas modelled the mechanical losses and the turbine performance under unsteady pulsating flow [21], L.B. Inhestern modelled turbines at extreme off-design conditions [22], P. Soler worked on the turbine acoustics [23], and V. Samala characterised the flow behaviour of twin-entry and dual-volute turbines under steady flow conditions [24].

1.2 Motivation

Greenhouse gases and pollutant emissions produced by the ICE must be reduced to diminish the effect of global warming and improve the air quality in urban areas. Since alternative cleaner technologies are still in development, the ICE efficiency must be improved to reduce fuel consumption and pollutant emissions. A solution extensively adopted is turbocharging the engine. The turbocharger increases the cylinder inlet pressure, achieving the same overall engine performance with a smaller engine. It leads to lower fuel consumption and pollutant emissions.

Twin-entry turbines are becoming the typical turbine configuration adopted by the manufacturers for multiple cylinder engines since they reduce the interferences between cylinders and improve the volumetric efficiency. Therefore, twin-entry turbines are a key component to improve the ICE efficiency, and they must be analysed thoroughly to optimise their performance. Flow patterns and physical phenomena within twin-entry turbines must be adequately examined to understand their behaviour.

4
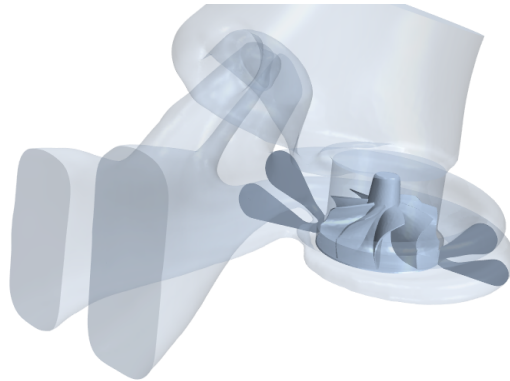
Figure 1.1: Twin-entry turbine

Three different flow admission conditions can be distinguished in twin-entry turbines:

- Full admission conditions: the mass flow rate of both branches is the same.

- Partial admission conditions: the total mass flow rate passes through only one branch.

- Unequal admission conditions: the mass flow rate is different in each branch.

Manufacturers usually provide performance maps with operating points under partial and full admission conditions. However, the most frequent admission conditions under realistic operating conditions are unequal admission conditions. The manufacturers do not often provide maps under these admission conditions, although they represent the most realistic operating conditions. Moreover, few experimental or computational works consider all flow admission conditions in twin-entry turbines.

Mass flow rates and expansion ratios are different in each branch under unequal admission conditions. Due to these different conditions, an interaction between branches could appear when they merge downstream of the volutes outlet. It is important to understand the physical phenomena produced by this interaction under unequal admission conditions and it has not been found in the literature.

Due to this lack of information, it would be valuable to design experimental tests and carry out CFD simulations to analyse the flow behaviour within twin-entry turbines under these unequal admission conditions. Particularly, the CFD simulations could help understand some phenomena produced within twin-entry turbines that are too complex and expensive to be assessed with experimental measurements, such as the contact between flow branches.

The fastest method to predict the engine performance is based on look-up tables. However, they offer low accuracy if there is not a significant number of operational points. The most accurate method is the 3D CFD simulations in which most physical phenomena are properly computed, although other phenomena such as turbulence are often modelled. However, the computational cost and the time spent calculating impede their use in real-time operation. One-dimensional models are the trade-off between those two methods. They are faster than the 3D CFD simulations and more accurate than methods based on look-up tables. They can be employed in real-time, achieving relatively good accuracy. Engine manufacturers use these models for engine development and predict the twin-entry turbine performance in real-time.

Although current models in the automotive industry predict the twin-entry turbine flow behaviour, their predictions under unequal admission conditions are not as suitable as under full and partial admission conditions. Therefore, the analysis and the information obtained from the experimental tests designed and the CFD simulations carried out could be used to develop reliable one-dimensional models. These models would consider the phenomena present under unequal admission conditions. They would properly predict the twin-entry turbine performance. This improved modelling could be used to potentially get higher twin-entry turbine efficiencies and higher engine volumetric efficiency with the corresponding reduction in fuel consumption and pollutant emissions.

1.3 Objectives

The aim of this work is helping to improve turbocharged ICE efficiency and reduce their fuel consumption and pollutant emissions, optimising the performance of twin-entry turbines. To achieve it, two main objectives are proposed.

The first objective is to thoroughly analyse the flow patterns and the physical phenomena within twin-entry turbines under all admission conditions by means of experimental tests and CFD simulations.

Once the twin-entry turbine flow behaviour is properly understood, the second objective is to develop flow capacity and efficiency models to accurately predict the twin-entry turbine performance in real-time. The developed models are based on the information obtained from the CFD simulations and the experimental measurements performed to achieve the first objective. These models try to adequately capture the flow behaviour under unequal admission conditions, which are the most common under realistic operating conditions.

Therefore, the performance of twin-entry turbines under unequal admission conditions could be properly predicted, which could potentially lead to improve the ICE efficiency and reducing their fuel consumption and pollutant emissions.

1.4 Working plan

Different experimental tests and CFD simulations are proposed to analyse the flow patterns and the physical phenomena within twin-entry turbines under all admission conditions.

On the experimental part, the first proposed campaign is to perform steady-state measurements under the whole range of admission conditions, focusing on the unequal admission conditions. Wider flow capacity and efficiency maps than those provided by the manufacturers are obtained. These measurements could also be used to validate the CFD simulations globally. The second proposed campaign is to perform laser Doppler anemometry (LDA) and temperature measurements at the rotor outlet to validate the hypothesis made on the one-dimensional models of studying twin-entry turbines as two single-entry turbines working in parallel. These measurements could also be used to validate the CFD simulations locally at the rotor outlet.

On the computational part, CFD simulations under the same admission conditions as the steady-state experimental measurements are carried out. First, a mesh independence study is performed to ensure accurate results with the lowest computational cost possible. Then, the flow capacity and efficiency maps obtained from the CFD simulations are compared to those measured experimentally to validate the simulations globally. Once the CFD simulations are globally validated, the flow behaviour and phenomena detected could be considered reliable. The mass flow passing through each twin-entry turbine branch can be differentiated for tracking them within the turbine and analysing their flow behaviour. The flow behaviour at the rotor outlet can be compared with the LDA measurements to validate the simulations locally. Moreover, the primary sources of losses could be identified and quantified for each branch. These losses are analysed separately for each twin-entry turbine part.

The information obtained in both the experimental measurements and the CFD simulations could be employed to develop flow capacity and efficiency models to predict the performance of twin-entry turbines. Based on the flow patterns within twin-entry turbines, the flow capacity could be modelled depending on the mass flow admission conditions. Some phenomena that produce the main sources of losses detected are modelled with physical models found in the literature, and others are developed specifically for this work. Therefore, the efficiency could be modelled based on the losses identified in the CFD analysis and quantified with these physical models.

It is interesting to develop steady models capable of properly predicting the actual physical phenomena in twin-entry turbines. Although it falls out of the scope of this thesis, these steady models can be easily coupled with quasi-2D models that capture the accumulation effects in the volutes. These effects are the main unsteady phenomena when working in pulsating flow since the rotor

performance can be considered as quasi-steady.

1.5 Contents

The current work has been structured as follows:

Chapter 2 presents a literature review on turbocharger characterisation and modelling, focusing on the twin-entry turbine additional modelling issues.

Chapter 3 presents the experimental measurements performed on the twin-entry turbine. First, the twin-entry turbine measured and the gas stand are described. Then, steady-state measurements are performed to obtain wider flow capacity and efficiency maps and validate the CFD simulations and the models developed in the following chapters. Additionally, LDA and temperature measurements are performed at the rotor outlet to locally validate the CFD simulations and validate the hypothesis made on the one-dimensional models of studying twin-entry turbines as two single-entry turbines working in parallel.

Chapter 4 presents the CFD simulations setup. A mesh independence study has been carried out. The CFD simulations have been globally validated with steady-state experimental measurements. These CFD simulations provide information that cannot be experimentally measured.

Chapter 5 presents a mass flow and losses analysis based on the CFD simulations. The behaviour of the rotor inlet and outlet areas and flow angles against the mass flow admission conditions is analysed. The primary sources of losses in each part of the twin-entry turbine are identified and quantified with physical models that describe the corresponding phenomenon. These losses are analysed under different admission conditions for each flow branch.

Chapter 6 presents two different numerical models. Both models are developed based on the experimental measurements and CFD simulations information obtained in the previous chapters. They are validated with the experimental measurements, achieving low errors. The first model is an effective area model that extrapolates the flow capacity map. The second model is a losses-based efficiency model that extrapolates the efficiency map.

Chapter 7 presents the extrapolation capacity of the models developed in the previous chapter. The effective area and efficiency models can extrapolate towards other admission conditions in the flow capacity and efficiency maps, respectively. Additionally, the performance of the extrapolations is compared with other current models to assess the benefits of the developed models. Finally, the models are applied to a different twin-entry turbine to corroborate that they appropriately predict the twin-entry turbine performance independently of its geometry.

Chapter 8 summarises the primary contributions and the information obtained in the current PhD Thesis. Furthermore, the limitations of the work and

the possible future works for improving these results are also described.

1.6 References

[6] European Comission. *Emissions in the automotive sector*. 2018. URL: https://ec.europa.eu/growth/sectors/automotive/environment-protection/emissions_en (cit. on pp. 2, 14).

[7] Environmental Protection Agency. *Environmental protection agency control of air pollution from motor vehicles: Tier 3 motor vehicle emission and fuel standards*. 2015. URL: https://www.epa.gov/regulations-emissions-vehicles-and-engines/final-rule-control-air-pollution-motor-vehicles-tier-3 (cit. on pp. 2, 14).

[8] H. Gong, Y. Ge, J. Wang, and H. Yin. "Light-duty vehicle emissions control: a brief introduction to the China 6 emissions standard". In: *Johnson Matthey Technology Review* 61 (2017), pp. 269–278. DOI: 10.1595/205651317X696199 (cit. on pp. 2, 14).

[9] International Council On Clean Transportation. *India Bharat Stage VI emission standards*. 2016. URL: https://theicct.org/sites/default/files/publications/India%20BS%20VI%20Policy%20Update%20vF.pdf (cit. on p. 2).

[10] European Environment Agency. *EEA Report No 13/2019, EMEP/EEA air pollutant emission inventory guidebook 2019*. 2019. DOI: 10.2800/293657 (cit. on p. 3).

[11] International Civil Aviation Organization. *Resolution A40-18: Consolidated statement of continuing ICAO policies and practices related to environmental protection - Climate change* (cit. on p. 3).

[12] T. Garrett, K. Newton, and W. Steeds. "Turbocharging and supercharging". In: *Motor Vehicle* (2000), pp. 556–589 (cit. on p. 3).

[13] F. Payri. "Predicción de las actuaciones de los grupos de sobrealimentación para motores diesel de automoción". PhD thesis. Universidad Politécnica de Madrid, 1973 (cit. on p. 4).

[14] J. R. Serrano Cruz. "Análisis y modelado de transitorios de carga en MEC turboalimentados". PhD thesis. Universitat Politècnica de València, 1999 (cit. on p. 4).

[15] A. Rodríguez. "Analisis comparativo y sintesis de la respuesta transitoria en motores diesel de inyeccion directa turboalimentados". PhD thesis. Universitat Politècnica de València, 2001 (cit. on p. 4).

[16] M. Á. Reyes-Belmonte. "Contribution to the experimental characterization and 1-D modelling of turbochargers for IC engines". PhD thesis. Universitat Politècnica de València, Dec. 2013. DOI: 10.4995/Thesis/10251/34777 (cit. on p. 4).

[17]   M. A. López Hidalgo. "Estudio teórico-experimental de la dinámica rota-
       cional de un turbocompresor de MCIA. Aplicación al diagnóstico de
       fallos". PhD thesis. Universitat Politècnica de València, 2014. DOI: 10.4
       995/Thesis/10251/37746 (cit. on p. 4).

[18]   A. Dombrovsky. "Synthesis of the 1D modelling of turbochargers and
       its effects on engine performance prediction". PhD thesis. Universitat
       Politècnica de València, 2017. DOI: 10.4995/Thesis/10251/82307 (cit.
       on p. 4).

[19]   C. Cervelló. "Contribución a la caracterización experimental y al mode-
       lado de turbinas de geometría variable en grupos de sobrealimentación".
       PhD thesis. Universitat Politècnica de València, 2005. DOI: 10.4995/Th
       esis/10251/1902 (cit. on p. 4).

[20]   P. Fajardo Peña. "Methodology for the numerical characterization of a
       radial turbine under steady and pulsating flow". PhD thesis. Universitat
       Politècnica de València, July 2012. DOI: 10.4995/Thesis/10251/16878
       (cit. on pp. 4, 73).

[21]   L. M. García-Cuevas González. "Experiments and modelling of automo-
       tive turbochargers under unsteady conditions". PhD thesis. Universitat
       Politècnica de València, 2014. DOI: 10.4995/Thesis/10251/48458 (cit.
       on pp. 4, 129, 159).

[22]   L. B. Inhestern. "Measurement, simulation, and 1D-modeling of tur-
       bocharger radial turbines at design and extreme off-design conditions".
       PhD thesis. Universitat Politècnica de València, 2019. DOI: 10.4995/Th
       esis/10251/119989 (cit. on p. 4).

[23]   P. Soler Blanco. "Simulation and modelling of the performance of radial
       turbochargers under unsteady flow". PhD thesis. Universitat Politècnica
       de València, 2020. DOI: 10.4995/Thesis/10251/141609 (cit. on p. 4).

[24]   V. Samala. "Experimental characterization and mean line modelling of
       twin-entry and dual-volute turbines working under different admission
       conditions with steady flow". PhD thesis. Universitat Politècnica de
       València, 2020. DOI: 10.4995/Thesis/10251/153475 (cit. on p. 4).

CHAPTER 2

Literature review

Contents

2.1 Introduction

A s was stated in the previous chapter, the most frequent radial turbines application is for turbocharging internal combustion engines (ICE), including aircraft powerplants [25, 26] and range extenders for electric vehicles [27, 28]. However, radial turbines have been implemented in a wider range of applications nowadays. They are employed in wave energy converters [29, 30], generator sets [31, 32], organic Rankine cycles (ORC) [33, 34] or distributed generation as microturbines [35, 36].

In the automotive industry, pollutant emissions and fuel consumption regulations are becoming increasingly stringent worldwide with new regulations in the European Union [6], China [8] or the United States of America [7]. These restrictions are hard to achieve with conventional ICE. Several techniques have been applied during the years to reduce pollutant emissions and fuel consumption, being the engine downsizing one of the most efficient techniques [37]. A turbocharger is used to increase the pressure and density of the intake flow. Therefore, the same mass flow needed to produce the required power has lower volume and the engine size can be reduced. This increased pressure is given by the turbocharger compressor placed at the engine intake that compresses the inlet air. This compressor is connected by a shaft to a turbine placed downstream of the exhaust manifold. The turbine uses the exhaust gases energy to rotate and produce power to move the compressor.

The turbocharger must be well coupled with the engine to reach better overall efficiencies. Therefore, one-dimensional models capable of accurately predicting the turbocharger performance maintaining reasonable computational cost are needed. Twin-entry turbines models present extra issues since they can experience different flow admission conditions that must be assessed. The different twin-entry turbine stations used in the models have been numbered as described in Table 2.1 and Fig. 2.1. Although there are twin-entry turbines with vanes between the volutes and the rotor, the current thesis is focused in nozzleless twin-entry turbines. So, there is no station between the volute outlet and the rotor inlet.

Table 2.1: Twin-entry turbine stations

Station	Description
0	Turbine inlet
1	Volute outlet
3	Rotor inlet
4	Rotor outlet
5	Turbine outlet
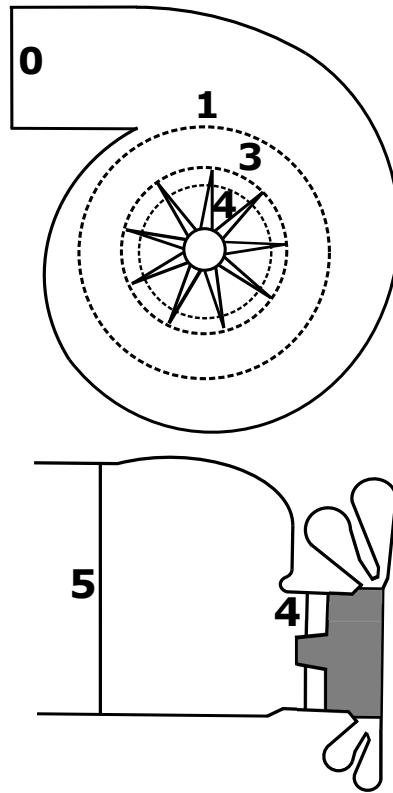
Figure 2.1: Twin-entry radial turbine stations

This chapter presents the main parameters that are used during the thesis. Then, it also presents a literature review of relevant researches about the radial turbocharger experimental and computational characterisation and modelling as well as the particularities of the twin-entry turbines.

2.2 Twin-entry radial turbines performance

Turbocharger manufacturers typically provide the turbine performance with flow capacity and efficiency maps. Thus, these data are also employed to develop one-dimensional models. The flow capacity map represents the reduced mass flow against the total-to-static expansion ratio, and the efficiency map represents the total-to-static efficiency against the blade speed ratio or also against the total-to-static expansion ratio. These parameters can also be obtained with experimental measurements or CFD simulations since they depend on easily measurable variables. In twin-entry turbines, those maps are defined for each branch separately.

15

The reduced mass flow $\dot{m}_{\mathrm{red}}$ is defined in Eq. 2.1. It depends on the radial turbine mass flow $\dot{m}$ and the total pressure $p_{0\mathrm{t}}$ and total temperature $T_{0\mathrm{t}}$ turbine inlet conditions.

$$\dot{m}_{\mathrm{red}} = \dot{m} \cdot \frac{\sqrt{T_{0\mathrm{t}}}}{p_{0\mathrm{t}}} \qquad (2.1)$$

The total-to-static expansion ratio π_{exp} is defined in Eq. 2.2. It is defined as the expansion ratio between total pressure at the turbine inlet and static pressure at the turbine outlet p_5.

$$\pi_{\mathrm{exp}} = \frac{p_{0\mathrm{t}}}{p_5} \qquad (2.2)$$

An additional parameter must be defined in twin-entry turbines to assess the mass flow admission conditions. Some authors, such as Chiong et al. [38] or Romagnoli et al. [39], use the mass flow parameter (*MFP*) to assess the mass flow admission conditions. Other authors, such as Uhlmann et al. [40], prefer to use the Mass Flow Ratio (*MFR*). The respondent has employed the Mass Flow Ratio (*MFR*) since it has demonstrated good correlations with relevant variables needed for the one-dimensional models, as will be described in the following chapters. The *MFR* is defined in Eq. 2.3 as the ratio between the mass flow passing through one branch and the combined mass flow passing through both branches. The subscript h stands for hub branch, which is the branch that discharges the flow near the rotor hub. The subscript sh stands for shroud branch, which is the branch that discharges the flow near the rotor shroud.

$$MFR = \frac{\dot{m}_{\mathrm{sh}}}{\dot{m}_{\mathrm{h}} + \dot{m}_{\mathrm{sh}}} \qquad (2.3)$$

When the *MFR* is equal to 0.5, the twin-entry turbine works under full admission conditions. When the *MFR* is equal to 0 or 1, the twin-entry turbine works under partial admission conditions. For all other *MFR* values, the twin-entry turbine works under unequal admission conditions.

The turbine total-to-static efficiency $\eta_{\mathrm{t,s}}$ is defined in Eq. 2.4. It is defined as the ratio between the turbine power $\dot{W}_{\mathrm{turb}}$ and the turbine isentropic power $\dot{W}_{\mathrm{turb,is}}$.

$$\eta_{\mathrm{t,s}} = \frac{\dot{W}_{\mathrm{turb}}}{\dot{W}_{\mathrm{turb,is}}} \qquad (2.4)$$

The turbine power and the turbine isentropic power are defined in Eq. 2.5 and 2.6, respectively. They depend on the mass flow and the mean specific heat capacity $\bar{C}_{\mathrm{p}}$. The turbine power is computed between the rotor inlet and rotor outlet total temperature conditions when the heat flow can be neglected, and

the turbine isentropic power between the turbine inlet total temperature and the turbine outlet static temperature.

$$\dot{W}_{\text{turb}} = \dot{m} \cdot \bar{C}_{\text{p}} \cdot (T_{3\text{t}} - T_{4\text{t}}) \tag{2.5}$$

$$\dot{W}_{\text{turb,is}} = \dot{m} \cdot \bar{C}_{\text{p}} \cdot (T_{0\text{t}} - T_5) \tag{2.6}$$

The turbine inlet total temperature conditions can be different in each twin-entry turbine branch under unequal admission conditions. Therefore, the total-to-static efficiency of each branch will be different for each branch. However, the rotor outlet total temperature $T_{4\text{t}}$ and the turbine outlet temperature T_5 cannot be experimentally measured for each flow branch separately since they are completely mixed in the region where the temperature sensors are placed. Thus, the efficiency experimentally measured will be called apparent efficiency η_{app} in the current work. The actual efficiency $\eta_{\text{t,s}}$ of each branch can be obtained by means of CFD simulations since the flow from each branch can be tracked and the rotor outlet total temperature of each branch can be computed separately.

The turbine blade speed ratio σ is defined in Eq. 2.7. This parameter is useful in the aerodynamic design since it provides different trends with the efficiency depending on its value. It is defined as the ratio between the rotor blade tip speed and the isentropic speed u_{is} computed with the turbine inlet total conditions and the turbine outlet static conditions.

$$\sigma = \frac{N \cdot r_3}{u_{\text{is}}} = \frac{N \cdot r_3}{\sqrt{2 \cdot \bar{C}_{\text{p}} \cdot T_{0\text{t}} \cdot \left[1 - \left(\dfrac{p_5}{p_{0\text{t}}} \right)^{\frac{\gamma-1}{\gamma}} \right]}} \tag{2.7}$$

The rotor blade tip speed depends on the turbine rotational speed N and the rotor inlet radius r_3. γ is the specific heat capacities ratio.

The data provided in the maps are generally grouped under isospeed lines with a constant reduced rotational speed parameter N_{red}. This parameter is defined in Eq. 2.8, and it depends on the turbine rotational speed and the turbine inlet total temperature. In the case of twin-entry turbines, the data are also grouped under different MFR values.

$$N_{\text{red}} = \frac{N}{\sqrt{T_{0\text{t}}}} \tag{2.8}$$

Turbine maps are usually measured utilising the turbocharger compressor as a brake for the turbine. Thus, the compressor power consumption increases with its rotational speed. This higher rotational speed is achieved by increasing

the turbine expansion ratio. Therefore, increasing the reduced rotational speed will be the same as increasing the turbine expansion ratio.

2.3 Experimental characterisation

Turbocharger turbines are typically measured in gas stands. There are standards and testing codes such as those proposed by the Society of Automotive Engineers (SAE) [41, 42]. They recommend the type of sensors employed to measure the different variables and the placing of these sensors. The mass flow is generally measured downstream of the turbine, although it is also measured upstream of both turbine inlets in twin-entry turbines. The pressure and temperature conditions should be measured 6 diameters upstream of the turbine inlet and downstream of the turbine outlet to guarantee developed flow in the placing of the sensors. There are two primary methods to power the turbocharger turbines in gas stands [43]: with natural gas burners or with an auxiliary air compressor.

When the turbocharger compressor is employed as a brake in the gas stands, the range that can be measured is limited due to surge and choke conditions under low and high pressure ratios, respectively. However, some authors, such as Serrano et al. [44], forced the mass flow rate of the turbocharger compressor to reach favourable pressure gradient and avoid possible surge problems. This method allows widening the measurable range since the expansion ratios achieved in the turbine can be smaller than those achieved when the compressor is used as a brake.

Twin-entry turbines have been experimentally measured under full and partial admission conditions in gas stands as described by Aghaali and Hajilouy-Benisi [45], evaluating the flow behaviour under these flow admission conditions.

Further works have also experimentally measured twin entry-turbines under unequal admission conditions. Brinkert et al. [46] varied the pressure ratio and the inlet temperature conditions of each branch to achieve unequal admission conditions. They evaluated the capability of some flow parameters to describe the flow similarity under unequal admission conditions. Romagnoli et al. compared the performance of twin-entry turbines under unequal admission conditions to the performance of a similar single-entry turbine [47] and a double-entry turbine [39]. They achieved the unequal admission conditions varying the pressure ratio of only one branch with a gas stand specially prepared to control the pressure and mass flow conditions of each branch separately. Usai and Marelli [48] also designed a gas stand to evaluate the performance of twin-entry turbines for heavy-duty application under different admission conditions.

CMT-Motores Térmicos also has a twin-entry turbine gas stand specially prepared to control the mass flow and pressure conditions of each branch sep-

arately, as described in Serrano et al. [49]. This gas stand allows evaluating the twin-entry turbine performance in terms of reduced rotational speed, *MFR*, expansion ratio and apparent efficiency. This gas stand will be thoroughly described in Chapter 3 since it is the one employed to carry out the current work experiments. It also has the capability of testing twin-entry turbines under pulsating flow conditions employing a rotating valve to generate the pulses and a beamforming technique to obtain a realistic acoustic characterisation, as described in Serrano et al. [50, 51].

Other authors have experimentally assessed local issues of twin-entry turbines. Morrison et al. [52] investigated a novel turbine housing to produce a non-uniform spanwise flow field at twin-entry turbine inlet. Jin et al. [53] evaluated the effect of employing a balance valve instead of a wastegate. Yeo and Baines [54] investigated the presence of the axial component of the velocity at the rotor inlet, especially under partial admission conditions.

The experimental characterisations found in the literature are focused on the global performance of twin-entry turbines. However, nobody has experimentally characterised the interaction between flow branches locally. Therefore, it would be interesting to investigate this interaction. This thesis presents an experimental characterisation of the flow of each branch at the rotor outlet section by means of LDA measurements to study this phenomenon.

2.4 CFD characterisation and modelling

There are different methods for solving the turbulence in CFD simulations. Direct Numerical Simulations (DNS) are capable of solving the Navier-Stokes equations, including all the information from the size of the whole computational domain down to the smaller scales where the turbulent eddies are dissipated due to the dynamic viscosity of the air. However, they have a large computational cost that makes it impossible to simulate complex geometries such as twin-entry turbines nowadays. Large eddy simulations (LES) are capable of solving the large turbulent scales, but they model the small turbulent scales. LES simulations have lower computational costs than DNS simulations, but they are still large.

A simpler, less expensive approach is to solve the Reynolds-averaged equations and to model all turbulent scales. This approach, called Reynolds-averaged Navier-Stokes simulations (RANS) inherently leads to a steady-state method. However, making the assumption that the time-scales of the turbulence are much smaller than the time-scales associated to changes in the mean flow, the equations can be solved in a time-marching manner, leading to the Unsteady Reynolds-averaged Navier-Stokes simulations (U-RANS). U-RANS simulations model all turbulent scales, but the computational cost is low since the mesh can

be coarser. The U-RANS simulations quality will depend on the setup of the simulations. However, they can achieve (and, indeed, they achieved, as it will be demonstrated in this thesis) enough accuracy and detail for the purpose of the current work.

U-RANS simulations introduce a new tensor into the equations, the so called Reynolds stress tensor, which includes the effects of the turbulence into the simulation. Closure equations are needed to compute this tensor and model the turbulence, and several methods can be used for that purpose, as compared by Aghaei et al. [55]. The Reynolds stresses models typically adopted to simulate turbochargers are based on Boussinesq's turbulent viscosity hypothesis, being the $k-\epsilon$ and $k-\omega$ two-equations models the most used. The $k-\epsilon$ model offers better results in free-stream than the $k-\omega$ model. On the other hand, the $k-\omega$ model offers better results near the walls than the $k-\epsilon$ model. The $k-\omega$ SST model [56] combines both methods to use the $k-\omega$ formulation near the walls and the $k-\epsilon$ formulation in the far field. This model is the most common model employed to simulate turbochargers, as evaluated by different authors like Menter et al. [57] or Galindo et al. [58].

The boundary conditions imposed generally in turbocharger turbines are total pressure and total temperature at the turbine inlet and static pressure at the turbine outlet. Moreover, these conditions are typically imposed far from the turbine inlet and outlet since it is where the experimental measurements employed to validate the simulations are recorded, and possible spurious wave reflections are avoided [59].

The rotor movement can be simulated with two different methods: with a multiple reference frame method (MRF) on a frozen mesh that introduces the centrifugal and Coriolis forces as source terms and with a sliding mesh model (SMM) that rotates the rotor mesh each time-step. The MRF method has a lower computational cost, but SMM provides more accurate results, as found by several authors like Galindo et al. [60], Fürst and Zák [61], Palfreyman and Martínez-Botas [62] or Jasak and Beaudoin [63].

CFD simulations are a powerful tool that allows optimising the design process with lower economic costs. In twin-entry turbines, the geometry can be optimised to improve their efficiency. Yokoyama et al. [64] designed new volutes to reduce the flow separation at the blade hub. Wang and Zheng [65] assessed that, in case of asymmetric entries, the bigger entry should be placed on the shroud side. Menaouar et al. [66] investigated the effect of extending the length of the separation wall between volutes to reduce the secondary flow losses, although it would be difficult to build due to thermal stress. Fan et al. [67] analysed the effect of including a nozzle only in one of the branches, keeping the other branch vaneless. Chebli et al. [68] evaluated the effect of including a variable outlet turbine that modifies the rotor outlet area.

Moreover, CFD simulations are also suitable for the flow performance analy-

sis stage. The steady and unsteady overall performance has been assessed by several authors such as Bencherif et al. [69], Cravero et al. [70], Ghenaiet and Cerdoun [71] or Muller et al. [72]. However, the numerical uncertainties produced when attempting to represent the physical problem must be considered to obtain reliable quantitative information, as described by Cravero and Ottonello [73].

Recently, more thorough analyses have been carried out to investigate the losses produced within twin-entry turbines. Hajilouy-Benisi et al. [74] performed an entropy analysis in the volutes and the rotor under full and partial admission conditions. They found that the twin-entry turbine efficiency is lower under partial admission conditions, describing the extra losses produced by the different incidence flow angles along the rotor blade height. Xue et al. [75] computed the losses by means of loss coefficients based on the stagnation pressure in the volutes, the stator and the rotor separately, focusing on the losses due to the incidence flow angles and the secondary flows under full and partial admission conditions. Cerdoun and Ghenaiet [76] described the secondary flows formation at the volutes and the interspace between volutes and rotor under partial admission conditions. Palenschat et al. [77] included in their analysis the performance under unequal admission conditions. They described the losses in the volutes and the passage and tip leakage losses in the rotor.

There are interesting losses studies in twin-entry turbines by means of CFD simulations that consider different sources of losses. However, no analysis of the losses due to the interaction between branches has been found in the literature. These losses are expected to be important under unequal admission conditions when the branches have different boundary conditions and should be assessed. Moreover, the flow distribution within twin-entry turbines is expected to change with the admission conditions. This thesis presents a CFD characterisation of the flow distribution at inlet and outlet sections as well as a detailed analysis of the sources of losses focusing on the interaction between branches.

2.5 One-dimensional models

One-dimensional models are a powerful tool to obtain fast and relatively accurate predictions of turbine performance. Their reliability allows properly defining the matching between turbocharger turbine and ICE in design working points, as described by Baines [78] or Payri et al. [79]. However, there is a need for better one-dimensional models to obtain reliable predictions in off-design conditions.

Some commercial software, such as GT-POWER, use semi-empirical one-dimensional models to predict the reduced mass flow and efficiency. The reduced mass flow rate depends on the blade speed ratio, and it is defined in Eq. 2.9. k_1

21

represents the mass flow rate at maximum efficiency, k_2 represents the reduced mass flow rate at zero blade speed ratio, k_3 represents the inverse of the blade speed ratio at maximum efficiency and k_4 represents an adjusting parameter that ranges from 2 to 4. The efficiency model is defined in Eq. 2.10, and it also depends on the blade speed ratio. It adds the k_5 parameter, representing an adjusting parameter ranging from 1.4 to 2.2. To model twin-entry turbines, GT-POWER adjusts these constants in multiple maps under different reduced *MFR* and interpolates between the results of these adjusted maps.

$$\dot{m}_{\mathrm{red}} = k_1 \cdot \left[k_2 + (1 - k_2) \cdot (k_3 \cdot \sigma)^{k_4} \right] \tag{2.9}$$

$$\eta_{\mathrm{t,s}} = \eta_{\mathrm{t,s,max}} \cdot \left[1 - (1 - k_3 \cdot \sigma)^{k_5} \right] \tag{2.10}$$

Some authors attempted to develop a more accurate one-dimensional model considering the different sources of losses found in turbocharger turbines. These losses reduce the power output from the ideal one in the efficiency computation. Romagnoli and Martínez-Botas [80] proposed a losses-based model that considered the pressure loss, swirl and blockage in the stator and the incidence, passage, tip clearance and disc friction losses in the rotor.

To model twin-entry turbines, Costall et al. [81] adapted the one-dimensional model of a single-entry turbine. The model considers the junction of the branches just downstream of the volutes, assessing there the mixing losses. This model could appropriately reproduce the twin-entry turbine performance under full admission conditions. However, it fails to predict the performance under unequal admission conditions adequately.

Chiong et al. [38] proposed five different approximations of different complexity to model the twin-entry turbine volutes. The model with the best performance implemented a junction at the volute tongue to allow interaction between the branches at that station. It provided relatively reliable results under full admission conditions. Following this work, Chiong et al. [82] also included the performance under partial admission conditions, showing better predictions in pulsating flow conditions [83].

One of the first attempts to develop a losses-based model was carried out by Fredriksson et al. [84]. This model takes into account the total pressure and angular momentum losses in the volutes and the stator, and the passage, incidence and tip losses in the rotor. Hajilouy-Benisi et al. [85] developed a losses-based model that considered the passage losses in the volutes and the interspace between volutes. The rotor sources of losses considered are incidence losses, passage losses, blade loading losses, tip clearance losses, mixing losses and exit losses. The model adequately predicts the twin-entry turbine performance under full admission conditions, but the predictions under unequal admission conditions are not as appropriate. Other authors, such as Xue et al.

[86], assessed how the losses were distributed within the twin-entry turbine, focusing on the formation of secondary flows to describe the differences under partial admission conditions.

Palenschat et al. [87] and Wei et al. [88, 89] developed similar one-dimensional losses-based models adapting a single-entry turbine one-dimensional model. They considered total pressure and swirl losses in the volutes, and passage, incidence, tip and disk friction losses in the rotor. They obtained accurate results under full and partial admission conditions. However, they still failed to predict the twin-entry turbine performance under unequal admission conditions adequately.

CMT-Motores Térmicos has developed its own turbocharger turbine one-dimensional model, which is included in the Virtual Engine Model (VEMOD) code. The twin-entry turbine model developed in the current work is based on the previously developed single-entry variable geometry turbine (VGT) model [79, 90, 91]. This single-entry model is a semi-empirical model.

The reduced mass flow rate is computed as defined in Eq. 2.11, considering the turbine as an equivalent nozzle defined by an effective area A_{Neq}. The area of the equivalent nozzle is estimated following Eq. 2.12, which depends on some geometrical parameters (i.e. the rotor inlet and outlet diameters, the throat area of the stator vanes $A_{2'}^{\mathrm{geom}}$ and the rotor outlet area A_4^{geom}), the blade speed ratio, the efficiency and 4 calibration coefficients (a, b, c and d) that must be adjusted employing experimental data. The d calibration coefficient is included through the term $\pi_{2',4}$, as defined in Eq. 2.13.

$$\dot{m}_{\mathrm{red}} = A_{\mathrm{Neq}} \cdot \sqrt{\frac{\gamma}{R}} \cdot \left(\frac{1}{\pi_{\exp}}\right)^{\frac{1}{\gamma}} \cdot \sqrt{\frac{2}{\gamma-1} \cdot \left[1 - \left(\frac{1}{\pi_{\exp}}\right)^{\frac{\gamma-1}{\gamma}}\right]} \tag{2.11}$$

$$A_{\mathrm{Neq}} = \frac{a \cdot A_4^{\mathrm{geom}} \cdot \sqrt{1 + \dfrac{\sigma^2 \cdot \left[\left(\dfrac{D_4}{D_3}\right)^2 - 1\right] + b}{\bar{\eta}_{\mathrm{t,s}}}}}{\sqrt{1 + \left(c \cdot \dfrac{A_4^{\mathrm{geom}}}{A_{2'}^{\mathrm{geom}}}\right)^2 \cdot \dfrac{\left(\dfrac{1}{\pi_{2',4}}\right)^2}{\left(1 - \bar{\eta}_{\mathrm{t,s}} \cdot \left[1 - \left(\dfrac{1}{\pi_{2',4}}\right)^{\frac{\gamma-1}{\gamma}}\right]\right)^2}}} \tag{2.12}$$

$$\pi_{2',4} = 1 + d \cdot \left[\pi_{\exp} - 1\right] \tag{2.13}$$

The efficiency is computed with Eq. 2.14. It depends on the blade speed ratio, geometrical parameters, the rotor inlet blade speed and some calibration coefficients included through the z parameter in the k_2 term defined in Eq. 2.15. The z parameter defined in Eq. 2.16 depends on 6 calibration coefficients (a', b', c', d', e', f'), the blade speed ratio, the reduced rotational speed and the VGT position.

$$\eta_{t,s} = -2 \cdot \left(\frac{r_4}{r_3}\right)^2 \cdot \sigma^2 + k_2 \cdot \left(1 - \frac{u_3^2}{2 \cdot C_p \cdot \sigma^2}\right)^{\frac{1}{\gamma-1}} \cdot \sigma \tag{2.14}$$

$$k_2 = 2 \cdot \frac{A_{\text{Neq}}}{A_0^{\text{geom}}} \cdot \left(z \cdot z_3^{\text{geom}} \cdot \sin \alpha_2^{\text{metal}} + \frac{r_4}{r_3} \cdot \tan \alpha_4^{metal}\right) \tag{2.15}$$

$$z = -\left(a' \cdot N_{\text{red}} + b'\right) \cdot \sigma + c' \cdot N_{\text{red}} + d' \cdot VGT^2 + e' \cdot VGT + f' \tag{2.16}$$

This model was adapted to work under pulsating flow conditions using a quasi-2D approximation to model the volutes [92, 93]. This approximation allows to properly capture the accumulation effects in the volutes, which are the reason for the turbine main non-quasi-steady behaviour.

Later, a losses-based one-dimensional model was developed to compute the VGT single-entry turbine efficiency [94]. The efficiency is obtained with a physical method that considers the different sources of losses instead of a semi-empirical method. Therefore, it can achieve better predictions of the turbine performance in off-design conditions. The efficiency is computed with Eq. 2.17. It depends on the turbine expansion ratio, the rotor expansion ratio, the enthalpy losses and the outlet meridional kinetic energy.

$$\eta_{t,s} = \frac{1 - \left(\frac{p_4}{p_{t,3}}\right)^{\frac{\gamma-1}{\gamma}} - \frac{c_{5,m}^2}{2 \cdot h_{t,0}} - \frac{\Delta h_{\text{loss,rot}}}{h_{t,0}} - \frac{\Delta h_{\text{loss,rot,tip}}}{h_{t,0}}}{1 - \left(\frac{p_5}{p_{t,0}}\right)^{\frac{\gamma-1}{\gamma}}} \tag{2.17}$$

This model considers losses in the stator, the interspace between stator outlet and rotor inlet and the rotor. The losses considered in the stator are passage losses and incidence losses, defined in Eq. 2.18 and 2.19, respectively. Both losses depend on the stator inlet kinetic energy and the difference between the stator inlet flow angle and the stator vane angle (i_1). The passage losses additionally depend on the stator outlet kinetic energy. Then, a fitting parameter (Z) for each source of losses must be adjusted with experimental data.

$$\frac{\Delta h_{\text{stat,pass}}}{h_{\text{t},0}} = Z_{\text{stat,pass}} \cdot \left(\cos(i_1)^2 \cdot \frac{c_1^2}{2 \cdot h_{\text{t},0}} + \frac{c_2^2}{2 \cdot h_{\text{t},0}} \right) \tag{2.18}$$

$$\frac{\Delta h_{\text{stat,inc}}}{h_{\text{t},0}} = Z_{\text{stat,inc}} \cdot \sin(i_1)^2 \cdot \frac{c_1^2}{2 \cdot h_{\text{t},0}} \tag{2.19}$$

The losses considered in the interspace between stator outlet and rotor inlet are passage losses, as defined in Eq. 2.20. In this case, the losses take into account the flow length of the streamline in the interspace (L_{int}), computed as the line integral of a logarithmic spiral. It also has a fitting parameter that must be adjusted with experimental data.

$$\frac{\Delta h_{\text{int}}}{h_{\text{t},0}} = Z_{\text{int}} \cdot L_{\text{int}} \cdot \frac{c_3^2}{2 \cdot h_{\text{t},0}} \tag{2.20}$$

The losses considered in the rotor are passage losses, incidence losses and tip leakage losses, defined in Eq. 2.21, 2.22 and 2.23. The passage and incidence losses depend on the rotor inlet relative kinetic energy and the difference between the rotor inlet flow angle and the optimum angle. Additionally, the passage losses depend on the rotor outlet relative kinetic energy and a fitting parameter. The tip losses depend on the incidence and friction driven tip leakage flow momentum (defined with the subscript -) and the pressure driven tip leakage flow momentum (defined with the subscript +). These losses include two fitting parameters through the relative kinetic energy terms that must be adjusted with experimental data.

$$\frac{\Delta h_{\text{rot,pass}}}{h_{\text{t},0}} = Z_{\text{rot,pass}} \cdot \left[\cos\left(\beta_3 - \beta_{3,\text{opt}}\right)^2 \cdot \frac{w_3^2}{2 \cdot h_{\text{t},0}} \cdot \frac{w_4^2}{2 \cdot h_{\text{t},0}} \right] \tag{2.21}$$

$$\frac{\Delta h_{\text{rot,inc}}}{h_{\text{t},0}} = \sin\left(\beta_3 - \beta_{3,\text{opt}}\right)^2 \cdot \frac{w_3^2}{2 \cdot h_{\text{t},0}} \tag{2.22}$$

$$\frac{\Delta h_{\text{rot,tip}}}{h_{\text{t},0}} = \frac{\dot{m}_{\text{tip},-}}{\dot{m}_{\text{turb}}} \cdot \frac{w_{\text{tip},\theta,-}^2}{2 \cdot h_{\text{t},0}} + \frac{\dot{m}_{\text{tip},+}}{\dot{m}_{\text{turb}}} \cdot \frac{w_{\text{tip},\theta,+}^2}{2 \cdot h_{\text{t},0}} \tag{2.23}$$

This losses model also considers discharge coefficients at the stator, interspace and rotor. Thus, it has a total of 8 fitting parameters to adjust with experimental data. The model provides reasonable extrapolations towards low expansion ratios and other VGT positions. Moreover, it can be applied to vaneless turbines skipping the stator outlet conditions.

In parallel to developing this losses-based single-entry turbine model, the semi-empirical single-entry turbine model was adapted to be employed in twin-entry turbines [95]. Twin-entry turbines are considered in the one-dimensional

model as two single-entry turbines working in parallel. This model computes the reduced mass flow employing the same equations that in the single-entry turbine (Eqs. 2.11 - 2.13), but computing it for each branch separately. The rotor inlet and rotor outlet areas for each branch are considered as half the total area. The efficiency is also computed for each branch separately, employing a slightly modified version of the equations employed in the single-entry turbine model (Eqs. 2.14 - 2.16). The z parameter is now defined as in Eq. 2.24, where the z' term described in Eq. 2.25 model the extra losses produced by the mixing of both flow branches (although it is not a physics-based model).

$$z = -b' \cdot \sigma + c' \cdot N_{\mathrm{red}} + f' + z' \tag{2.24}$$

$$z' = MFR \cdot \ln\left[(MFR - 0.5)^{k_0} + k_1 \cdot \sigma\right] \cdot \left[k_2 + k_3 \cdot \sigma \cdot N_{\mathrm{red}} - \frac{k_4 \cdot N_{\mathrm{red}}^2}{MFR - 0.5 + \sigma}\right] \tag{2.25}$$

The final semi-empirical efficiency model has a total of 11 fitting parameters: 5 of them are common for both branches (k_0, k_1, k_2, k_3 and k_4) and 3 additional parameters for each branch (b', c' and f').

This semi-empirical model has provided accurate predictions under different admission conditions. However, it could be possible to improve it by adapting the losses-based model for single-entry turbines to twin-entry turbines, which is an objective of the current work.

There are twin-entry turbine models such as this semi-empirical model that provide relatively good performance predictions. However, their worst predictions are under unequal admission conditions. So, physical models that considers the effects of the interaction between branches could provide better predictions under unequal admission conditions. This thesis presents flow capacity and efficiency models that consider this interaction between branches and improve the results of other state-of-the-art twin-entry turbine models.

2.6 Summary

This chapter presents the main parameters to describe the performance of twin-entry turbines. It also presents a literature review of relevant researches about twin-entry turbines divided into three approaches: experimental characterisation, CFD characterisation and one-dimensional models.

Few experimental works measuring twin-entry turbines under unequal admission conditions have been found in the literature. Since there is a gas stand designed specifically to measure twin-entry turbines in CMT-Motores Térmicos, it would be relevant to perform different experimental measurements under unequal admission conditions to obtain wider performance maps and be able to validate the CFD simulations and the models developed. These tests are described in Chapter 3.

There are numerous researches about CFD simulations of twin-entry turbines under full and partial admission conditions assessing some interesting physical phenomena. However, few CFD analyses under unequal admission conditions have been found. It would be important to carry out CFD simulations to understand the physical phenomena in these cases since they are the most frequent in realistic operating conditions. These CFD simulations are described and shown in Chapter 4 and Chapter 5.

The one-dimensional models of single-entry turbines are thoroughly investigated even in off-design conditions. However, current state-of-the-art twin-entry turbine models do not predict their performance under unequal admission conditions as well as they do under full or partial admission conditions. An empirical model to predict the twin-entry turbine performance has been developed previously in CMT-Motores Térmicos. However, a losses-based model that provides more suitable predictions could be developed with a more thorough analysis of the phenomena observed in the CFD simulations. The methodology to develop this losses-based model could be similar to the previously used to develop a losses-based model for single-entry turbines [94]. Chapter 6 describes in detail this losses-based model.

2.7 References

[6] European Comission. *Emissions in the automotive sector*. 2018. URL: https://ec.europa.eu/growth/sectors/automotive/environment-protection/emissions_en (cit. on pp. 2, 14).

[7] Environmental Protection Agency. *Environmental protection agency control of air pollution from motor vehicles: Tier 3 motor vehicle emission and fuel standards*. 2015. URL: https://www.epa.gov/regulations-emissions-vehicles-and-engines/final-rule-control-air-pollution-motor-vehicles-tier-3 (cit. on pp. 2, 14).

[8] H. Gong, Y. Ge, J. Wang, and H. Yin. "Light-duty vehicle emissions control: a brief introduction to the China 6 emissions standard". In: *Johnson Matthey Technology Review* 61 (2017), pp. 269–278. DOI: 10.1595/205651317X696199 (cit. on pp. 2, 14).

[25] A. P. Carlucci, A. Ficarella, D. Laforgia, and A. Renna. "Supercharging system behavior for high altitude operation of an aircraft 2-stroke diesel engine". In: *Energy Conversion and Management* 101 (2015), pp. 470–480. DOI: 10.1016/j.enconman.2015.06.009 (cit. on p. 14).

[26] A. Luongo, P. Nuccio, and M. Vignoli. "Optimization of a light aircraft spark-ignition engine". In: *SAE Technical Paper Series*. Vol. Paper No: 2006-01-2420. SAE International, Aug. 2006. DOI: 10.4271/2006-01-2420 (cit. on p. 14).

[27] A. Keromnes, B. Delaporte, G. Schmitz, and L. L. Moyne. "Development and validation of a 5 stroke engine for range extenders application". In: *Energy Conversion and Management* 82 (2014), pp. 259–267. DOI: 10.1016/j.enconman.2014.03.025 (cit. on p. 14).

[28] D. S. Puma-Benavides, J. Izquierdo-Reyes, J. de Dios Calderon-Najera, and R. A. Ramirez-Mendoza. "A systematic review of technologies, control methods, and optimization for extended-range electric vehicles". In: *Applied Sciences* 11.15 (July 2021), p. 7095. DOI: 10.3390/app11157095 (cit. on p. 14).

[29] A. Falcao, L. Gato, J. Henriques, J. Borges, B. Pereiras, and F. Castro. "A novel twin-rotor radial-inflow air turbine for oscillating-watercolumn wave energy converters". In: *Energy* 93 (2015), pp. 2116–2125. DOI: 10.1016/j.energy.2015.10.046 (cit. on p. 14).

[30] T. Setoguchi, S. Santhakumar, M. Takao, T. H. Kim, and K. Kaneko. "A performance study of a radial turbine for wave energy conversion". In: *Proceedings of the Institution of Mechanical Engineers, Part A: Journal of Power and Energy* 216.1 (Feb. 2002), pp. 15–22. DOI: 10.1243/095765002760024917 (cit. on p. 14).

[31] M. Malin, C. Redtenbacher, G. Lurf, N. Wermuth, and A. Wimmer. "Evaluation of strategies for highly transient operation of diesel-gas engines". In: *Internal Combustion Engine Division Fall Technical Conference*. Vol. Volume 1: Large Bore Engines; Fuels; Advanced Combustion. Paper No: ICEF2018-9710, V001T01A010. ASME, 2018. DOI: 10.1115/ICEF2018-9710 (cit. on p. 14).

[32] K. Ntonas, N. Aretakis, I. Roumeliotis, E. Pariotis, Y. Paraskevopoulos, and T. Zannis. "Integrated simulation framework for assessing turbocharger fault effects on diesel-engine performance and operability". In: *Journal of Energy Engineering* 146.4 (Aug. 2020), p. 04020023. DOI: 10.1061/(asce)ey.1943-7897.0000673 (cit. on p. 14).

[33] T. Yamamoto, T. Furuhata, N. Arai, and K. Mori. "Design and testing of the Organic Rankine Cycle". In: *Energy* 26 (2001), pp. 239–251. DOI: 10.1016/S0360-5442(00)00063-3 (cit. on p. 14).

[34] S. H. Kang. "Design and experimental study of ORC (Organic Rankine Cycle) and radial turbine using R245fa working fluid". In: *Energy* 41 (2012), pp. 514–524. DOI: 10.1016/j.energy.2012.02.035 (cit. on p. 14).

[35] W. El-Khattam and M. Salama. "Distributed generation technologies, definitions and benefits". In: *Electric Power Systems Research* 71 (2004), pp. 119–128. DOI: 10.1016/j.epsr.2004.01.006 (cit. on p. 14).

[36] E. Facchinetti, D. Favrat, and F. Marechal. "Design and optimization of an innovative solid oxide fuel cell gas turbine hybrid cycle for small scale distributed generation". In: *Fuell Cells* 14 (2014), pp. 595–606. DOI: 10.1002/fuce.201300196 (cit. on p. 14).

[37] N. Fraser, H. Blaxill, G. Lumsden, and M. Bassett. "Challenges for increased efficiency through gasoline engine downsizing". In: *SAE International Journal of Engines* 2 (2009), pp. 991–1008. DOI: 10.4271/2009-01-1053 (cit. on p. 14).

[38] M. S. Chiong, S. Rajoo, R. F. Martinez-Botas, and A. W. Costall. "Engine turbocharger performance prediction: One-dimensional modelling of a twin entry turbine". In: *Energy Conversion and Management* 57 (2012), pp. 68–78. DOI: 10.1016/j.enconman.2011.12.001 (cit. on pp. 16, 22).

[39] A. Romagnoli, C. D. Copeland, R. Martinez-Botas, M. Seiler, S. Rajoo, and A. Costall. "Comparison between the steady performance of double-entry and twin-entry turbocharger turbines". In: *Journal of Turbomachinery* 135.1 (Oct. 2012). DOI: 10.1115/1.4006566 (cit. on pp. 16, 18).

[40] T. Uhlmann, D. Lückmann, R. Aymanns, J. Scharf, B. Höpke, M. Scassa, O. Rütten, N. Schorn, and H. Kindl. "Development and matching of double entry turbines for the next generation of highly boosted gasoline engines". In: *Anais do XXII Simpósio Internacional de Engenharia Automotiva*. Vol. 1. 2. Editora Edgard Blücher, Aug. 2014. DOI: 10.5151/eng pro-simea2014-100 (cit. on p. 16).

[41] SAE. *Supercharger testing standard*. SAE J1723. Society of Automotive Engineers, Aug. 1995 (cit. on p. 18).

[42] SAE. *Turbocharger gas stand test code*. SAE J1826. Society of Automotive Engineers, Mar. 1995 (cit. on p. 18).

[43] J. M. Luján, V. Bermúdez, J. R. Serrano, and C. Cervelló. *Test bench for turbocharger groups characterization*. SAE Technical Paper 2002-01-0163. SAE International, Mar. 2002. DOI: 10.4271/2002-01-0163 (cit. on p. 18).

[44] J. R. Serrano, A. Tiseira, L. M. García-Cuevas, L. B. Inhestern, and H. Tartoussi. "Radial turbine performance measurement under extreme off-design conditions". In: *Energy* 125 (Apr. 2017), pp. 72–84. DOI: 10.10 16/j.energy.2017.02.118 (cit. on p. 18).

[45] H. Aghaali and A. Hajilouy-Benisi. "Experimental and theoretical investigation of twin-entry radial inflow gas turbine with unsymmetrical volute under full and partial admission conditions". In: *Turbo Expo: Power for Land, Sea and Air*. Paper No: GT2007-27807. ASME, Jan. 2007, pp. 1099–1107. DOI: 10.1115/GT2007-27807 (cit. on p. 18).

[46] N. Brinkert, S. Sumser, S. Weber, K. Fieweger, A. Schulz, and H. J. Bauer. "Understanding the twin scroll turbine: flow similarity". In: *Journal of Turbomachinery* 135 (2 2013), p. 021039. DOI: 10.1115/1.4006607 (cit. on p. 18).

[47] A. Romagnoli, R. F. Martinez-Botas, and S. Rajoo. "Steady state performance evaluation of variable geometry twin-entry turbine". In: *International Journal of Heat and Fluid Flow* 32.2 (2011), pp. 477–489. DOI: 10.1016/j.ijheatfluidflow.2010.12.002 (cit. on p. 18).

[48] V. Usai and S. Marelli. "Steady state experimental characterization of a twin entry turbine under different admission conditions". In: *Energies* 14.8 (Apr. 2021), p. 2228. DOI: 10.3390/en14082228 (cit. on p. 18).

[49] J. R. Serrano, F. J. Arnau, L. M. García-Cuevas, V. Samala, and L. Smith. "Experimental approach for the characterization and performance analysis of twin entry radial-inflow turbines in a gas stand and with different flow admission conditions". In: *Applied Thermal Engineering* 159 (2019).

DOI: 10.1016/j.applthermaleng.2019.113737 (cit. on pp. 19, 39, 40, 87, 129, 211).

[50]   J. R. Serrano, F. J. Arnau, L. M. García-Cuevas, P. Soler, L. Smith, R. Cheung, and B. Pla. "An experimental method to test twin and double entry automotive turbines in realistic engine pulse conditions". In: *SAE Technical Papers* (2019). DOI: doi:10.4271/2019-01-0319 (cit. on p. 19).

[51]   J. R. Serrano, F. J. Arnau, L. M. García-Cuevas, and P. Soler. "Experimental validation of a one-dimensional twin-entry radial turbine model under non-linear pulse conditions". In: *International Journal of Engine Research* (2019). DOI: 10.1177/1468087419869157 (cit. on p. 19).

[52]   R. Morrison, C. Stuart, S. I. Kim, S. Spence, A. Starke, and T. Leonard. "Investigation of a novel turbine housing to produce a non-uniform span-wise flow field at the inlet to a mixed flow turbine and provide variable geometry capabilities". In: *Proceedings of the ASME Turbo Expo 2021: Turbomachinery Technical Conference and Exposition*. Vol. Volume 2D: Turbomachinery - Multidisciplinary Design Approaches, Optimization, and Uncertainty Quantification; Radial Turbomachinery Aerodynamics; Unsteady Flows in Turbomachinery. American Society of Mechanical Engineers, June 2021. DOI: 10.1115/gt2021-59382 (cit. on p. 19).

[53]   J. Jin, J. Pan, Z. Lu, Q. Wu, and L. Xu. "Effect of balance valve on an asymmetric twin-scroll turbine for heavy-duty diesel engine." In: *International Journal of Engine Research* (2020). DOI: 10.1177/1468087420930162 (cit. on p. 19).

[54]   J. H. Yeo and N. C. Baines. "Laser velocity measurements in a twin-entry vaneless radial turbocharger turbine." In: *JSME International Journal Series B* 37.4 (1994), pp. 861–870. DOI: 10.1299/jsmeb.37.861 (cit. on p. 19).

[55]   R. Aghaei, A. M. Tousi, and A. Tourani. "Comparison of turbulence methods in CFD analysis of compressible flows in radial turbomachines". In: *Aircraft Engineering and Aerospace Technology: An International Journal* (2008), pp. 657–665. ISSN: 0002-2667. DOI: 10.1108/00022660810911608 (cit. on p. 20).

[56]   F. R. Menter. "Two-equation eddy-viscosity turbulence models for engineering applications". In: *AIAA journal* 32.8 (1994), pp. 1598–1605. DOI: 10.2514/3.12149 (cit. on p. 20).

[57]   F. R. Menter, R. Langtry, and T. Hansen. "CFD simulation of turbo-machinery flows - verification, validation and modelling". In: *European Congress on Computational Methods in Applied Sciences and Engineering*. Ed. by ECCOMAS2004. 2004 (cit. on p. 20).

[58]   J. Galindo, S. Hoyas, P. Fajardo, and R. Navarro. "Set-up analysis and optimization of CFD simulations for radial turbines". In: *Engineering Applications of Computational Fluid Mechanics* 7 (2013), pp. 441–460. DOI: 10.1080/19942060.2013.11015484 (cit. on pp. 20, 73).

[59]   M. Cerdoun and A. Ghenaiet. "Characterization of a twin-entry radial turbine under pulsatile flow condition". In: *International Journal of Rotating Machinery* (2016), pp. 1–15. DOI: 0.1155/2016/4618298 (cit. on p. 20).

[60]   J. Galindo, P. Fajardo, R. Navarro, and L. M. García-Cuevas. "Characterization of a radial turbocharger turbine in pulsating flow by means of CFD and its application to engine modelling". In: *Applied Energy* 103 (2013), pp. 116–127. DOI: 10.1016/j.apenergy.2012.09.013 (cit. on p. 20).

[61]   J. Fürst and Z. Žák. "CFD analysis of a twin scroll radial turbine". In: *EPJ Web of Conferences*. Vol. 180. 2018. DOI: 10.1051/epjconf/201818 002028 (cit. on p. 20).

[62]   D. Palfreyman and R. F. Martinez-Botas. "The pulsating flow field in a mixed flow turbocharger turbine: An experimental and computational study". In: *Journal of turbomachinery* 127 (1 2005), pp. 144–155. DOI: 10.1115/1.1812322 (cit. on p. 20).

[63]   H. Jasak and M. Beaudoin. "OpenFOAM Turbo tools: from general purpose CFD to turbomachinery simulations". In: *ASME-JSME-KSME 2011 Joint Fluids Engineering Conference*. Vol. Volume 1, Symposia - Parts A, B, C, and D. ASMEDC, Jan. 2011. DOI: 10.1115/ajk2011-05015 (cit. on p. 20).

[64]   T. Yokoyama, T. Hoshi, T. Yoshida, and K. Wakashima. "Development of twin-entry scroll radial turbine for automotive turbochargers using unsteady numerical simulation". In: *11th International Conference on Turbochargers and Turbocharging* (2014), pp. 471–478. DOI: 10.1533/9 78081000342.471 (cit. on p. 20).

[65]   A. Wang and X. Zheng. "Design criterion for asymmetric twin-entry radial turbine for efficiency under steady and pulsating inlet conditions". In: *Proceedings of the Institution of Mechanical Engineers, Part D: Journal of Automobile Engineering* 233.8 (Mar. 2018), pp. 2246–2256. DOI: 10.1177/0954407018757926 (cit. on p. 20).

[66] B. M. Menaouar, H. Mohamed, B. Mohamed, G. Ahmed, and H. M. Kamel. "The separation wall effect of a volute twin entry cross section area on the mixed inflow turbine performance." In: *Engineering Review* 41 (2020), pp. 11–20. DOI: 10.30765/er.1383 (cit. on p. 20).

[67] H. Fan, J. Ni, X. Shi, D. Qu, Y. Zheng, and Y. Zheng. "Simulation optimization of a new twin-entry turbocharger turbine with double incidence angles". In: *Journal of Engineering for Gas Turbines and Power* 141.5 (Mar. 2019). DOI: 10.1115/1.4041315 (cit. on p. 20).

[68] E. Chebli, M. Casey, R. Martinez-Botas, S. Sumser, M. Müller, S. Künzel, J. Leweux, A. Gorbach, and W. Schmidt. "The variable outlet turbine concept for turbochargers". In: *Journal of Turbomachinery* 136.12 (Aug. 2014). DOI: 10.1115/1.4028231 (cit. on p. 20).

[69] M. M. Bencherif, M. K. Hamidou, M. Hamel, and M. Abidat. "Study of unsteady performance of a twin-entry mixed flow turbine". In: *Journal of Applied Mechanics and Technical Physics* 57.2 (Mar. 2016), pp. 300–307. DOI: 10.1134/s0021894416020139 (cit. on p. 21).

[70] C. Cravero, D. D. Domenico, and A. Ottonello. "Numerical simulation of the performance of a twin scroll radial turbine at different operating conditions". In: *International Journal of Rotating Machinery* 2019 (June 2019), pp. 1–13. DOI: 10.1155/2019/5302145 (cit. on p. 21).

[71] A. Ghenaiet and M. Cerdoun. "Simulations of steady and unsteady flows through a twin-entry radial turbine". In: *Turbo Expo: Power for Land, Sea and Air*. Vol. Paper No: GT2014-25764. ASME, 2014. DOI: 10.1115/GT2014-25764 (cit. on p. 21).

[72] M. Müller, T. Streule, S. Sumser, G. Hertweck, A. Nolte, and W. Schmid. "The asymmetric twin scroll turbine for exhaust gas turbochargers". In: *Proceedings of ASME Turbo Expo 2008: Power for Land, Sea and Air*. Vol. Volume 6: Turbomachinery, Parts A, B, and C. ASMEDC, Jan. 2008. DOI: 10.1115/gt2008-50614 (cit. on p. 21).

[73] A. Cravero and A. Ottonello. "Uncertainty quantification methodologies applied to the rotor tip clearance effect in a twin scroll radial turbine." In: *Fluids* 5 (2020). DOI: 10.3390/fluids5030114 (cit. on p. 21).

[74] A. Hajilouy-Benisi, M. Rad, and M. R. Shahhosseini. "Flow and performance characteristics of twin-entry radial turbine under full and extreme partial admission conditions". In: *Archive of Applied Mechanics* 79.12 (Jan. 2009), pp. 1127–1143. DOI: 10.1007/s00419-008-0295-5 (cit. on p. 21).

[75] Y. Xue, M. Yang, R. F. Martinez-Botas, B. Yang, and K. Deng. "Unsteady performance of a mixed-flow turbine with nozzled twin-entry volute confronted by pulsating incoming flow". In: *Aerospace Science and Technology* 95 (2019). DOI: 10.1016/j.ast.2019.105485 (cit. on p. 21).

[76] M. Cerdoun and A. Ghenaiet. "Unsteady behaviour of a twin entry radial turbine under engine like inlet flow conditions". In: *Applied Thermal Engineering* 130 (2018), pp. 93–111. DOI: 10.1016/j.applthermaleng.2017.11.001 (cit. on pp. 21, 96).

[77] T. Palenschat, P. Newton, R. F. Martinez-Botas, M. Müller, and J. Leweux. "3-D Computational loss analysis of an asymmetric volute twin-scroll turbocharger". In: *Proceedings of ASME Turbo Expo 2017: Turbomachinery Technical Conference and Exposition*. Vol. Volume 8: Microturbines, Turbochargers and Small Turbomachines; Steam Turbines. American Society of Mechanical Engineers, June 2017. DOI: 10.1115/gt2017-64190 (cit. on p. 21).

[78] N. Baines. "Turbocharger turbine pulse flow performance and modelling - 25 years on". In: *9th International conference on turbochargers and turbocharging*. 2010, pp. 347–362 (cit. on p. 21).

[79] F. Payri, J. R. Serrano, P. Fajardo, M. A. Reyes-Belmonte, and R. Gozalbo-Belles. "A physically based methodology to extrapolate performance maps of radial turbines". In: *Energy Conversion and Management* 55 (Mar. 2012), pp. 149–163. DOI: 10.1016/j.enconman.2011.11.003 (cit. on pp. 21, 23, 131).

[80] A. Romagnoli and R. Martinez-Botas. "Performance prediction of a nozzled and nozzleless mixed-flow turbine in steady conditions". In: *International Journal of Mechanical Sciences* 53.8 (2011), pp. 557–574. ISSN: 0020-7403. DOI: 10.1016/j.ijmecsci.2011.05.003 (cit. on p. 22).

[81] A. W. Costall, R. M. McDavid, R. F. Martinez-Botas, and N. C. Baines. "Pulse performance modeling of a twin entry turbocharger turbine under full and unequal admission". In: *Journal of Turbomachinery* 133.2 (Oct. 2010). DOI: 10.1115/1.4000566 (cit. on p. 22).

[82] M. S. Chiong, S. Rajoo, A. Romagnoli, A. W. Costall, and R. F. Martinez-Botas. "Assessment of partial-admission characteristics in twin-entry turbine pulse performance modelling". In: *Proceedings of ASME Turbo Expo 2015*. Vol. Volume 2C: Turbomachinery. American Society of Mechanical Engineers, June 2015. DOI: 10.1115/gt2015-42687 (cit. on p. 22).

[83] M. S. Chiong, S. Rajoo, A. Romagnoli, A. W. Costall, and R. F. Martinez-Botas. "One-dimensional pulse-flow modeling of a twin-scroll turbine". In: *Energy* 115 (Nov. 2016), pp. 1291–1304. DOI: 10.1016/j.energy.2016.09.041 (cit. on pp. 22, 142).

[84] C. F. Fredriksson, X. Qiu, N. C. Baines, M. Müller, N. Brinkert, and C. Gutmann. "Meanline modeling of radial inflow turbine with twin-entry scroll". In: *Proceedings of ASME Turbo Expo 2012*. Vol. Volume 5: Manufacturing Materials and Metallurgy; Marine; Microturbines and Small Turbomachinery; Supercritical CO2 Power Cycles. American Society of Mechanical Engineers, June 2012. DOI: 10.1115/gt2012-69018 (cit. on p. 22).

[85] A. Hajilouy-Benisi, M. Rad, and M. R. Shahhosseini. "Modeling of twin-entry radial turbine performance characteristics based on experimental investigation under full and partial admission conditions". In: *Scientia Iranica* (2009), pp. 281–290. URL: http://scientiairanica.sharif.edu/article_3231.html (cit. on pp. 22, 108).

[86] Y. Xue, M. Yang, R. F. Martinez-Botas, A. Romagnoli, and K. Deng. "Loss analysis of a mix-flow turbine with nozzled twin-entry volute at different admissions". In: *Energy* 166 (Jan. 2019), pp. 775–788. DOI: 10.1016/j.energy.2018.10.075 (cit. on p. 23).

[87] T. Palenschat, M. Mueller, S. Rajoo, M. S. Chiong, P. Newton, R. Martinez-Botas, and F. X. Tan. "Steady-state experimental and meanline study of an asymmetric twin-scroll turbine at full and unequal and partial admission conditions". In: *SAE Technical Paper* (2018). DOI: 10.4271/2018-01-0971 (cit. on pp. 23, 108, 116).

[88] J. Wei, Y. Xue, K. Deng, M. Yang, and Y. Liu. "A direct comparison of unsteady influence of turbine with twin-entry and single-entry scroll on performance of internal combustion engine." In: *Energy* 212 (2020), pp. 93–111. DOI: 10.1016/j.energy.2020.118638 (cit. on p. 23).

[89] J. Wei, Y. Xue, M. Yang, K. Deng, C. Wang, and X. Wu. "A reduced-order model of twin-entry nozzleless radial turbine based on flow characteristics". In: *Energy* 214 (Jan. 2021), p. 118890. DOI: 10.1016/j.energy.2020.118890 (cit. on p. 23).

[90] J. R. Serrano, F. J. Arnau, V. Dolz, A. Tiseira, and C. Cervelló. "A model of turbocharger radial turbines appropriate to be used in zero- and one-dimensional gas dynamics codes for internal combustion engines modelling". In: *Energy Conversion and Management* 49.12 (Dec. 2008), pp. 3729–3745. DOI: 10.1016/j.enconman.2008.06.031 (cit. on p. 23).

[91]   J. R. Serrano, F. J. Arnau, L. M. García-Cuevas, A. Dombrovsky, and H. Tartoussi. "Development and validation of a radial turbine efficiency and mass flow model at design and off-design conditions". In: *Energy Conversion and Management* 128 (2016), pp. 281–293. DOI: 10.1016/j.enconman.2016.09.032 (cit. on pp. 23, 131).

[92]   J. Galindo, A. Tiseira, P. Fajardo, and L. M. García-Cuevas. "Development and validation of a radial variable geometry turbine model for transient pulsating flow applications". In: *Energy Conversion and Management* 85 (2014), pp. 190–203. DOI: 10.1016/j.enconman.2014.05.072 (cit. on pp. 24, 92).

[93]   A. Torregrosa, L. M. García-Cuevas, L. Inhestern, and P. Soler. "Radial turbine sound and noise characterisation with acoustic transfer matrices by means of fast one-dimensional models". In: *International Journal of Engine Research* (2019). DOI: 10.1177/1468087419889429 (cit. on p. 24).

[94]   J. R. Serrano, F. J. Arnau, L. M. García-Cuevas, and L. B. Inhestern. "An innovative losses model for efficiency map fitting of vaneless and variable vaned radial turbines extrapolating towards extreme off-design conditions". In: *Energy* 180 (2019), pp. 626–639. DOI: 10.1016/j.energy.2019.05.062 (cit. on pp. 24, 27, 139, 210).

[95]   J. R. Serrano, F. J. Arnau, L. M. García-Cuevas, and V. Samala. "A robust adiabatic model for a quasi-steady prediction of far-off non-measured performance in vaneless twin-entry or dual-volute radial turbines". In: *Applied Sciences* 10.1955 (2020). DOI: 10.3390/app10061955 (cit. on pp. 25, 193).

Experimental tests in twin-entry turbines

Contents

Figures

Tables

3.1   Introduction

T WIN-ENTRY turbines can be analysed with several tools, and sometimes these tools are combined. In the current thesis, experimental measurements and CFD simulations are combined, obtaining first the experimental measurements for later comparison and validation of the CFD simulations and the one-dimensional models proposed.

Experimental measurements are always necessary for validating these CFD simulations and models since, as they are based on extensive simplifications of the actual physics, they are not reliable enough on their own. Therefore, steady-state measurements can be obtained for global validation. In addition, it is possible to measure certain regions of the twin-entry turbine for local validation of some results. As observed in the previous chapter, it is especially relevant to perform these measurements under unequal admission conditions to obtain wider performance maps and analyse the flow behaviour in these cases.

This chapter presents first the main characteristics of the twin-entry turbine measured and describes the test bench used for measuring it. Then, the setup for the steady-state measurements as well as the experimental measurements obtained are described. Finally, the setup for performing local measurements at the outlet with a Laser Doppler Anemometry (LDA) technique as well as the outlet temperature measurements at different depths are exposed.

3.2   Twin-entry turbine

The twin-entry turbine measured in the current work is shown in Fig. 3.1. It has asymmetrical entries as shown in Fig. 3.2. Hub branch is the branch that discharges the air near the rotor hub, and shroud branch is the branch that discharges the air near the rotor shroud. This twin-entry turbine also has a wastegate. However, the wastegate is kept closed in all the measurements of the current work, as analysing and modelling its behaviour is out of the scope of this thesis.

This twin-entry turbine is used in a four-cylinder gasoline engine. Its main geometrical parameters are summarised in Table 3.1.

3.3   Test bench

The experimental measurements have been carried out in a test facility at CMT-Motores Térmicos. As explained in Serrano et al. [49], twin-entry turbines are typically measured at full and partial admission conditions. The flow at partial admission conditions passes only through one branch. The same flow passes through both branches at full admission conditions. The whole range

Figure 3.1: Twin-entry turbine entries and rotor
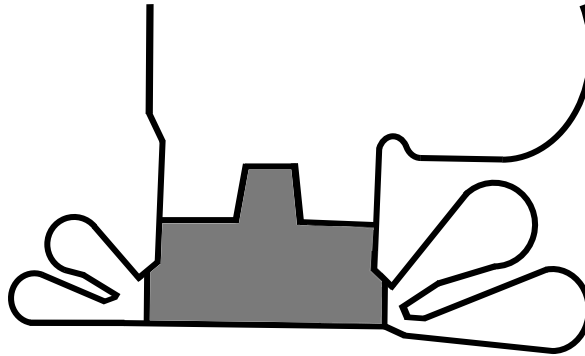
Figure 3.2: Radial view of the twin-entry turbine

of unequal admission conditions were measured using the test rig proposed in Serrano et al. [49].

A scheme of the test bench used is shown in Fig. 3.3 and its different parts are summarised in Table 3.2. The main parts of the test bench are the compressor to feed the system (Compressor), the turbocharger (C and T) and the lubricant system (LS). A combustion chamber (CC) able to reach temperatures up to 1200 K and a coolant system (CS) are also available in the test bench, but they are not used in the current work. All the measurements have been carried out at nearly ambient conditions. Although the actual turbine temperature boundary conditions are higher, these colder conditions should be representative of the flow patterns and the losses mechanisms found in twin-entry turbines. The possible thermal stress problems in the turbine materials when reaching high temperatures are out of the scope of this work since it is focused on the flow behaviour. Moreover, all performance parameters are reduced to avoid the dependence on the temperature conditions. Therefore, the twin-entry performance maps at nearly ambient conditions are expected to be similar to the ones

Table 3.1: Twin-entry turbine geometrical parameters and engine parameters.

Parameter	Value
Rotor inlet diameter [mm]	45.1
Rotor outlet diameter [mm]	40.9
Rotor nose diameter [mm]	12.1
Number of blades	9
Blade inlet height [mm]	6.6
Blade inlet angle [deg]	0
Mean blade outlet angle [deg]	56
Mean blade thickness [mm]	1.2
Mean tip clearance [mm]	0.39
Hub branch inlet area [mm^2]	369
Shroud branch inlet area [mm^2]	290
Hub branch A/R [m]	0.0071
Shroud branch A/R [m]	0.0058
Engine type	Gasoline
Car segment	D
Number of cylinders	4
Engine displacement [L]	2

at hotter conditions.

The compressor used to feed the system is an oil-free, two-stage, radial compressor. It is powered by a 450 kW electric motor, and the maximum pressure that it can provide is 5 bar. The compressed air pressure and mass flow rate can be controlled electronically by a set of bleeding valves (VBs) and two general valves (VG1 and VG2). A high-volume plenum after the general valves allows the mass flow to be stabilised.

There are two valves downstream of the plenum used to choose between heating the mass flow in the combustion chamber (VCC) or measuring in cold conditions (VCS). There are also other discharge valves for controlling the mass flow rate in the hot line (Vbypass) and the cold line (VIC).

After these valves, the compressed air is split into two independent sets of pipe-work. Each set is only connected to one entry of the twin-entry turbine. The mass flow passing through each of them can be controlled with two valves (VT1 and VT2). These valves measure a whole range of mass flow admission conditions of the twin-entry turbine, including unequal admission conditions.

Then, the air is expanded in the twin-entry turbine (T). It moves the compressor (C), which is connected to the ambient. The pressure ratio of the compressor can be controlled electronically with back-pressure valves (Vbp1 and Vbp2).
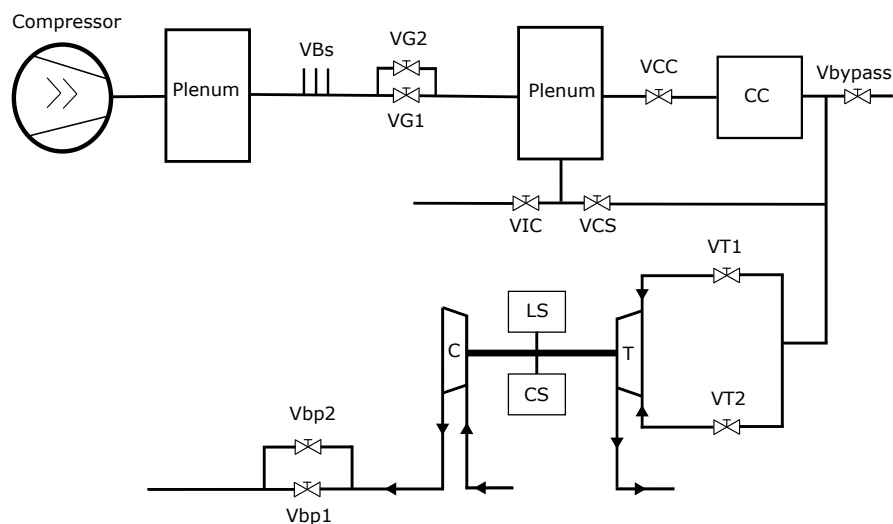
Figure 3.3: Test bench scheme

Table 3.2: Different parts of the test bench.

Part	Action	Symbol
Feeding Compressor	Feed air to the system	Compressor
Bleeding valves	Discharge compressed air	VBs
General valve 1	Control pressure and mass flow	VG1
General valve 2	Control pressure and mass flow	VG2
Plenum	Stabilise the flow	Plenum
Combustion chamber	Heat the air	CC
Comb. chamber valve	Control hot/cold air	VCC
Cold air valve	Control hot/cold air	VCS
Discharge valve	Discharge compressed air	VIC
Bypass valve	Control comb. chamber outlet	Vbypass
Turbine inlet valve 1	Control flow through inlet 1	VT1
Turbine inlet valve 2	Control flow through inlet 2	VT2
Turbocharger turbine	Expand the air	T
Turbocharger compressor	Compress the air	C
Lubricant system	Lubricate the turbocharger	LS
Coolant system	Cooling the systems	CS
Backpressure valve 1	Control compressor backpressure	Vbp1
Backpressure valve 2	Control compressor backpressure	Vbp2

Therefore, the compressor working point can be chosen from choke to surge conditions.

The turbocharger has an independent lubrication system. This lubrication system includes an electrical heater for controlling the oil temperature. The oil mass flow can also be controlled with a piloted valve along with a recirculation circuit.

All pipes connected to the turbocharger and the turbocharger itself are insulated to ensure the losses due to heat transfer to the ambient are minimized and to achieve the most adiabatic conditions. Fig. 3.4 shows how these parts are insulated.
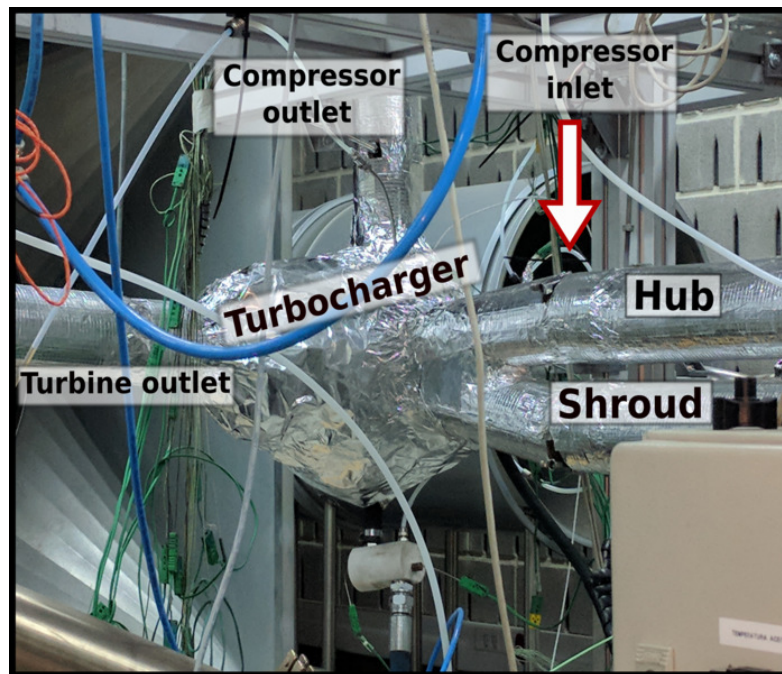
Figure 3.4: Test bench insulation

The sensors used to obtain measurements and their range and expanded uncertainty are summarised in Table 3.3. The expanded uncertainty is computed with a coverage factor of 3 for normal distributions. It is used on the basis of a level of confidence of 99.7% of the real values of the measurements [96].

The air mass flow upstream and downstream of the turbine is measured using V-cone type sensors. Upstream of the twin-entry turbine, there is one V-cone in each branch for measuring independently the mass flow passing through each branch. Downstream of the turbine, another V-cone is placed to measure the total mass flow passing through the turbine. The mass flow upstream of the compressor is measured with a hot-plate flow-meter. Moreover, the mass flow

Table 3.3: Test bench measurement sensors and precision.

Variable	Sensor type	Range	Expanded uncertainty
Gas mass flow	V-cone, Thermal and Vortex	45-1230 $\mathrm{kg\,h^{-1}}$	$\leq 2\%$
Gas pressure	Piezoresistive	0-500 kPa	12.5 hPa
Gas/metal temperature	K-type thermocouple	273-1500 K	1.5 K
Turbocharger speed	Inductive sensor	≤ 300 krpm	500 rpm
Oil Temperature	RTD	173-723 K	≤ 0.5 K
Oil mass flow	Coriolis-type	Few tens $\mathrm{g\,s^{-1}}$	2%

downstream of the compressor is measured with a vortex type meter.

Pressure at both twin entry turbine inlets, turbine outlet and compressor inlet and outlet are measured with piezoresistive sensors. Temperature is also measured at the same sections using arrays of four K-type thermocouples. Rotational speed of the turbocharger is measured using an inductive sensor.

Temperature of the lubrication system is measured with low uncertainty platinum resistance temperature detectors, and oil mass flow is measured with a Coriolis-type flow meter.

Moreover, the average and maximum uncertainty of the measured and computed turbine variables are also calculated and exposed in Table 3.4 according to the method described by Olmeda et al. [96]. These values are computed over the whole range of operating conditions measured.

3.4 Steady-state measurements

Steady-state measurements are carried out within the range of *MFR* values, measuring at partial, full and several unequal admission conditions. Moreover, the same measurements are also carried out at different rotational speeds. The *MFR* and reduced rotational speed values measured are indicated in Table 3.5. Different expansion ratios were measured for each *MFR* and reduced rotational speed for a total of 233 different working points.

The steady-state measurements are shown in Fig. 3.5 and Fig. 3.6. Fig. 3.5 shows the flow capacity map, plotting the reduced mass flow ($\dot{m}_{\mathrm{red}}$) against the expansion ratio (π_{exp}). Fig. 3.6 shows the apparent efficiency map, plotting it against the blade speed ratio (σ). The symbols differentiate the reduced rotational speeds measured, and the colours the *MFR* values measured. Moreover, the figure is divided in two plots with the measurements of each flow branch for

Table 3.4: Average and maximum uncertainties of the measured and computed turbine variables.

Parameter	Average uncertainty	Maximum uncertainty	Units
Temperature	0.47	0.47	K
Mass flow	203	252	$\mathrm{mg\,s^{-1}}$
Pressure	7.3	7.3	hPa
Rotational speed	500	500	rpm
Reduced speed	3.7	4.7	$\mathrm{rpm\,K^{-0.5}}$
Expansion ratio	0.015	0.023	-
Apparent efficiency	0.020	0.049	-
Power	95	216	W
Reduced mass flow	3.45×10^{-8}	6.32×10^{-8}	$\mathrm{m\,s\,K^{0.5}}$
MFR	0.0017	0.0054	-

Table 3.5: Values of *MFR* and reduced rotational speed measured.

MFR [-]
0
0.2
0.33
0.43
0.53
0.57
0.67
0.8
1

N_{red} [rpm/$\sqrt{\mathrm{K}}$]
3700
4700
5800
6900
7400

clarity.

The flow capacity map shows that increasing the reduced rotational speed means increasing the expansion ratio. This behaviour was expected since the rotational speed was fixed experimentally, varying the total inlet pressure. As the turbocharger compressor acts as a brake for the turbine, and its power consumption increases with its rotational speed, higher turbine pressure ratios are needed for higher reduced rotational speeds.

The reduced mass flow decreases with the *MFR* value for the hub branch and increases for the shroud branch. This behaviour was also expected since there is lower mass flow in *MFR* values near 0 for the hub branch and near 1 for the shroud branch.
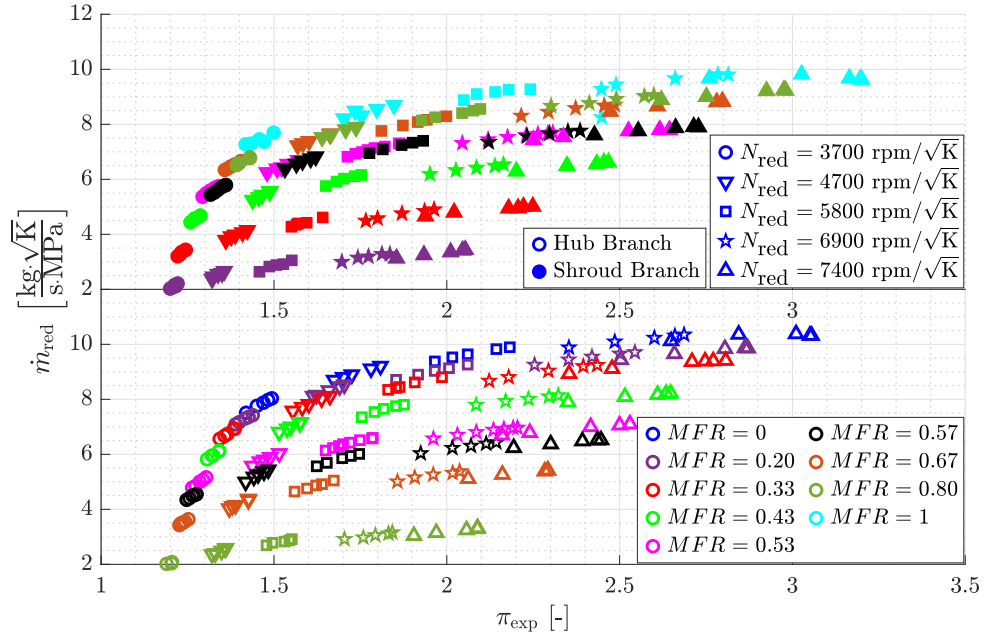
Figure 3.5: Experimental flow capacity map.
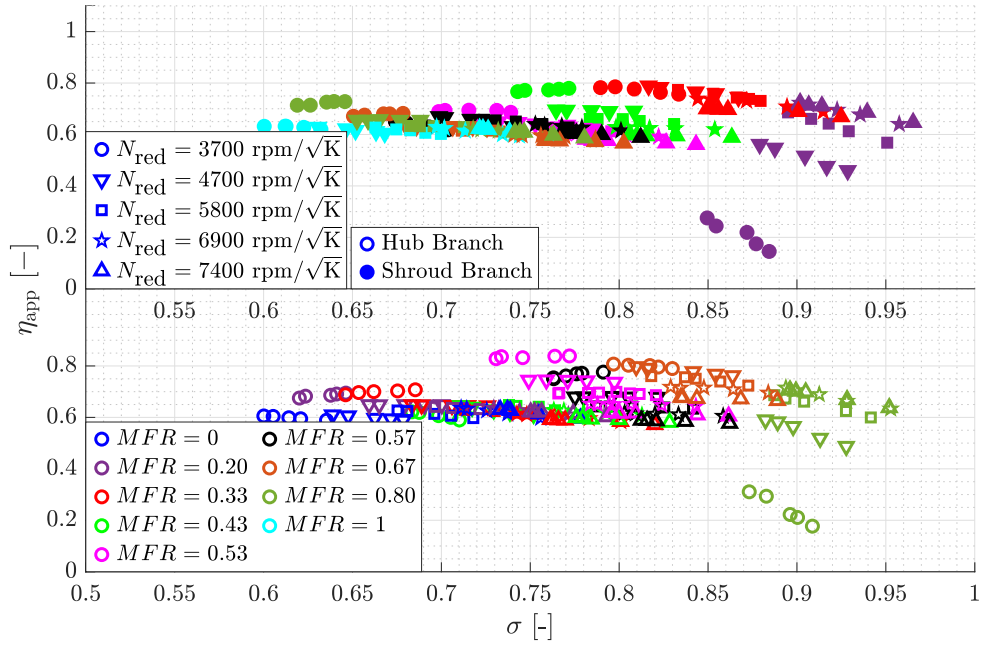
Figure 3.6: Apparent efficiency map.

The efficiency map shows the apparent efficiency results. The outlet temperature measured is the same for both branches. Therefore, the efficiency obtained experimentally is the apparent efficiency calculated with this mixed temperature. If the outlet temperature of each flow branch could be measured separately, the actual efficiency of each flow branch could be obtained experimentally.

The reduced rotational speed has little effect on the apparent efficiency when there is higher mass flow in the branch of study (*MFR* near 0 for the hub branch and near 1 for the shroud branch). It seems to have more effect when there is lower mass flow in the branch of study. However, the apparent efficiency measured at *MFR* 0.2 for the shroud branch and 0.8 for the hub branch at reduced rotational speed $3700 \mathrm{rpm\,K}^{-0.5}$ could be wrong. The mass flow measured in these cases is very low and could introduce high uncertainties in the measurements. Although the efficiency is corrected due to the residual heat transfer effects, the uncertainty of this correction may become non-negligible and difficult to assess for very low mass flows. The heat transfer effects are computed following the method described in Serrano et al. [97]. The conductive conductances and capacitances are estimated based on the material properties and simple geometrical parameters

The *MFR* has a more evident effect on the apparent efficiency, increasing it for the hub branch and decreasing it for the shroud branch. Moreover, the maximum apparent efficiency is reached at higher blade speed ratios when the *MFR* increases for the hub branch and decreases for the shroud branch. This behaviour was expected since the blade speed ratio decreases with the expansion ratio and the expansion ratio decreases with the *MFR* for the hub branch and increases for the shroud branch in the current measurements.

These measurements will be used to globally validate the CFD simulations presented in the following chapter and the models developed in Chapter 6.

3.5 LDA tests

Although the steady-state measurements allow globally validating the results from the CFD simulations, it would be interesting to validate locally some results inferred from those simulations. Therefore, an LDA technique test has been carried out to measure the velocity and the particle concentration fields at the rotor outlet.

LDA technique has been used for different applications like analysing the flame structure and burning velocity of ammonia/air turbulent premixed flames [98], developing a ventilation method to prevent obstruction phenomenon within sewer networks [99] or helping to improve the pulmonary photodynamic therapy [100]. Moreover, Fischer [101] and Grosjean et al. [102] carried out different studies to assess the LDA technique suitability for obtaining the velocity and

the particle concentration fields comparing it with similar techniques. The LDA technique has also been utilised in the turbomachinery field, such as studying the flow in centrifugal pumps [103, 104] or the losses in axial fans [105].

3.5.1 Setup

The LDA system utilised is the DANTEC Dynamics system shown in Fig. 3.7. This system can conduct bi-directional measurements at high temporal and spatial resolution. It uses a Bragg cell in each direction as a beam splitter with a back-scatter configuration for easier alignment. The maximum power of the system is 500 mW per wavelength. Fig. 3.7 also shows the traverse system where the LDA system is mounted. It allows moving the optical head and the intersection volume. Therefore, it is capable of mapping the flow field.

Figure 3.7: LDA system and traverse system.

A seed particle generator, shown in Fig. 3.8, injects small oil particles upstream of the V-cone sensors at the twin-entry turbine inlets. Therefore, these particles are taken into account when the mass flow is measured at both inlets, although the oil mass flow is small compared to the air mass flow. The seed particle generator has three valves that control the oil mass flow injected. The oil used has a kinematic viscosity of $10^{-6} \mathrm{m}^2 \mathrm{s}^{-1}$ and a refractive index of 1.334.

The current LDA test has been designed for taking measurements at the rotor outlet. Thus, optical access just at the rotor outlet is required. Since the

Figure 3.8: Seed particles generator.

turbine case is opaque, it needs to be machined. The machining has been made to insert a borosilicate glass pipe with the same internal radius as the turbine case and avoid air leakage. Fig. 3.9 shows how this pipe has been inserted into the turbine. The distinct parts that can be differentiated are the volutes (1), the rotor blades (2), the rotor nose (3) and the borosilicate glass pipe (4). Fig. 3.10 shows how the laser beams cross inside the borosilicate glass pipe.

The cylindrical form of the pipe avoids producing any additional losses. However, it constrains to perform the measurements only at its centre line. The laser beam incident angles to the pipe are different from each other in the vertical axis in other cases, which hinders the laser beams from crossing properly. Moreover, the measurements must be performed in positions relatively far from the pipe walls to minimise the reflections and noisy signals. The traverse system shown in Fig. 3.7 allows adjusting accurately the laser beams crossing position.

Therefore, the measurements must be performed radially at the centre line and far from the walls. Fig. 3.11 shows the points selected. The axial position chosen is 3 mm downstream of the rotor nose and 13 mm downstream of the rotor trailing edge to reach enough separation from the rotor nose wall. Then, 6 points radially separated are selected. The number of each point in Fig. 3.11 indicates the percentage of the rotor channel width from hub to shroud at which they are measured. Positions at more than 74% of the rotor channel width were
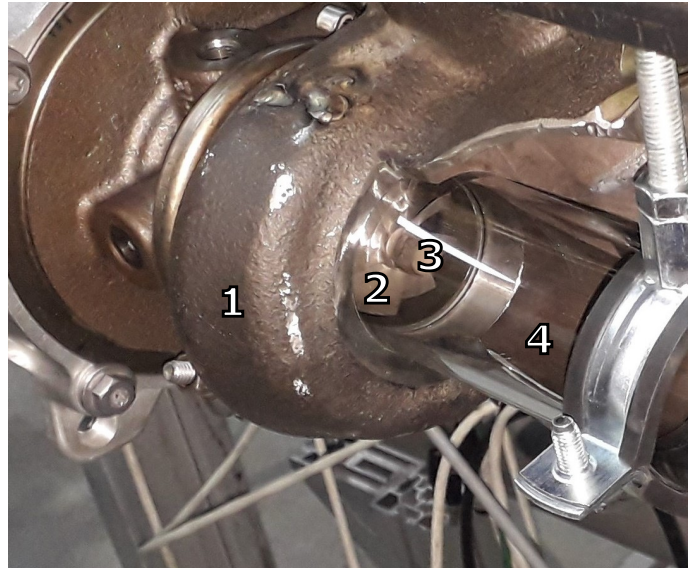
Figure 3.9: Rotor outlet optical access.
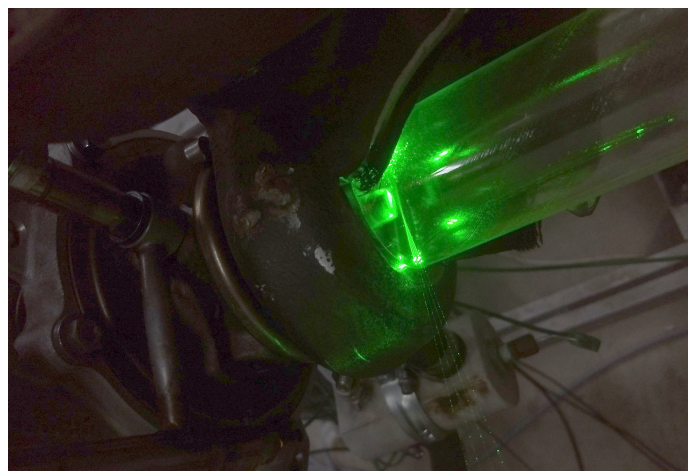
Figure 3.10: Laser beams crossing.

too close to the glass pipe to capture enough noiseless measurements.
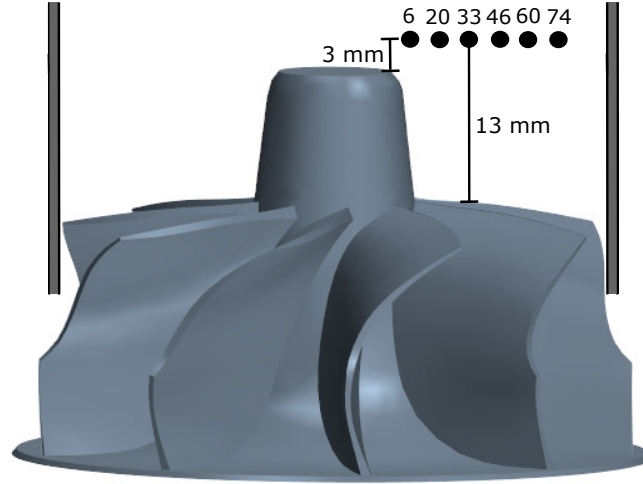
Figure 3.11: LDA measurement points.

Additionally, a valve downstream of the seed particle generator allows choosing which flow branch the particles are injected in. Thus, these six radially separated points are measured twice for each working point. The oil particles are injected into the hub branch first. Then, the valve is switched to inject the oil particles into the shroud branch. This procedure allows to differentiate the mass flow from each flow branch at each measured position.

These measurements have been performed at different *MFR* and reduced rotational speed values. The working points measured are summarised in Table 3.6.

Table 3.6: *MFR* and reduced rotational speed values measured.

MFR [-]	N_{red} [rpm K$^{-0.5}$]
0.1	3400
0.2	4000
0.32	4600
0.5	
0.68	
0.8	
0.9	

The procedure to adjust the working point is similar to steady-state measurements. The flow capacity map obtained in these tests is shown in Fig. 3.12.

The same trends as in Fig. 3.5 are observed. The reduced mass flow decreases with the *MFR* value for the hub branch and increases for the shroud branch. The steady-state measurements under $N_{\mathrm{red}} = 4700$ rpm K$^{-0.5}$ are included in the plot with black-face markers to compare them with the LDA measurements under $N_{\mathrm{red}} = 4600$ rpm K$^{-0.5}$.
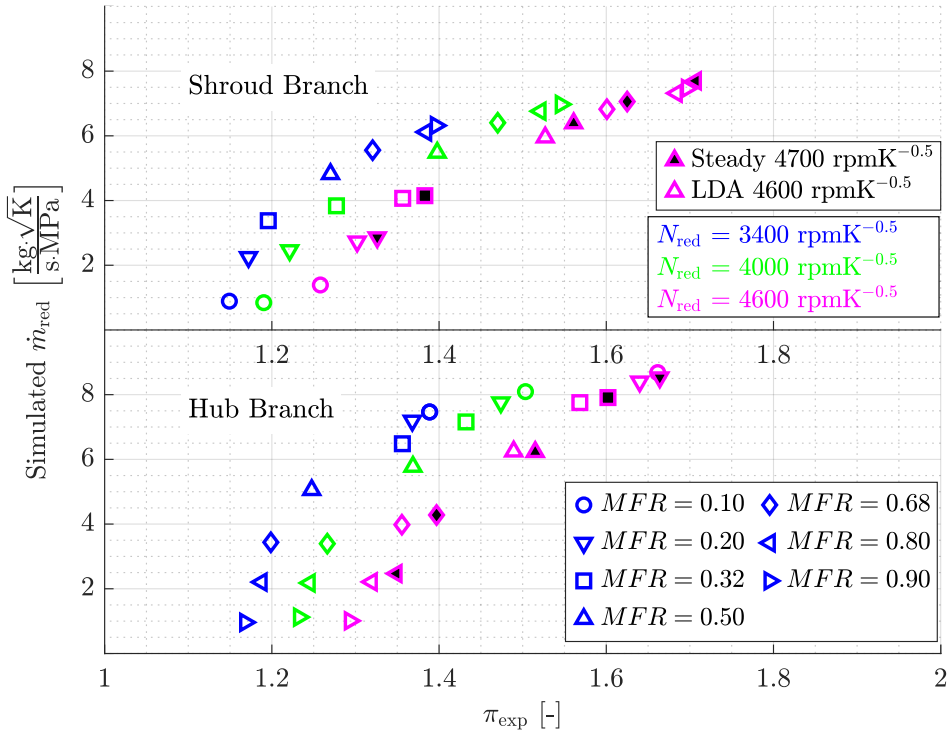
Figure 3.12: Flow capacity map obtained in the LDA measurements.

Although the geometry is different due to the optical access and the reduced rotational speeds measured are not exactly the same, the results under $N_{\mathrm{red}} = 4600$ rpm K$^{-0.5}$ ranging from *MFR* 0.2 to 0.8 for the LDA measurements and the results under $N_{\mathrm{red}} = 4700$ rpm K$^{-0.5}$ in the same *MFR* values for the steady-state measurements are quite similar. There are discrepancies in mass flow rate lower than 0.3 kg K$^{0.5}$ s^{-1} MPa^{-1} and discrepancies in expansion ratio lower than 0.02.

3.5.2 LDA Measurements

Mach number and rotor outlet flow angle

The location of the LDA system in the current tests allows for measuring the axial and the tangential velocity components. The mean value of the axial and tangential Mach number has been calculated from these velocity components using the turbine outlet temperature to obtain the speed of sound. Both components are plotted against the percentage of the rotor channel width from hub to shroud in Fig. 3.13 for the axial component and Fig. 3.14 for the tangential component. For the sake of clarity, both figures have been divided into subfigures representing an *MFR* value in each one. The empty symbols represent the measurements when the oil particles are injected through the hub branch, and the filled symbols represent the measurements when the oil particles are injected through the shroud branch.
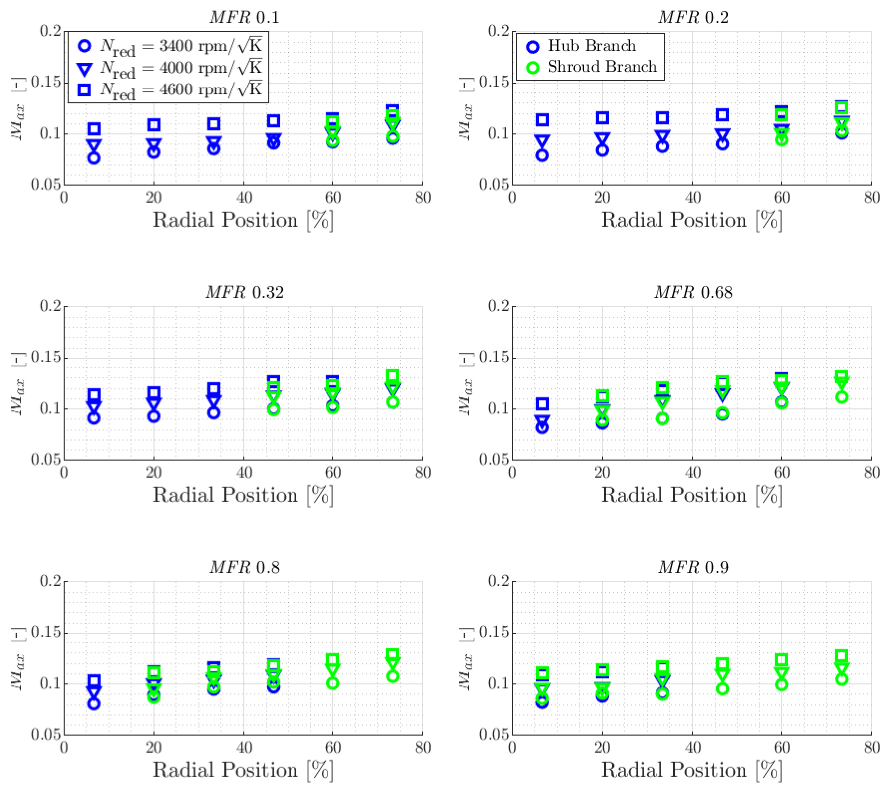
Figure 3.13: Axial Mach number obtained in each radial position from hub to shroud.

Some measured working points are not plotted in these figures because the
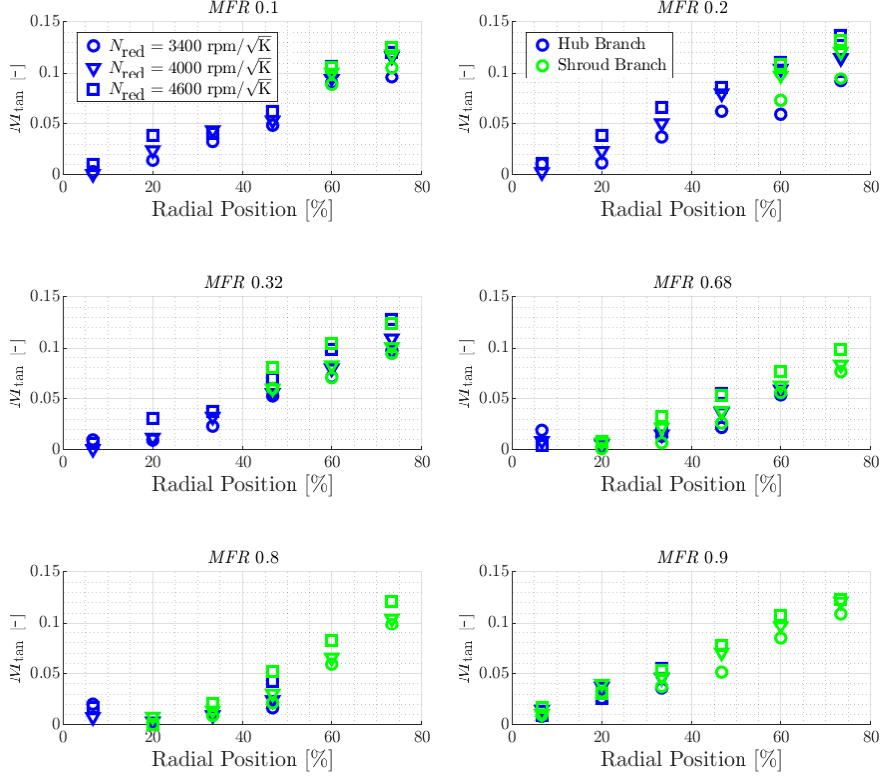
Figure 3.14: Tangential Mach number obtained in each radial position from hub to shroud.

system did not capture enough oil particles to ensure accurate statistical results. The oil particles injected through the shroud branch were insufficient at radial positions close to the hub (near 0) for low *MFR* values. The oil particles injected through the hub branch were insufficient at radial positions close to the shroud (near 100) for high *MFR* values.

Fig. 3.13 shows that the axial Mach number increases with the reduced rotational speed. This behaviour was expected since the reduced rotational speed is fixed varying the expansion ratio. The axial Mach number also increases with the percentage of the rotor channel width from hub to shroud. A sudden expansion downstream of the rotor nose has been observed and will be adequately defined in Chapter 5. This sudden expansion reduces the axial Mach number near the rotor nose. Therefore, the axial Mach number distribution with the percentage of the rotor channel width from hub to shroud is reasonable.

Fig. 3.14 shows that the tangential Mach number also increases with the reduced rotational speed for the same reason as the axial Mach number. The

tangential Mach number also increases with the percentage of the rotor channel width from hub to shroud. This behaviour was expected since the absolute tangential velocity increases with the rotor radius.

Both Fig. 3.13 and Fig. 3.14 show the mean values of the Mach number components obtained. However, the uncertainty of the measurements is as relevant as the mean value. The LDA system software calculates the root mean square error of the measurements. Thus, the uncertainty could be calculated employing Eq. 3.1. RMSE stands for the root mean square error and n_{samples} for the number of samples detected. This uncertainty is produced due to noise measurement and actual turbulent fluctuations.

$$u_M = \frac{\text{RMSE}}{\sqrt{n_{\text{samples}}}} \tag{3.1}$$
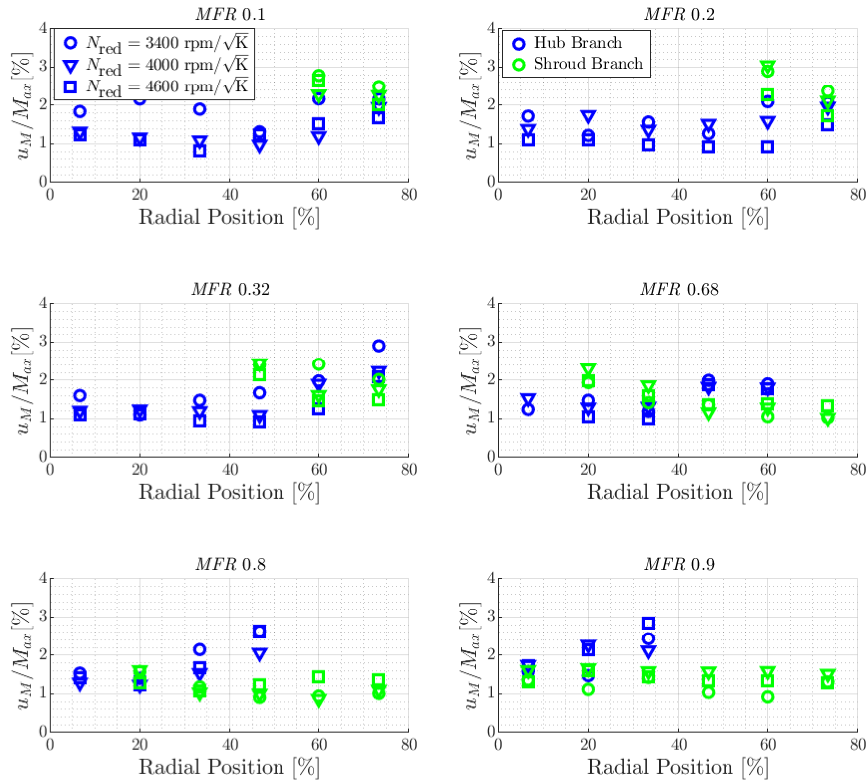
Figure 3.15: Axial Mach number uncertainty computed at each radial position from hub to shroud.

The uncertainty obtained from Eq. 3.1 can be divided by the mean value measured to compute the uncertainty in terms of percentage. Fig. 3.15 and Fig.

3.16 show the uncertainty in terms of percentage for the axial Mach number and the tangential Mach number, respectively.
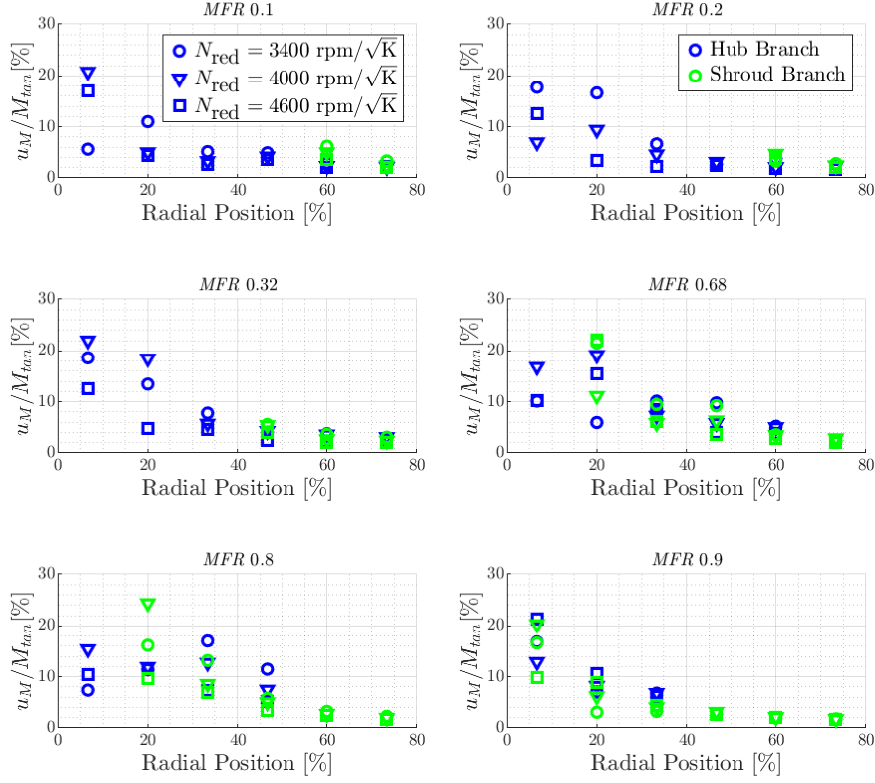
Figure 3.16: Tangential Mach number uncertainty computed at each radial position from hub to shroud.

The maximum axial Mach number uncertainty in terms of percentage shown in Fig. 3.15 is 3%. Hence, the actual axial Mach number will be the one shown in Fig. 3.13 ±3% with a 68% confidence level.

However, the tangential Mach number uncertainty in terms of percentage shown in Fig. 3.16 is remarkably higher, reaching values as high as 25%. These higher values are obtained in radial positions near the rotor hub. The reason for these high uncertainty values is that the value plotted is divided by the mean tangential Mach number. Radial positions near the rotor hub have a tangential Mach number near 0, as shown in Fig. 3.14. Therefore, the uncertainty is more significant at these positions.

Then, the rotor outlet flow angle can be calculated by combining the results obtained of the axial and the tangential Mach number components, as described in Eq. 3.2.

$$\beta_{out} = \arccos\left(\frac{M_{\mathrm{ax}}}{M_{\mathrm{tan}}}\right) \tag{3.2}$$

The actual blade outlet angle is not constant. Table 3.1 indicates the mean blade angle is 56°, but it varies along the radial coordinate. The actual blade outlet angle takes values between 44° near the rotor hub and 67° near the shroud. Thus, the rotor outlet flow angle is expected to increase with the radial position.
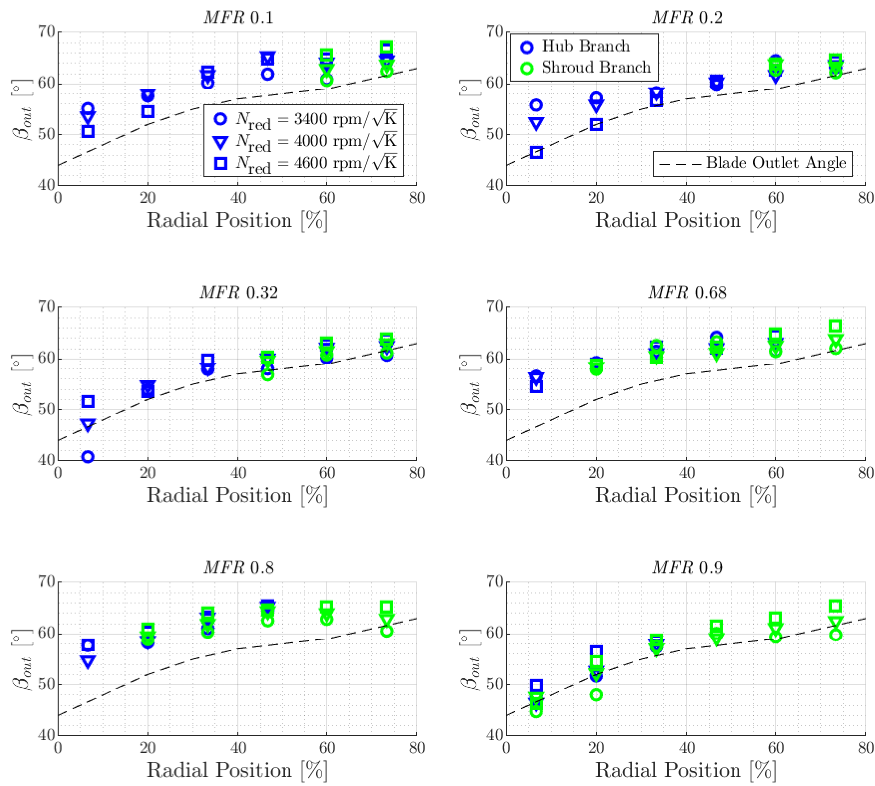
Figure 3.17: Rotor outlet flow angle computed at each radial position from hub to shroud.

The rotor outlet flow angle calculated from the LDA measurements is shown in Fig. 3.17. It can be observed that the main variations are with the radial position as expected due to the variation of the blade outlet angle. The influence of the *MFR* and reduced rotational speed in the rotor outlet flow angle distribution is low. It seems that the rotor outlet flow angle increases with the reduced rotational speed in most cases.

57

Local concentration

The number of samples recorded in the given time of the LDA system is also provided by its software. Moreover, each working point is measured twice, maintaining the same boundary conditions: the first time injecting the oil particles on the hub branch and the second time on the shroud branch. Therefore, the number of samples recorded each time can be compared to estimate the proportion of mass flow coming from each flow branch at each radial position.

The local concentration of particles coming from the shroud branch is defined in Eq. 3.3, and it is locally calculated at each working point. The ratio between the number of samples recorded when the oil particles are injected through the shroud branch and the number of samples recorded in both cases is defined as *SPC* (shroud particle concentration).

$$SPC = \frac{n\text{ShroudParticles}}{n\text{ShroudParticles} + n\text{HubParticles}} \tag{3.3}$$

The *SPC* represents a direct sample of the probability distribution of having flow coming from the shroud branch instead of having flow coming from the hub branch over the rotor outlet section. The *SPC* should be close to 1 if the mass flow corresponds primarily to the shroud branch for not-mixed flows and close to 0 if the mass flow corresponds primarily to the hub branch.

Fig. 3.18 shows the *SPC* value plotted against the percentage of the rotor channel width from hub to shroud at which they are measured for different *MFR* and reduced turbocharger speed values. To clarify the results, it has been divided into sub-plots representing an *MFR* value at each one.

The reduced rotational speed has little effect on the *SPC* value. However, the *SPC* distribution along the radial position from hub to shroud varies with the *MFR* value.

The overall proportion of mass flow from the shroud branch increases with the *MFR* value inside the turbine. Thus, the overall proportion of mass flow from the shroud branch is remarkably higher at *MFR* values closer to 1 than at *MFR* values closer to 0. Fig. 3.18 shows that the *SPC* value follows similar trends against *MFR*.

The radial position from hub to shroud also produces a considerable influence on the *SPC* value. Fig. 3.18 shows that the *SPC* value near the rotor hub is always lower than the *SPC* value near the pipe wall for all measured *MFR* values.

The overall proportion of mass flow coming from the shroud branch is lower in *MFR* values closer to 0 like the cases of *MFR* 0.1 or 0.2. The *SPC* is nearly 0 near the rotor hub in these cases. However, the *SPC* value is higher at radial positions closer to the pipe wall. Therefore, the mass flow from the shroud branch is still concentrated near the pipe wall at the measured outlet section.
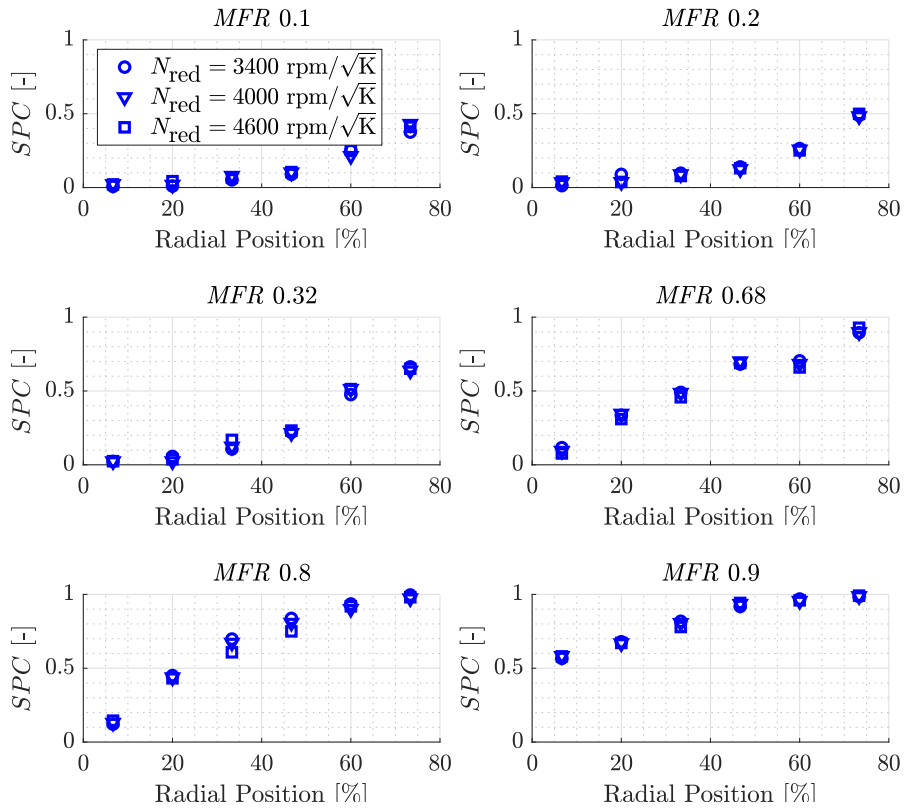
Figure 3.18: Shroud particle concentration (*SPC*) computed at each radial position from hub to shroud.

The overall proportion of mass flow coming from the shroud branch is higher in *MFR* values closer to 1 like the cases of *MFR* 0.8 or 0.9. The *SPC* is nearly 1 near the pipe wall in these cases. However, the *SPC* value is lower in radial positions closer to the rotor hub. Therefore, the mass flow coming from the shroud branch is still concentrated near the pipe wall at the measured outlet section also in these cases.

Figures 3.19, 3.20 and 3.21 show the axial Mach number and the *SPC* values for a more comprehensive understanding. Each sub-figure is for a different reduced rotational speed, and each one shows the results at different *MFR* values. The region shown in these figures is only the region where the experimental measurements have been performed (i.e. from 6% to 74% of the rotor channel width from hub to shroud). There is no data near the pipe wall or the middle of the section to be plotted. Although the results for each *MFR* is plotted in different tangential sectors, they still represent the measurements performed at the centre line.
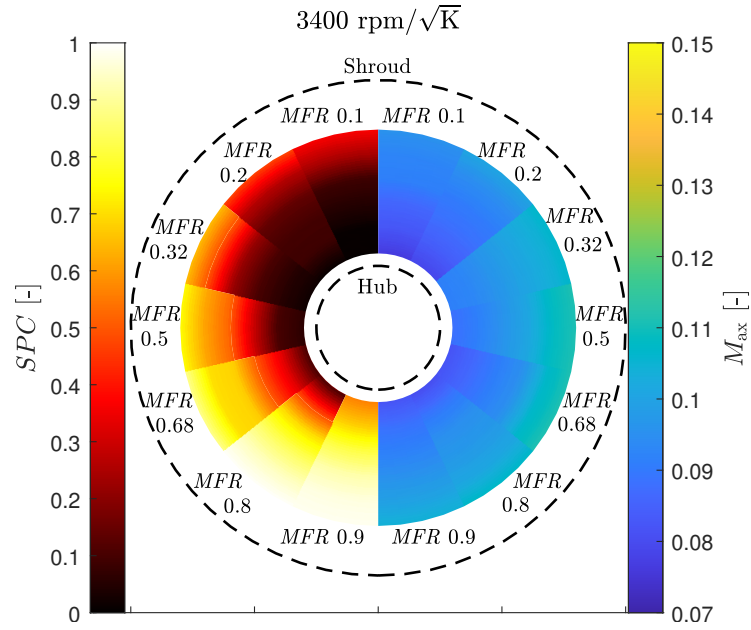
Figure 3.19: Axial Mach number and shroud particle concentration (*SPC*) for different *MFR* values at 3400 rpm K$^{-0.5}$.

Figure 3.20: Axial Mach number and shroud particle concentration (*SPC*) for different *MFR* values at 4000 rpm K$^{-0.5}$.
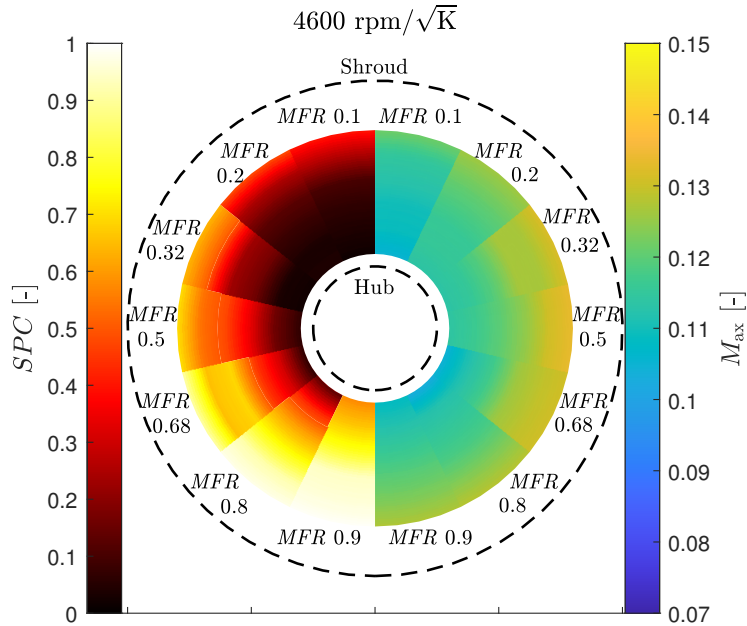
Figure 3.21: Axial Mach number and shroud particle concentration (*SPC*) for different *MFR* values at 4600 rpm K$^{-0.5}$.

The axial Mach number is higher when the reduced rotational speed is increased, as expected. Moreover, the increase with the radial coordinate is clearly observable for all *MFR* values. There is a difference higher than 0.04 in Mach number for all reduced rotational speeds from the closest measured point to the centre to the closest measured point to the pipe wall. This difference is explained by the sudden expansion produced downstream of the rotor nose that reduces the axial Mach number near the rotor hub.

The reduced rotational speed has a slight effect on the *SPC* distribution along the radial position. However, *MFR* has a strong effect on it. The *SPC* value increases with *MFR* for all radial positions since the overall proportion of air from the shroud branch is also higher. Furthermore, *SPC* increases with the radial position from hub to shroud. Hence, the flow is not homogeneous at the outlet section measured. This behaviour means that the flow coming from each flow branch is not fully mixed at the outlet section measured downstream of the rotor.

These measurements will be used to locally validate the CFD simulations presented in Chapter 4 and the effective area model developed in Chapter 6.

3.6 Outlet temperature measurements

Additionally, other campaign has been performed to assess the temperature at the same section where the LDA measurements were performed. The idea is to corroborate that the temperature also varies along the radial axis depending on the *MFR* value.

The borosilicate glass pipe has been removed and replaced by a metallic pipe, as shown in Fig. 3.22(a). A K-type thermocouple like the ones defined in Table 3.3 has been placed at the same axial section where the LDA measurements were performed. This thermocouple can be moved radially thanks to the screw shown in Fig. 3.22(a). The pipe has been insulated to avoid thermal losses to the ambient, as shown in Fig. 3.22(b).

(a) New rotor outlet pipe.   (b) Pipe Insulation.
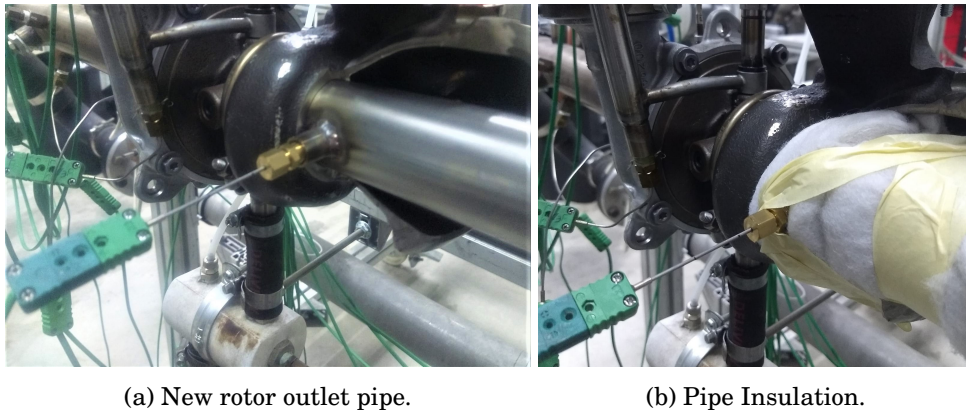
Figure 3.22: Outlet temperature measurements.

Then, the outlet temperature is plotted against the percentage of the rotor channel width from hub to shroud in Fig. 3.23. To clarify the results, it has been divided into sub-plots representing an *MFR* value at each one.

Fig. 3.23 shows that the outlet temperature decreases with the reduced rotational speed. This behaviour was expected since the reduced rotational speed depends directly on the expansion ratio in these measurements. The outlet temperature increases with the percentage of the rotor channel width from hub to shroud at *MFR* values under 0.5 and decreases at *MFR* values above 0.5.

The inlet temperature of the branch with the higher mass flow rate is a bit higher than the inlet temperature of the other branch in extreme *MFR* values due to the low mass flow has less energy. Moreover, the expansion ratio of the branch with the higher mass flow rate is greater. The difference in expansion ratios between flow branches increases when *MFR* goes towards extreme unequal admission conditions (values near 0 and 1). Since *SPC* distribution studied in
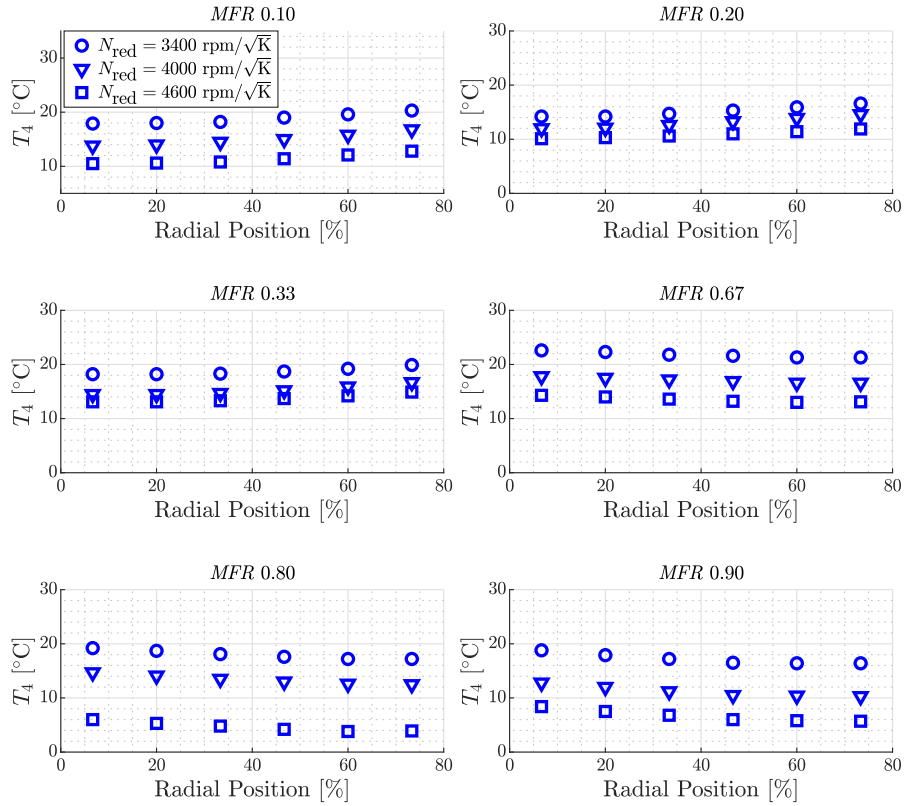
Figure 3.23: Temperature measured at different radial positions from hub to shroud.

the previous section has proven that the flow from each branch is not fully mixed at the outlet section measured, the outlet temperature is expected to vary along the radial position.

The mass flow rate in the cases with an *MFR* value under 0.5 is higher in the hub branch. Therefore, the outlet temperature is expected to be lower near the rotor hub. The mass flow rate in the cases with an *MFR* value above 0.5 is higher in the shroud branch. Therefore, the outlet temperature is expected to be lower near the rotor shroud.

Figures 3.24, 3.25 and 3.26 show the increment of outlet temperature based on the minimum temperature measured in the corresponding case for a more comprehensive understanding. Each sub-figure is for a different reduced rotational speed, and each one shows the results at different *MFR* values. The region shown in these figures is only the region where the experimental measurements have been performed (i.e. from 6% to 74% of the rotor channel width from hub

to shroud). There is no data near the pipe wall or the middle of the section to be plotted. Although the results for each *MFR* is plotted in different tangential sectors, they still represent the measurements performed at the centre line where the sensor is placed.
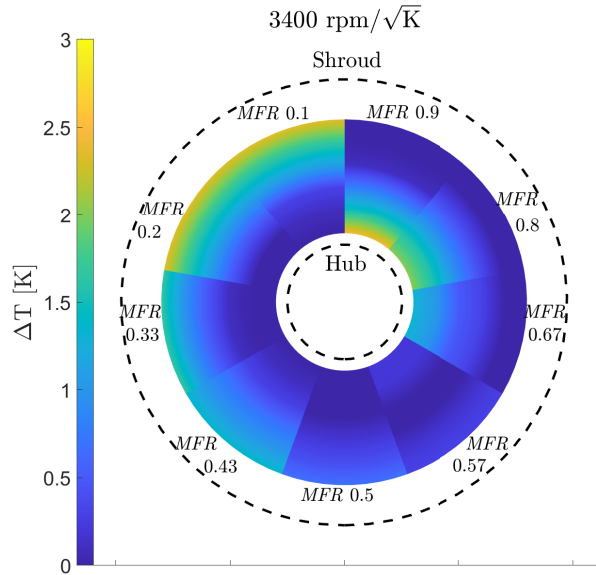

Figure 3.24: Increment of outlet temperature based on the minimum temperature measured along the radial position for different *MFR* values at 3400 $\mathrm{rpm\,K}^{-0.5}$.

The outlet temperature increment with the radial position is clearly observable for *MFR* values under 0.5, while it decreases with the radial position for *MFR* values above 0.5. The highest outlet temperature increment appears at *MFR* values under 0.2 and above 0.8. There is a difference up to 3 K for all reduced rotational speeds under these extreme unequal admission conditions. However, the outlet temperature increment in intermediate *MFR* values is limited. The difference in *MFR* values like 0.5 or 0.57 is lower than 0.5 K. Although the pipe has been insulated, there could still be a slight effect of the thermal losses to the ambient. It would explain that the temperature under *MFR* 0.57 has a lower variation than under *MFR* 0.5.

Therefore, the outlet temperature is not constant along the radial position depending on *MFR*. These outlet temperature variations corroborate the flow behaviour detected with the LDA measurements: the flow is not homogeneous at the outlet section measured. The flow coming from each branch is not fully mixed at the outlet section measured downstream of the rotor.
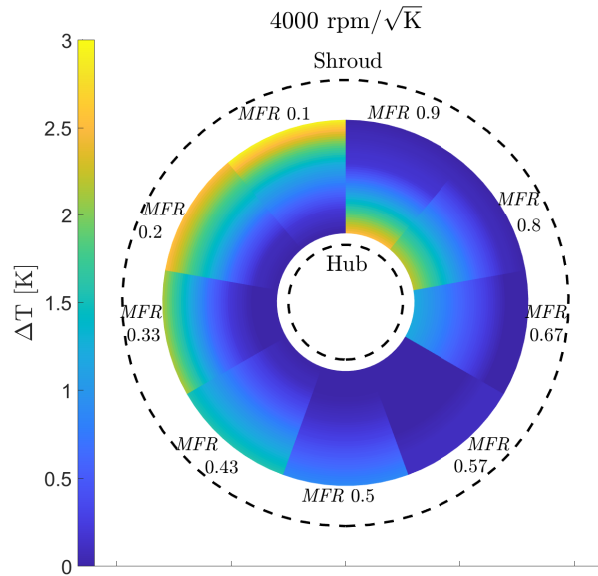
Figure 3.25: Increment of outlet temperature based on the minimum temperature measured along the radial position for different *MFR* values at 4000 rpm K$^{-0.5}$.
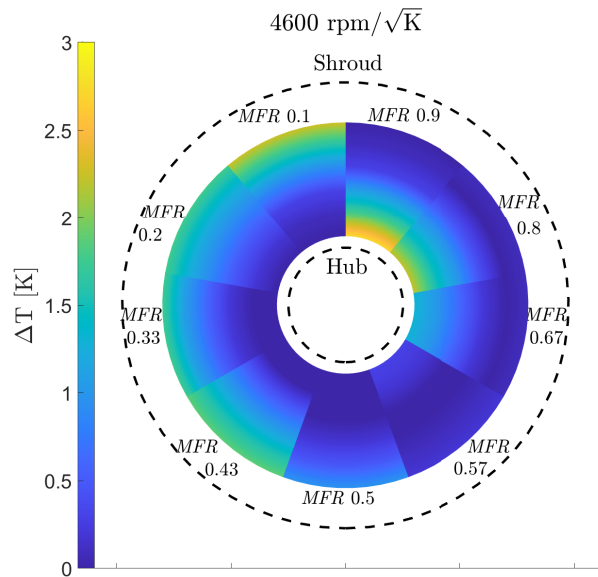
Figure 3.26: Increment of outlet temperature based on the minimum temperature measured along the radial position for different *MFR* values at 4600 rpm K$^{-0.5}$.

3.7 Summary

This chapter presents the characteristics of the twin-entry turbine studied and the configuration of the test bench where it has been experimentally measured. Then, the different measurements performed are also presented.

The first campaign is to measure steady-state working points. Several *MFR* values and reduced rotational speeds are measured for a total of 233 working points. The flow capacity map obtained shows that the reduced mass flow decreases with the *MFR* value for the hub branch and increases for the shroud branch. The apparent efficiency map shows that the apparent efficiency increases with the *MFR* value for the hub branch and decreases for the shroud branch. These measurements will be used to globally validate the CFD simulations and the models developed in the following chapters.

The second campaign measures the velocity and mass concentration fields at the rotor outlet section with an LDA technique. The measurements show that the axial Mach number increases with the radial position from hub to shroud due to a sudden expansion downstream of the rotor nose. The tangential Mach number also increases with the radial position from hub to shroud since the absolute tangential velocity increases with the rotor radius. The rotor outlet flow angle has slight variations with the reduced rotational speed and the *MFR*, but it also depends on the radial position from hub to shroud because the blade outlet angle also changes in that direction.

The concentration of particles coming from the shroud branch is also computed in the LDA measurements. It depends strongly on the *MFR* value since the global proportion of mass flow from the shroud branch changes. Moreover, it also varies with the radial position from hub to shroud. Additionally, the outlet temperature also varies with the radial position from hub to shroud. Therefore, the flow is not homogeneous at the outlet section measured; the mass flow coming from each flow branch is not fully mixed. These measurements will be used to locally validate the CFD simulations and the effective area model developed in the following chapters.

3.8 References

[49] J. R. Serrano, F. J. Arnau, L. M. García-Cuevas, V. Samala, and L. Smith. "Experimental approach for the characterization and performance analysis of twin entry radial-inflow turbines in a gas stand and with different flow admission conditions". In: *Applied Thermal Engineering* 159 (2019). DOI: 10.1016/j.applthermaleng.2019.113737 (cit. on pp. 19, 39, 40, 87, 129, 211).

[96] P. Olmeda, A. Tiseira, V. Dolz, and L. M. García-Cuevas. "Uncertainties in power computations in a turbocharger test bench". In: *Measurement* 59 (2015), pp. 363–371. DOI: 10.1016/j.measurement.2014.09.055 (cit. on pp. 43, 44).

[97] J. R. Serrano, P. Olmeda, F. J. Arnau, and V. Samala. "A holistic methodology to correct heat transfer and bearing friction losses from hot turbocharger maps in order to obtain adiabatic efficiency of the turbomachinery". In: *International Journal of Engine Research* 21.8 (Mar. 2019), pp. 1314–1335. DOI: 10.1177/1468087419834194 (cit. on p. 47).

[98] Q. Fan, X. Liu, L. Xu, A. A. Subash, C. Brackmann, M. Aldén, X.-S. Bai, and Z. Li. "Flame structure and burning velocity of ammonia/air turbulent premixed flames at high Karlovitz number conditions". In: *Combustion and Flame* 238 (Apr. 2022), p. 111943. DOI: 10.1016/j.combustflame.2021.111943 (cit. on p. 47).

[99] H. Adouni, Y. Chouari, H. Bournot, W. Kriaa, and H. Mhiri. "A novel ventilation method to prevent obstruction phenomenon within sewer networks". In: *International Journal of Heat and Mass Transfer* 184 (Mar. 2022), p. 122335. DOI: 10.1016/j.ijheatmasstransfer.2021.122335 (cit. on p. 47).

[100] J. Lehmann, M. R. Agel, K. H. Engelhardt, S. R. Pinnapireddy, S. Agel, L. Duse, E. Preis, M. Wojcik, and U. Bakowsky. "Improvement of pulmonary photodynamic therapy: Nebulisation of curcumin-loaded tetraether liposomes". In: *Pharmaceutics* 13.8 (Aug. 2021), p. 1243. DOI: 10.3390/pharmaceutics13081243 (cit. on p. 47).

[101] A. Fischer. "Fundamental flow measurement capabilities of optical Doppler and time-of-flight principles." In: *Experiments in Fluids* 62 (2021). DOI: 10.1007/s00348-020-03127-x (cit. on p. 47).

[102] N. Grosjean, L. Graftieaux, M. Michard, W. Hübner, C. Tropea, and J. Volkert. "Combining LDA and PIV for turbulence measurements in unsteady swirling flows." In: *Measurement Science and Technology* 8.12 (1997). DOI: 10.1088/0957-0233/8/12/015 (cit. on p. 47).

[103]   N. Pedersen, P. S. Larsen, and C. B. Jacobsen. "Flow in a centrifugal pump impeller at design and off-design conditions - Part I: Particle Image Velocimetry (PIV) and Laser Doppler Velocimetry (LDV) measurements." In: *Journal of Fluids Engineering* 125 (2003), pp. 61–72. DOI: 10.1115 /1.1524585 (cit. on p. 48).

[104]   N. Zhang, F. Zheng, X. Liu, B. Gao, and G. Li. "Unsteady flow fluctuations in a centrifugal pump measured by laser Doppler anemometry and pressure pulsation." In: *Physics of Fluids* 32 (2020). DOI: 10.1063/5.00 29124 (cit. on p. 48).

[105]   A. Theis, T. Reviol, and M. Böhle. "Analysis of the losses in an axial fan with small blade aspect ratios using CFD-technique and laser Doppler anemometry." In: *Proceedings of the ASME Turbo Expo 2020: Turbomachinery Technical Conference and Exposition. Volume 2A: Turbomachinery* (2020). DOI: 10.1115/GT2020-14283 (cit. on p. 48).

CHAPTER 4

CFD simulations setup

Contents

Figures

Tables

4.1 Introduction

ALTHOUGH the experimental turbocharger measurements presented in the previous chapter are the current state of the art, they have limitations. The flow behaviour and the losses produced in the different twin-entry turbine parts cannot be well captured. However, these experimental measurements are essential to validate the CFD simulations presented in this chapter.

CFD simulations have less limitations in studying the insights of the different twin-entry turbine parts. However, they need a long time and a high computational cost to obtain acceptable results. The most reliable CFD simulations are direct numerical simulations (DNS). DNS simulations solve all the equations without modelling any result. However, they need a very fine mesh, and it takes a very long time and high computational cost to obtain the results. Indeed, it is actually impossible to perform DNS simulations inside a turbine working with high flow speeds with the current computational resources. Large eddy simulations (LES) solve the large scales of the turbulence and model the small scales so that a coarser mesh can be used. LES simulations need less time and computational cost to obtain the results than the DNS simulations, but they are still large. Unsteady Reynolds-averaged Navier-Stokes simulations (U-RANS) model all scales, but they need less time and computational cost since the mesh can be coarser. The quality of the U-RANS simulations results will depend on the setup of the simulations, but they can reach enough quality for the purpose of the current work.

As depicted in Chapter 2, it would be relevant to carry out CFD simulations under unequal admission conditions. However, the methodology to ensure reliable numerical results must be assessed before carrying out those simulations.

This chapter presents the twin-entry turbine CFD simulations setup. The models to properly simulate the geometry are selected, and a mesh independence study is performed to select the mesh that provides a trade-off between the accuracy of the results and computational costs. Then, the flow capacity and efficiency maps obtained from the CFD simulations are globally validated with the steady-state measurements described in Chapter 3.

4.2 CFD simulations setup

The geometry to study is the same measured in the test bench described in Chapter 3. All twin-entry turbine parts, including the inlet and outlet straight ducts, have been scanned with a conventional 3D scanner. The rotor and the inlet and outlet ducts are easy to digitalise with this scanner. However, the volutes and the rotor outlet plenum have difficult access for this scanner. Therefore, they are digitalised using a non-destructive inverse process: the volutes and

rotor outlet plenum are filled with liquid silicone. This silicone is extracted when cured, obtaining silicone moulds of the volutes and rotor outlet plenum. These silicone moulds are more accessible to scan. They are not perfect because there could be air bubbles or small fissures. However, these imperfections can be adequately corrected using pre-processing tools on the computer-aided design (CAD) files generated. Thus, all necessary parts have been digitalised, whether directly or from silicone moulds, and prepared to use in CFD software, as shown in Fig. 4.1.
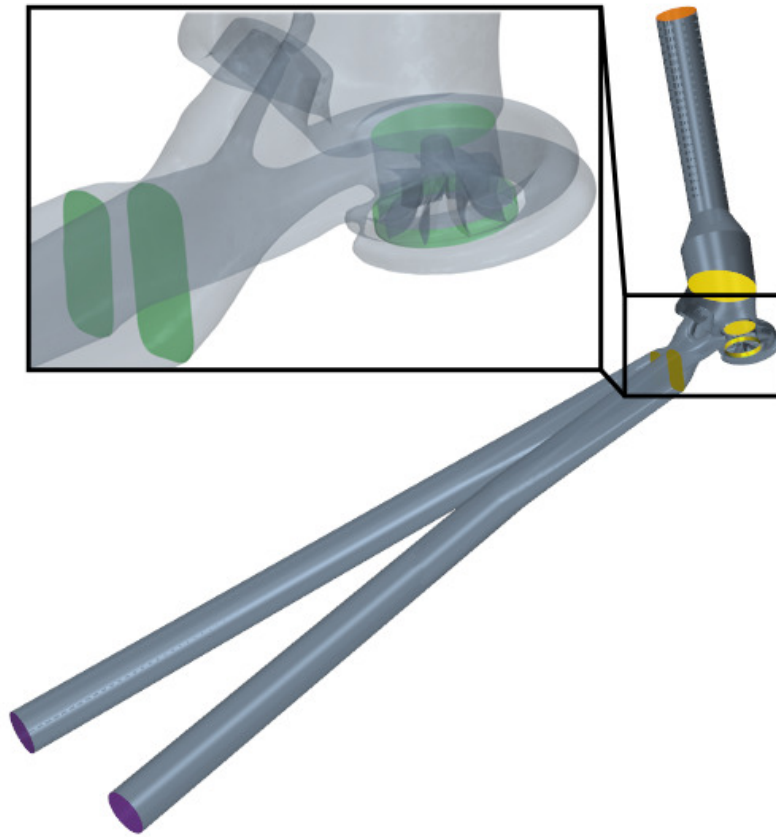
Figure 4.1: Twin-entry turbine CAD model

The CFD domain has been sub-divided into different parts to mesh it properly. All meshes are non-structured polyhedral meshes. Since the two inlet ducts and the outlet duct are long and straight, the mesh can be coarser. The other parts are the volutes, the interspace between volutes and rotor, rotor and rotor outlet plenum. The mesh refinement for capturing localised phenomena can be adjusted using these domain sub-divisions. A prism layer mesher is used in all parts to define the boundary layer properly. Moreover, the different stations

71

have been numbered as described in Table 4.1 and Fig. 4.2.

Table 4.1: Twin-entry turbine stations

Station	Description
0	Turbine inlet
1	Volute outlet
3	Rotor inlet
4	Rotor outlet
5	Turbine outlet
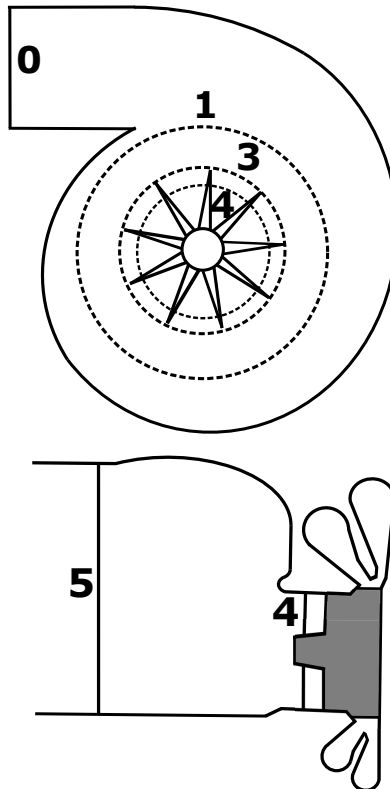
Figure 4.2: Twin-entry turbine stations

The purpose of carrying out CFD simulations in the current work is to characterise the flow patterns inside a twin-entry turbine and identify the main sources of losses. The CFD simulations carried out are U-RANS simulations using the commercial software package Simcenter STAR-CCM+.

The model used to describe the turbulence is a $k-\omega$ SST model with a Durbin scale limiter that constrains the turbulent time scale and a compressibility

correction, following the trends for simulating turbomachinery, as detailed by Fajardo [20]. The solver employed is an upwind, second-order, coupled flow solver with a Roe's flux-difference splitting scheme prepared for using with Weiss-Smith preconditioning for all-speed flows. The unsteady solver employed is a second-order, implicit scheme that allows controlling the time-step size [106].

A multi-component gas option is used to differentiate the air passing through each entry. The air passing through the hub branch will be called *hub air* and the air passing through the shroud branch will be called *shroud air*. Both airs have the same properties. However, differentiating them allows tracking of the air coming from each branch along the whole domain. They are modelled as an ideal gas with temperature-dependent specific heat and dynamic viscosity. It allows employing the experimental results measured with clean air to validate the results.

The boundary conditions imposed are steady. The flow conditions provided at both inlets are total pressure, total temperature, composition and turbulence specification. The flow conditions provided at the outlet are static pressure and turbulence specification. The static temperature and composition are also provided at the outlet in case of backflow. However, this backflow only appears briefly in the transient phase of the current simulations when the solution has not converged yet. The inlet and outlet ducts are as long as the distance where the sensors are placed in the experimental measurements presented in Chapter 3. Therefore, the boundary conditions imposed will be based on the experimental data available, and they are supposed constant and perfectly distributed in these sections.

A steady solver based on a multiple reference frame is used initially to simulate the rotor movement. The converged solution is then used as initial conditions for the unsteady solver based on a sliding mesh of the rotor region (U-RANS) for simulating the rotor movement. The results obtained with a multiple reference frame are not as accurate as those obtained with a sliding mesh for the same mesh size. However, they are helpful for achieving a quick, reasonable approximation to initialise the sliding mesh simulation. Then, the sliding mesh simulation will converge faster. The time-step chosen for each simulation is the time corresponding to rotate $1°$, as described by Galindo et al. [58]. The simulations take 20 inner iterations each time step to ensure the convergence of the results. This inner iterations value was chosen to obtain momentum residuals lower than 10^{-4} and a continuity residual lower than 10^{-3} with the least iterations possible. Once the error committed in computing the average value of the important parameters through 40 time steps (the time spent in rotate one rotor channel) is lower than a certain value depending on the parameter, the solution will be considered converged.

A mesh independence study has been carried out to ensure the validity of the

73

results, increasing the number of cells. A case with a reduced turbocharger speed of $3700\,\mathrm{rpm\,K^{-0.5}}$ and an *MFR* 0.53 is used to carry out this mesh independence study. These boundary conditions were selected arbitrarily with the only purpose of carrying out the mesh independence study. Total pressure at the rotor inlet, efficiency, torque and reduced mass flow are compared in Table 4.2. Then, the mesh selected is the one that provides better precision than the experimental data uncertainty with a lower computational cost. Therefore, the optimum mesh for carrying out the simulations is the one with 5.5 million cells.

Table 4.2: Mesh independence study: variation of total pressure at rotor inlet, efficiency, torque and reduced mass flow rate and GOA and GCI obtained for these variables.

N of cells ($\cdot 10^6$)	Total pressure [kPa]	η [-]	M [N·m]	$\dot{m}_{\mathrm{red}}$ [$\frac{\mathrm{kg}\cdot\sqrt{\mathrm{K}}}{\mathrm{s}\cdot\mathrm{MPa}}$]
1.59	135.9	0.6888	0.2101	10.654
2.83	136.1	0.6979	0.2132	10.672
4.46	136.4	0.7034	0.2151	10.681
5.54	136.5	0.7040	0.2153	10.684
8.28	136.5	0.7041	0.2154	10.685
GOA	1.958	1.740	1.741	1.851
GCI (%)	0.05	0.08	0.08	0.07

Table 4.2 also presents the global order of accuracy (GOA) and the global convergence index (GCI) of the studied variables. The GOA considers the local order of accuracy of the numerical methods used for modelling the advective and diffusive terms of the Navier-Stokes equations. It also considers the propagation and the accumulation of errors outside the stencil due to grid shape effects. The GOA values should be close to 2 in the current simulations since the solver used is a second-order solver. The GCI is calculated using the method defined by Roache [107], and it is lower than 0.1% for all the studied variables. Both coefficients corroborate the selection of the 5.5 million cells mesh. The final mesh selected is shown in Fig. 4.3.

The selected mesh has a non-dimensional distance to the centroid of the first layer of cells close to the walls (Y^+) lower than 2 for all the geometry. The order of magnitude of this value is reasonable when using the $k-\omega$ SST model. It should be enough to capture the behaviour of the viscous sublayer of the boundary layer adequately. Fig. 4.4 shows the Y^+ value at the rotor where the most complex phenomena arise.

The twin-entry turbine has been simulated at four different rotational speeds and nine different *MFR* values for each turbocharger speed. Therefore, there
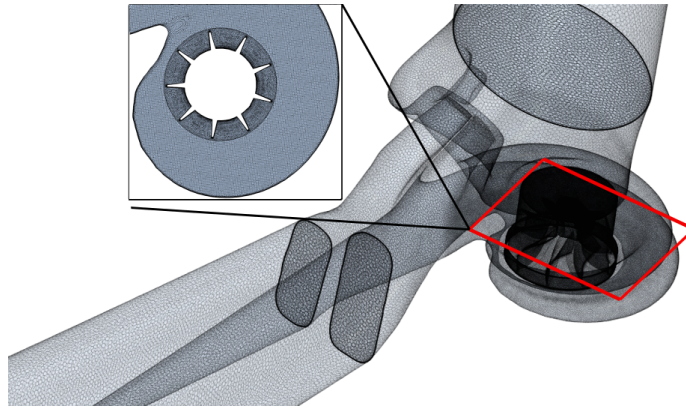
(a) General view of the mesh.
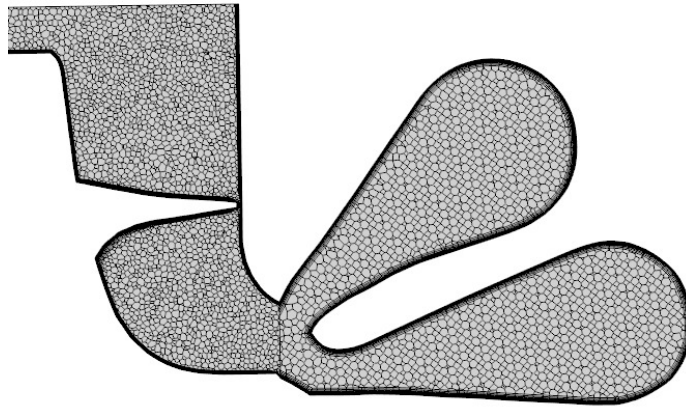
(b) Zoom at rotor and volutes mesh.

Figure 4.3: Selected mesh.

are 36 cases simulated at the rotational speeds and *MFR* values defined in Table 4.3. The values selected are based on the available experimental measurements to be able to validate the simulations later.

Fig. 4.5 and Fig. 4.6 show the reduced mass flow versus expansion ratio and apparent efficiency versus blade speed ratio maps obtained with the CFD simulations, respectively. Both figures show the maps for each flow branch separately. The results shown in both maps are the average values computed across one rotation of the turbine rotor.

The reduced mass flow decreases with the *MFR* in the hub branch for all rotational speeds. It has the opposite behaviour against the *MFR* in the shroud branch. The apparent efficiency increases slightly with the *MFR* in the hub branch, and it decreases in the shroud branch.
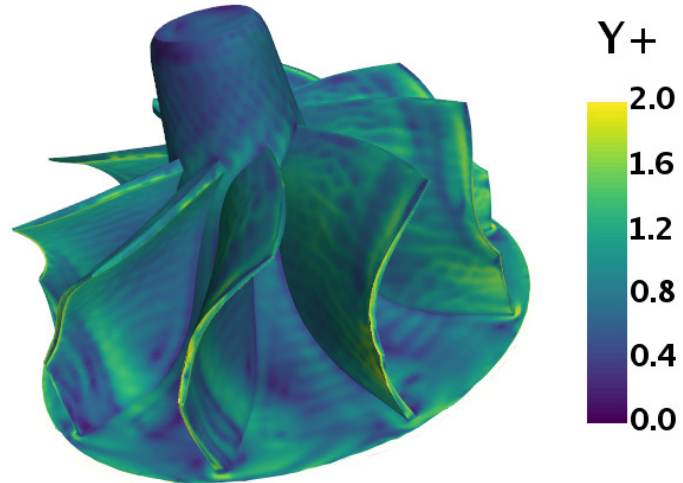
Figure 4.4: Y^+ value at the rotor.

Table 4.3: Values of *MFR* and reduced rotational speed simulated.

MFR [-]	N_{red} [rpm/$\sqrt{\mathrm{K}}$]
0	
0.2	
0.33	3700
0.43	4700
0.53	5800
0.57	7400
0.67	
0.8	
1	
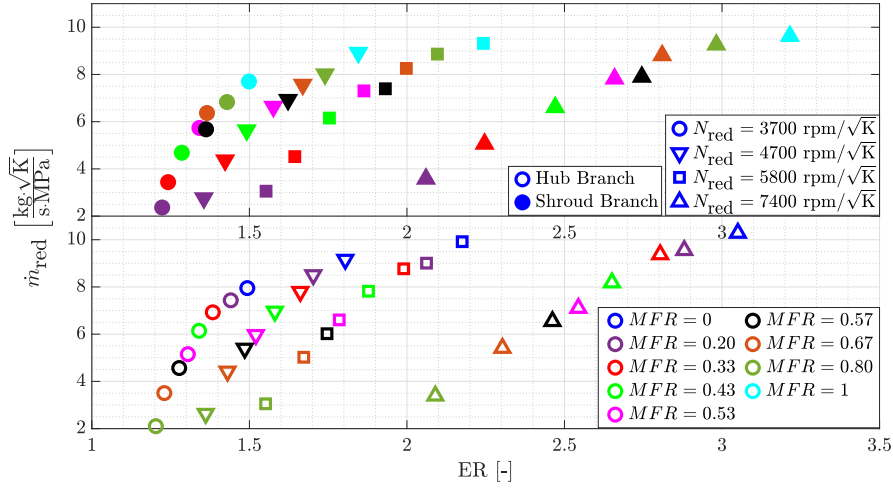
Figure 4.5: CFD flow capacity map.
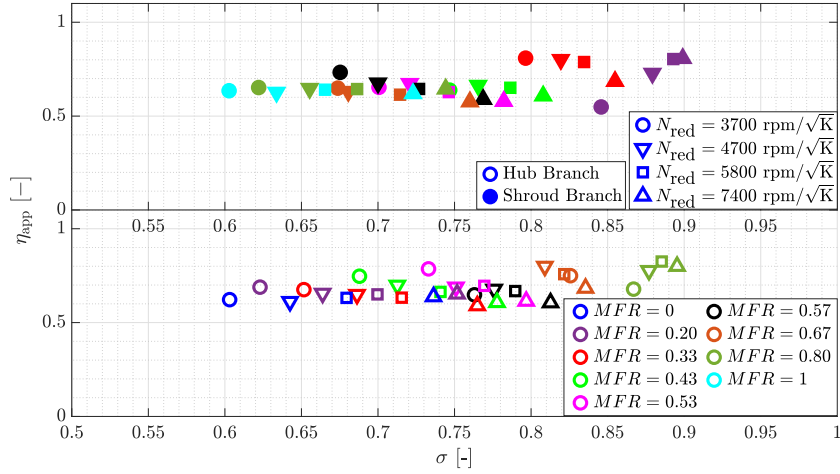
Figure 4.6: Efficiency map.

4.3 Global validation

CFD simulations must be validated with experimental data for relying on them. The current simulations have been globally validated with the experimental measurements described in Chapter 3.

Fig. 4.7 shows the reduced mass flow obtained from the CFD simulations plotted against the reduced mass flow measured experimentally. The black straight line represents perfect concordance between CFD simulations and experimental measurements. The dotted lines represent ±3%, which correspond with the expanded uncertainty of the experimental data. The concordance between CFD simulations and experimental measurements at all rotational speed and *MFR* values is good, having discrepancies lower than 3%. The CFD simulations error in reduced mass flow is consistently lower than the expanded uncertainty of the measurements. Moreover, the R^2 value is high for both flow branches. Therefore, the flow capacity map has been globally validated.
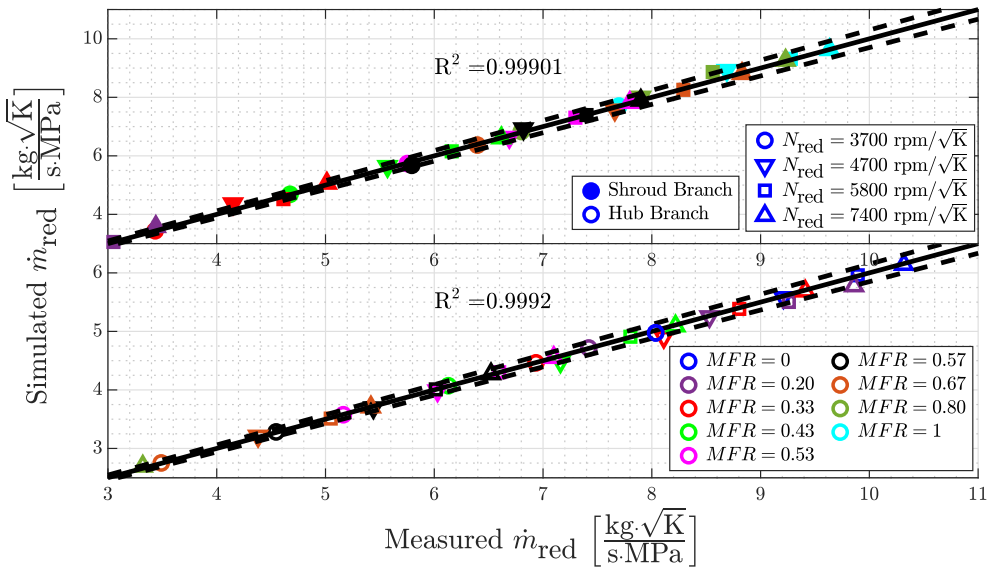
Figure 4.7: Flow capacity map validation.

Fig. 4.8 shows the efficiency obtained from the CFD simulations plotted against the efficiency measured experimentally. The black straight line represents perfect concordance between CFD simulations and experimental measurements. The dotted lines represent ±5 percentage points of efficiency, which also correspond with the expanded uncertainty of the experimental data. The concordance between CFD simulations and experimental measurements at all rotational speed and *MFR* values is good, having discrepancies lower than 5%. Moreover, the R^2 value is high for both flow branches. Thus, the efficiency map

can be considered reliable.
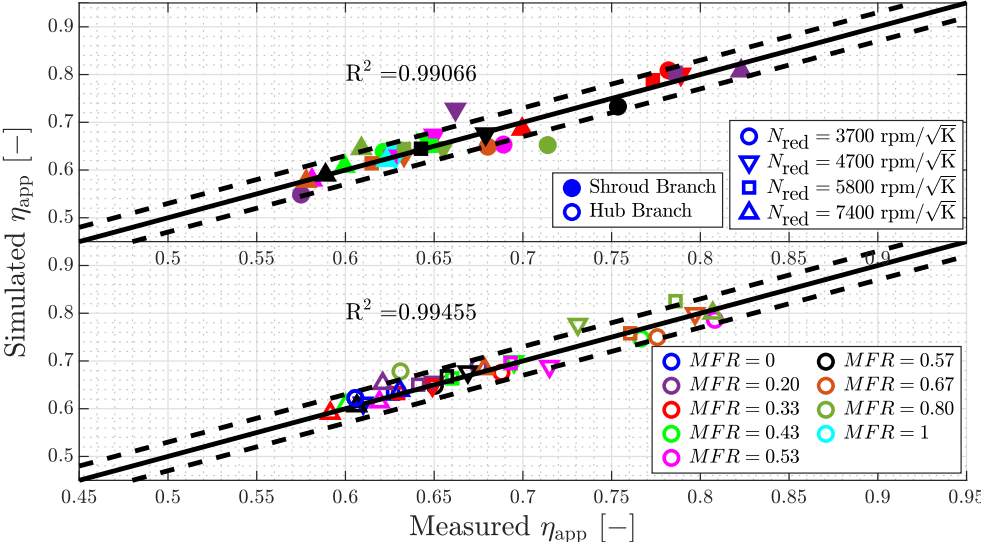
Figure 4.8: Efficiency map validation.

4.4 Summary

This chapter presents the configuration employed in the radial twin-entry turbine CFD simulations carried out during the current work and the validation of the results obtained.

First, the different stations of the twin-entry turbine have been defined. Then, U-RANS simulations are chosen since the accuracy of the results is considered enough for the main purpose of the current work. These CFD simulations are carried out with the $k - \omega$ SST turbulence model, using air as ideal gas differentiated for each flow branch and a sliding mesh to simulate the rotor movement.

After performing a mesh independence study, a mesh of 5.5 million cells has been chosen. Then, nine different *MFR* values and four different rotational speeds are selected based on the experimental data available to carry out a total of 36 CFD simulations. Therefore, a wide range of cases under unequal admission conditions are simulated, as pointed out in Chapter 2.

Finally, the flow capacity and the efficiency maps have been globally validated against the steady-state measurements exposed in Chapter 3. The reduced mass flow obtained from the simulations has a lower error than the expanded uncertainty of the experimental data, and the efficiency has an error lower than 5%. Therefore, the CFD simulations can be considered reliable.

These CFD simulations can be analysed thoroughly to obtain flow patterns and identify the main sources of losses. These results can be used to further develop simplified one-dimensional models capable of extrapolating the flow capacity and efficiency maps.

Therefore, the next step is to analyse the flow behaviour of each branch and identify the phenomena within twin-entry turbines that are producing the most significant losses.

4.5 References

[20] P. Fajardo Peña. "Methodology for the numerical characterization of a radial turbine under steady and pulsating flow". PhD thesis. Universitat Politècnica de València, July 2012. DOI: 10.4995/Thesis/10251/16878 (cit. on pp. 4, 73).

[58] J. Galindo, S. Hoyas, P. Fajardo, and R. Navarro. "Set-up analysis and optimization of CFD simulations for radial turbines". In: *Engineering Applications of Computational Fluid Mechanics* 7 (2013), pp. 441–460. DOI: 10.1080/19942060.2013.11015484 (cit. on pp. 20, 73).

[106] *Simcenter STAR-CCM+ Documentation*. Siemens. 2019 (cit. on p. 73).

[107] P. J. Roache. "Perspective: A method for uniform reporting of grid refinement studies". In: *Journal of Fluids Engineering* 116.3 (Sept. 1994), pp. 405–413. ISSN: 0098-2202. DOI: 10.1115/1.2910291 (cit. on p. 74).

CFD simulations flow and losses analysis

Contents

Figures

5.1 Introduction

O NCE the CFD simulations are globally validated with the steady-state measurements performed in Chapter 3, the next step is to analyse the flow behaviour inside twin-entry turbines.

The data that can be experimentally measured inside a twin-entry turbine is limited. But in CFD, relevant variables like pressure, temperature or mass flow can be obtained at any domain point. There is no limitation in the placement of the sensors. Therefore, the mass flow at a certain point of the domain or the total pressure drop in a given part can be easily obtained. The figures presented as contour plots of some twin-entry turbine part in this chapter represent the variables shown in a certain time-stamp. The figures presented as x-y or bar plots represent the variables shown averaged across one rotation of the turbine rotor.

The information obtained from this CFD analysis combined with the information extracted from the experimental tests could be valuable to develop reliable one-dimensional models in the following chapters.

This chapter presents a flow analysis of the twin-entry turbine using these CFD simulations. First, the mass flow from each branch is analysed within the twin-entry turbine, focusing on the study of the rotor inlet and outlet areas' behaviour against the *MFR*. Then, the losses produced within twin-entry turbines are located and quantified with physical models. This losses analysis is divided into the different twin-entry turbine parts, and all the main losses detected are combined at the end.

5.2 Mass flow analysis

The mass flow from each flow branch has been differentiated using the multi-component gas option explained in the previous chapter. Thus, the flow behaviour of each branch can be analysed within the whole domain. It would be meaningful to know the behaviour of each flow branch against each other once they are united at the volutes' outlets.

The gas concentration of one of the branches can be plotted for following in which part of the turbine it is located. Fig. 5.1 shows the shroud air concentration in a section that includes the volutes, the interspace, the rotor and the rotor outlet. The cases shown as examples in Fig. 5.1 are at reduced rotational speed $3700 \, \text{rpm} \, \text{K}^{-0.5}$ and *MFR* 0.57 (sub-figure 5.1(a)) and at reduced rotational speed $5800 \, \text{rpm} \, \text{K}^{-0.5}$ and *MFR* 0.43 (sub-figure 5.1(b)).

The flow inside the volutes is totally differentiated since there is no flow recirculation in this case. Therefore, the shroud air concentration is one in the shroud volute branch and 0 in the hub volute branch.
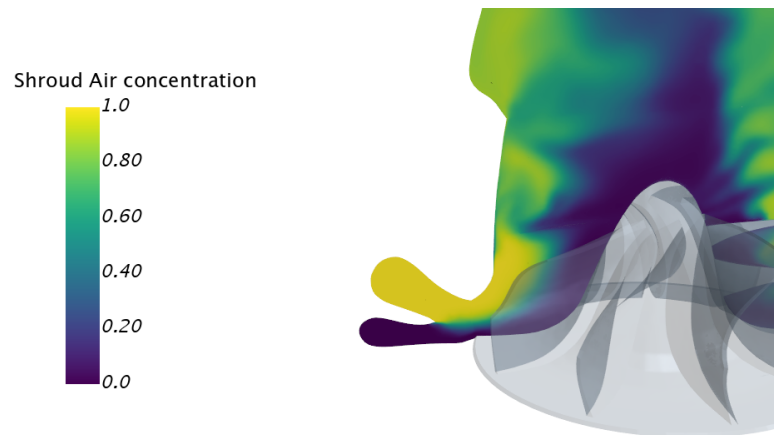
(a) *MFR* 0.57, reduced rotational speed $3700 \, \text{rpm} \, \text{K}^{-0.5}$
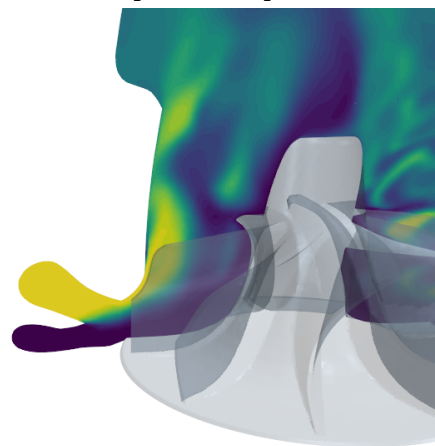
(b) *MFR* 0.43, reduced rotational speed $5800 \, \text{rpm} \, \text{K}^{-0.5}$

Figure 5.1: Shroud air concentration within the twin-entry turbine.

Moreover, the flows do not fully mix neither in the interspace nor in the rotor. There is some mixing in the middle of the channel, but it is not significant compared to the region where the flows are not mixed. Thus, there is high shroud air concentration near the rotor shroud while there is low shroud air concentration near the rotor hub.

This behaviour can be observed until the rotor outlet. The complete mixing of both flows takes place downstream of the rotor blades trailing edge. A more uniform value of shroud air concentration is found in the outlet plenum. Although there are still regions with more or less shroud air concentration, the shroud air concentration at the outlet plenum has values around 0.57 in sub-figure 5.1(a) and around 0.43 in sub-figure 5.1(b). This value is expected in those cases since they show cases with those *MFR* values.

This mass flow behaviour corresponds with the hypothesis made by the experimental data analysis described in [49]. It says that twin-entry turbines could be modelled as two separated single entry VGT turbines working in parallel. The implications of this hypothesis will be further studied in Chapter 6.

Additionally, the region where the shroud air concentration is close to 1 changes from case to case. Figures 5.2, 5.3 and 5.4 show the shroud air concentration in a radial section of the rotor for different *MFR* and reduced rotational speed values for a more thorough analysis of this behaviour.

The three figures show a clear trend: the region where the shroud air concentration is close to 1 increases with the *MFR* value. Fig. 5.2 shows that the shroud air is confined in a small zone near the rotor shroud, and most of the rotor channel has hub air. In the opposite case, Fig. 5.4 shows that the shroud air comprises most of the rotor channel, and there is only a small part near the rotor hub where the hub air is predominant. Fig. 5.3 shows a middle case where the region where the shroud air is predominant and the region where the hub air is predominant are similar.

The reduced rotational speed seems to have little influence on this behaviour. Qualitatively, the shroud air concentration is similar for the same *MFR* value, although the reduced rotational speed changes.

Moreover, the rotor channels situated at the southeast of the radial section plotted have different behaviour from the rest of the rotor channel in most cases. This region of the radial section corresponds with the tongue of the turbine, where the behaviour of the flow is slightly different. However, the effect of this behaviour is small in the general behaviour of the twin-entry turbine.

Therefore, the percentage of volume corresponding to each flow branch should depend principally on the *MFR* value. The area corresponding to each flow branch at rotor inlet and rotor outlet sections could quantitatively represent this effect of the *MFR* value. Fig. 5.5 shows how the rotor inlet and rotor outlet areas occupied by each flow branch vary against *MFR*. The different reduced rotational speeds are differentiated with symbols. The empty symbols and the
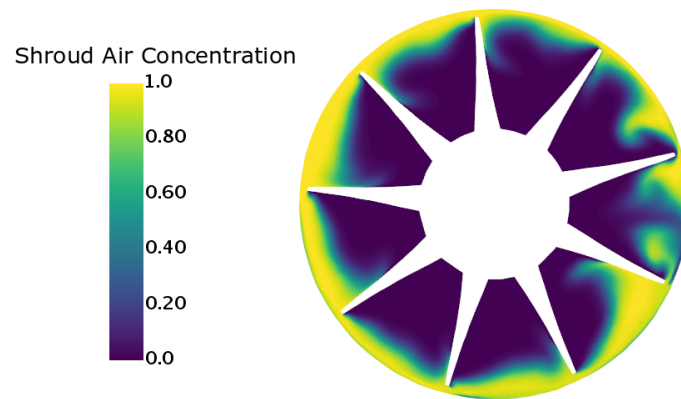
(a) Reduced rotational speed $4700 \, \mathrm{rpm \, K^{-0.5}}$
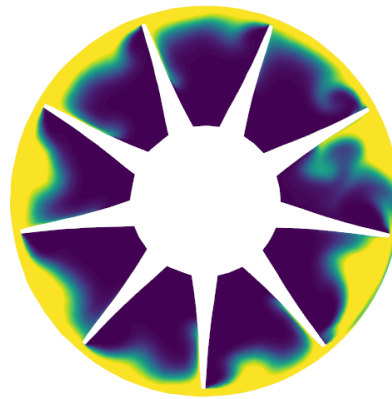
(b) Reduced rotational speed $7400 \, \mathrm{rpm \, K^{-0.5}}$

Figure 5.2: Shroud air concentration in a radial section at *MFR* 0.33.
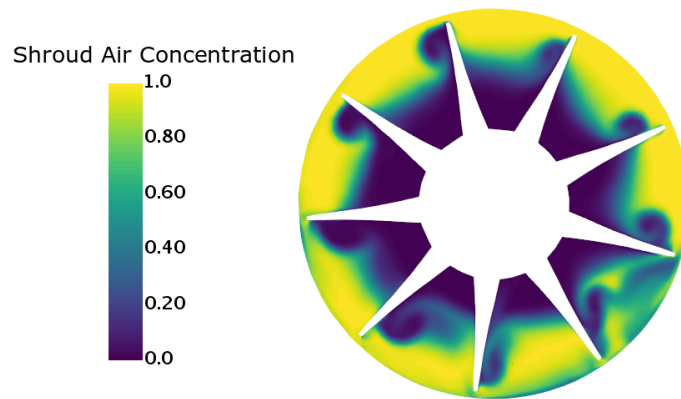
(a) Reduced rotational speed $4700 \, \mathrm{rpm \, K}^{-0.5}$
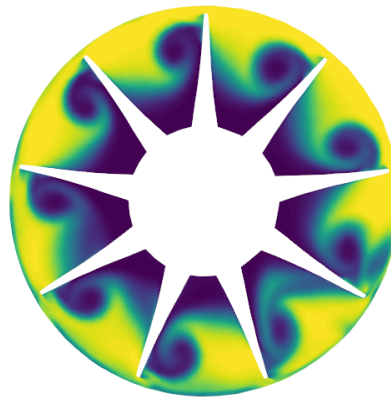
(b) Reduced rotational speed $7400 \, \mathrm{rpm \, K}^{-0.5}$

Figure 5.3: Shroud air concentration in a radial section at *MFR* 0.53.
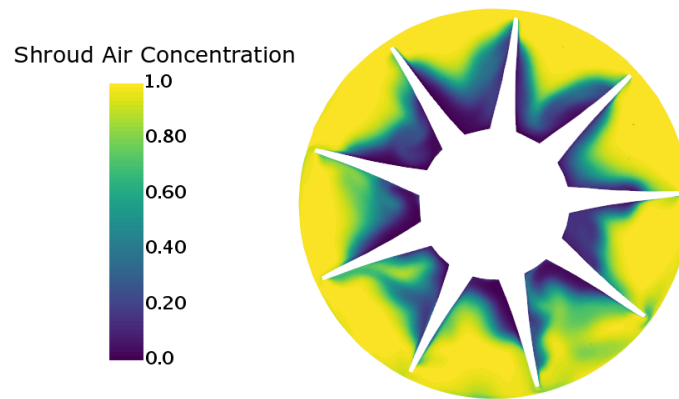
(a) Reduced rotational speed $4700 \, \text{rpm} \, \text{K}^{-0.5}$
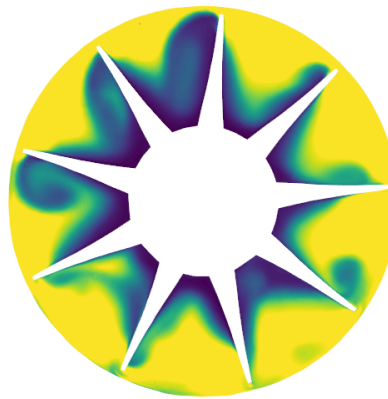
(b) Reduced rotational speed $7400 \, \text{rpm} \, \text{K}^{-0.5}$

Figure 5.4: Shroud air concentration in a radial section at *MFR* 0.67.

dotted line correspond to the area occupied by the hub branch. The filled symbols and the straight line correspond to the area occupied by the shroud branch.
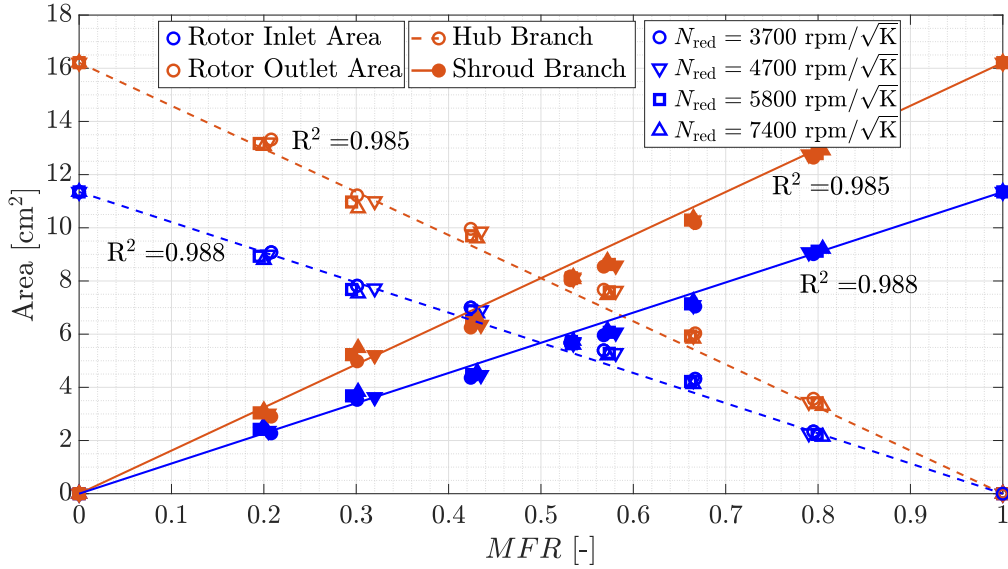
Figure 5.5: Effect of the *MFR* value and the reduced rotational speed on the rotor inlet and rotor outlet areas occupied by each flow branch.

The influence of the reduced rotational speed on the rotor inlet and rotor outlet area variations is negligible as it was inferred from figures 5.2, 5.3 and 5.4. However, the rotor inlet and rotor outlet areas of each flow branch are strongly dependent on *MFR*. Furthermore, both rotor inlet and outlet areas follow a nearly linear trend with *MFR*. Fig. 5.5 also shows the R^2 value for each flow branch and for both rotor inlet and rotor outlet areas. The R^2 values are high in all cases, but a little higher for the results of the rotor inlet area. This difference could be due to the little mixing that might occur inside the rotor channel. However, this effect could be considered negligible since the rotor outlet area behaviour against *MFR* is similar to the rotor inlet area behaviour. Therefore, a rotor inlet and rotor outlet area linearity with *MFR* assumption could be made to develop the effective area one-dimensional model in Chapter 6.

The mass flow depends proportionally on density, area and velocity normal to this area. Therefore, the area linear dependence on *MFR* could be corroborated by studying the density and the normal velocity behaviour against the *MFR*. The product of density and average radial velocity corresponding to one of the branches at the rotor inlet divided by the same product of the other branch is plotted in Fig. 5.6. The same ratio but using axial velocity instead of radial velocity is computed at the rotor outlet section and plotted in Fig. 5.6.
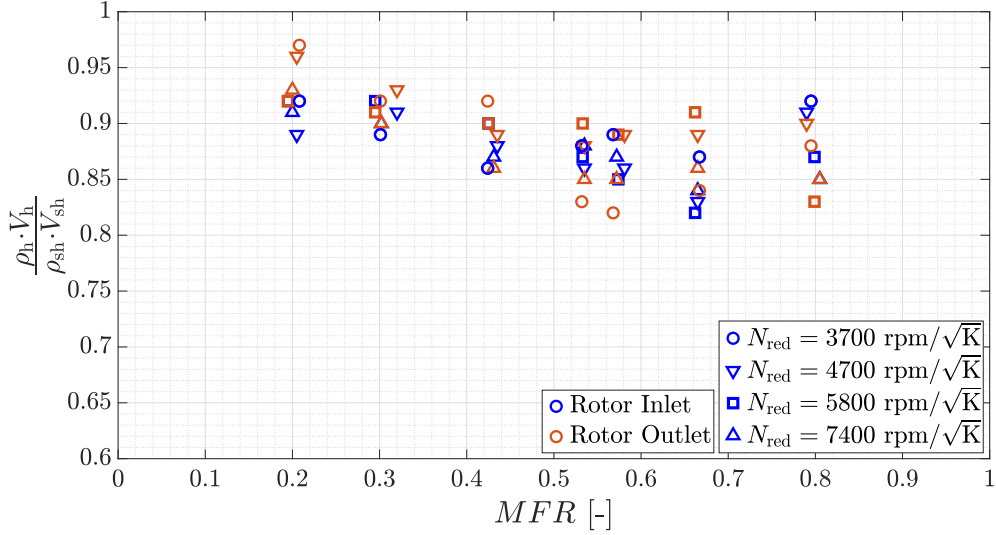
Figure 5.6: Corroboration of the rotor inlet and rotor outlet area linearity with the *MFR* assumption.

Both ratios show a similar behaviour: they are relatively close to one for all *MFR* values. These ratios being close to one means that the rotor inlet and rotor outlet areas could be considered linear with *MFR*. Thus, the assumptions of rotor inlet and rotor outlet area linearity with *MFR* inferred from the mass flow behaviour shown in figures 5.1 to 5.4 would be corroborated.

Other relevant parameters that can be studied from the mass flow behaviour in these CFD simulations are the rotor inlet and rotor outlet flow angles. These parameters are helpful to develop one-dimensional models, as will be described in Chapter 6. The rotor inlet flow angle has been commonly considered constant in single entry turbines, as described in Chiong et al. [108] and Galindo et al. [92]. There are two clearly differentiated regions where there is mass flow only from one of the flow branches in twin-entry turbines. Therefore, two different rotor inlet flow angle values are expected, one for each flow branch.

The total pressure at the rotor inlet section can be obtained for each flow branch from the CFD simulations to ensure that the assumption of constant rotor inlet flow angle is acceptable. Fig. 5.7 and 5.8 show the total pressure at the rotor inlet section against the position around the rotor for each branch, respectively.

Fig. 5.7 and 5.8 show that the total pressure at the rotor inlet section is nearly constant around the rotor for both flow branches in all simulated cases. There are variations in the region near the tongue, but this region is small compared to the entire section, and its typical deviation is low. Thus, the
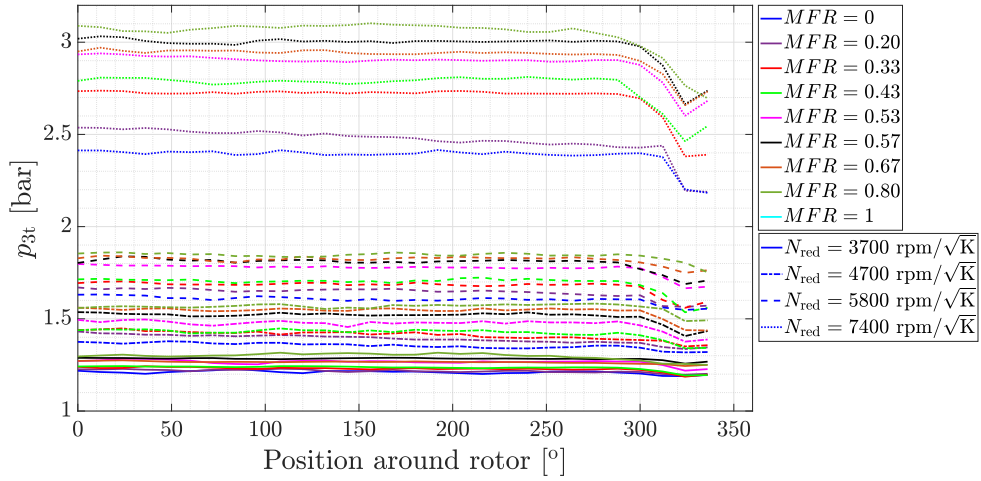
Figure 5.7: Total pressure at the rotor inlet section. Hub branch.
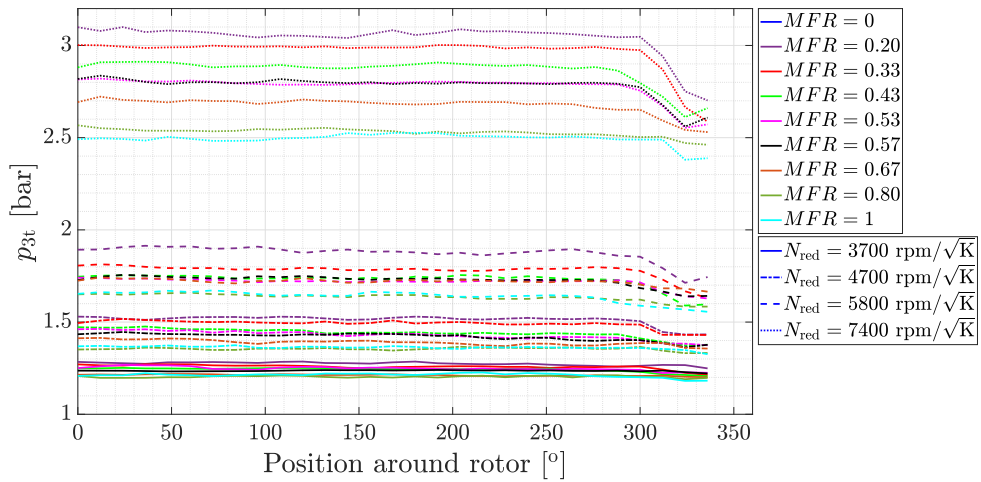
Figure 5.8: Total pressure at the rotor inlet section. Shroud branch.

constant rotor inlet flow angle assumption could be considered acceptable. The rotor inlet flow angle is computed from the radial axis, as shown in Fig. 5.9.

The rotor outlet flow angle is not constant along the radial position as the blade outlet angle also varies. However, it can be considered constant along the circumferential position since the rotor channels have the same geometry and the rotor blades move as a rigid solid. Therefore, a mean rotor outlet flow angle can be computed as the mean value of the angle obtained at different radial positions. The rotor outlet flow angle is computed from the axial axis, as shown in Fig. 5.9.
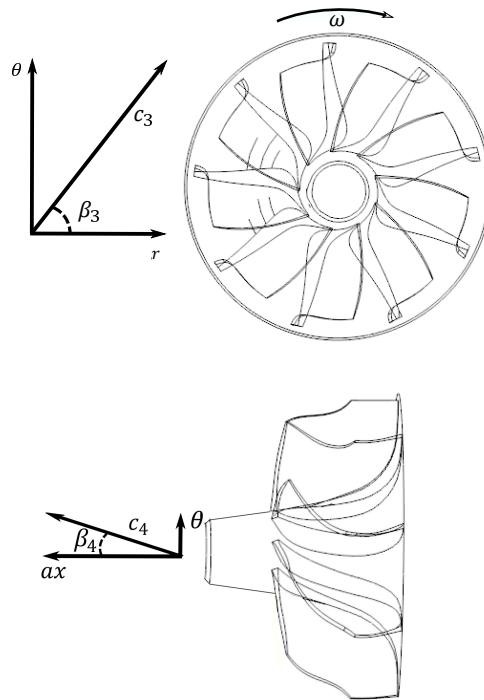
Figure 5.9: Computation of rotor inlet and rotor outlet flow angles.

The effect of the *MFR* value and the reduced rotational speed on the rotor inlet and rotor outlet flow angles, taking into account the previous considerations, is shown in Fig. 5.10. It shows the rotor inlet and rotor outlet flow angles for both branches separately.

The effect of the reduced rotational speed on the rotor inlet flow angle is low. This flow angle is nearly the same for a given *MFR* value and variation of the reduced rotational speed. Nevertheless, the *MFR* value has a relevant effect on the rotor inlet flow angle. This flow angle decreases with *MFR* for the hub branch and increases for the shroud branch. Moreover, it seems to follow a linear
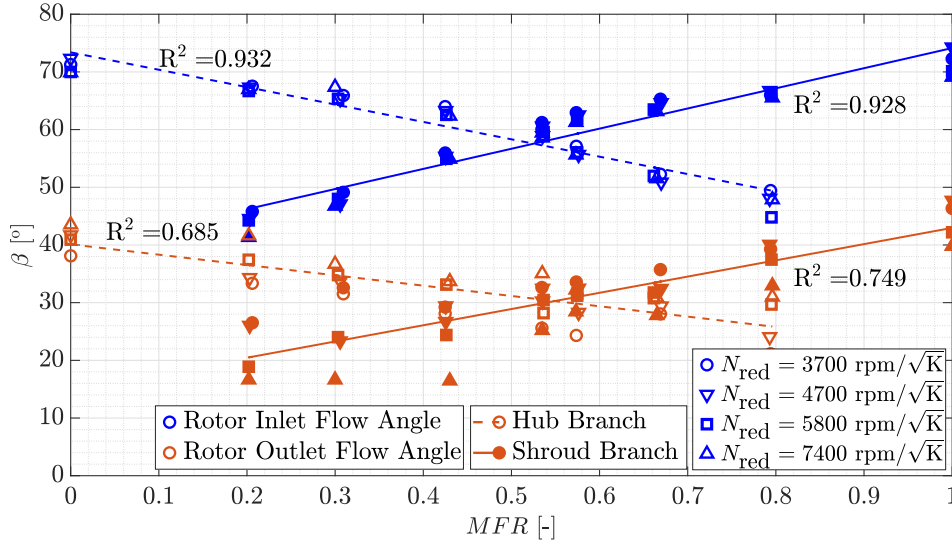
Figure 5.10: Effect of the *MFR* value and the reduced rotational speed on the rotor inlet and rotor outlet flow angles.

trend with *MFR*. There is an excellent correlation between rotor inlet flow angle and *MFR* value, as indicated by the high R^2 values for both branches. Again, the behaviour of the rotor inlet flow angle with *MFR* found in the CFD simulations could help develop the one-dimensional efficiency model in Chapter 6.

The effect of the reduced rotational speed on the rotor outlet angle is higher than on the rotor inlet flow angle. The rotor outlet flow angle increases with the reduced rotational speed for the hub branch and decreases for the shroud branch. Although only one rotor outlet flow angle is shown for each simulation, it is computed as an average value of the rotor outlet flow angle within the radial position. The rotor blade angle is not constant in the radial position and the flow from each branch has been demonstrated to be separated in this section. Combining both considerations, the rotor outlet flow angle is expected to behave different in each branch when the reduced rotational speed varies. Furthermore, the rotor outlet flow angle has a similar behaviour against the *MFR* value than the rotor inlet flow angle. It decreases with *MFR* for the hub branch and increases for the shroud branch. However, the correlation between rotor outlet flow angle and *MFR* value is not as straightforward as the rotor inlet flow angle since there is also a strong dependence on the reduced rotational speed.

95

5.3 Losses analysis

The losses analysis can focus on each twin-entry turbine part in terms of total pressure losses. Thus, the volute losses are first analysed, followed by the interspace losses, the rotor losses and the outlet losses. The losses have been quantified in each part. The quantification of these losses has been made for each branch separately. Moreover, the assumption of area linearity with *MFR* found in the previous section has been employed to obtain the different variables in the CFD simulations.

Then, the primary sources of these losses have been defined, trying to correlate them with some simple physics-based models. The effect of *MFR* and reduced rotational speed on the losses has also been studied, finding that they have a considerable influence on most losses.

5.3.1 Volute losses

The twin-entry turbine volutes are smooth; they have no sudden expansions inside them. They do not have interaction between flow branches or any mobile part. Therefore, the volutes are expected to be the part with the lowest losses. Twin-entry turbine volutes can present some unsteadiness, as it has been studied by some authors like Cerdoun and Ghenaiet [76]. However, it depends on the geometry, and it can be solved. The current analysis will not consider this possible unsteadiness since it seems to be an exceptional problem.

Hence, the main volute losses are due to the friction with the walls. A feasible approach for quantifying the friction losses in the volutes could be the passage losses model described by Futral et al. [109]. This passage losses model is defined in Eq. 5.1, where ρ stands for the density, v for the absolute velocity and K is an adjustable coefficient. The density and velocity values are the turbine inlet values (station 0) for each flow branch extracted from the CFD simulations.

$$\Delta p_{\text{pass}} = K \cdot \rho \cdot v^2 \tag{5.1}$$

The losses computed with Eq. 5.1 can be compared with the total pressure losses extracted directly from the CFD simulations. These total pressure losses are obtained by computing the total pressure values at the turbine inlet and the volute outlet sections for each flow branch.

The total pressure losses quantified with Eq. 5.1 are shown in Fig. 5.11 for the hub branch and the shroud branch separately. Fig. 5.11 also illustrates the difference between the total pressure losses quantified with Eq. 5.1 and the total pressure losses extracted directly from the CFD simulations with green bars. The quantified total pressure losses under-predict the total pressure losses when

the green bars are at the top of the bar. They over-predict the total pressure losses when the green bars are at the bottom, under 0.
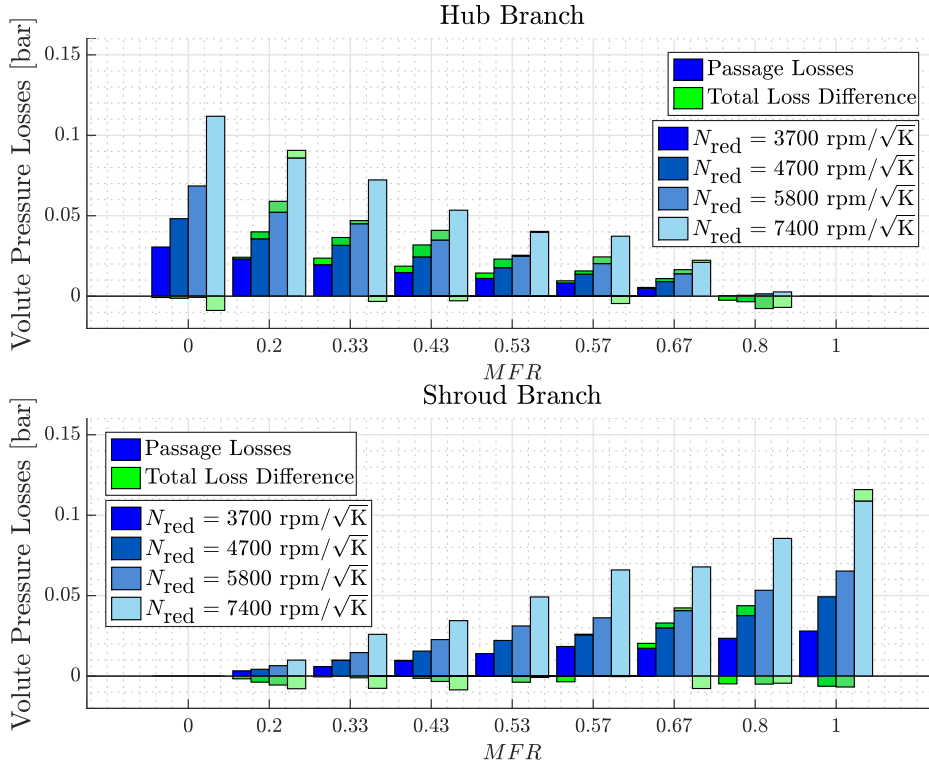
Figure 5.11: Volute total pressure losses

The total loss difference between the passage model and the total pressure losses extracted directly from the CFD simulations is slight for all simulated cases. Therefore, the passage model proposed reasonably captures the volute pressure losses without considering other sources of losses.

Moreover, the effect of the *MFR* and the reduced rotational speed on the volute pressure losses can also be inferred from Fig. 5.11.

The volute pressure losses increase with the reduced rotational speed. This behaviour was expected since increasing the reduced rotational speed means increasing the expansion ratio in the current simulations.

The volute pressure losses decrease with the *MFR* for the hub branch and increase for the shroud branch. This behaviour was also expected since the mass flow passing through the hub branch decreases with the *MFR*, and the mass flow passing through the shroud branch increases. The passage losses model proposed computes higher losses when there is higher mass flow passing through the branch of study.

97

5.3.2 Interspace losses

The interspace is the part between the volutes outlet and the rotor inlet. The flow branches are joined in this part. However, they do not fully mix as described in the previous section. Despite being a smaller region, there are more complex phenomena in the interspace than in the volutes. The junction of both flow branches could generate some losses. Moreover, a sudden expansion downstream of the volutes union could appear depending on the boundary conditions.

The first cases to examine are those with similar boundary flow conditions in both flow branches. Those cases have *MFR* values close to full admission conditions, i.e. *MFR* from 0.4 to 0.6. The losses produced by the junction of both flow branches or sudden expansions are expected to be low in these cases. Therefore, the primary source of losses in the interspace in these cases should be the friction with the walls as in the volutes.

The entropy generation in the interspace could be plotted to corroborate this assumption. If the higher entropy generation is located near the walls, the primary source of losses will be the friction losses. The entropy generation in interspace sections at 90° and 180° from the tongue is shown in Fig. 5.13 for a case with a reduced rotational speed of $4700\,\mathrm{rpm\,K^{-0.5}}$ and *MFR* 0.53. Fig. 5.12 shows where the tongue is considered in the studied twin-entry turbine and where the sections presented in Fig. 5.13 and 5.14 are placed.
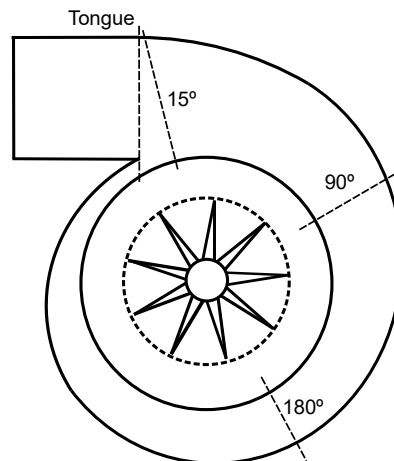
Figure 5.12: Tongue and sections used in the interspace losses analysis.

The primary entropy generation in both sections is located near the walls. The maximum entropy generation found is around $50\,\mathrm{J\,kg^{-1}\,K^{-1}}$, and it is marked in red in both sections. This behaviour is similar in almost all sections.
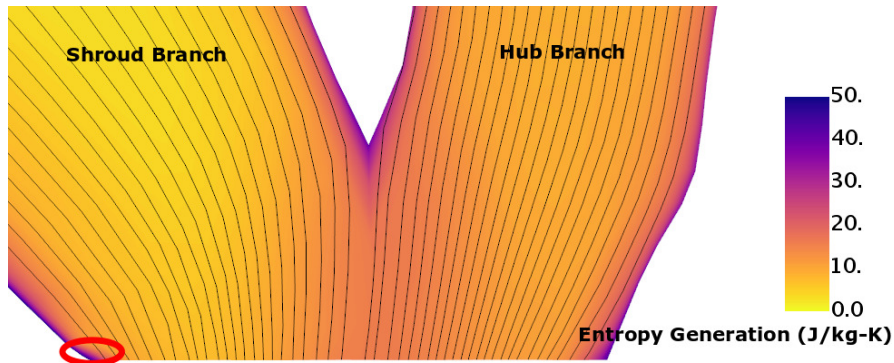
(a) Section at 90° from the tongue.
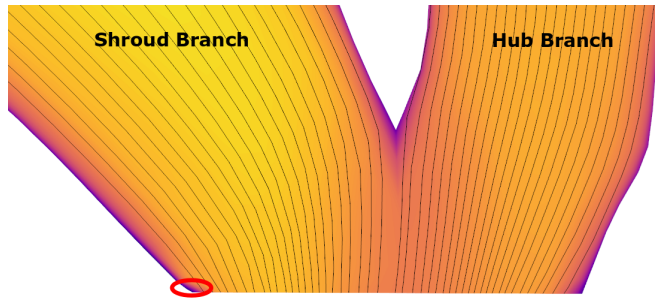
(b) Section at 180° from the tongue.

Figure 5.13: Entropy generation in two interspace sections for an *MFR* 0.53.

However, a higher entropy generation has been found in the sections near the tongue that range between 0° and 30°. Fig. 5.14 shows a section at 15° from the tongue for the same simulated case where this effect can be observed. The junction between the incoming mass flow and the mass flow from the end of the volutes (section 360°) could be causing this higher entropy generation.
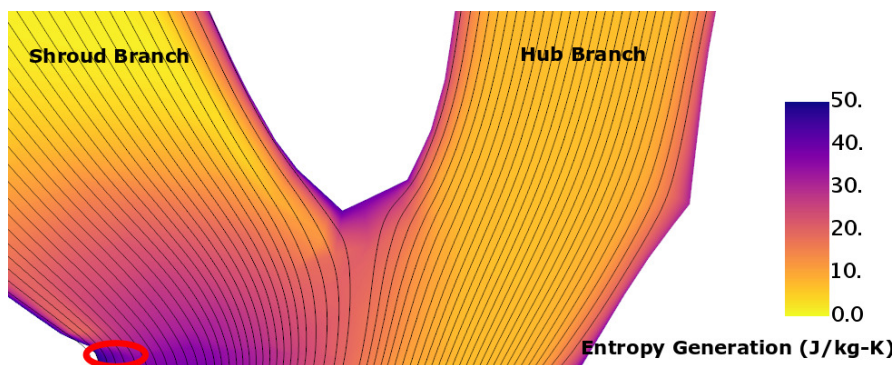
Figure 5.14: Entropy generation at 15° from the tongue for an *MFR* 0.53.

This higher entropy generation far from the wall is still lower than the entropy generation near the walls. The highest entropy generation in Fig. 5.14 is marked in red, and it is also around $50 \, \mathrm{J \, kg^{-1} \, K^{-1}}$. Moreover, it is only found in a confined region of the interspace (30° from the total 360°). Therefore, the friction losses would constitute the primary source of losses in the cases near full admission conditions.

The interspace total pressure losses produced by the wall friction could be quantified with the passage losses model proposed by Futral et al. [109] as in the volutes. The density and the velocity are evaluated at the volute outlet of each flow branch (station 1). The adjustable coefficient K should be capable of including the additional losses produced near the tongue.

Then, the losses computed with the passage losses model can be compared with the total pressure losses extracted directly from the CFD simulations. The total pressure losses are now evaluated between the volute outlet and the rotor inlet sections for each flow branch. The interspace total pressure losses quantified with the passage losses model and the difference between this quantification and the total pressure losses extracted directly from the CFD simulations are plotted in Fig. 5.15 for the hub branch and the shroud branch separately. The quantified total pressure losses under-predict the total pressure losses when the green bars are at the top of the bar. They over-predict the total pressure losses when the green bars are at the bottom, under 0.

The interspace total pressure losses computed with the passage losses model are adequately captured for cases near full admission conditions. However, the quantification does not correctly represent the total pressure losses at *MFR* values far from full admission conditions. The model under-predicts the interspace total pressure losses when high mass flow passes through the branch of study (*MFR* near 0 for the hub branch and near 1 for the shroud branch). It over-predicts the interspace total pressure losses when low mass flow passes through the branch of study (*MFR* near 1 for the hub branch and near 0 for the shroud branch). Thus, additional physical phenomena must be taken into account for quantifying the interspace losses properly.

A sudden expansion has been observed at the junction of the volutes when there are *MFR* values far from full admission conditions. An interspace section at 90° from the tongue is shown in Fig. 5.16 at *MFR* values of 0.67 and 0.20 and both at reduced rotational speed of $3700 \, \mathrm{rpm \, K^{-0.5}}$ for examining this sudden expansion. The shroud air concentration is plotted in addition to velocity convolution lines for clarity of the results. Fig. 5.16 shows that this sudden expansion is experienced by the hub branch when the *MFR* value is lower than 0.4 and by the shroud branch when the *MFR* value is higher than 0.6. The flow branch with higher mass flow occupies higher volume and rotor inlet area as described in the previous section. Therefore, this sudden expansion is consistent with the mass flow behaviour described.
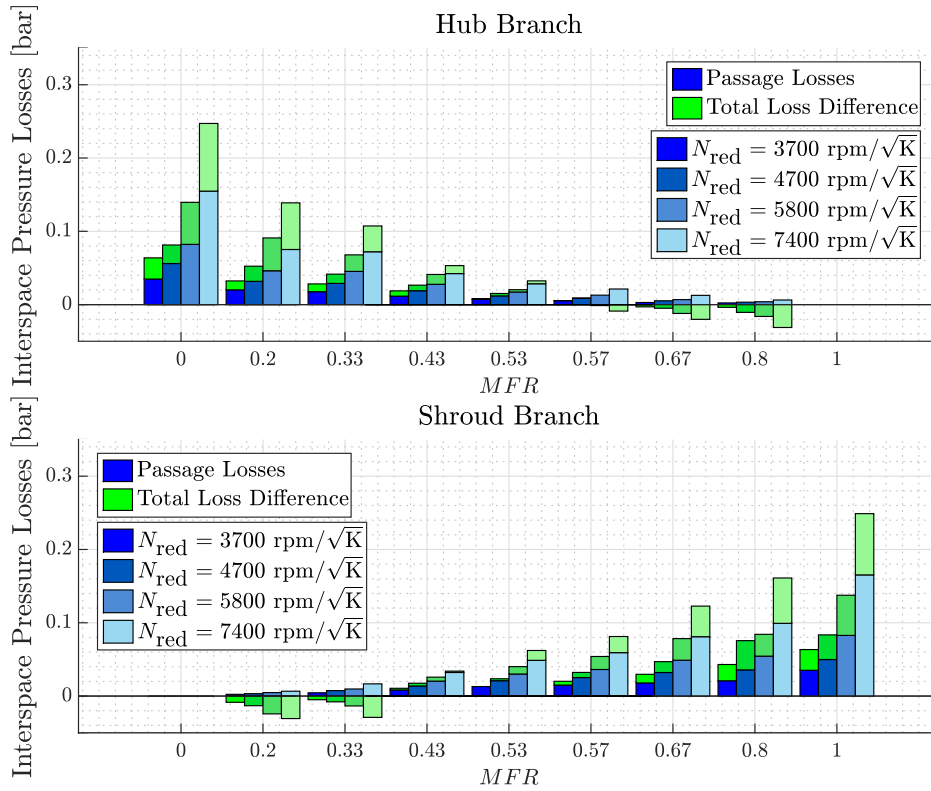
Figure 5.15: Interspace total pressure losses.

This sudden expansion generates considerable losses in cases with highly unequal admission conditions. It can even induce recirculation into the other volute in extreme *MFR* values. This recirculation could particularly appear in partial admission conditions, where no mass flow is coming through the other branch. Fig. 5.17 shows the same section at 90° from the tongue for a case with a reduced rotational speed of $3700 \, \mathrm{rpm} \, \mathrm{K}^{-0.5}$ and an *MFR* 1 where all the mass flow comes from the shroud branch. The entropy generation is plotted in this case in addition to the velocity convolution lines. The recirculation in the hub branch has a high entropy generation (with a maximum value of $122 \, \mathrm{J} \, \mathrm{kg}^{-1} \, \mathrm{K}^{-1}$ at the centre). It means that the total pressure losses are larger in these extreme cases.

The quantification of the losses produced by this sudden expansion in the interspace could be modelled with the Borda-Carnot equation. The model proposed for this quantification is defined in Eq. 5.2. ρ and v stand again for the density and the absolute velocity respectively, K is an adjustable coefficient and A_{in} and A_{out} are the inlet and outlet areas occupied by each flow branch. Density, velocity and inlet area are evaluated at each volute outlet (station 1),
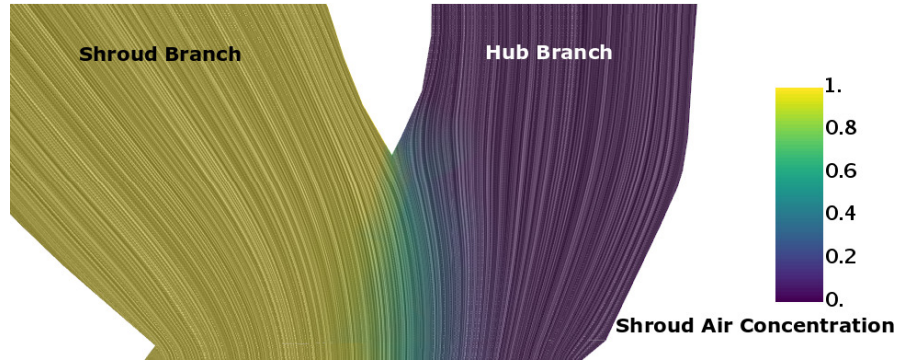
(a) *MFR* 0.67
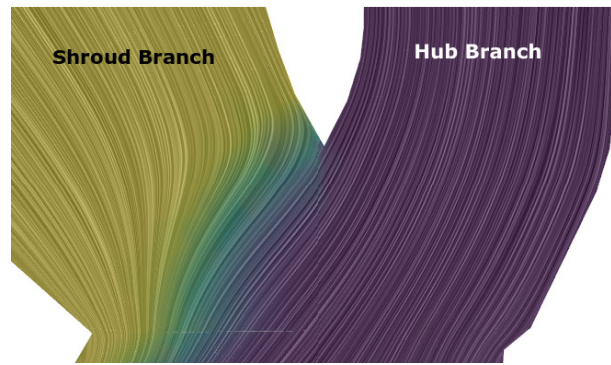
(b) *MFR* 0.20

Figure 5.16: Interspace sudden expansion in a section at 90 degrees from the tongue.
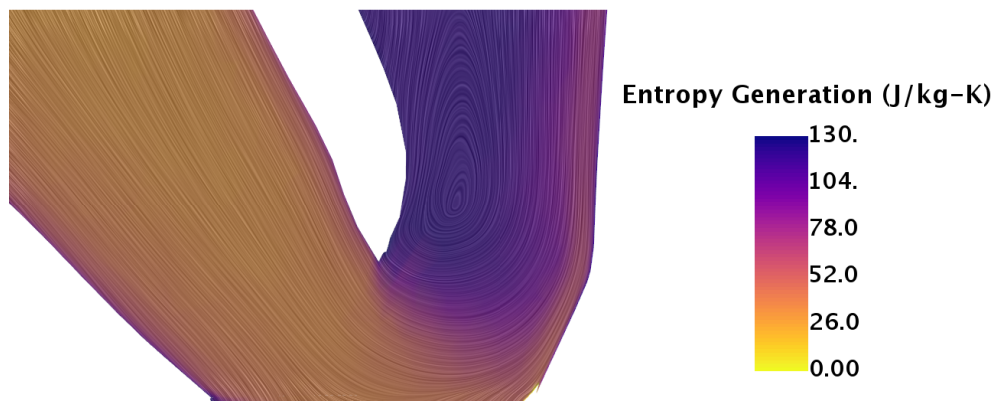
Figure 5.17: Interspace recirculation for a case with *MFR* 1.

and the outlet area is evaluated at the rotor inlet (station 3) for each flow branch. These losses will only be computed in the cases with *MFR* lower than 0.4 for the hub branch and higher than 0.6 for the shroud branch since this sudden expansion does not exist in other cases.

$$\Delta p_{\text{SudExp}} = K \cdot \rho \cdot v^2 \cdot (1 - A_{\text{in}}/A_{\text{out}}) \tag{5.2}$$

An additional source of losses has been detected in the interspace. These losses are due to the interaction between flow branches. The boundary conditions of each branch are different in unequal admission conditions. These differences are still remarkable at the volutes outlet. Therefore, the momentum of each branch, when they are joined, is different. This different momentum generates an interaction between flow branches where they exchange momentum to achieve an intermediate steady state.

Fig. 5.18(a) shows the interface velocity map for a case of *MFR* 0.67 and a reduced rotational speed of $5800\,\text{rpm}\,\text{K}^{-0.5}$ in a section at 90° from the tongue. There is a remarkable difference between the velocities of both flow branches. This velocity difference generates a velocity gradient in the normal direction of the flow. Both flow branches do not fully mix in the interspace, as explained in the previous section. The thin region where they have mixed is marked in red in Fig. 5.18(b). It shows the shroud air concentration in the same section, and the region marked in red is the region where the shroud air concentration is 0.5 ± 0.2. This small region could be considered as the contact surface between flow branches. Thus, the velocity gradient generated in the normal direction of the flow will be normal to this contact surface.

The difference of momentum between flow branches produces a transmission of momentum from the flow branch with higher momentum to the flow branch with lower momentum when they are in contact. The region where this momentum exchange between flow branches is produced is the contact surface remarked in Fig. 5.18(b).

There are total pressure losses in the flow branch with higher momentum due to this momentum exchange between flow branches. Nevertheless, the flow branch with lower momentum is experiencing gains in total pressure instead of losses since its momentum is increasing. This behaviour could explain why the interspace losses in *MFR* values where there is low mass flow (near 1 for the hub branch and near 0 for the shroud branch) have lower total pressure losses.

A more thorough analysis of these losses could be made for trying to quantify them. They should depend directly on the velocity difference between flow branches and the size of the contact area. The thickness of the contact area seems to be constant in Fig. 5.18(b), so these losses should depend only on the length of the contact area. However, this momentum exchange between flow branches is a turbulent phenomenon. Therefore, some turbulent parameters

(a) Velocity map.

(b) Contact surface between flow branches.
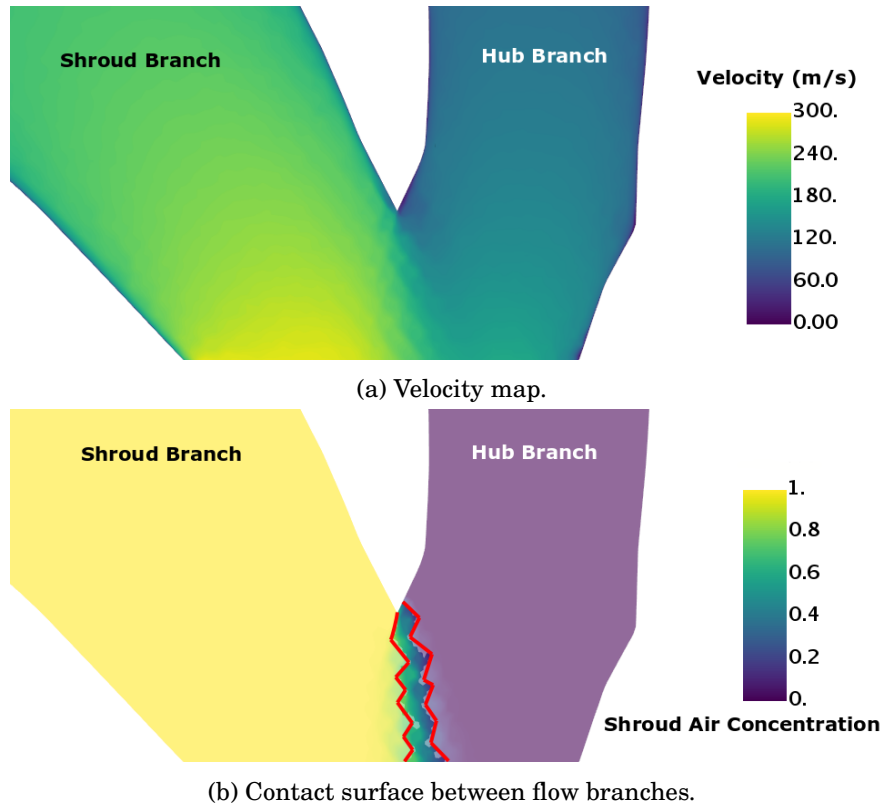
Figure 5.18: Interface contact surface and velocity map for a case of *MFR* 0.67 in a section at 90° from the tongue.

such as the turbulent characteristic length or the turbulent viscosity could be studied to detect if these losses depend on any of them.

The specific dissipation rate (ω) and the turbulent kinetic energy (k) have been extracted from the CFD simulations computing them as the mean value of the interspace cells for all simulated cases. The turbulent characteristic length and the turbulent viscosity can be calculated employing the specific dissipation rate and the turbulent kinetic energy in the equations of the $k - \omega$ SST model selected to carry out the CFD simulations. The turbulent characteristic length is calculated with Eq. 5.3, where β^* is a turbulent model coefficient that can be approximated to 0.09. The turbulent viscosity is calculated with Eq. 5.4, where ρ is the mean interspace density.

$$L_{\mathrm{t}} = \frac{\sqrt{k}}{\beta^{*\,0.25} \cdot \omega} \tag{5.3}$$

$$\mu_{\text{t}} = \frac{\rho \cdot k}{\omega} \tag{5.4}$$

The turbulent characteristic length and the turbulent viscosity computed for each simulated case are plotted in Fig. 5.19 and 5.20, respectively. The turbulent characteristic length seems to be practically constant, and its dependence on the *MFR* and the reduced rotational speed is slight. The thickness of the contact area is of the same order of magnitude as the turbulent characteristic length. Thus, the assumption of constant thickness of the contact area is reasonable.

The turbulent viscosity is plotted against the absolute value of the velocity difference between flow branches to assess its effect on the turbulent viscosity. The cases with a lower velocity difference correspond to those with an *MFR* near full admission conditions where both flow branches have similar boundary conditions. The cases with a higher velocity difference correspond to those with an *MFR* near partial admission conditions where the boundary conditions of both flow branches are completely different. The dependence of the turbulent viscosity on the velocity difference between flow branches is small. Therefore, its dependence on the *MFR* value is also slight. However, it increases with the reduced rotational speed. An increase in reduced rotational speed means an increase in inlet total pressure conditions for the CFD simulations carried out, as explained in Chapter 4. Thus, the density also increases with the reduced rotational speed. As the turbulent viscosity is directly proportional to the density, it also increases with the reduced rotational speed.
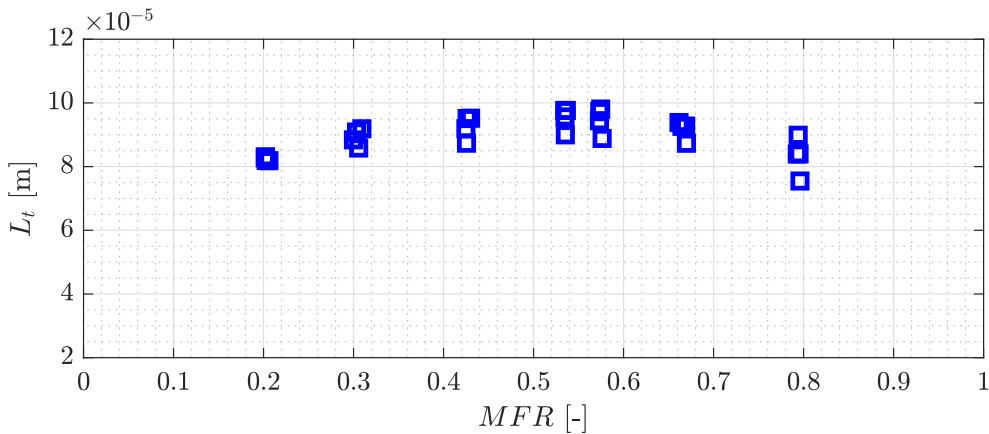
Figure 5.19: Interspace turbulent characteristic length.

Therefore, the total pressure losses due to the momentum exchange between flow branches could be modelled as a function of the velocity difference between flow branches, the length of the contact area and the turbulent viscosity. The model proposed for computing these losses is defined in Eq. 5.5. L_{CA} is the
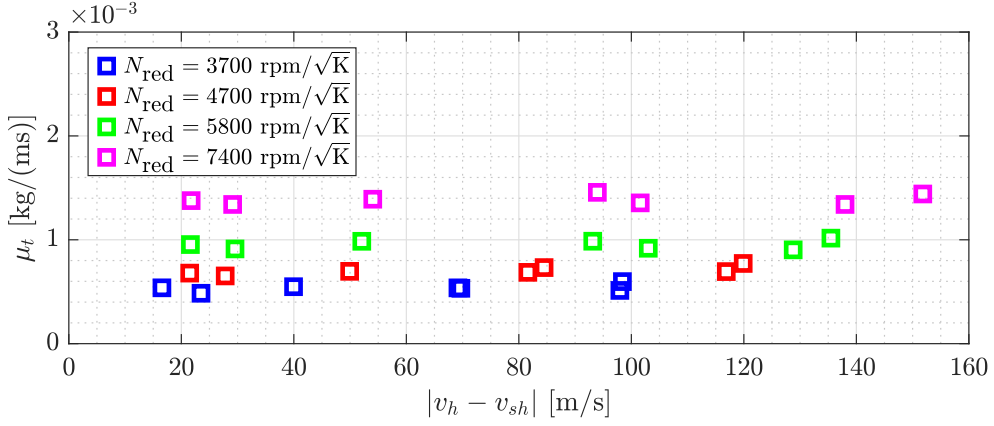
Figure 5.20: Interspace turbulent viscosity.

length of the contact area, v is the velocity for the hub branch and the shroud branch respectively, and Z_{ME} is an adjustable coefficient that includes the effect of the turbulent viscosity.

$$\Delta p_{\text{ME}} = Z_{\text{ME}} \cdot L_{\text{CA}} \cdot (v_{\text{h}} - v_{\text{sh}})^2 \qquad (5.5)$$

The total pressure losses due to the sudden expansion downstream of the junction of the volutes and to the momentum exchange between flow branches have been quantified for all simulated cases. Then, they have been added to the previous quantification of the passage losses and compared to the interspace total pressure losses extracted directly from the CFD simulations in Fig. 5.21 for the hub branch and the shroud branch separately. The quantified interspace total pressure losses under-predict the total pressure losses when the yellow bars are at the top of the bar. They over-predict the total pressure losses when the yellow bars are at the bottom, under 0.

The effect of the reduced rotational speed on the interspace total pressure losses is clear for all simulated cases: they increase with the reduced rotational speed. This behaviour was expected since the reduced rotational speed is directly correlated with the Reynolds number in the current CFD simulations.

A noticeable trend is also observed with the *MFR* value. The interspace total pressure losses decrease with the *MFR* for the hub branch and increase for the shroud branch. The partial admission cases have the most significant interspace total pressure losses. Fig. 5.21 shows that the partial admission cases have the most significant passage and sudden expansion losses quantified.

The passage losses model takes into account the friction losses. The partial admission cases have the highest wetted area since the flow branch occupies all the interspace geometry, while this wetted area is distributed between the two flow branches in the unequal admission cases. Thus, the passage losses are
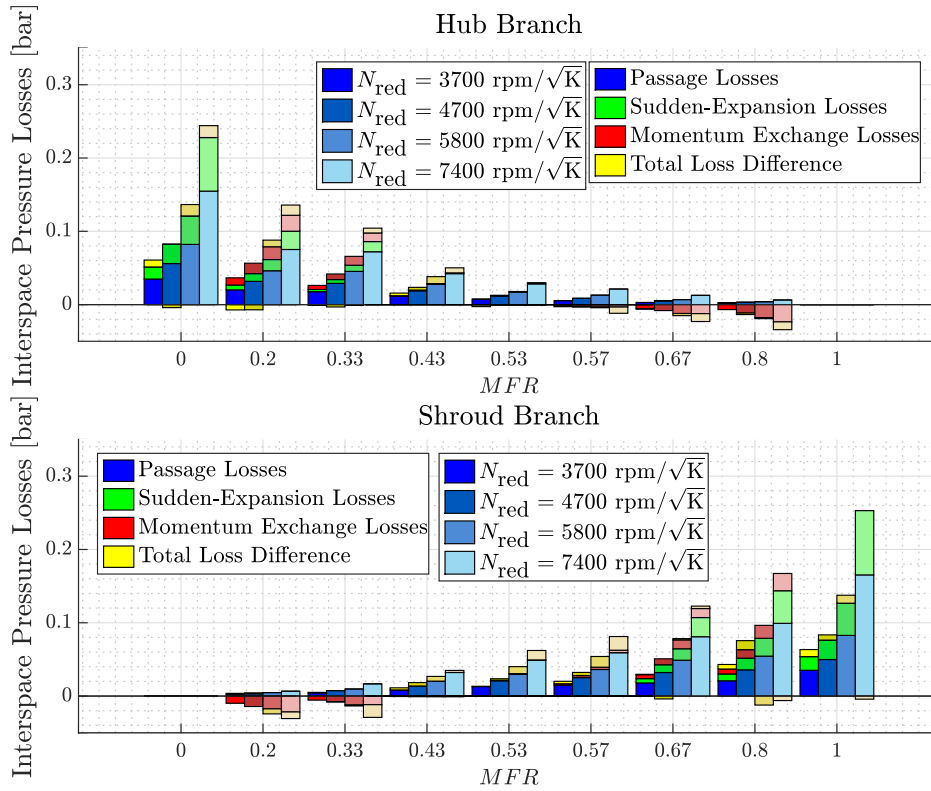
Figure 5.21: Interspace total pressure losses taking into account the losses due to the sudden expansion and to the momentum exchange between flow branches.

expected to decrease with *MFR* for the hub branch and increase for the shroud branch.

The sudden expansion losses are only computed for *MFR* values lower than 0.4 for the hub branch and higher than 0.6 for the shroud branch since these are the cases where the sudden expansion takes place. Moreover, Fig. 5.17 shows that there is a recirculation into the other volute in extreme *MFR* values, being the partial admission conditions the most extreme *MFR* values since there is no mass flow coming through the other branch. Therefore, the most significant total pressure losses due to the sudden expansion downstream of the junction of the volutes are expected to be in the partial admission conditions cases.

The losses due to the momentum exchange between flow branches are not computed in partial admission cases since there is only mass flow coming from one of the branches. Moreover, they exercise little influence on the cases near full admission conditions. Fig. 5.21 shows that the red bars in cases from 0.43 to 0.57 are tiny for both branches. These losses become significant in highly unequal admission cases. They are of the same order of magnitude as the sudden

expansion losses in the cases with *MFR* 0.2 and 0.33 for the hub branch and 0.67 and 0.8 for the shroud branch. However, their most relevant effect is detected in the opposite flow branches, in cases with *MFR* 0.67 and 0.8 for the hub branch and 0.2 and 0.33 for the shroud branch. There are total pressure gains instead of total pressure losses in these cases. This behaviour is possible since there is momentum transmitted from the flow branch with higher momentum to the flow branch with lower momentum. Therefore, the flow branch with lower momentum increases its momentum and total pressure when they are joined. These total pressure gains are shown in Fig. 5.21 with the red bars under 0 in these cases.

The difference between the quantified total pressure losses and the interspace total pressure losses extracted directly from the CFD simulations has been reduced significantly with the addition of the sudden expansion losses and the losses due to momentum exchange between flow branches. The cases with *MFR* 0.67 and 0.8 for the hub branch and 0.2 and 0.33 for the shroud branch are especially better captured since their losses were strongly over-predicted taking into account only the passage losses. The gains produced by the momentum exchange between flow branches in these cases allow capturing their total pressure losses better.

Therefore, the interspace total pressure losses could be well quantified by computing the passage losses, the sudden expansion losses downstream of the junction of the volutes and the losses due to the momentum exchange between flow branches. These last losses are especially relevant since they have not been found in the literature. They explain the interspace losses found at unequal admission conditions.

5.3.3 Rotor losses

The rotor total pressure losses are expected to be the most relevant since it is a mobile part and complex phenomena can arise because of its motion. Traditionally, the sources of rotor total pressure losses considered in the rotor part have been the incidence losses and the friction losses [87]. The losses due to secondary flows, such as the losses produced in the blade tip, has also been considered by some authors [85].

The flow branches do not fully mix inside the rotor, as explained in the previous section. Therefore, the losses due to the momentum exchange between flow branches described in the interspace could also be relevant in the rotor, although they have not been taken into account by other authors. The influence of the reduced rotational speed and the *MFR* value on these sources of losses has been analysed as in the volutes and the interspace parts.

The rotor total pressure losses produced by the friction and the interaction with the walls of the blades could be quantified with the passage losses model

proposed for the volutes and the interspace (Eq. 5.1) since the source of these losses is similar and it has been validated in the literature [109]. Density and velocity are evaluated at the rotor inlet of each flow branch (station 3) in this case. The velocity employed should be the relative velocity instead of the absolute velocity since it is the actual velocity that affects the rotor. These passage losses are expected to vary with *MFR* since the percentage of volume of each flow branch changes with it.

The other typical source of losses considered in the literature is the total pressure losses due to the rotor inlet incidence angle. They are produced when the rotor inlet incidence angle (β_3) differs from the optimum angle (β_{opt}). The mass flow analysis described in the previous section has found that the rotor inlet incidence angle could be considered constant around the rotor. Moreover, each flow branch has a different rotor inlet incidence angle since they are clearly separated.

The effect of the rotor inlet incidence angle could be studied thoroughly by plotting the entropy generation at different blade heights. Fig. 5.22 shows it along with relative velocity convolution lines for clearness in a case with an *MFR* 0.67 and a reduced rotational speed of 4700 rpm K$^{-0.5}$. Fig. 5.22(a) shows a section at 90% of the blade height, which corresponds clearly with the mass flow coming from the shroud branch. Fig. 5.22(b) shows a section at 10% of the blade height, which corresponds clearly with the mass flow coming from the hub branch.

The current twin-entry turbine has an optimum rotor inlet incidence angle of $-23.7°$ in terms of relative velocity. This optimum angle has been obtained following the method proposed by Chen and Baines [110]. The flow is aligned with the geometry, and the total pressure losses are minimised when the rotor inlet incidence angle is equal to the optimum. The section at 90% shown in Fig. 5.22(a) has a rotor inlet incidence angle close to this optimum angle. The entropy generation due to the rotor inlet incidence angle in this section is low since the flow is attached to the geometry. The higher entropy generation observed near the blade could relate more to the passage losses. However, the section at 10% shown in Fig. 5.22(b) has a rotor inlet incidence angle different from the optimum angle. This different angle induces recirculation in the pressure side of the blades. This recirculation means a higher entropy generation and higher total pressure losses.

Thus, the flow behaviour in each flow branch is different in unequal admission cases. The rotor total pressure losses due to the rotor inlet incidence angle will be different depending on the boundary conditions of each flow branch. The flow branch with higher kinetic energy (*MFR* lower than 0.5 for the hub branch and higher than 0.5 for the shroud branch) will trend to a rotor inlet incidence angle closer to the optimum since it is the flow branch that is primarily impelling the rotor blades. The flow branch with lower kinetic energy (*MFR*

109
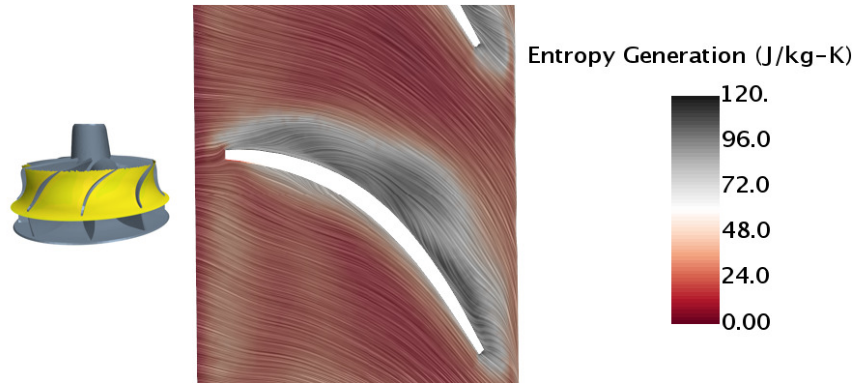
(a) Section at 90 % of the blade height, corresponding to the shroud branch.
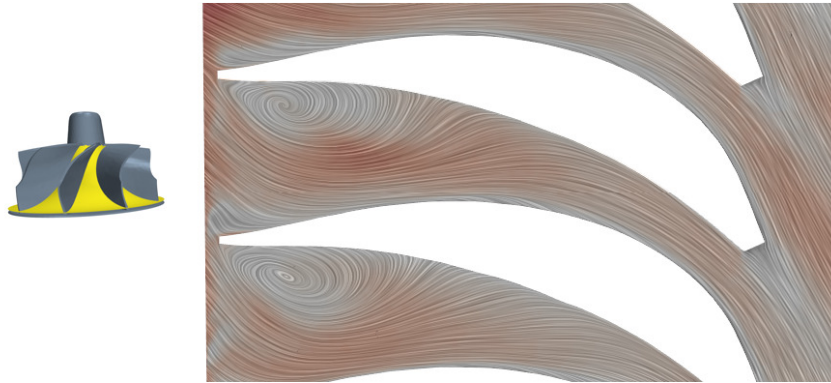
(b) Section at 10 % of the blade height, corresponding to the hub branch.

Figure 5.22: Entropy generation in a case of *MFR* 0.67 at different blade heights for assessing the rotor inlet incidence angle effect.

higher than 0.5 for the hub branch and lower than 0.5 for the shroud branch) will have a rotor inlet incidence angle farther from the optimum since the rotor will be moving faster due to the greater impelling of the other flow branch. If the kinetic energy difference between both branches is high, a flow detachment could appear in the pressure side of the blades, as observed in Fig. 5.22(b). Therefore, the total pressure losses due to the rotor inlet incidence angle will depend on the *MFR* value and the flow branch of study.

The incidence losses could be quantified employing the model described by Chen and Baines [110] for each flow branch. The model proposed for computing these losses is defined in Eq. 5.6. w is the relative velocity at the rotor inlet for each flow branch, β and β_{opt} are the rotor inlet incidence angle and the optimum angle, respectively, and K is an adjustable coefficient.

$$\Delta p_{\mathrm{inc}} = K \cdot w^2 \cdot (\sin (\beta - \beta_{\mathrm{opt}}))^2 \tag{5.6}$$

The third source of losses in the rotor frequently considered is due to secondary flows in the blade tip. These tip losses have been appropriately defined by Serrano et al. [111, 112] for single-entry turbines. This model should be valid for quantifying the tip losses in twin-entry turbines. The tip losses will only affect the shroud branch for all *MFR* values but 0, when there is no mass flow from the shroud branch. The tip losses model employed is defined in Eq. 5.7. ρ is the density evaluated at the rotor inlet, M_- and M_+ are modelled mass flow coefficients that depend on the tip geometry and w_- and w_+ are modelled velocities that are also dependent on the tip geometry. The computation of these modelled mass flow coefficients and velocities will be adequately explained in Chapter 6.

$$\Delta p_{\text{tip}} = \rho \cdot (M_- \cdot w_-^2 + M_+ \cdot w_+^2) \tag{5.7}$$

The quantification of the passage losses, the incidence losses and the tip losses with the proposed models are shown in Fig. 5.23 for the hub branch and the shroud branch separately. This quantification is compared with the total pressure losses extracted directly from the CFD simulations. The quantified total pressure losses under-predict the total pressure losses when the yellow bars are at the top of the bar. They over-predict the total pressure losses when the yellow bars are at the bottom, under 0.

The passage losses constitute the primary source of losses in general terms. However, the incidence losses become relevant in cases with low kinetic energy (*MFR* higher than 0.5 for the hub branch and lower than 0.5 for the shroud branch). The tip losses are not as relevant as the other two sources of losses, but they reduce the difference between the total pressure losses quantification and the one extracted directly from the CFD simulations.

The cases at partial admission conditions and the cases near full admission conditions are captured adequately with this quantification. However, the difference in total pressure losses is higher in the cases at unequal admission conditions. The rotor total pressure losses are under-predicted in cases with higher mass flow ratios and over-predicted in cases with lower mass flow ratios. Therefore, another rotor source of losses should be taken into account to capture these differences properly.

This behaviour is similar to the one detected in the interspace. This source could be the momentum exchange between flow branches since the flow branches do not fully mix inside the rotor. The shroud air concentration could be followed within the rotor for corroborating this assumption. The shroud air concentration has been plotted for a case with *MFR* 0.67 and reduced rotational speed 7400 rpm K$^{-0.5}$ in a section at the middle of a rotor channel in Fig. 5.24. The region considered as the contact surface area between flow branches comprises
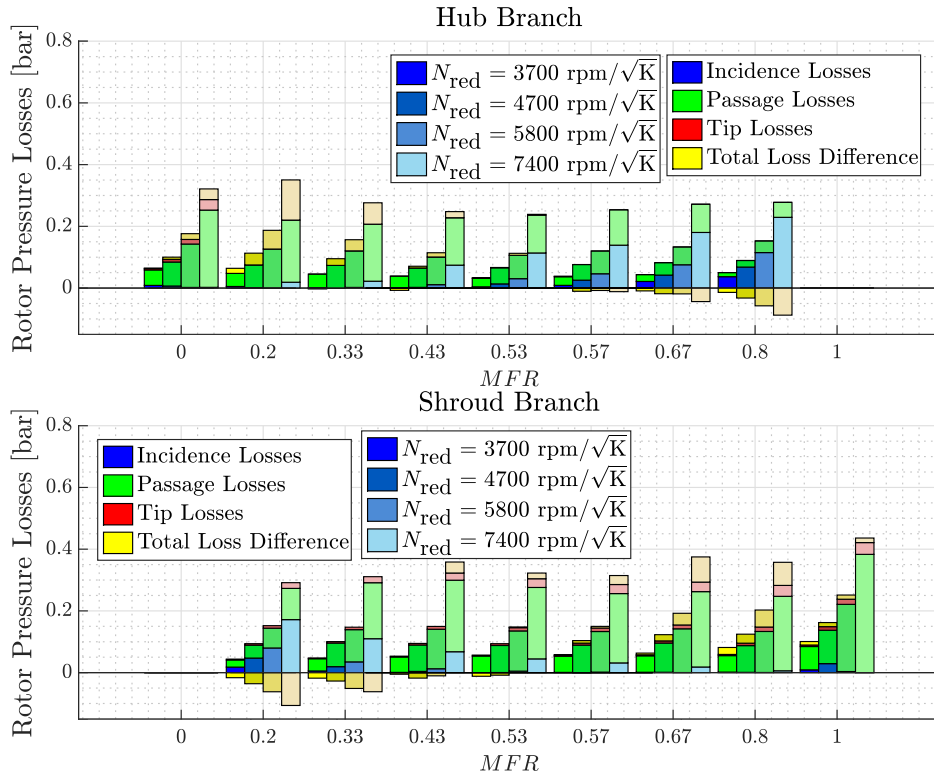
Figure 5.23: Rotor total pressure losses.

the region where the shroud air concentration is 0.5 ± 0.2. This region is marked in Fig. 5.24.

The contact surface is thinner at the rotor inlet, and it becomes larger toward the rotor outlet. However, the flow branches are still clearly separated at the rotor outlet. Therefore, the losses due to the momentum exchange between flow branches could also be relevant in the rotor. The flow branch with higher momentum transmits some of its momentum to the other flow branch in this contact surface at unequal admission conditions when the rotor inlet flow conditions are different for each flow branch. Thus, the flow branch with higher momentum will experience total pressure losses, and the flow branch with lower momentum will experience total pressure gains.

These losses could be modelled as in the interspace since they primarily depend on the velocity difference between flow branches and the length of the contact area. However, the turbulent characteristic length and the turbulent viscosity could also be analysed to detect if they maintain the same effect in the rotor than in the interspace.

The rotor turbulent characteristic length and turbulent viscosity computed

Shroud Air Concentration

Figure 5.24: Shroud air concentration in a section at the middle of a rotor channel.

for each simulated case are plotted in Fig. 5.25 and 5.26, respectively. The turbulent characteristic length seems to be independent of the *MFR* value, but it depends on the reduced rotational speed in this part. Increasing the reduced rotational speed is the same as increasing the Reynolds number in the current simulations. Therefore, the flow branches possess more kinetic energy when the reduced rotational speed increases and the size of the bigger eddies also increases. Moreover, the variation of the rotor motion with the reduced rotational speed could enhance some turbulent phenomena that affect the turbulent characteristic length like flow detachments.
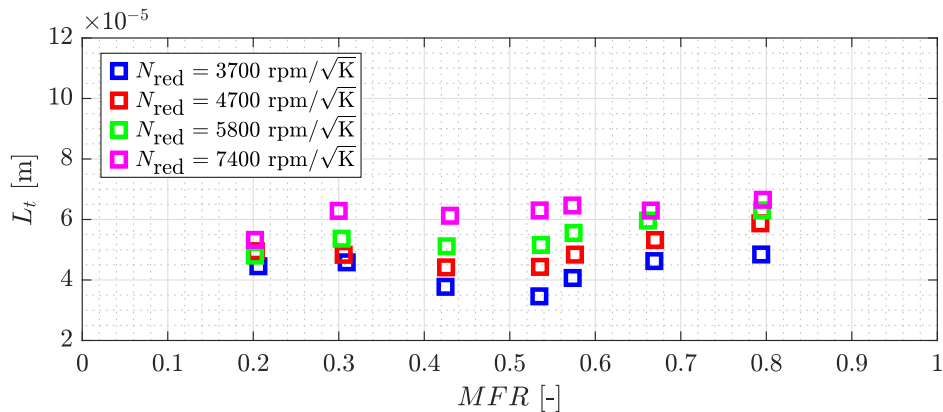
Figure 5.25: Rotor turbulent characteristic length.

The rotor turbulent viscosity is plotted against the absolute value of the velocity difference between flow branches to assess its effect on the turbulent
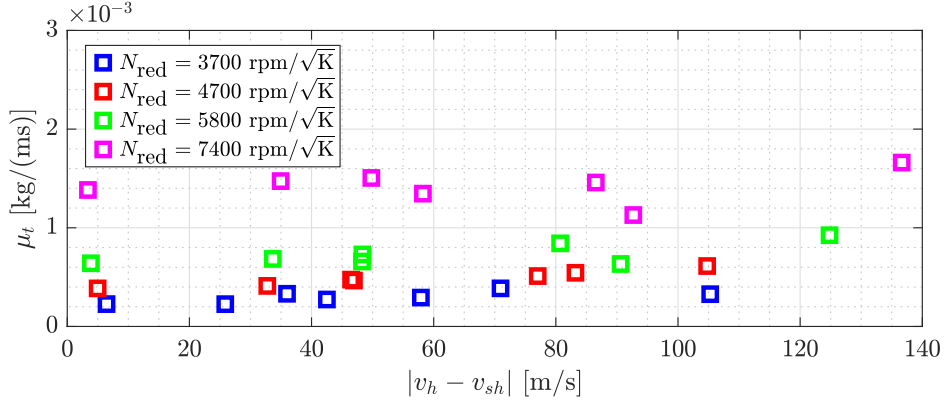
Figure 5.26: Rotor turbulent viscosity.

viscosity. The cases with a lower velocity difference correspond to those with an *MFR* near full admission conditions where both flow branches have similar boundary conditions. The cases with a higher velocity difference correspond to those with an *MFR* near partial admission conditions where the boundary conditions of both flow branches are completely different. The behaviour of the turbulent viscosity against the velocity difference between flow branches, the *MFR* value and the reduced rotational speed in the rotor is similar to their behaviour in the interspace. The dependence of the turbulent viscosity on the velocity difference between flow branches is slight. Therefore, its dependence on *MFR* is small. However, it increases with the reduced rotational speed. Increasing the reduced rotational speed is the same that increasing the Reynolds number in the current simulations. Thus, the density also increases with the reduced rotational speed. As the turbulent viscosity is directly proportional to the density, it also increases with the reduced rotational speed.

Therefore, the total pressure losses due to the momentum exchange between flow branches in the rotor could be modelled as a function of the velocity difference between flow branches, the length of the contact area, the turbulent characteristic length and the turbulent viscosity. The model proposed for computing these losses is the same as for the interspace and is defined in Eq. 5.5. The effect of the turbulent characteristic length is expected to be captured by the adjustable coefficient as it seems to be small compared to the other effects.

The total pressure losses due to the momentum exchange between flow branches in the rotor have been quantified for all simulated cases. Then, they have been added to the previous quantification of the passage, incidence and tip losses and compared to the rotor total pressure losses extracted directly from the CFD simulations in Fig. 5.27 for the hub branch and the shroud branch separately. The quantified rotor total pressure losses under-predict the total pressure losses when the yellow bars are at the top of the bar. They over-predict

the total pressure losses when the yellow bars are at the bottom, under 0.
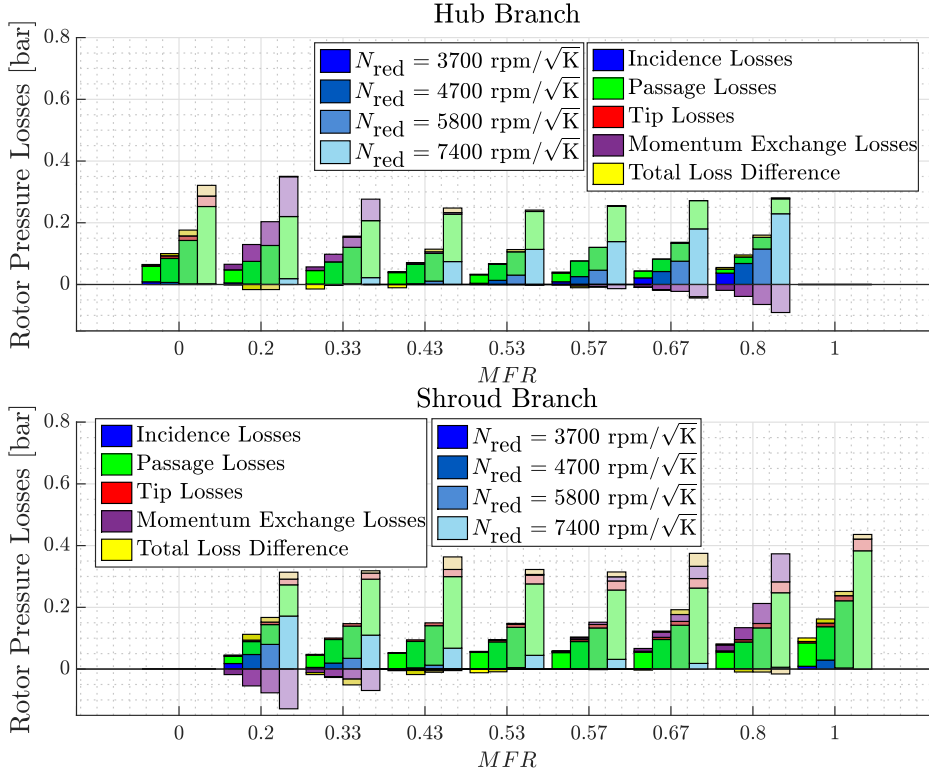
Figure 5.27: Rotor total pressure losses taking into account the losses due to the momentum exchange between flow branches.

The effect of the reduced rotational speed on the rotor total pressure losses is clear for all simulated cases: they increase with the reduced rotational speed. This behaviour was expected since the reduced rotational speed is directly correlated with the Reynolds number in the current CFD simulations. The rotor total pressure losses seem to be constant with the *MFR* value. However, the source of the losses varies with the *MFR*.

The losses due to the momentum exchange between flow branches are not computed in partial admission cases since there is only mass flow coming from one of the branches. Moreover, their influence on the cases near full admission conditions is narrow. Fig. 5.27 shows that the purple bars in cases from 0.43 to 0.57 are tiny for both branches. These losses become significant in highly unequal admission cases. Their most relevant effect is detected in the flow branches with lower mass flow, in cases with *MFR* 0.67 and 0.8 for the hub branch and 0.2 and 0.33 for the shroud branch. There are total pressure gains instead of total pressure losses in these cases. This behaviour is possible since

there is momentum transmitted from the flow branch with higher momentum to the flow branch with lower momentum. Therefore, the flow branch with lower momentum increases its momentum and total pressure due to the contact with the other branch. These total pressure gains are shown in Fig. 5.27 with the purple bars under 0.

The difference between the quantified total pressure losses and the rotor total pressure losses extracted directly from the CFD simulations has been reduced significantly in the unequal admission conditions with the addition of the losses due to momentum exchange between flow branches. Therefore, the rotor total pressure losses are adequately captured in all admission conditions employing the quantification with passage, incidence and tip losses and the losses due to the momentum exchange between flow branches. These last losses are especially relevant to properly capture the losses at unequal admission conditions, and they have not been found in the literature.

5.3.4 Outlet losses

The outlet total pressure losses should not be as relevant as the rotor total pressure losses since the outlet is a static part. However, there are sudden expansions downstream of the rotor nut and to connect with the outlet plenum that could generate significant losses. These losses are expected to constitute the primary source of losses in the outlet region, as pointed out by Palenschat et al. [87].

As exposed in the previous section, the outlet part is where the flow branches fully mix. Therefore, losses due to the mixing of the flow branches should be expected in the outlet part. Moreover, losses due to the momentum exchange between flow branches could be found since the flow branches are still separated at the beginning of the outlet part. These two losses have not been taken into account by other authors, but they could be relevant for better quantification of the losses in the outlet region. The influence of the reduced rotational speed and the *MFR* value on these sources of losses will also be analysed.

The first source of losses to analyse is the sudden expansions produced downstream of the rotor nut and downstream of the connection with the outlet plenum. An axial-radial plane showing the entropy generation in the outlet region and velocity convolution lines is plotted in Fig. 5.28 for a case with reduced rotational speed $5800\,\mathrm{rpm\,K^{-0.5}}$ and *MFR* 0.33.

There is an increase in the entropy generation just downstream of the rotor nut due to the large eddies produced by the sudden expansion. There are large eddies inside the outlet plenum due to the sudden expansion produced when the case becomes wider to include the wastegate. Moreover, there is a slighter eddy located at the left side of Fig. 5.28 when the rotor case is connected to the outlet plenum case. There is also an increment of entropy generation in these regions.
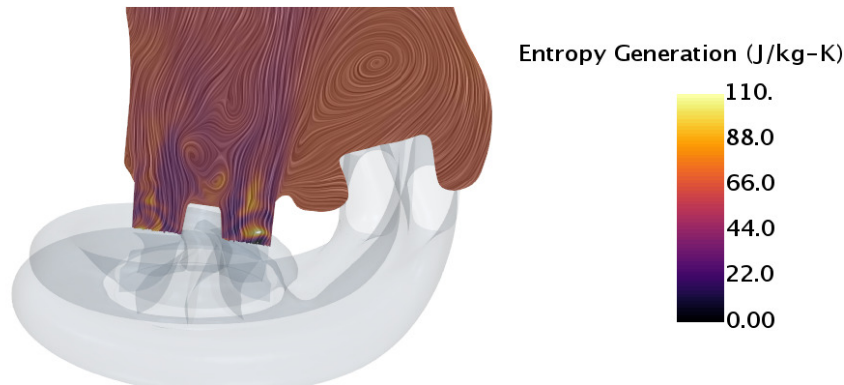
Figure 5.28: Entropy generation due to sudden expansions in the outlet region.

These sudden expansions are expected to constitute the primary source of losses in the outlet region. Therefore, they could be quantified to see if they provide enough accuracy compared to the total pressure losses extracted directly from the CFD simulations. The model proposed to quantify the outlet total pressure losses due to the sudden expansions is the same Borda-Carnot model employed in the interspace part and defined in Eq. 5.2.

The quantification of the sudden expansion losses with the proposed model is presented in Fig. 5.29 for the hub branch and the shroud branch separately. This quantification is compared with the total pressure losses extracted directly from the CFD simulations. The quantified total pressure losses under-predict the total pressure losses when the green bars are at the top of the bar. They over-predict the total pressure losses when the green bars are at the bottom, under 0.

The difference in total pressure losses is almost 0 in partial admission conditions. There is only mass flow from one branch in these cases. Thus, losses due to the mixing of the flow branches cannot exist, and the sudden expansions constitute the primary source of losses here. However, the quantification is poorer in all other admission conditions despite the sudden expansion losses seem to constitute the most significant source of losses. Other sources of losses should be taken into account for properly capturing the outlet total pressure losses in unequal admission conditions.

The flow branches fully mix in the outlet region, which could constitute a relevant source of losses. The shroud air concentration in the outlet region is shown in Fig. 5.30 for a case with a reduced rotational speed of $3700 \, \mathrm{rpm\,K^{-0.5}}$ and *MFR* 0.53. The region where the shroud air concentration is 0.53 ± 0.2 has been highlighted. This highlighted region will be considered the region where both flows are already mixed.

Most of the section just at the rotor outlet is not highlighted. It means that
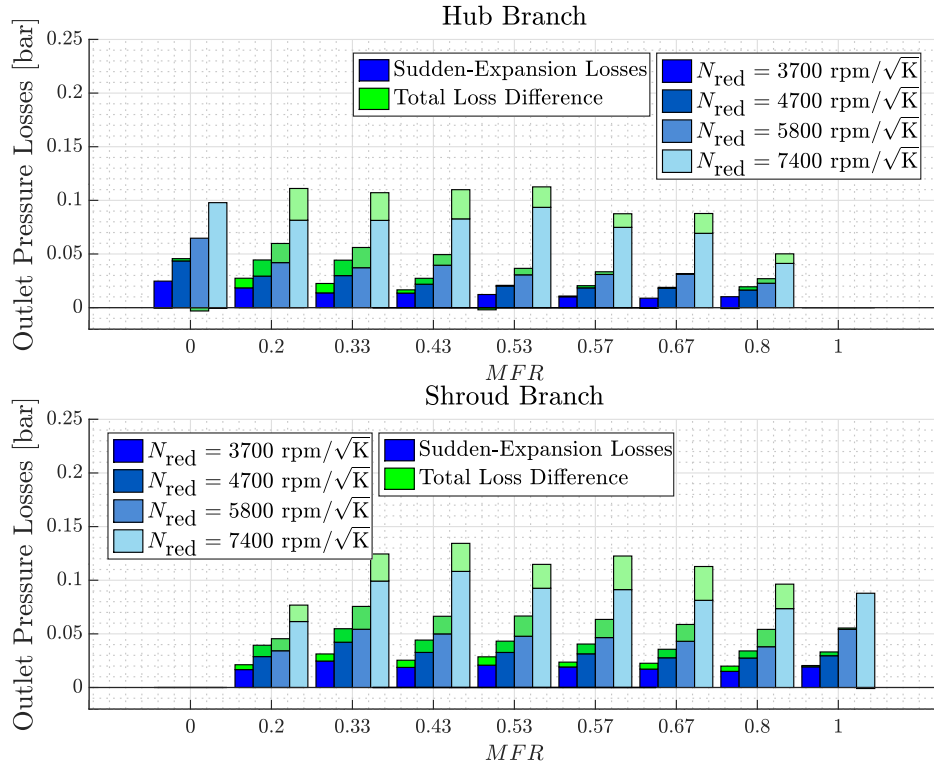
Figure 5.29: Outlet total pressure losses.
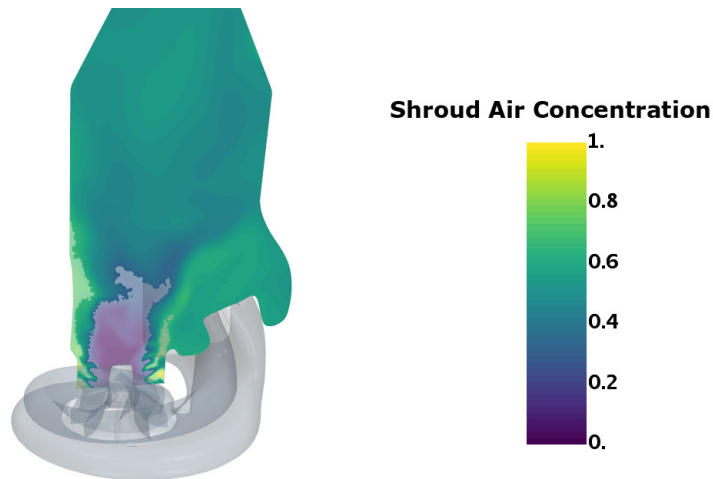
Figure 5.30: Shroud air concentration in the outlet region for a case with *MFR* 0.53.

the flow branches just at the rotor outlet are still separated. Moreover, the mass flow comes primarily from the hub branch just downstream of the rotor nut. So, the flow branches fully mix inside the outlet plenum. Furthermore, the shroud air concentration at the exit of the outlet plenum is practically constant and with values close to 0.53 for this case, as expected.

This flow mixing is a turbulent phenomenon that produces losses in both flow branches. The quantification of the losses produced by the mixing phenomenon could be computed employing the model for junction losses proposed by Winterbone and Pearson [113] and defined in Eq. 5.8. ρ and v are the density and the absolute velocity evaluated at the outlet section (station 5), K is an adjustable coefficient and AG is a geometrical parameter that will be explained more thoroughly in Chapter 6. These losses will only be computed in unequal admission conditions cases since there is only mass flow from one of the branches in partial admission conditions.

$$\Delta p_{\mathrm{mix}} = K \cdot \rho \cdot v^2 \cdot AG \tag{5.8}$$

The losses due to the momentum exchange between flow branches could be relevant also in the outlet region since there is a part of the outlet region where the flow branches are still separated, as observed in Fig. 5.30. The flow branch with higher momentum will transmit some of its momentum to the flow branch with lower momentum. The model employed for quantifying the losses due to momentum exchange between flow branches could be the same model employed in the interspace and the rotor parts and defined in Eq. 5.5.

The total pressure losses due to the flow branches mixing and to the momentum exchange between flow branches in the outlet have been quantified for all unequal admission conditions cases. Then, they have been added to the previous quantification of the sudden expansion losses and compared to the outlet total pressure losses extracted directly from the CFD simulations in Fig. 5.31 for the hub branch and the shroud branch separately. The quantified outlet total pressure losses under-predict the total pressure losses when the yellow bars are at the top of the bar. They over-predict the total pressure losses when the yellow bars are at the bottom, under 0.

The effect of the reduced rotational speed on the outlet total pressure losses is the same as that for the other twin-entry turbine parts. The outlet total pressure losses increase with the reduced rotational speed. This behaviour was expected since the reduced rotational speed is directly correlated with the Reynolds number in the current CFD simulations. The outlet total pressure losses are more or less constant with *MFR* despite there are some cases that have lower losses.

The mixing losses are relevant for all unequal admission conditions cases. These mixing losses represent between 10% and 20% of the outlet total pressure
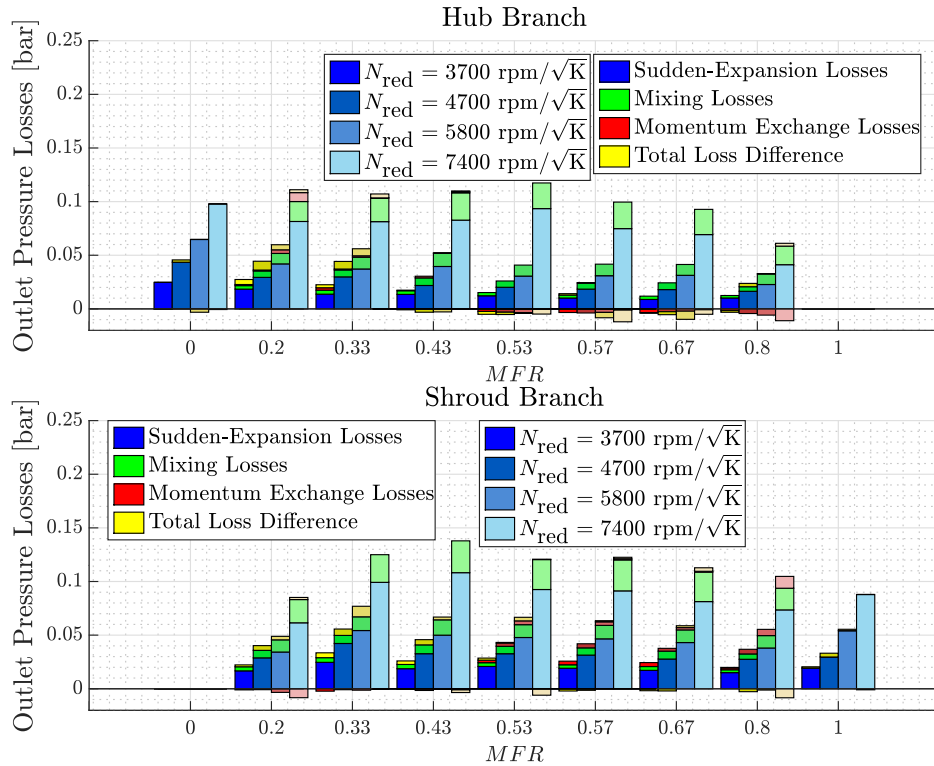
Figure 5.31: Outlet total pressure losses taking into account the losses due to the momentum exchange between flow branches and the mixing losses.

losses. The losses due to the momentum exchange between flow branches are less relevant in most cases since the region where the flow branches are still separated is small. Their effect is only significant in extreme *MFR* values like 0.2 or 0.8. The flow branch with higher momentum experiences losses due to this momentum exchange between flow branches, and the flow branch with lower momentum experiences gains since its momentum is increasing. These total pressure gains are shown in Fig. 5.31 with the red bars under 0.

The difference between the quantified total pressure losses and the outlet total pressure losses extracted directly from the CFD simulations has been reduced significantly in the unequal admission conditions with the addition of the mixing losses and the losses due to momentum exchange between flow branches to a lesser extent. Therefore, the outlet total pressure losses are adequately captured in all admission conditions employing the quantification with the sudden expansion losses, the mixing losses and the losses due to the momentum exchange between flow branches.

5.3.5 Overall Losses

The total pressure losses have been analysed for each twin-entry turbine part separately. However, it could be interesting to analyse the impact of each part on the overall total pressure losses.

The quantified total pressure losses of each part have been added and compared to the total pressure losses extracted directly from the CFD simulations in Fig. 5.32 for the hub branch and the shroud branch separately. The quantified total pressure losses under-predict the total pressure losses when the yellow bars are at the top of the bar. They over-predict the total pressure losses when the yellow bars are at the bottom, under 0. The difference between the quantified total pressure losses and the total pressure losses extracted directly from the CFD simulations is slight. The worst over and under-predictions represent less than 8% of the overall total pressure losses.
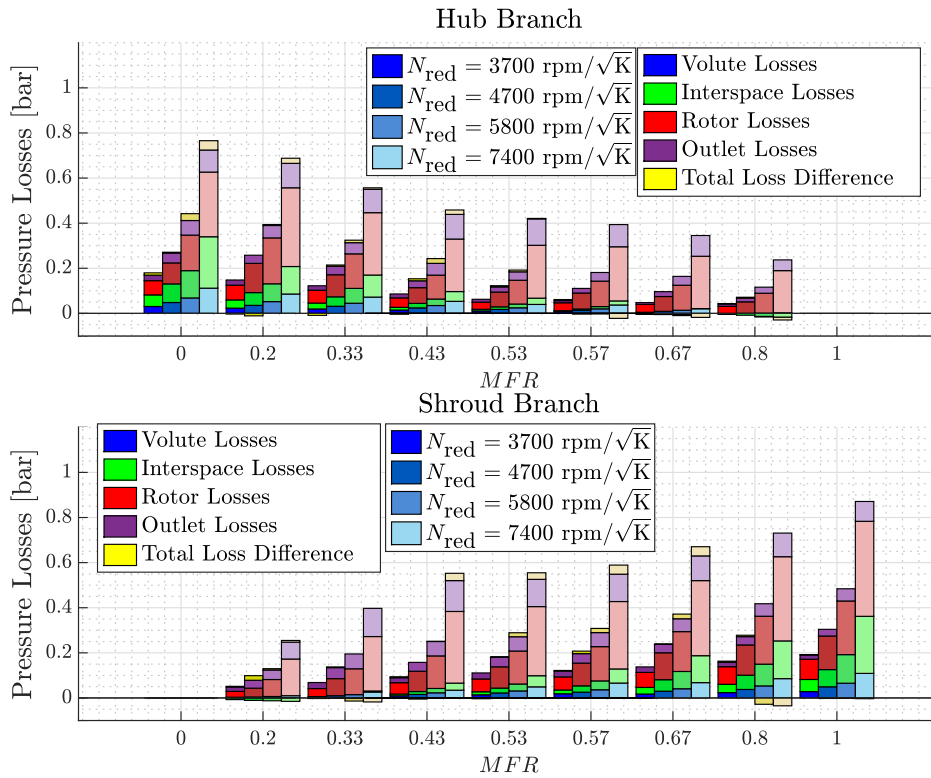
Figure 5.32: Total pressure losses distribution by parts.

The effect of the reduced rotational speed on each twin-entry turbine part is the same since the reduced rotational speed is directly correlated with the Reynolds number in the current CFD simulations. Therefore, an increment in the reduced rotational speed means an increment in the overall total pressure

losses.

The overall total pressure losses decrease with *MFR* for the hub branch and increase for the shroud branch. However, the impact of each twin-entry turbine part changes with the *MFR* value.

The volute total pressure losses decrease with *MFR* for the hub branch and increase for the shroud branch. The unique source of losses considered in the volutes is the passage losses that depend directly on the mass flow rate. Therefore, this behaviour with *MFR* was expected. The volute total pressure losses are the less relevant losses. However, they can represent up to 15% of the overall total pressure losses in some cases.

The interspace total pressure losses also decrease with *MFR* for the hub branch and increase for the shroud branch. The influence of the *MFR* is stronger in the interspace. The interspace losses can represent up to 30% in partial admission conditions. There is a sudden expansion downstream of the junction of the volutes found at *MFR* values under 0.4 for the hub branch and over 0.6 for the shroud branch. Fig. 5.32 shows that these cases exhibit the highest interspace total pressure losses. However, the interspace total pressure losses can even become gains in the flow branch with lower mass flow, i.e. *MFR* 0.8 for the hub branch or 0.2 for the shroud branch. The momentum exchange between flow branches produces losses in the flow branch with higher momentum and gains in the flow branch with lower momentum. These gains can be larger than the passage losses in these extreme *MFR* values.

The rotor total pressure losses also decrease with *MFR* for the hub branch and increase for the shroud branch, but they have a weaker dependence on *MFR* than the interspace total pressure losses. The quantification of passage, incidence and tip losses together is more or less constant with the *MFR*. The losses due to the momentum exchange between flow branches produce this slight dependence on *MFR*. The rotor total pressure losses are the most relevant in the overall total pressure losses. They represent more than 40% of the overall total pressure losses in all simulated cases.

The outlet total pressure losses are practically constant with the *MFR*. The primary source of losses considered in the outlet is the sudden expansion losses present at all admission conditions. The mixing losses and the momentum exchange between flow branches affect the unequal admission conditions cases, but they are considerably lower than the sudden expansion losses. The outlet total pressure losses represent up to 25% of the overall total pressure losses.

5.4 Summary

This chapter presents an analysis of the mass flow within the twin-entry turbine and the quantification of the total pressure losses produced in each of

its parts, focusing on the phenomena under unequal admission conditions.

The mass flow coming from each branch has been tracked within the turbine employing the multi-component gas option of the software and plotting the mass flow concentration from one of the branches. The mass flow from the hub branch remains close to the rotor hub until the rotor outlet, and the mass flow from the shroud branch remains close to the rotor shroud until the rotor outlet. Both flow branches do not fully mix within the rotor. Therefore, twin-entry turbines could be modelled as two separated single entry turbines working in parallel.

The rotor inlet and rotor outlet areas corresponding to each flow branch depend linearly on *MFR*, and they are independent of the reduced rotational speed. The rotor inlet flow angle has been considered constant around the rotor, and it depends linearly on *MFR*. The mean rotor outlet flow angle also depends on *MFR*, but it depends on other variables such as the reduced rotational speed.

The volute total pressure losses have been quantified employing a passage losses model. These losses decrease with *MFR* for the hub branch and increase for the shroud branch.

The interspace total pressure losses have been quantified employing a passage losses model, a sudden expansion model for the sudden expansion found downstream of the junction of the volutes at *MFR* lower than 0.4 for the hub branch and higher than 0.6 for the shroud branch and momentum exchange between flow branches model. These last losses are due to the contact between flow branches without fully mixing. The flow branch with higher momentum transmits some of its momentum to the flow branch with lower momentum. Therefore, the flow branch with higher momentum will exhibit losses, and the flow branch with lower momentum will experience gains due to this momentum exchange. The interspace total pressure losses decrease with *MFR* for the hub branch and increase for the shroud branch.

The rotor total pressure losses have been quantified with a passage model, an incidence model, a tip losses model and a momentum exchange between flow branches model. These last losses are also significant in the rotor since the flow branches do not fully mix within the rotor. The rotor total pressure losses are the most relevant, and they decrease with *MFR* for the hub branch and increase for the shroud branch.

The outlet total pressure losses have been quantified with a sudden expansion model, a mixing flow model and a momentum exchange between flow branches model. The primary source of losses is the sudden expansions downstream of the rotor nut and to connect to the outlet plenum case. The flow branches fully mixing is produced in this region. Thus, the mixing losses must be considered here. The momentum exchange between flow branches could also be considered since there is a small region where the flow branches are still separated.

Hence, the main phenomena that define the performance under unequal

admission conditions are identified and described. This information, combined with the information extracted from the experimental measurements described in Chapter 3, is valuable to develop physics-based models that accurately predict the performance under unequal admission conditions.

Therefore, the next chapter is dedicated to using all this information to develop reliable twin-entry turbine models capable of predicting their performance under unequal admission conditions appropriately.

5.5 References

[49] J. R. Serrano, F. J. Arnau, L. M. García-Cuevas, V. Samala, and L. Smith. "Experimental approach for the characterization and performance analysis of twin entry radial-inflow turbines in a gas stand and with different flow admission conditions". In: *Applied Thermal Engineering* 159 (2019). DOI: 10.1016/j.applthermaleng.2019.113737 (cit. on pp. 19, 39, 40, 87, 129, 211).

[76] M. Cerdoun and A. Ghenaiet. "Unsteady behaviour of a twin entry radial turbine under engine like inlet flow conditions". In: *Applied Thermal Engineering* 130 (2018), pp. 93–111. DOI: 10.1016/j.applthermaleng.2017.11.001 (cit. on pp. 21, 96).

[85] A. Hajilouy-Benisi, M. Rad, and M. R. Shahhosseini. "Modeling of twin-entry radial turbine performance characteristics based on experimental investigation under full and partial admission conditions". In: *Scientia Iranica* (2009), pp. 281–290. URL: http://scientiairanica.sharif.edu/article_3231.html (cit. on pp. 22, 108).

[87] T. Palenschat, M. Mueller, S. Rajoo, M. S. Chiong, P. Newton, R. Martinez-Botas, and F. X. Tan. "Steady-state experimental and meanline study of an asymmetric twin-scroll turbine at full and unequal and partial admission conditions". In: *SAE Technical Paper* (2018). DOI: 10.4271/2018-01-0971 (cit. on pp. 23, 108, 116).

[92] J. Galindo, A. Tiseira, P. Fajardo, and L. M. García-Cuevas. "Development and validation of a radial variable geometry turbine model for transient pulsating flow applications". In: *Energy Conversion and Management* 85 (2014), pp. 190–203. DOI: 10.1016/j.enconman.2014.05.072 (cit. on pp. 24, 92).

[108] M. S. Chiong, S. Rajoo, A. Romagnoli, A. W. Costall, and R. F. Martinez-Botas. "Integration of meanline and one-dimensional methods for prediction of pulsating performance of a turbocharger turbine". In: *Energy Conversion and Management* 81 (May 2014), pp. 270–281. DOI: 10.1016/j.enconman.2014.01.043 (cit. on p. 92).

[109] S. Futral, C. Wasserbauer, A. USN, and S. Administration. *Off-design performance prediction with experimental verification for a radial-inflow turbine*. Tech. rep. NASA TN D-2621, 1965. URL: http://books.google.es/books?id=N1kzLAHfK-IC (cit. on pp. 96, 100, 109, 142).

[110] H. Chen and N. C. Baines. "The aerodynamic loading of radial and mixed-flow turbines". In: *International Journal of Mechanical Sciences* 36 (1994), pp. 63–79. DOI: 10.1016/0020-7403(94)90007-8 (cit. on pp. 109, 110, 147).

[111] J. R. Serrano, R. Navarro, L. M. García-Cuevas, and L. B. Inhestern. "Turbocharger turbine rotor tip leakage loss and mass flow model valid up to extreme off-design conditions with high blade to jet speed ratio". In: *Energy* 147 (Mar. 2018), pp. 1299–1310. DOI: 10.1016/j.energy.2018.01.083 (cit. on pp. 111, 147, 148).

[112] J. R. Serrano, R. Navarro, L. M. García-Cuevas, and L. B. Inhestern. "Contribution to tip leakage loss modeling in radial turbines based on 3D flow analysis and 1D characterization". In: *International Journal of Heat and Fluid Flow* 78 (2019). DOI: 10.1016/j.ijheatfluidflow.2019.108423 (cit. on pp. 111, 147).

[113] D. E. Winterbone and R. J. Pearson. *Theory of engine manifold design: wave action methods for IC engines*. Ed. by P. E. Pub. Professional Engineering Pub., 2000. ISBN: 978-1-86058-209-7 (cit. on pp. 119, 152).

1D twin-entry turbine modelling

Contents

Figures

Tables

6.1 Introduction

T HIS chapter presents the one-dimensional models developed from the information obtained in the CFD simulations and the experimental data described in Chapter 3 to Chapter 5. These models will be employed to extrapolate the flow capacity and the efficiency maps of twin-entry turbines.

One-dimensional models are a widespread tool for simulating whole engines. Most relevant effects on the flow performance in components such as the turbine are adequately captured. Moreover, its low computational cost makes them an excellent tool in the engine design and optimisation phases.

The radial turbines are modelled as actuator disks in one-dimensional models. These actuator disks introduce the momentum and enthalpy source terms for modelling the turbine behaviour. The momentum and enthalpy source terms strength depend on the turbine working points. The maps provided by the manufacturer can be employed as interpolation lookup tables. Nevertheless, these maps are typically limited, providing only a few working points. Therefore, extrapolation models are needed to predict the turbine behaviour at operational points not provided by the manufacturer. Furthermore, the twin-entry turbine models have an additional issue since the interaction between both flow branches must be assessed.

Two different models have been developed, although they depend on each other. The first model is an effective area model based on the information extracted from the mass flow analysis presented in the previous chapter and the experimental data recorded. This model allows extrapolating in the flow capacity map. The second model is a losses-based efficiency model based on the information extracted from the losses analysis described in the previous chapter. This model allows extrapolating in the efficiency map. Both models are then implemented in the radial turbine model included in the VEMOD code presented by García-Cuevas [21].

The twin-entry turbine stations employed for distinguishing the different parts are numbered in Table 6.1 and Fig. 6.1. Therefore, the volutes are between stations 0 and 1, the interspace between stations 1 and 3, the rotor between stations 3 and 4 and the outlet between stations 4 and 5. This numbering will be employed in both models. The subscripts h and sh will be used to differentiate the hub and shroud branches if necessary.

The hypothesis made by the experimental data analysis described in [49] and corroborated with the flow analysis described in Chapter 5 is applied to develop these models. It says twin-entry turbines could be modelled as two separated single entry VGT turbines working in parallel. Therefore, both models will be applied to each branch separately.

Table 6.1: Twin-entry turbine stations

Station	Description
0	Turbine inlet
1	Volute outlet
3	Rotor inlet
4	Rotor outlet
5	Turbine outlet
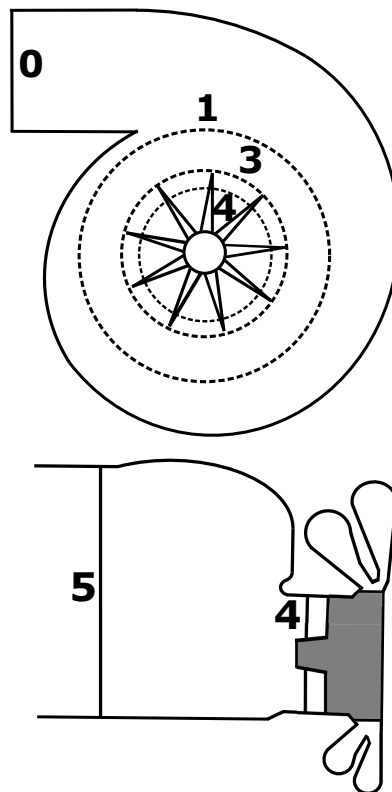
Figure 6.1: Twin-entry turbine stations used in the models.

6.2 Effective area model

The effective area model is developed to extrapolate in the flow capacity map. The model employed is based on the model proposed by Serrano et al. [91]. Each flow branch will be modelled as a single equivalent nozzle, as shown in Fig. 6.2.
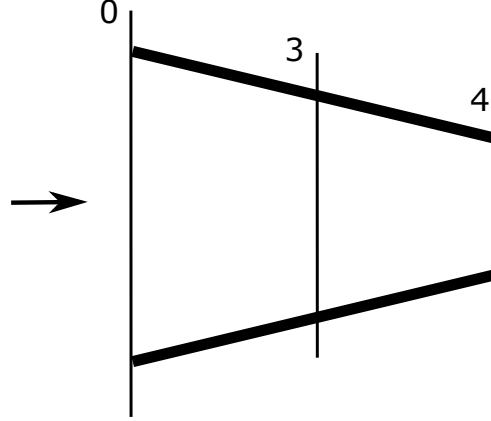
Figure 6.2: Twin-entry turbine equivalent nozzle.

The effective area of the equivalent nozzle is based on the continuity equation applied to the interspace, the rotor and the equivalent nozzle, as defined in Eq. 6.1. $\dot{m}_{\text{turb}}$ is the mass flow rate of the turbine, A the area, ρ the density and v and w the absolute and the relative velocity respectively. The variables in the equivalent nozzle are indicated with the subscript Neq. The effective area of the equivalent nozzle can be obtained as explained by Payri et al. [79] and defined in Eq. 6.2.

$$\dot{m}_{\text{turb}} = A_3 \cdot \rho_3 \cdot v_3 = A_4 \cdot \rho_4 \cdot w_4 = A_{Neq} \cdot \rho_4 \cdot v_{Neq} \tag{6.1}$$

$$A_{\text{Neq}} = A_4 \sqrt{\frac{1 + \left(\dfrac{u_4}{v_{\text{Neq}}}\right)^2 - \left(\dfrac{u_3}{v_{\text{Neq}}}\right)^2 + \left(\dfrac{w_3}{v_{\text{Neq}}}\right)^2}{\left(\dfrac{A_4}{A_3}\right)^2 \left(\dfrac{\rho_4}{\rho_3}\right)^2 + 1}} \tag{6.2}$$

The effective area depends on variables that do not appear on the manufacturer's map and are difficult to measure experimentally. Therefore, Eq. 6.2 can be simplified, as described by Serrano et al. [91]. The equation obtained (Eq. 6.3) only depends on variables provided in the twin-entry turbine maps and geometrical parameters. However, 4 calibration coefficients are needed for adjustment.

$$A_{\text{Neq}} = \dfrac{a \cdot A_4^{\text{geom}} \sqrt{1 + \dfrac{\sigma^2 \cdot \left[\left(\dfrac{D_4}{D_3} \right)^2 - 1 \right] + b}{\eta_{\text{t,s}}}}}{\sqrt{1 + \left[c \cdot \dfrac{A_4^{\text{geom}}}{A_3^{\text{geom}} \cdot \cos\left(\beta_3 \right)} \right]^2 \cdot \dfrac{\pi_{1,4}^{-2}}{\left[1 - \eta_{\text{t,s}} \cdot \left(1 - \pi_{1,4}^{\frac{1-\gamma}{\gamma}} \right) \right]^2}}} \qquad (6.3)$$

The a calibration coefficient represents the rotor discharge coefficient. It is related to the rotor outlet geometrical area, as described in Eq. 6.4. The b calibration coefficient represents the ratio between the rotor inlet relative kinetic energy and the nozzle isentropic kinetic energy. It is challenging to compute experimentally. However, the order of magnitude can be estimated as described in Eq. 6.5. The c calibration coefficient represents the rotor and interspace discharge coefficients ratio. It can be related to the a calibration coefficient, as described in Eq. 6.6. The d calibration coefficient is included through the term $\pi_{1,4}$ defined in Eq. 6.8, computing d as described in Eq. 6.7.

$$A_4 = A_4^{\text{geom}} \cdot a \qquad (6.4)$$

$$b = \left(\frac{v_0}{c_{is}} \right)^2 + \left(\frac{w_3}{c_{is}} \right)^2 = \frac{A_{\text{Neq}}}{A_0} \cdot \left(\frac{1}{\pi_{\text{exp}}} \right)^{\frac{1}{\gamma}} + O\left[10^{-1} \right] \qquad (6.5)$$

$$c = \frac{a}{CD_{\text{int}}} \qquad (6.6)$$

$$d = \frac{p_3 - p_4}{p_{0t} - p_4} \qquad (6.7)$$

$$\pi_{1,4} = 1 + d \cdot \left[\pi_{0t,4} - 1 \right] \qquad (6.8)$$

These calibration coefficients can be adjusted employing experimentally measured working points. However, they could depend on the mass flow admission conditions. Therefore, the behaviour of these calibration coefficients with the *MFR* value should be analysed.

The effective area of the equivalent nozzle must be computed with Eq. 6.3 for each flow branch separately. Therefore, the calibration coefficients must be adjusted for each branch separately. Moreover, there are geometrical parameters that need to be changed to set each flow branch geometry appropriately.

The mass flow CFD analysis carried out in the previous chapter has exposed that the rotor inlet and rotor outlet areas corresponding to each flow branch

vary linearly with *MFR*. This CFD analysis can be locally validated at the outlet section with the LDA measurements described in Chapter 3.

The rotor outlet area of each flow branch could be estimated utilising the *SPC* obtained in these LDA measurements. Since the *SPC* measures the concentration of particles coming from the shroud branch, the region where the *SPC* value is higher than 0.5 could be considered the rotor outlet area corresponding to the shroud branch. Thus, the region where the *SPC* value is lower than 0.5 would be considered the rotor outlet area corresponding to the hub branch. The radial position where the *SPC* takes the value 0.5 is shown in Fig. 6.3 for different *MFR* values.
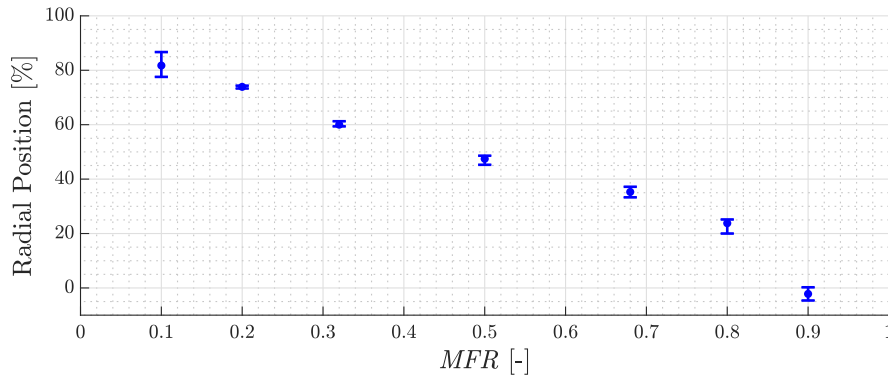
Figure 6.3: Radial position in terms of percentage of rotor channel from hub to shroud where the *SPC* value is closer to 0.5.

The mean radial positions for each *MFR* value have been computed, interpolating the results from the measured points. The whiskers denote the variations with the reduced rotational speed. There are slight variations with the reduced rotational speed in extreme *MFR* values. Nevertheless, *MFR* values closer to full admission conditions are practically independent of the reduced rotational speed. The radial position where the *SPC* is 0.5 decreases with the *MFR*. It moves toward the rotor hub. The area corresponding to each flow branch can be computed assuming this radial position as the limit between them. The rotor outlet area of each branch estimated with this approximation can be compared with the CFD results, as shown in Fig. 6.4.

The percentage of rotor outlet area occupied by each branch computed with this approximation offers similar values to the rotor outlet area obtained from the CFD simulations. It decreases with *MFR* for the hub branch and increases for the shroud branch. Moreover, the dependence on *MFR* could be assumed as linear. The straight lines in Fig. 6.4 could represent the behaviour of the rotor outlet area of each flow branch in the one-dimensional model. Therefore, the assumption of rotor outlet area linear variation with *MFR* inferred from the

133
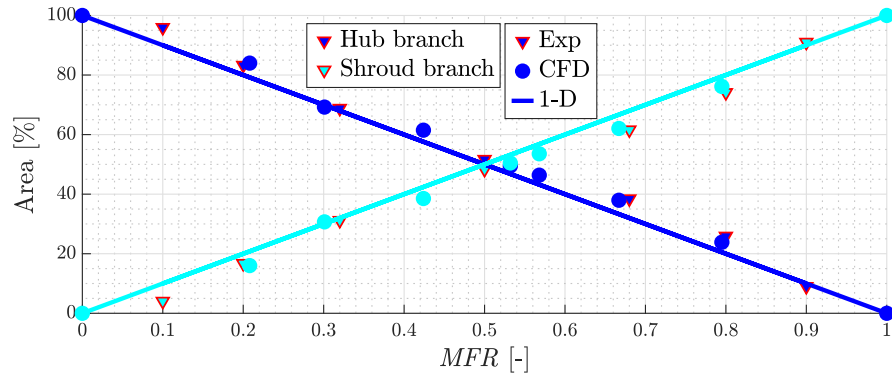
Figure 6.4: Rotor outlet area computed from the LDA measurements and from the CFD simulations.

CFD simulations has been corroborated with the LDA measurements.

There is no local validation of the rotor inlet area since it was not possible to access that twin-entry turbine region optically. However, if the flow branches are still separated at the rotor outlet, they should also be separated at the rotor inlet since it is upstream of the section measured with the LDA technique. Thus, the effective area model will employ the assumption of rotor inlet area variation with *MFR* found in the CFD simulations.

The geometrical parameters that could be modified in the effective area model (Eq. 6.3) considering these assumptions are represented in Fig. 6.5.
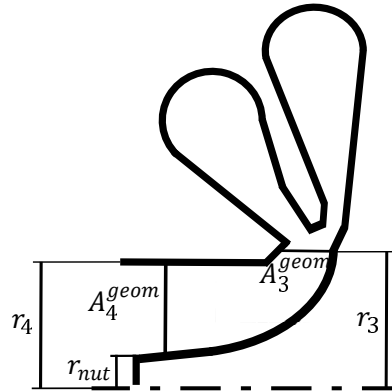
Figure 6.5: Geometrical parameters affecting the effective area model.

The rotor inlet radius (r_3) does not vary with *MFR* since it is constant along the blade leading edge. However, the rotor inlet area varies linearly with *MFR*, as observed in the CFD simulations. The rotor inlet area (A_3^{geom}) can be estimated as a cylindrical section as defined in Eq. 6.9. The rotor inlet area only depends on the rotor inlet radius and the blade height (h_{blade}). The blade height

should vary linearly with the *MFR* value since the rotor inlet radius is constant. Therefore, the rotor inlet areas estimated for each flow branch are defined in Eq. 6.10 and 6.11 for the hub and shroud branches, respectively.

$$A_3^{\text{geom}} = 2 \cdot \pi \cdot r_3 \cdot h_{\text{blade}} \tag{6.9}$$

$$A_{3h}^{\text{geom}} = 2 \cdot \pi \cdot r_3 \cdot h_{\text{blade}} \cdot (1 - MFR) \tag{6.10}$$

$$A_{3sh}^{\text{geom}} = 2 \cdot \pi \cdot r_3 \cdot h_{\text{blade}} \cdot MFR \tag{6.11}$$

The rotor outlet area (A_4^{geom}) can be estimated as a ring area depending on the rotor nut radius and the rotor outlet wheel radius as defined in Eq. 6.12. The rotor outlet area corresponding to each branch could be computed employing an intermediate radius that allows considering the assumption of rotor outlet area variation with *MFR*. The rotor outlet area corresponding to each flow branch is defined in Eq. 6.13 and 6.14 for the hub and shroud branches, respectively. The intermediate radius is computed as described in Eq. 6.15 for imposing the assumption of area linearity with *MFR*.

$$A_4^{\text{geom}} = \pi \cdot \left(r_4^2 - r_{nut}^2 \right) \tag{6.12}$$

$$A_{4h}^{\text{geom}} = \pi \cdot \left(r_i^2 - r_{nut}^2 \right) \tag{6.13}$$

$$A_{4sh}^{\text{geom}} = \pi \cdot \left(r_4^2 - r_i^2 \right) \tag{6.14}$$

$$r_i = \sqrt{(1 - MFR) \cdot r_4^2 + MFR \cdot r_{\text{nut}}^2} \tag{6.15}$$

These modifications of the geometrical parameters are introduced into the effective area model (Eq. 6.3) for each flow branch. Once these modifications are introduced, the calibration coefficients can be adjusted. The procedure followed is to adjust them for each measured *MFR* value separately to identify their dependence on *MFR*. Fig. 6.6 shows the value of the four calibration coefficients in each flow branch adjusted for each measured *MFR* value.

The *a* calibration coefficient could be assumed constant with *MFR* for both flow branches. The effect of *MFR* on the rotor outlet area has been included through the term A_4^{geom}. Therefore, the *a* calibration coefficient, which is the rotor outlet discharge coefficient, does not have to include this effect. It could be assumed as constant with *MFR*.

The *b* calibration coefficient also could be assumed constant with *MFR* for both flow branches. The effect of *MFR* on the rotor inlet relative kinetic energy
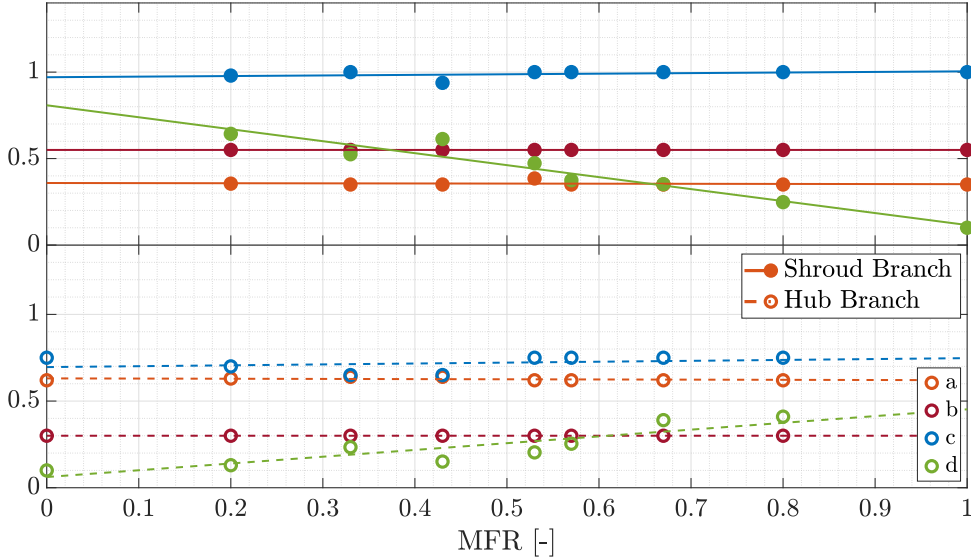
Figure 6.6: Effective area calibration coefficients.

has been included through the variation of the rotor inlet area with the *MFR* value. Therefore, the *b* calibration coefficient does not have to include this effect.

The *c* calibration coefficient represents the ratio between the rotor outlet discharge coefficient and the rotor inlet discharge coefficient. The rotor outlet discharge coefficient is the *a* calibration coefficient, assumed constant with *MFR*. However, the rotor inlet discharge coefficient could depend on *MFR*. In the previous chapter, the rotor inlet flow angle has been found dependent on the *MFR*. The behaviour of the rotor inlet flow angle could be separated from the rotor inlet discharge coefficient. The effect of the rotor inlet flow angle on the effective area model has been included dividing the ratio of geometrical areas by the cosine of the rotor inlet flow angle in Eq. 6.3. The *c* calibration coefficient could be assumed as constant with *MFR* if the effect of the rotor inlet flow angle is extracted from the rotor inlet discharge coefficient, as shown in Fig. 6.6.

The *d* calibration coefficient seems to have linear trends with *MFR*. It increases with *MFR* for the hub branch and decreases for the shroud branch. The *d* calibration coefficient stands for the ratio between the static pressure drop in the rotor and the total-to-static pressure drop from the turbine inlet to the rotor outlet. Therefore, the *d* calibration coefficient indeed represents the trend towards increasing the pressure ratio in the interspace when the mass flow increases in one branch compared to the other. The *d* calibration coefficient increases with *MFR* for the hub branch because the mass flow of the hub branch decreases compared to the mass flow of the shroud branch and, so, the hub branch has a lower interspace pressure ratio. The *d* calibration

coefficient decreases with *MFR* for the shroud branch because the mass flow of the shroud branch increases compared to the mass flow of the hub branch, and the interspace pressure ratio of the shroud branch becomes higher. Fig. 6.6 shows that the assumption of d calibration coefficient linearity with *MFR* could be reasonable.

The a, b and c calibration coefficients can be considered constant with *MFR*, and the d calibration coefficient can be considered linear with *MFR*. Hence, the effective area model presented only needs 5 parameters to be adjusted for each flow branch.

6.2.1 Effective area model validation

The effective area model presented has been implemented in the radial turbine model included in the VEMOD code. This model and the efficiency model presented in the following section are coupled. Since the efficiency model will depend on some parameters of the effective area model such as the c calibration coefficient, the effective area is adjusted first using the apparent efficiency from the performance maps.

The effective area model is solved for both branches separately, and the calibration coefficients have been adjusted with a constrained Levenberg-Marquardt non-linear optimisation fitter [114]. This fitter minimises the error produced in the computation of the reduced mass flow rate of each branch, as defined in Eq. 6.16, where n is the number of operational points computed.

$$\epsilon = \sqrt{\frac{\Sigma\left(\frac{\dot{m}-\dot{m}_{\mathrm{Exp}}}{\dot{m}_{\mathrm{Exp}}}\right)^2}{n}} \qquad (6.16)$$

The effective area model has been fitted employing the steady-state experimentally measured data presented in Chapter 3. The model requires initial values and upper and lower bounds of each calibration coefficient to adjust them, minimising the error. The calibration coefficients obtained from adjusting the model for each *MFR* value with the CFD data are used as initial values. The upper and lower bounds are defined as the range that makes physical sense for each calibration coefficient. a, b, c and the constant term of d have a range between 0 and 1 for both branches. The slope of d must be positive for the hub branch and negative for the shroud branch. The effective area calibration coefficients adjusted for each flow branch are summed up in Table 6.2.

The reduced mass flow computed employing the effective area model with these calibration coefficients can be compared to the reduced mass flow measured experimentally. Thus, the quality of the effective area model can be validated. Fig. 6.7 shows a comparison of the reduced mass flow computed with the effective area model and the one experimentally measured for each flow branch

Table 6.2: Effective area calibration coefficients for each twin-entry turbine branch.

Coefficient	Hub Branch	Shroud Branch
a	0.728	0.447
b	0.201	0.536
c	0.794	0.995
d	$0 + 0.4 \cdot MFR$	$0.653 - 0.6 \cdot MFR$

separately. The straight line represents a perfect concordance between model and experiment, and the dotted lines indicate a $\pm5\%$ error.

The effective area model adequately reproduces the reduced mass flow of both branches. The R^2 value of both flow branches is high, indicating an excellent correlation between the modelled and measured reduced mass flow.

Moreover, the root mean square error (RMSE) has been computed for both flow branches separately, giving an RMSE lower than 2.5%. The expanded uncertainty of the steady-state experimental measurements was 3%. The modelled reduced mass flow has lower error than the expanded uncertainty of the measurements.

6.3 Losses-based efficiency model

The efficiency model is developed to extrapolate in the twin-entry turbine efficiency map. The model proposed is based on the losses observed in the CFD loss analysis of the previous chapter. The source of losses detected in each twin-entry turbine part has been correlated with simple physical models at all admission conditions. However, the analysis has been focused on the unequal admission conditions, which are the most realistic operating conditions.

The manufacturer's maps typically provide working points at full and partial admission conditions. Thus, the existent extrapolation models are fitted without working points under unequal admission conditions. The current efficiency model will consider the operation under unequal admission conditions. The efficiency model considers the twin-entry turbine as two single-entry turbines working in parallel, as the effective area model. Thus, the equations employed within the efficiency model are applied separately in both flow branches.

The total-to-static actual efficiency of each flow branch is defined in Eq. 6.17. The actual efficiency depends on the enthalpies at rotor inlet and outlet and turbine inlet and outlet. These enthalpies are divided by the turbine inlet total enthalpy ($h_{\text{t},0}$) to make them non-dimensional. All the enthalpy losses and kinetic energies defined in the current model are also divided by the turbine
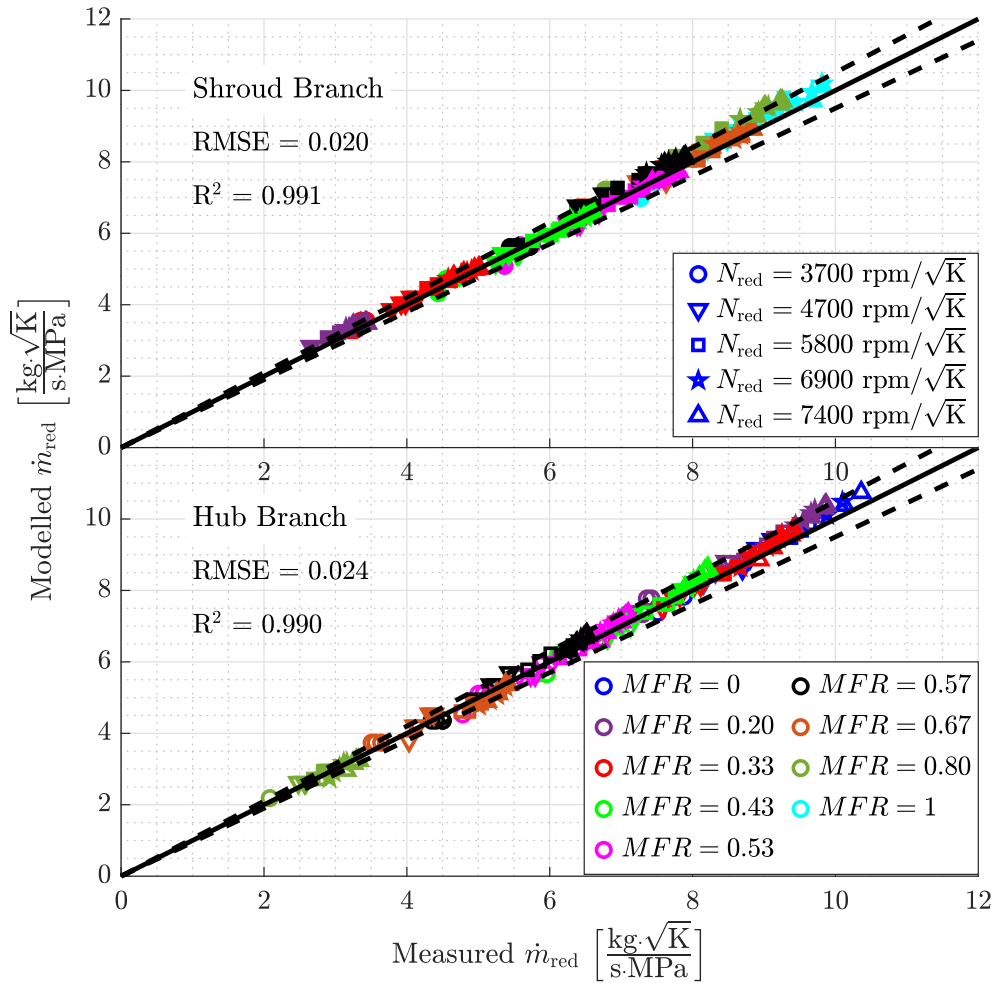
Figure 6.7: Validation of the adjusted effective area model.

inlet total enthalpy. These non-dimensional enthalpies and kinetic energies allow an inlet temperature to be assumed to compute the efficiency. Moreover, it is not required to compute the densities in each twin-entry turbine part, as described in [94].

$$\eta_{\text{ts}} = \frac{\frac{h_{\text{t},3}}{h_{\text{t},0}} - \frac{h_{\text{t},4}}{h_{\text{t},0}}}{\frac{h_{\text{t},0}}{h_{\text{t},0}} - \frac{h_5}{h_{\text{t},0}}} \tag{6.17}$$

The enthalpy varies within the turbine due to the losses produced in each twin-entry turbine part and the work produced by the rotor. These variations in the non-dimensional form are illustrated in an enthalpy-entropy diagram in Fig.

6.8, where the losses produced in each part are indicated. The actual efficiency considering this behaviour has been defined in Eq. 6.18.
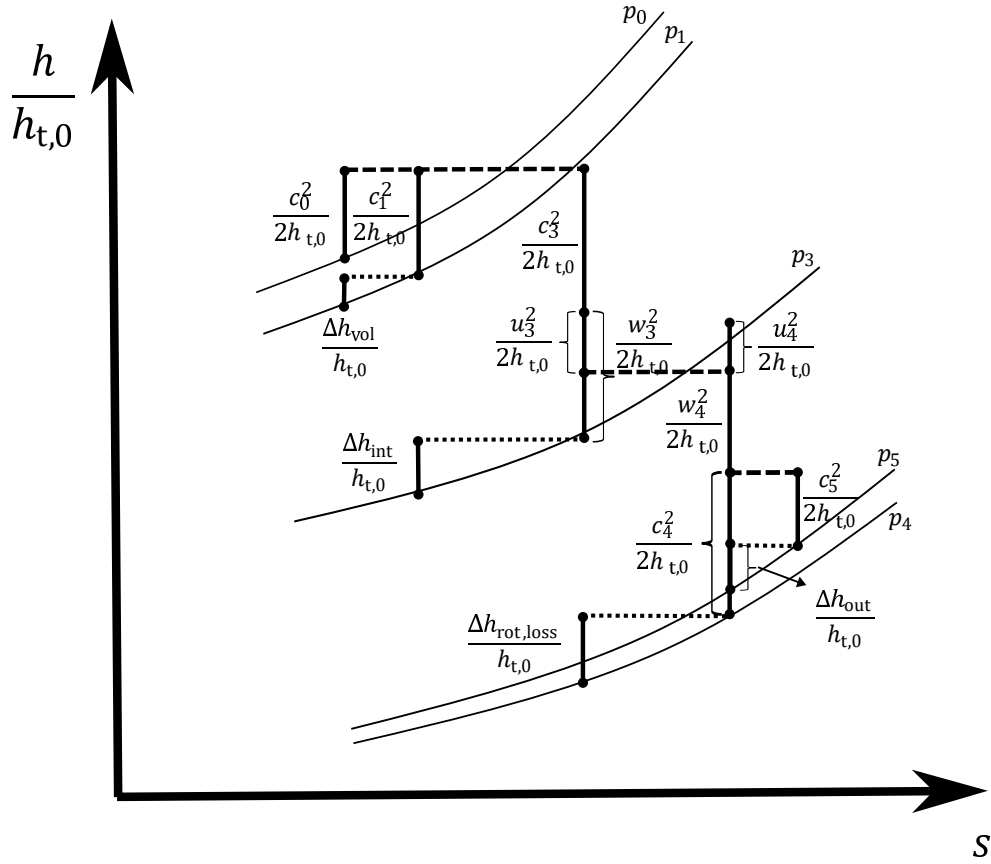
Figure 6.8: Enthalpy variation in a twin-entry turbine branch.

$$\eta_{ts} = \frac{1 - \left(\frac{p_{t,4}}{p_{t,3}}\right)^{\frac{\gamma-1}{\gamma}} - \frac{\Delta h_{loss,rot}}{h_{t,0}}}{1 - \left(\frac{p_5}{p_{t,0}}\right)^{\frac{\gamma-1}{\gamma}}}$$

(6.18)

However, the actual efficiency of each flow branch cannot be measured experimentally. The mass flow at the outlet is mixed. Therefore, the outlet temperature measured corresponds to the mixing of both flow branches. This mixed outlet temperature could be employed to compute the apparent efficiency for each flow branch, the experimentally measured efficiency.

The actual and apparent non-dimensional enthalpy variations of each flow branch are illustrated in Fig. 6.9. The apparent enthalpy variation is indicated with the subscript app. Since the outlet conditions measured are the same for

140

both flow branches, the apparent enthalpy variation is different from the actual enthalpy variation.
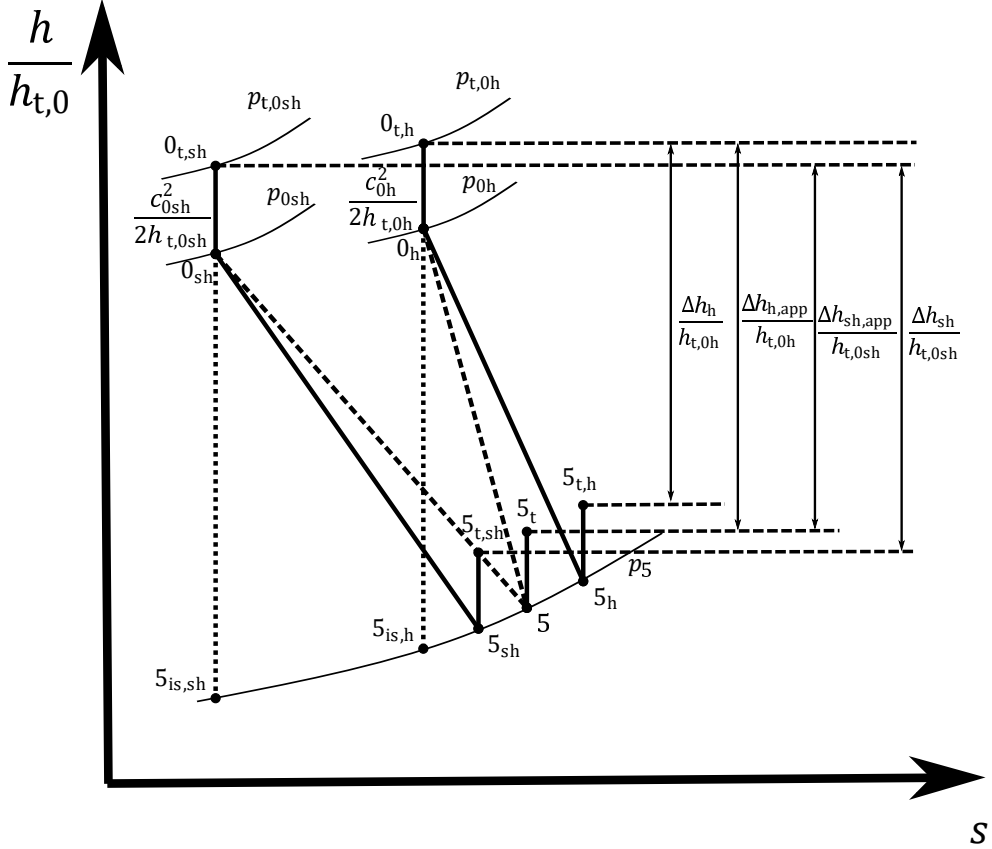
Figure 6.9: Enthalpy variation in a twin-entry turbine for obtaining the apparent efficiency.

Therefore, the apparent efficiency can be computed with Eq. 6.19 for each flow branch. P_c is a control parameter whose value is $1 - MFR$ for the hub branch and MFR for the shroud branch. The subscript *other* refers to that variable in the other flow branch. The validation of the current model has to be assessed with the apparent efficiency since it is the efficiency that can be compared to the experimentally measured efficiency.

$$\eta_{\text{app}} = P_{\text{c}} \cdot \eta_{\text{ts}} +$$

$$\frac{1 - P_{\text{c}}}{1 - \left(\frac{p_{\text{t},0}}{p_5}\right)^{\frac{1-\gamma}{\gamma}}} \cdot \left[1 + \left(\eta_{\text{ts,other}} \cdot \left[1 - \left(\frac{p_{\text{t},0,\text{other}}}{p_5}\right)^{\frac{1-\gamma}{\gamma}}\right] - 1\right) \cdot \frac{T_{\text{t},0}}{T_{\text{t},0,\text{other}}}\right] \quad (6.19)$$

The equations employed to compute the losses and all the required variables for the efficiency model are described in the following subsections part by part.

6.3.1 Volutes

The first part to model is the volutes. The volute inlet kinematic conditions must be assessed. Thus, the volute inlet kinetic energy could be computed knowing the reduced mass flow, as defined in Eq. 6.20. A_0 is the volute inlet area, R is the gas constant, and C_p is the specific heat capacity.

$$\frac{c_0^2}{2 \cdot h_{t,0}} = \frac{R^2 \cdot \dot{m}_{red}^2}{2 \cdot A_0^2 \cdot C_p} \tag{6.20}$$

The volutes are the most isentropic part of the twin-entry turbines. However, the CFD losses analysis presented in Chapter 5 detected significant losses produced by the wall friction. The model proposed for modelling these losses is the passage losses described by Futral et al. [109]. The non-dimensional formulation of this model is defined in Eq. 6.21. $Z_{vol,pass}$ is a fitting parameter that needs to be adjusted. L_{vol} stands for the mean volute streamline length, considered half the volute length since it is the mean path length that the flow travels before leaving the volute. This approximation is consistent with other 1D simulation approaches made by authors such as Chiong et al. [83].

$$\frac{\Delta h_{vol}}{h_{t,0}} = Z_{vol,pass} \cdot L_{vol} \cdot \frac{c_0^2}{2 \cdot h_{t,0}} \tag{6.21}$$

The volute outlet kinematic conditions must also be assessed. The kinetic energy at the volute outlet could be computed from the reduced mass flow, as defined in Eq. 6.22. A_1 is the volute outlet area, and α_1 is the volute outlet flow angle. It also depends on the total pressure ratio between the volute inlet and outlet.

$$\frac{c_1^2}{2 \cdot h_{t,0}} = \frac{R^2 \cdot \dot{m}_{red}^2}{A_1^2 \cdot 2 \cdot C_p \cdot \cos(\alpha_1)} \cdot \left(\frac{p_{t,0}}{p_{t,1}}\right)^{\frac{\gamma-1}{\gamma}} \tag{6.22}$$

The total pressure ratio between volute inlet and outlet is defined in Eq. 6.25. This equation is obtained from the volute isentropic pressure ratio defined in Eq. 6.23 and the volute outlet effective pressure ratio defined in Eq. 6.24. It includes the volute losses computed in Eq. 6.21.

$$\frac{p_{t,0}}{p_1} = \left(\frac{1}{1 - \frac{c_1^2}{2 \cdot h_{t,0}} - \frac{\Delta h_{vol}}{h_{t,0}}}\right)^{\frac{\gamma}{\gamma-1}} \tag{6.23}$$

$$\frac{p_{t,1}}{p_1} = \left(\frac{1}{1 - \frac{c_1^2}{2 \cdot h_{t,0}}} \right)^{\frac{\gamma}{\gamma - 1}} \tag{6.24}$$

$$\frac{p_{t,0}}{p_{t,1}} = \left(\frac{1 - \frac{c_1^2}{2 \cdot h_{t,0}}}{1 - \frac{c_1^2}{2 \cdot h_{t,0}} - \frac{\Delta h_{vol}}{h_{t,0}}} \right)^{\frac{\gamma}{\gamma - 1}} \tag{6.25}$$

The volute outlet flow angle is computed from both momentum and mass flow conservations in Eq. 6.26. D_0 is the volute inlet diameter of each flow branch.

$$\alpha_1 = \operatorname{atan} \left(\frac{4 \cdot A_1}{D_0^2} \cdot \left(\frac{p_{t,1}}{p_{t,0}} \right)^{\frac{1}{\gamma}} \cdot \frac{\sqrt{\frac{c_1^2}{2 \cdot h_{t,0}}}}{\sqrt{\frac{c_0^2}{2 \cdot h_{t,0}}}} \right) \tag{6.26}$$

The volute total pressure ratio and the volute outlet flow angle depend on the volute outlet kinetic energy. Therefore, the volute outlet kinetic energy defined in Eq. 6.22 must be calculated iteratively. Brent's method [115] was selected to carry out this iterative computation and obtain the volute outlet kinetic energy.

6.3.2 Interspace

The following part to model is the interspace between the volute outlet and rotor inlet. The CFD losses analysis presented in Chapter 5 found three different sources of losses that must be considered: passage losses, sudden expansion losses and losses due to the momentum exchange between flow branches. The enthalpy losses produced by these sources of losses can be added to compute the overall enthalpy losses in the interspace, as defined in Eq. 6.27.

$$\frac{\Delta h_{int}}{h_{t,0}} = \frac{\Delta h_{int,pass}}{h_{t,0}} + \frac{\Delta h_{int,SudExp}}{h_{t,0}} + \frac{\Delta h_{int,ME}}{h_{t,0}} \tag{6.27}$$

The passage losses are modelled with the same non-dimensional model employed in the volutes but evaluated in the interspace, as defined in Eq. 6.28. $Z_{int,pass}$ is a fitting parameter that needs to be adjusted. L_{int} stands for the mean interspace streamline length, considered as the line integral of a logarithmic spiral.

$$\frac{\Delta h_{int,pass}}{h_{t,0}} = Z_{int,pass} \cdot L_{int} \cdot \frac{c_1^2}{2 \cdot h_{t,0}} \tag{6.28}$$

The sudden expansion non-dimensional enthalpy losses are modelled with a Borda-Carnot based model, as defined in Eq. 6.29. $Z_{\text{int,SudExp}}$ is a fitting parameter that needs to be adjusted, and A_1 and A_3 are the interspace inlet and outlet areas. A_3 is computed for each flow branch as explained in the effective area model. The sudden expansion losses can not be found under all admission conditions, as described in Chapter 5. Therefore, these losses are only computed when the ratio between interspace inlet and outlet areas is lower than one. There is no sudden expansion in the other cases, and it must not be calculated.

$$\frac{\Delta h_{\text{int,SudExp}}}{h_{\text{t,0}}} = Z_{\text{int,SudExp}} \cdot \frac{c_1^2}{2 \cdot h_{\text{t,0}}} \cdot \left(1 - \frac{A_1}{A_3}\right) \tag{6.29}$$

The losses due to the momentum exchange between flow branches are modelled with the simple model presented in Chapter 5. The non-dimensional form of this model is formulated in Eq. 6.30. Z_{ME} is a fitting parameter that needs to be adjusted. $L_{\text{int,ME}}$ stands for the interspace contact length between flow branches, estimated as the radial interspace length. These losses also depend on the velocity difference between flow branches at the interspace inlet, as indicated by the h and sh subscripts. These losses do not affect the cases under partial admission conditions since there is only flow passing through one of the branches. Moreover, these losses are computed for the flow branch with the higher mass flow (*MFR* lower than 0.5 for the hub branch and higher than 0.5 for the shroud branch). The flow branch with lower mass flow gains the energy that the other has lost since the momentum is transmitted from one flow branch to the other.

$$\frac{\Delta h_{\text{int,ME}}}{h_{\text{t,0}}} = Z_{\text{ME}} \cdot L_{\text{int,ME}} \cdot \left(\sqrt{\frac{c_{1,h}^2}{2 \cdot h_{\text{t,0}}}} - \sqrt{\frac{c_{1,sh}^2}{2 \cdot h_{\text{t,0}}}}\right)^2 \tag{6.30}$$

The interspace outlet kinematic conditions must also be assessed. The kinetic energy at the interspace outlet could be computed from the reduced mass flow, as defined in Eq. 6.31. α_3 is the interspace outlet flow angle. It also depends on the total pressure ratio between volute inlet and outlet and the total pressure ratio between interspace inlet and outlet.

$$\frac{c_3^2}{2 \cdot h_{\text{t,0}}} = \frac{R^2 \cdot \dot{m}_{\text{red}}^2}{A_3^2 \cdot 2 \cdot C_{\text{p}} \cdot \cos(\alpha_3)} \cdot \left(\frac{p_{\text{t,0}}}{p_{\text{t,1}}} \cdot \frac{p_{\text{t,1}}}{p_{\text{t,3}}}\right)^{\frac{\gamma-1}{\gamma}} \tag{6.31}$$

The total pressure ratio between interspace inlet and outlet is defined in Eq. 6.34. This equation is obtained from the interspace isentropic pressure ratio defined in Eq. 6.32 and the interspace outlet effective pressure ratio defined in Eq. 6.33. It includes the interspace losses computed in Eq. 6.27.

144

$$\frac{p_{t,1}}{p_3} = \left(\frac{1}{1 - \frac{c_3^2}{2 \cdot h_{t,0}} - \frac{\Delta h_{int}}{h_{t,0}}} \right)^{\frac{\gamma}{\gamma - 1}} \tag{6.32}$$

$$\frac{p_{t,3}}{p_3} = \left(\frac{1}{1 - \frac{c_3^2}{2 \cdot h_{t,0}}} \right)^{\frac{\gamma}{\gamma - 1}} \tag{6.33}$$

$$\frac{p_{t,1}}{p_{t,3}} = \left(\frac{1 - \frac{c_3^2}{2 \cdot h_{t,0}}}{1 - \frac{c_3^2}{2 \cdot h_{t,0}} - \frac{\Delta h_{int}}{h_{t,0}}} \right)^{\frac{\gamma}{\gamma - 1}} \tag{6.34}$$

The interspace outlet flow angle is computed as formulated in Eq 6.35. r_1 is the interspace inlet radius, h_3 is the interspace outlet height, and CD_{int} is the interspace discharge coefficient previously computed for the c calibration coefficient in the effective area model.

$$\alpha_3 = \text{atan} \left(\frac{2 \cdot \pi \cdot r_1 \cdot h_3 \cdot CD_{int}}{A_0} \cdot \left(\frac{p_{t,1}}{p_{t,3}} \right)^{\frac{-1}{\gamma}} \right) \tag{6.35}$$

The interspace total pressure ratio and the interspace outlet flow angle depend on the kinetic energy of the interspace outlet. Therefore, the interspace outlet kinetic energy defined in Eq. 6.31 must be calculated iteratively. Brent's method [115] has been chosen again to carry out this iterative computation and obtain the interspace outlet kinetic energy.

6.3.3 Rotor

The following part to model is the rotor. The rotor inlet kinematic conditions must be assessed. The relative kinematic conditions are also required since the rotor is a moving part. Thus, all the components of the velocity triangle at the rotor inlet are computed. The velocity triangle at the rotor inlet is shown in Fig. 6.10, where the subscript r refers to the radial component and the subscript θ refers to the tangential component.

The radial and tangential components of the absolute velocity are computed from the absolute velocity and the interspace outlet flow angle in Eq. 6.36 and 6.37, respectively.

$$\frac{c_{3,r}^2}{2 \cdot h_{t,0}} = \frac{c_3^2}{2 \cdot h_{t,0}} \cdot \cos(\alpha_3)^2 \tag{6.36}$$

$$\frac{c_{3,\theta}^2}{2 \cdot h_{t,0}} = \frac{c_3^2}{2 \cdot h_{t,0}} \cdot \sin(\alpha_3)^2 \tag{6.37}$$

145
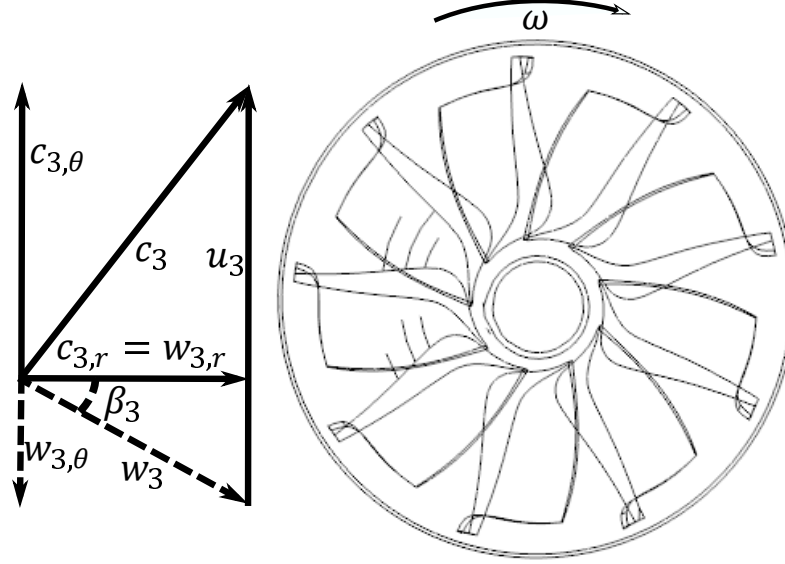
Figure 6.10: Velocity triangle at rotor inlet.

The linear velocity of the rotor is computed from the reduced rotational speed in $\mathrm{Hz\,K^{-0.5}}$ and the rotor inlet diameter in Eq. 6.38.

$$\frac{u_3^2}{2 \cdot h_{t,0}} = \frac{(N_{red} \cdot \pi \cdot D_3)^2}{2 \cdot C_p} \tag{6.38}$$

The radial component of the relative velocity is the same as the absolute velocity radial component. The tangential component of the relative velocity is computed with the difference between the tangential component of the absolute velocity and the linear velocity of the rotor, as defined in Eq. 6.39. The relative velocity is computed employing both its radial and tangential components, as defined in Eq. 6.40.

$$\frac{w_{3,\theta}^2}{2 \cdot h_{t,0}} = \left(\sqrt{\frac{c_{3,\theta}^2}{2 \cdot h_{t,0}}} - \sqrt{\frac{u_3^2}{2 \cdot h_{t,0}}} \right)^2 \tag{6.39}$$

$$\frac{w_3^2}{2 \cdot h_{t,0}} = \frac{w_{3,\theta}^2}{2 \cdot h_{t,0}} + \frac{c_{3,r}^2}{2 \cdot h_{t,0}} \tag{6.40}$$

The rotor inlet relative flow angle is computed in Eq. 6.41, employing the relative velocity components.

$$\beta_3 = \text{atan}\left(\frac{\sqrt{\frac{w_{3,\theta}^2}{2 \cdot h_{t,0}}}}{\sqrt{\frac{w_{3,r}^2}{2 \cdot h_{t,0}}}}\right) \tag{6.41}$$

The CFD losses analysis presented in Chapter 5 found four different sources of losses that must be considered in the rotor: passage, incidence and tip losses and losses due to the momentum exchange between flow branches. The enthalpy losses produced by these sources of losses can be added to compute the overall enthalpy losses in the rotor, as defined in Eq. 6.42.

$$\frac{\Delta h_{\text{rot,loss}}}{h_{t,0}} = \frac{\Delta h_{\text{rot,pass}}}{h_{t,0}} + \frac{\Delta h_{\text{rot,inc}}}{h_{t,0}} + \frac{\Delta h_{\text{rot,tip}}}{h_{t,0}} + \frac{\Delta h_{\text{rot,ME}}}{h_{t,0}} \tag{6.42}$$

The passage losses are modelled with a similar non-dimensional model than the employed in the volutes and the interspace. However, it is evaluated with the relative velocity and also considers the rotor outlet kinematic conditions, as defined in Eq. 6.43. $Z_{\text{rot,pass}}$ is a fitting parameter that needs to be adjusted. These losses depend on the difference between the rotor inlet relative flow angle and the optimum angle ($\beta_{3,\text{opt}}$). The optimum angle is estimated in Eq. 6.44 with the definition suggested by Chen and Baines [110].

$$\frac{\Delta h_{\text{rot,pass}}}{h_{t,0}} = Z_{\text{rot,pass}} \cdot \left(\frac{w_3^2}{2 \cdot h_{t,0}} \cdot \cos\left(\beta_3 - \beta_{3,\text{opt}}\right)^2 + \frac{w_4^2}{2 \cdot h_{t,0}}\right) \tag{6.43}$$

$$\beta_{3,\text{opt}} = \text{asin}\left(\sqrt{1 - \frac{2 \cdot \sin\left(\frac{\pi}{n_{\text{blade}}}\right)}{\pi \cdot \left[1 + \sin\left(\frac{\pi}{n_{\text{blade}}}\right)\right]}}\right) - \frac{\pi}{2} \tag{6.44}$$

The non-dimensional incidence enthalpy losses are modelled with the model proposed by Chen and Baines [110] in Eq. 6.45. $Z_{\text{rot,inc}}$ is a fitting parameter that needs to be adjusted. These losses also depend on the difference between the rotor inlet relative flow angle and the optimum angle.

$$\frac{\Delta h_{\text{rot,inc}}}{h_{t,0}} = Z_{\text{rot,inc}} \cdot \frac{w_3^2}{2 \cdot h_{t,0}} \cdot \sin\left(\beta_3 - \beta_{3,\text{opt}}\right)^2 \tag{6.45}$$

The tip leakage non-dimensional enthalpy losses are based on the model proposed by Serrano et al. [111, 112] for single-entry turbines. The model defined in Eq. 6.46 depends on the incidence and friction-driven tip leakage flow momentum (-) and the pressure-driven tip leakage flow momentum (+). The subscript *tip* refers to the tip clearance.

$$\frac{\Delta h_{\text{rot,tip}}}{h_{\text{t,0}}} = \frac{\dot{m}_{\text{tip,}-}}{\dot{m}_{\text{turb}}} \cdot \frac{w_{\text{tip,}\theta,-}^2}{2 \cdot h_{\text{t,0}}} + \frac{\dot{m}_{\text{tip,}+}}{\dot{m}_{\text{turb}}} \cdot \frac{w_{\text{tip,}\theta,+}^2}{2 \cdot h_{\text{t,0}}} \tag{6.46}$$

The mass flow coefficients are calculated in Eq. 6.47 and 6.48 for the friction-driven and the pressure-driven tip leakage flow momentum, respectively, as described in Serrano et al. [111].

$$\frac{\dot{m}_{\text{tip,}-}}{\dot{m}_{\text{turb}}} = \frac{A_{\text{tip}}}{\dot{m}_{\text{red,turb}}} \cdot \frac{w_{\text{tip,}\theta,-}}{\sqrt{2 \cdot h_{\text{t,0}}}} \cdot \frac{1}{\pi_{\text{turb}}} \cdot \frac{\sqrt{C_{\text{p}}}}{R} \tag{6.47}$$

$$\frac{\dot{m}_{\text{tip,}+}}{\dot{m}_{\text{turb}}} = \frac{A_{\text{tip}}}{\dot{m}_{\text{red,turb}}} \cdot \frac{w_{\text{tip,}\theta,+}}{\sqrt{2 \cdot h_{\text{t,0}}}} \cdot \frac{1}{\pi_{\text{turb}}} \cdot \frac{\sqrt{C_{\text{p}}}}{R \cdot \cos\left(\beta_3 - \beta_{3,\text{opt}}\right)} \tag{6.48}$$

The modelled velocities are calculated in Eq. 6.49 and 6.50 for the friction-driven and the pressure-driven tip leakage flow momentum, respectively, as described in Serrano et al. [111]. K^- and K^+ are fitting parameters that need to be adjusted. $\bar{r}_{\text{tip}}$ is the mean blade radius estimated as the mean value between the rotor inlet radius and the rotor outlet radius. $\bar{r}_{\text{sh}}$ is the mean shroud radius estimated following Eq. 6.51. $\Delta\bar{r}_{\text{tip}}$ is the tip clearance gap. $\Delta p_{\text{PS,SS}}$ is the pressure difference between the suction side and pressure side of the blade, μ is the viscosity, and $\Delta\theta$ is the blade width in the tangential direction.

$$w_{\text{tip,}\theta,-} = K^- \cdot \frac{\frac{\bar{r}_{\text{sh}}^2 - \bar{r}_{\text{tip}}^2}{2 \cdot \bar{r}_{\text{tip}}^2} + \ln\left(\frac{\bar{r}_{\text{tip}}}{\bar{r}_{\text{sh}}}\right)}{\frac{\bar{r}_{\text{sh}}}{\bar{r}_{\text{tip}}^2} - \frac{1}{\bar{r}_{\text{sh}}}} \cdot \frac{\omega \cdot \bar{r}_{\text{sh}}}{\Delta\bar{r}_{\text{tip}}} \tag{6.49}$$

$$w_{\text{tip,}\theta,+} = \frac{\frac{\bar{r}_{\text{sh}}^2 - \bar{r}_{\text{tip}}^2}{2 \cdot \bar{r}_{\text{tip}}^2} + \ln\left(\frac{\bar{r}_{\text{tip}}}{\bar{r}_{\text{sh}}}\right)}{\frac{\bar{r}_{\text{sh}}}{\bar{r}_{\text{tip}}^2} - \frac{1}{\bar{r}_{\text{sh}}}} \cdot \left[-\frac{1}{2 \cdot \mu} \cdot \frac{\Delta p_{\text{PS,SS}}}{\Delta\theta \cdot \Delta\bar{r}_{\text{tip}}} \cdot \bar{r}_{\text{sh}} \cdot \ln\left(\frac{\bar{r}_{\text{sh}}}{\bar{r}_{\text{tip}}}\right) \right]$$
$$+ \left[\frac{\bar{r}_{\text{tip}}^2 - \bar{r}_{\text{sh}}^2}{4} + \frac{\bar{r}_{\text{sh}}^2}{2} \cdot \ln\left(\frac{\bar{r}_{\text{sh}}}{\bar{r}_{\text{tip}}}\right) \right] \cdot \frac{1}{2 \cdot \mu} \cdot \frac{\Delta p_{\text{PS,SS}}}{\Delta\theta \cdot \Delta\bar{r}_{\text{tip}}} \tag{6.50}$$

$$\bar{r}_{\text{sh}} = \bar{r}_{\text{tip}} + K^+ \cdot \Delta\bar{r}_{\text{tip}} \tag{6.51}$$

These tip enthalpy losses are only computed for the shroud branch for all *MFR* values but 0 since these losses are concentrated in a region near the rotor shroud.

The losses due to the momentum exchange between flow branches are modelled with the same model as in the interspace, but the relative velocity is employed in this case. The non-dimensional form of this model for the rotor is formulated in Eq. 6.52. Z_{ME} is the same fitting parameter as for the interspace.

$L_{\text{rot,ME}}$ stands for the rotor contact length between flow branches, estimated as defined in Eq. 6.53. This contact length should be similar to the rotor height. Since this geometrical parameter is not usually provided (although it can be measured), the contact length has been related with the rotor inlet radius. The current twin-entry turbine has a height to radius proportion of 2/3. This rotor contact length between flow branches estimation is independent of the working point, and it should provide accurate estimations for other geometries with similar rotor proportions. If the ratio between rotor inlet diameter and rotor height is noticeably different, the 2/3 value should be revised. Nevertheless, the possible error produced could be taken up by the adjustment of Z_{ME}.

These losses do not affect the cases under partial admission conditions since there is only flow passing through one of the branches. Moreover, these losses are computed for the flow branch with the higher mass flow (*MFR* lower than 0.5 for the hub branch and higher than 0.5 for the shroud branch). The flow branch with lower mass flow gains the energy that the other has lost since the momentum is transmitted from one flow branch to the other.

$$\frac{\Delta h_{\text{rot,ME}}}{h_{\text{t,0}}} = Z_{\text{ME}} \cdot L_{\text{rot,ME}} \cdot \left(\sqrt{\frac{w_{3,\text{h}}^2}{2 \cdot h_{\text{t,0}}}} - \sqrt{\frac{w_{3,\text{sh}}^2}{2 \cdot h_{\text{t,0}}}} \right)^2 \tag{6.52}$$

$$L_{\text{rot,ME}} \approx \frac{2}{3} \cdot r_3 \tag{6.53}$$

The rotor outlet kinematic conditions must also be assessed. The relative kinematic conditions are also required since the rotor is a moving part. Thus, all the components of the velocity triangle at the rotor outlet are computed. The velocity triangle at the rotor outlet is shown in Fig. 6.11, where the subscript ax refers to the axial component.

The axial component of the absolute velocity could be computed from the reduced mass flow, as defined in Eq. 6.54. A_4 is the rotor outlet area corresponding to each flow branch. It also depends on the total pressure ratio between volute inlet and outlet, the total pressure ratio between interspace inlet and outlet and the total pressure ratio between rotor inlet and outlet.

$$\frac{c_{4,ax}^2}{2 \cdot h_{\text{t,0}}} = \frac{R^2 \cdot \dot{m}_{\text{red}}^2}{A_4^2 \cdot 2 \cdot C_p} \cdot \left(\frac{p_{\text{t,0}}}{p_{\text{t,1}}} \cdot \frac{p_{\text{t,1}}}{p_{\text{t,3}}} \cdot \frac{p_{\text{t,3}}}{p_{\text{t,4}}} \right)^{\frac{\gamma-1}{\gamma}} \tag{6.54}$$

The relative velocity is computed from the rothalpy conservation, as defined in Eq. 6.55. It depends on the kinematic conditions at the rotor inlet, the linear velocity of the rotor at the outlet section (defined in Eq. 6.56), the rotor enthalpy losses and the total pressure ratio between rotor inlet and outlet. $\bar{D}_4$ stands for the mean rotor outlet diameter, as defined in Eq. 6.57. As explained in the effective area model, the subscript $outer$ refers to the rotor outlet wheel diameter
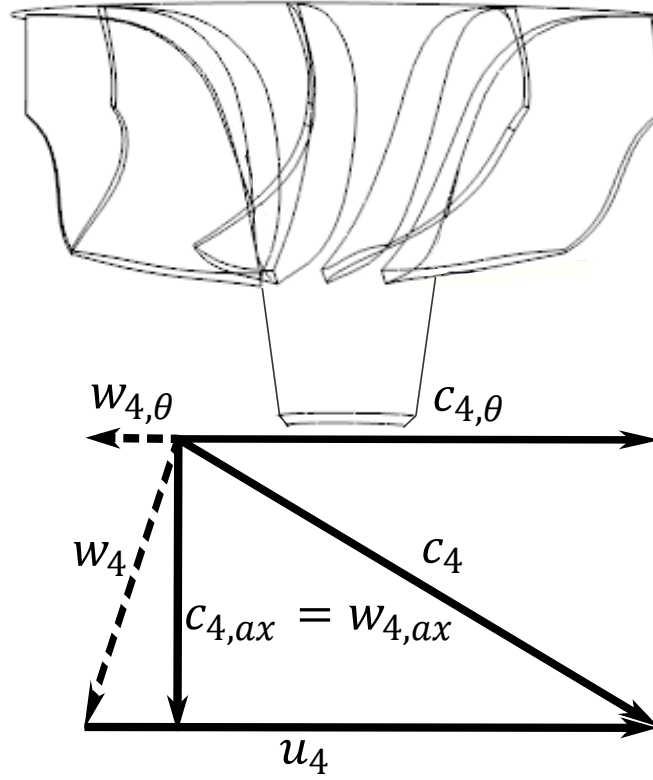
Figure 6.11: Velocity triangle at rotor outlet.

for the shroud branch and the intermediate radius between flow branches for the hub branch. The subscript *inner* refers to the rotor outlet nut diameter for the hub branch and the intermediate radius between flow branches for the shroud branch.

$$\frac{w_4^2}{2 \cdot h_{t,0}} = 1 - \frac{c_3^2}{2 \cdot h_{t,0}} + \frac{w_3^2}{2 \cdot h_{t,0}} - \left(\frac{p_{t,4}}{p_{t,3}}\right)^{\frac{\gamma-1}{\gamma}} - \frac{\Delta h_{\text{rot,loss}}}{h_{t,0}} + \frac{u_4^2}{2 \cdot h_{t,0}} - \frac{u_3^2}{2 \cdot h_{t,0}} \qquad (6.55)$$

$$\frac{u_4^2}{2 \cdot h_{t,0}} = \frac{\left(N_{\text{red}} \cdot \pi \cdot \bar{D}_4\right)^2}{2 \cdot C_p} \qquad (6.56)$$

$$\bar{D}_4 = \sqrt{\frac{D_{4,\text{outer}}^2 + D_{4,\text{inner}}^2}{2}} \qquad (6.57)$$

The rotor outlet relative kinematic energy defined in Eq. 6.55 has to be computed iteratively since it depends on the enthalpy losses and the enthalpy

losses depend on the rotor outlet relative kinematic energy. Brent's method [115] has been chosen again to carry out this iterative computation and obtain the rotor outlet relative kinetic energy. The rotor total pressure ratio is imposed with an initial condition, and there is an external iterative calculation together with the outlet part to obtain this rotor total pressure ratio.

6.3.4 Outlet

The final part to model is the outlet. The other rotor outlet velocity triangle components must be assessed for modelling the outlet part. The axial component of the rotor outlet relative velocity is the same as the absolute velocity axial component. The tangential component of the rotor outlet relative velocity can be computed employing the rotor outlet relative velocity and the axial component of the rotor outlet radial velocity, as defined in Eq. 6.58.

$$\frac{w_{4,\theta}^2}{2 \cdot h_{t,0}} = \frac{w_4^2}{2 \cdot h_{t,0}} - \frac{w_{4,ax}^2}{2 \cdot h_{t,0}} \tag{6.58}$$

The tangential component of the rotor outlet absolute velocity is computed with the difference between the tangential component of the rotor outlet relative velocity and the linear velocity of the rotor outlet, as defined in Eq. 6.59. The rotor outlet relative velocity is computed employing both its axial and tangential components, as defined in Eq. 6.60.

$$\frac{c_{4,\theta}^2}{2 \cdot h_{t,0}} = \left(\sqrt{\frac{w_{4,\theta}^2}{2 \cdot h_{t,0}}} - \sqrt{\frac{u_4^2}{2 \cdot h_{t,0}}} \right)^2 \tag{6.59}$$

$$\frac{c_4^2}{2 \cdot h_{t,0}} = \frac{c_{4,\theta}^2}{2 \cdot h_{t,0}} + \frac{c_{4,ax}^2}{2 \cdot h_{t,0}} \tag{6.60}$$

The CFD losses analysis presented in Chapter 5 found three different sources of losses that must be considered in the outlet: sudden expansion losses, mixing losses and losses due to the momentum exchange between flow branches. The enthalpy losses produced by these sources of losses can be added to compute the overall enthalpy losses in the outlet, as defined in Eq. 6.61.

$$\frac{\Delta h_{out}}{h_{t,0}} = \frac{\Delta h_{out,SudExp}}{h_{t,0}} + \frac{\Delta h_{out,mix}}{h_{t,0}} + \frac{\Delta h_{out,ME}}{h_{t,0}} \tag{6.61}$$

The sudden expansion non-dimensional enthalpy losses are modelled with a Borda-Carnot based model, as defined in Eq. 6.62. $Z_{out,SudExp}$ is a fitting parameter that needs to be adjusted, and A_4 and A_5 are the rotor outlet and

turbine outlet areas, respectively. A_4 is computed for each flow branch as explained in the effective area model.

$$\frac{\Delta h_{\text{out,SudExp}}}{h_{\text{t,0}}} = Z_{\text{out,SudExp}} \cdot \frac{c_4^2}{2 \cdot h_{\text{t,0}}} \cdot \left(1 - \frac{A_4}{A_5}\right) \tag{6.62}$$

The mixing non-dimensional enthalpy losses are modelled with the model proposed by Winterbone and Pearson [113], as defined in Eq. 6.63. $Z_{\text{out,mix}}$ is a fitting parameter that needs to be adjusted. P_c is a control parameter whose value is $1 - MFR$ for the hub branch and MFR for the shroud branch. These losses do not affect the cases under partial admission conditions since there is only flow passing through one of the branches.

$$\frac{\Delta h_{\text{out,mix}}}{h_{\text{t,0}}} = Z_{\text{out,mix}} \cdot \frac{c_5^2}{2 \cdot h_{\text{t,0}}} \cdot$$
$$\left(\frac{4 \cdot A_5}{A_5 + \frac{A_4}{P_c}} \cdot \left(1 - \frac{A_5}{A_4} \cdot P_c\right) + \left(\frac{A_5}{A_4} \cdot P_c\right)^2 - 1\right) \tag{6.63}$$

The losses due to the momentum exchange between flow branches are modelled with the same model as the interspace and the rotor. The non-dimensional form of this model for the outlet is formulated in Eq. 6.64. Z_{ME} is the same fitting parameter as for the interspace and the rotor. $L_{\text{out,ME}}$ stands for the outlet contact length between flow branches. Since the region where this source of losses is relevant is small, $L_{\text{out,ME}}$ could be estimated as 2% of the rotor outlet wheel diameter. This percentage has been set as the average of the value measured in all CFD simulations. However, since these losses are not much relevant in the outlet section, the results obtained using a slightly different value such as $1-3\%$ would not change significantly.

These losses do not affect the cases under partial admission conditions since there is only flow passing through one of the branches. Moreover, these losses are computed for the flow branch with the higher mass flow (MFR lower than 0.5 for the hub branch and higher than 0.5 for the shroud branch). The flow branch with lower mass flow gains the energy that the other has lost since the momentum is transmitted from one flow branch to the other.

$$\frac{\Delta h_{\text{out,ME}}}{h_{\text{t,0}}} = Z_{\text{ME}} \cdot L_{\text{out,ME}} \cdot \left(\sqrt{\frac{c_{4,h}^2}{2 \cdot h_{\text{t,0}}}} - \sqrt{\frac{c_{4,sh}^2}{2 \cdot h_{\text{t,0}}}}\right)^2 \tag{6.64}$$

The turbine outlet kinematic conditions must also be assessed. The axial component of the turbine outlet velocity could be computed from the reduced mass flow, as defined in Eq. 6.65. It depends on the total-to-static pressure ratio

between turbine inlet and outlet. The turbine outlet isentropic pressure ratio is defined in Eq. 6.66.

$$\frac{c_{5,ax}^2}{2 \cdot h_{t,0}} = \frac{R^2 \cdot \dot{m}_{red}^2}{A_5^2 \cdot 2 \cdot C_p} \cdot \left(\frac{p_{t,0}}{p_{t,1}} \cdot \frac{p_{t,1}}{p_{t,3}} \cdot \frac{p_{t,3}}{p_{t,4}} \cdot \frac{p_{t,4}}{p_5} \right)^{\frac{\gamma-1}{\gamma}} \tag{6.65}$$

$$\frac{p_{t,4}}{p_5} = \left(\frac{1}{1 - \frac{c_5^2}{2 \cdot h_{t,0}} - \frac{\Delta h_{out}}{h_{t,0}}} \right)^{\frac{\gamma}{\gamma-1}} \tag{6.66}$$

The tangential component of the turbine outlet velocity is computed with the ratio between rotor outlet and turbine outlet mean diameters, as defined in Eq. 6.67. $\bar{D}_5$ is calculated as described in Eq. 6.68. The turbine outlet velocity is computed employing both its axial and tangential components, as defined in Eq. 6.69.

$$\frac{c_{5,\theta}^2}{2 \cdot h_{t,0}} = \frac{c_{4,\theta}^2}{2 \cdot h_{t,0}} \cdot \frac{\bar{D}_4^2}{\bar{D}_5^2} \tag{6.67}$$

$$\bar{D}_5 = \sqrt{\frac{2 \cdot A_5}{\pi}} \tag{6.68}$$

$$\frac{c_5^2}{2 \cdot h_{t,0}} = \frac{c_{5,\theta}^2}{2 \cdot h_{t,0}} + \frac{c_{5,ax}^2}{2 \cdot h_{t,0}} \tag{6.69}$$

The turbine outlet isentropic pressure ratio depends on the turbine outlet kinetic energy. Moreover, the turbine outlet axial kinematic energy defined in Eq. 6.65 depends on the enthalpy losses, and the enthalpy losses depend on the turbine outlet kinematic energy. Therefore, the turbine outlet axial kinetic energy has to be computed iteratively. Brent's method [115] has been chosen again to carry out this iterative computation and obtain the turbine outlet axial kinetic energy.

The turbine outlet pressure ratio obtained after the iterative calculation is employed to re-calculate the rotor total pressure ratio and compute the rotor part again. This iterative procedure is carried out until the error between iterations could be considered admissible.

6.3.5 Efficiency model solving scheme

Once all twin-entry turbine parts have been modelled, the efficiency can be obtained. This model requires the reduced mass flow as an input parameter for adjusting the fitting parameters, which implies that both the effective area and the efficiency models are coupled. Therefore, the solving scheme for computing the efficiency iteratively in each flow branch is illustrated in Fig. 6.12.
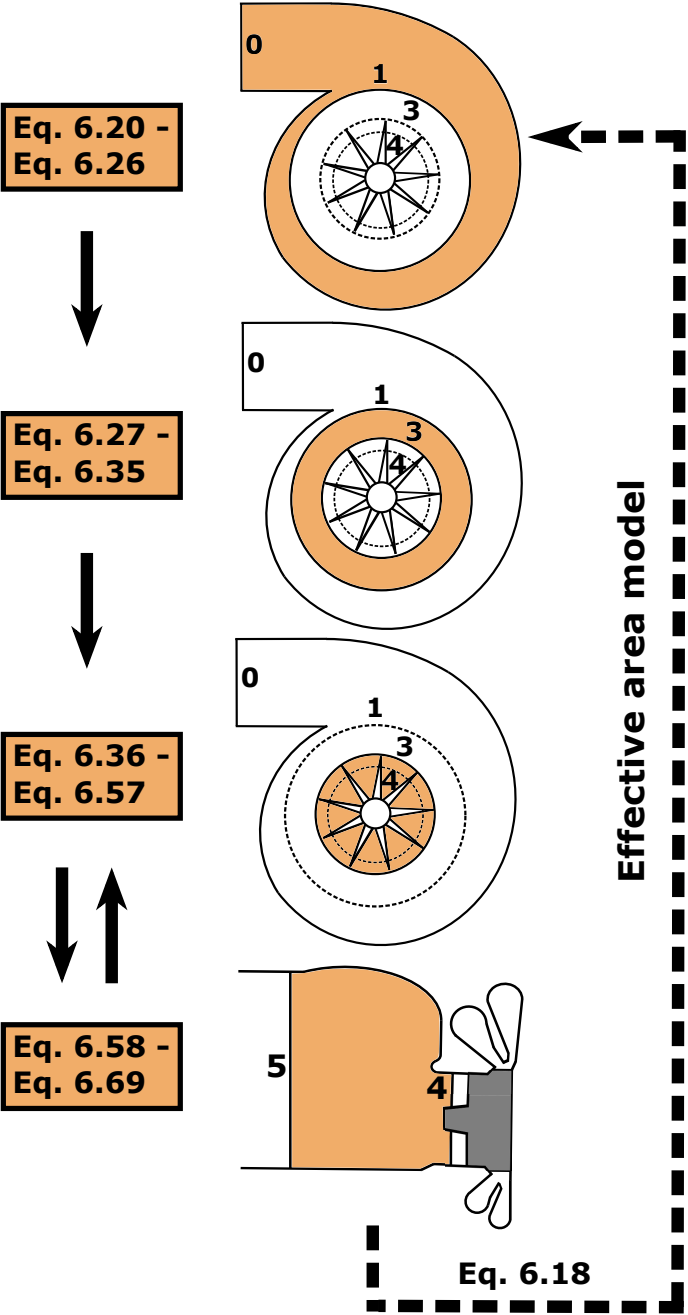
Figure 6.12: Efficiency model solving scheme.

6.3.6 Efficiency model validation

The efficiency model presented has been implemented in the radial turbine model included in the VEMOD code. As explained in the previous subsection, this model and the effective area model are coupled. The effective area model is computed first with the apparent efficiency of the performance maps, and the results are used to compute then the efficiency model

The efficiency model is solved for both branches, and the fitting parameters have been adjusted with a constrained Levenberg-Marquardt non-linear optimisation fitter [114]. This fitter computes first the error produced in the computation of the apparent efficiency of each branch, as defined in Eq. 6.70, where n is the number of operational points computed. Since there are fitting parameters common for both branches, it minimises the combined error calculated with Eq. 6.71. The combined error of Eq. 6.71 has been chosen as cost function as it ensures that not only the error of both branches is minimised, but also that the error is similar in both branches.

$$\epsilon_{\mathrm{app}} = \sqrt{\frac{\Sigma\left(\eta_{\mathrm{app}} - \eta_{\mathrm{Exp}}\right)^2}{n}} \tag{6.70}$$

$$\epsilon = \epsilon_{\mathrm{app,h}} + \epsilon_{\mathrm{app,sh}} + \left|\epsilon_{\mathrm{app,h}} - \epsilon_{\mathrm{app,sh}}\right| \tag{6.71}$$

The efficiency model has been fitted employing the steady-state experimentally measured data presented in Chapter 3. The model requires initial values and upper and lower bounds of each fitting parameter for adjusting them, minimising the error. The fitting parameters obtained in the CFD analysis presented in Chapter 5 are used as initial values. The upper and lower bounds are defined as the range that makes physical sense for each calibration coefficient. The efficiency model fitting parameters adjusted for each flow branch are summed up in Table 6.3.

The incidence losses fitting parameter ($Z_{\mathrm{rot,inc}}$) is common for both flow branches since the blade leading edge is straight and parallel to the rotor inlet section. The tip losses fitting parameters (K^+ and K^-) are also common for both flow branches. As explained in the rotor modelling subsection, the tip losses are produced in the shroud branch. They only affect the hub branch when the *MFR* value is 0. The fitting parameter for the losses due to the momentum exchange between flow branches (Z_{ME}) is common for both branches. Furthermore, it takes up the same value for the interspace, rotor and outlet parts. The contact length between flow branches computed in each part allows considering the difference between these parts. Hence, the efficiency model needs 16 fitting parameters to be adjusted: 4 fitting parameters common for both flow branches and 6 additional fitting parameters adjusted for each flow branch separately.

155

Table 6.3: Efficiency model fitting parameters for each flow branch.

Parameter	Hub Branch	Shroud Branch
Volute		
$Z_{\text{vol,pass}}$	0.080	0.071
Interspace		
$Z_{\text{int,pass}}$	0.089	0.063
$Z_{\text{int,SudExp}}$	0.095	0.105
Rotor		
$Z_{\text{rot,pass}}$	0.122	0.121
$Z_{\text{rot,inc}}$	0.150	
K^+	0.040	
K^-	0.110	
Outlet		
$Z_{\text{out,SudExp}}$	0.005	0.010
$Z_{\text{out,mix}}$	0.007	0.011
Common		
Z_{ME}	0.085	

The apparent efficiency computed with Eq. 6.19 and obtained from the actual efficiency provided by the efficiency model can be compared with the experimentally measured efficiency. Therefore, the quality of the efficiency model can be validated. Fig. 6.13 shows a comparison of the apparent efficiency computed with the efficiency model and the experimentally measured efficiency for each flow branch separately under different *MFR* and reduced rotational speed values. The straight line represents a perfect concordance between the model and experiment, and the dotted lines indicate a discrepancy of ±5 percentage points of efficiency.

The efficiency model adequately reproduces the apparent efficiency of both flow branches. The R^2 value is high in both flow branches, which indicates an excellent correlation between the modelled and measured efficiency. Moreover, the root mean square error (RMSE) of the efficiency model has been computed as a unique value for both flow branches. The RMSE obtained is 0.0680, representing a combined RMSE lower than 7%. This error could be considered low in efficiency terms, and the apparent efficiency provided by the model could be considered reliable.
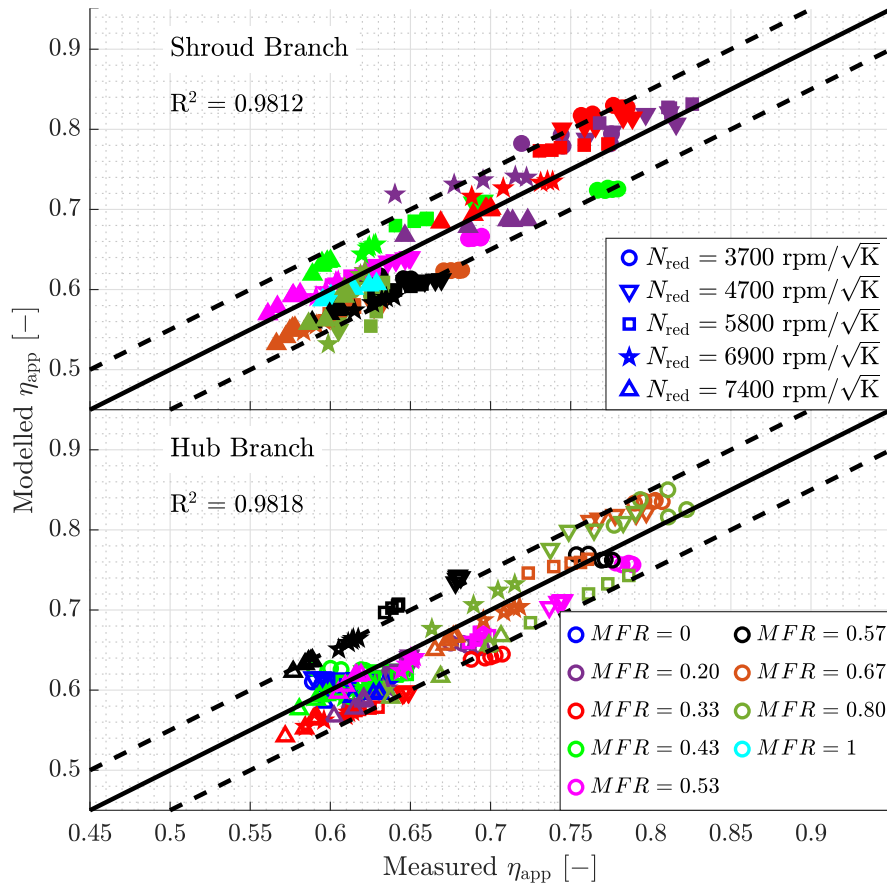
Figure 6.13: Validation of the adjusted efficiency model.

6.4 Adjusting procedure

As mentioned in the previous sections, the effective area and efficiency models are adjusted together since they depend on each other. The procedure followed to adjust the models is shown in Fig. 6.14.

First, the effective area fitting parameters are adjusted for each branch separately, using the apparent efficiency from the performance maps. The model minimises the error computed as defined in Eq. 6.16. Once the fitting parameters of the effective are model are adjusted, the parameters required are introduced into the efficiency model. Then, the efficiency fitting parameters are adjusted, minimising the error as computed with Eq. 6.16 and 6.71. Since the efficiency model has common fitting parameters for both branches, they must be adjusted together.

Once the fitting parameters of the models are adjusted, the reduced mass
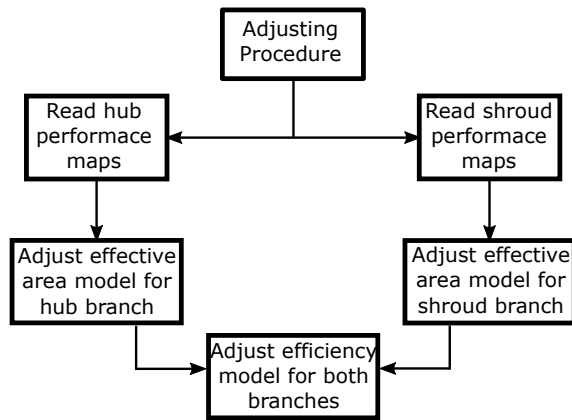
Figure 6.14: Adjusting procedure.

flow rate and efficiency predictions are computed with an iterative calculation of the effective area and the efficiency given the boundary conditions of the operating point, as shown in Fig. 6.15. The apparent efficiency of each branch is computed with Eq. 6.19 from the results of the actual efficiency of both branches.
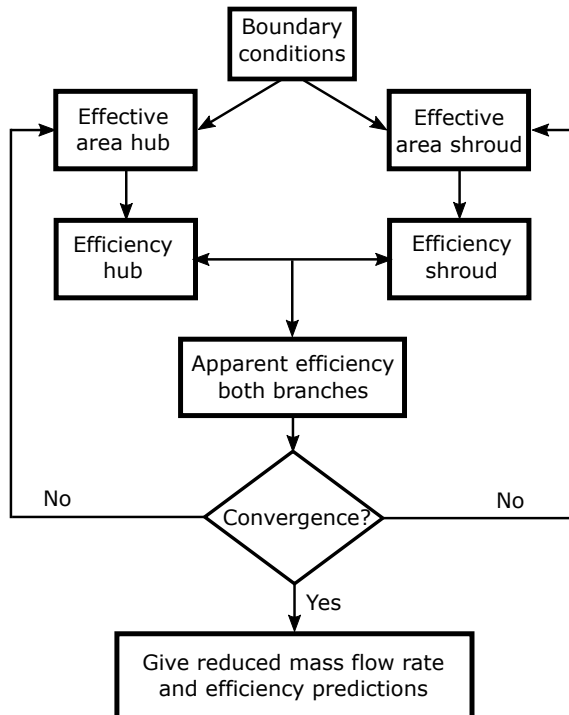
Figure 6.15: Models extrapolation procedure.

6.5 Summary

This chapter presents the effective area and efficiency models developed during the thesis, based on the information obtained from the CFD simulations and the experimental measurements described in Chapter 3 to Chapter 5. These models are employed to extrapolate the flow capacity and the efficiency maps, and they have been implemented in the radial turbine model included in the VEMOD code presented by García-Cuevas [21]. The hypothesis of modelling twin-entry turbines as two separated single entry VGT turbines working in parallel corroborated in Chapter 5 has been employed to develop both models.

6.5.1 Effective area model

The effective area model allows extrapolating of the flow capacity map. It considers each flow branch as a single equivalent nozzle. This equivalent nozzle has an effective area that needs to be modelled. Some geometrical parameters have to be modified for considering the rotor inlet and rotor outlet areas behaviour with the *MFR* value found in Chapter 5. Implementing these modifications, the effective area model only needs 5 parameters to be adjusted with experimental data for each flow branch.

The effective area model has been validated with the steady-state experimental data presented in Chapter 3. The RMSE in both flow branches is lower than the expanded uncertainty of the experimental measurements. Therefore, the effective area model could be considered reliable.

The extrapolation capacity of this model is corroborated in the next chapter using some of the experimental data to feed the model and the other to verify that the extrapolations are accurate.

6.5.2 Efficiency model

The efficiency model allows extrapolating in the efficiency map, and it is coupled with the effective area model. It considers the different sources of losses produced in the volutes, the interspace between volutes and rotor, the rotor and the outlet regions separately. The primary contributors to the twin-entry turbine losses found in Chapter 5 have been modelled with simple models.

The momentum exchange between flow branches is a relevant phenomenon that affects the interspace, the rotor and the outlet regions since the flow branches do not fully mix until the outlet plenum. Other efficiency models have not considered this phenomenon, and it is relevant to predict the flow behaviour under unequal admission conditions appropriately.

The efficiency model has 6 fitting parameters for each flow branch and 4 additional fitting parameters that are common for both flow branches. Thus, the

model needs 16 fitting parameters to be adjusted with experimental data. The model has been validated with the steady-state experimental data presented in Chapter 3, obtaining an acceptable error.

The extrapolation capacity of this model is also corroborated in the next chapter using some of the experimental data to feed the model and the other to verify that the extrapolations are accurate.

6.6 References

[21] L. M. García-Cuevas González. "Experiments and modelling of automotive turbochargers under unsteady conditions". PhD thesis. Universitat Politècnica de València, 2014. DOI: 10.4995/Thesis/10251/48458 (cit. on pp. 4, 129, 159).

[49] J. R. Serrano, F. J. Arnau, L. M. García-Cuevas, V. Samala, and L. Smith. "Experimental approach for the characterization and performance analysis of twin entry radial-inflow turbines in a gas stand and with different flow admission conditions". In: *Applied Thermal Engineering* 159 (2019). DOI: 10.1016/j.applthermaleng.2019.113737 (cit. on pp. 19, 39, 40, 87, 129, 211).

[79] F. Payri, J. R. Serrano, P. Fajardo, M. A. Reyes-Belmonte, and R. Gozalbo-Belles. "A physically based methodology to extrapolate performance maps of radial turbines". In: *Energy Conversion and Management* 55 (Mar. 2012), pp. 149–163. DOI: 10.1016/j.enconman.2011.11.003 (cit. on pp. 21, 23, 131).

[83] M. S. Chiong, S. Rajoo, A. Romagnoli, A. W. Costall, and R. F. Martinez-Botas. "One-dimensional pulse-flow modeling of a twin-scroll turbine". In: *Energy* 115 (Nov. 2016), pp. 1291–1304. DOI: 10.1016/j.energy.2016.09.041 (cit. on pp. 22, 142).

[91] J. R. Serrano, F. J. Arnau, L. M. García-Cuevas, A. Dombrovsky, and H. Tartoussi. "Development and validation of a radial turbine efficiency and mass flow model at design and off-design conditions". In: *Energy Conversion and Management* 128 (2016), pp. 281–293. DOI: 10.1016/j.enconman.2016.09.032 (cit. on pp. 23, 131).

[94] J. R. Serrano, F. J. Arnau, L. M. García-Cuevas, and L. B. Inhestern. "An innovative losses model for efficiency map fitting of vaneless and variable vaned radial turbines extrapolating towards extreme off-design conditions". In: *Energy* 180 (2019), pp. 626–639. DOI: 10.1016/j.energy.2019.05.062 (cit. on pp. 24, 27, 139, 210).

[109] S. Futral, C. Wasserbauer, A. USN, and S. Administration. *Off-design performance prediction with experimental verification for a radial-inflow turbine*. Tech. rep. NASA TN D-2621, 1965. URL: http://books.google.es/books?id=N1kzLAHfK-IC (cit. on pp. 96, 100, 109, 142).

[110] H. Chen and N. C. Baines. "The aerodynamic loading of radial and mixed-flow turbines". In: *International Journal of Mechanical Sciences* 36 (1994), pp. 63–79. DOI: 10.1016/0020-7403(94)90007-8 (cit. on pp. 109, 110, 147).

[111] J. R. Serrano, R. Navarro, L. M. García-Cuevas, and L. B. Inhestern. "Turbocharger turbine rotor tip leakage loss and mass flow model valid up to extreme off-design conditions with high blade to jet speed ratio". In: *Energy* 147 (Mar. 2018), pp. 1299–1310. DOI: 10.1016/j.energy.2018.01.083 (cit. on pp. 111, 147, 148).

[112] J. R. Serrano, R. Navarro, L. M. García-Cuevas, and L. B. Inhestern. "Contribution to tip leakage loss modeling in radial turbines based on 3D flow analysis and 1D characterization". In: *International Journal of Heat and Fluid Flow* 78 (2019). DOI: 10.1016/j.ijheatfluidflow.2019.108423 (cit. on pp. 111, 147).

[113] D. E. Winterbone and R. J. Pearson. *Theory of engine manifold design: wave action methods for IC engines*. Ed. by P. E. Pub. Professional Engineering Pub., 2000. ISBN: 978-1-86058-209-7 (cit. on pp. 119, 152).

[114] C. Kanzow, N. Yamashita, and M. Fukushima. "Levenberg–Marquardt methods with strong local convergence properties for solving nonlinear equations with convex constraints". In: *Journal of Computational and Applied Mathematics* 172.2 (Dec. 2004), pp. 375–397. DOI: 10.1016/j.cam.2004.02.013 (cit. on pp. 137, 155).

[115] R. P. Brent. "An algorithm with guaranteed convergence for finding a zero of a function". In: *The Computer Journal* 14.4 (Apr. 1971), pp. 422–425. DOI: 10.1093/comjnl/14.4.422 (cit. on pp. 143, 145, 151, 153, 212).

Results

Contents

Figures

Tables

7.1 Introduction

THE flow behaviour in twin-entry turbines has been analysed both experimentally and computationally under unequal admission conditions in Chapter 3 to Chapter 5. The information extracted from those analyses has been used to develop an effective area model and an efficiency model in Chapter 6. Since these models are based on the phenomena observed under unequal admission conditions, they are expected to provide suitable extrapolations towards these admission conditions.

This chapter presents the extrapolation capacity of the models developed and validated in Chapter 6. The effective area model extrapolates towards other mass flow admission conditions in the flow capacity map. The efficiency model extrapolates towards other mass flow admission conditions in the efficiency map. Then, the predictions of these models are compared to the predictions of an empirical and a commercial model to corroborate its benefits.

Additionally, the same flow analysis carried out in the previous chapters and the models developed in Chapter 6 are applied to a different geometry to corroborate their validity independently of the twin-entry turbine geometry.

7.2 Flow capacity map extrapolation

There is available a considerable number of experimental measurements under different admission conditions. All these data have been employed to adjust the calibration coefficients and validate the model in the previous chapter. Nevertheless, the maps typically provided by the manufacturer are limited. Thus, the model could be fed with only some of the experimental measurements to examine if the model is capable of extrapolating in the flow capacity map. The data not used to feed the model could be employed to check the robustness of the flow capacity map extrapolation toward other *MFR* values.

The experimental data at *MFR* values of 0, 0.43, 0.57 and 1 and all the reduced rotational speeds have been utilised to feed the model. The most common maps usually provided by the manufacturers are at partial and full admission conditions. So, the *MFR* selected to feed the model are those at partial admission conditions and two *MFR* near full admission conditions. The flow capacity map extrapolation obtained is shown in figures 7.1 - 7.5 for each measured reduced rotational speed, respectively. These figures are divided into two sub-figures showing the extrapolation for each flow branch separately. The lines represent the extrapolation provided by the model. The circles with the black face represent the measured working points employed for the fitting. The squares with the white face represent the measured working points not employed for the fitting.
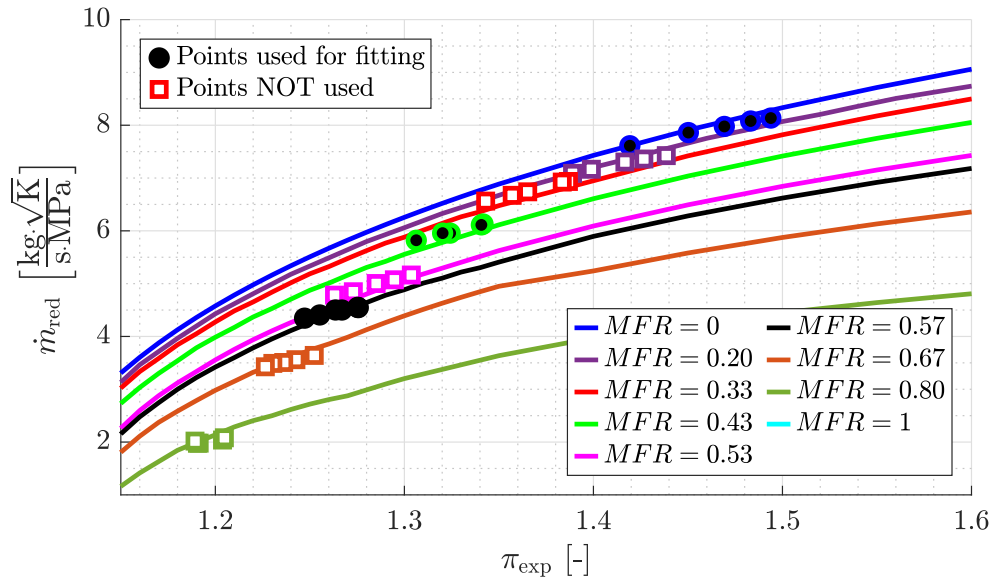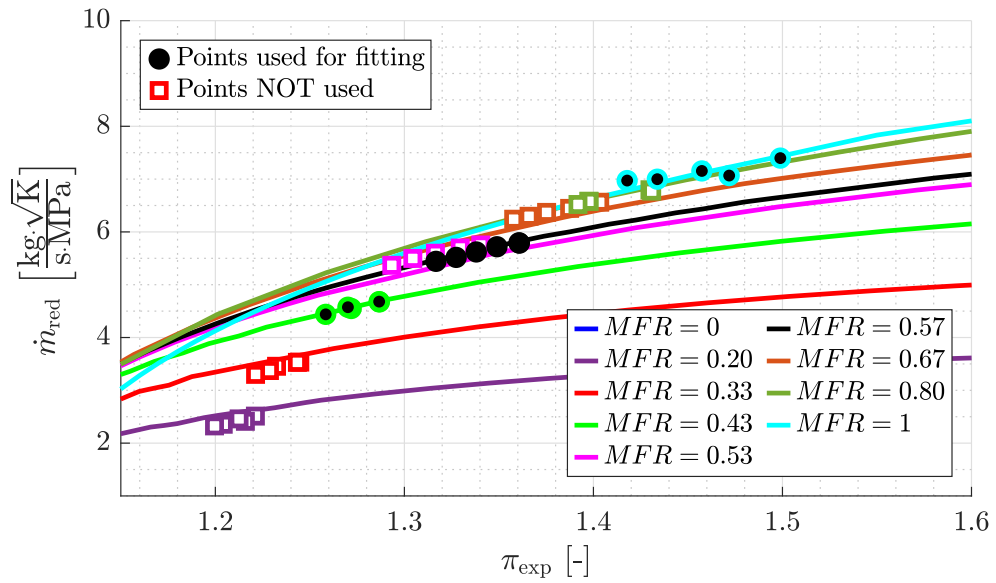
(a) Hub branch

(b) Shroud branch

Figure 7.1: Flow capacity extrapolation map at reduced rotational speed $3700\,\mathrm{rpm\,K^{-0.5}}$.
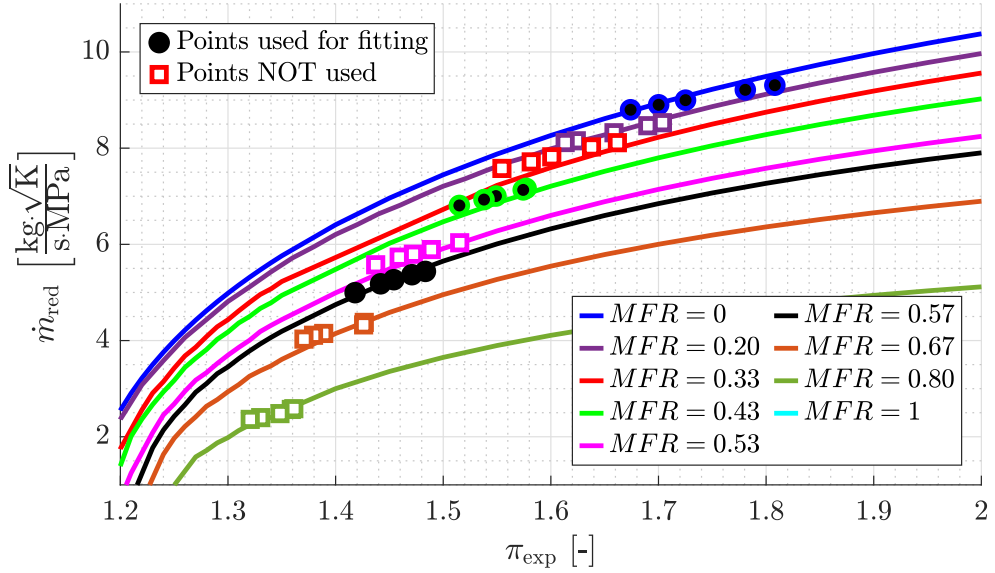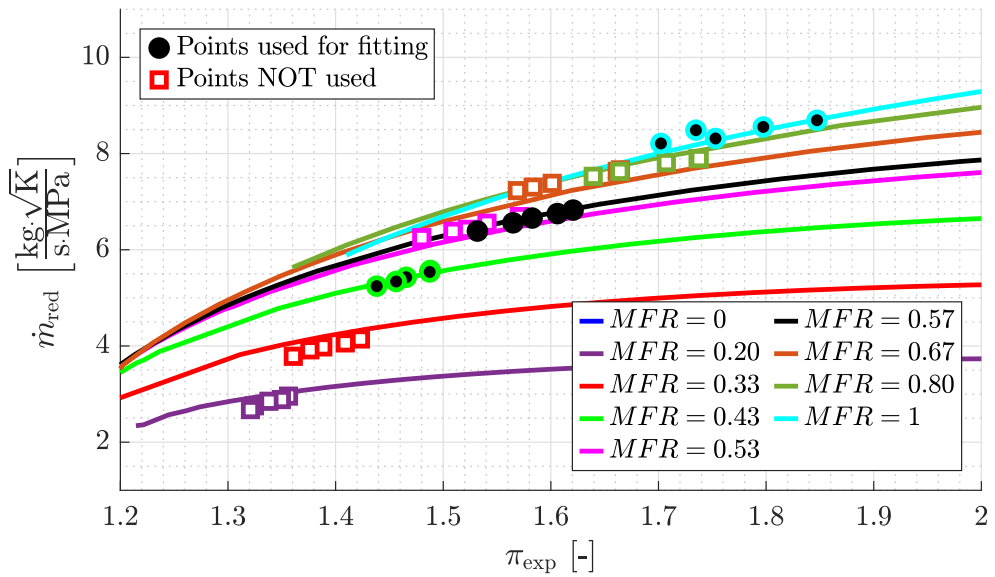
(a) Hub branch

(b) Shroud branch

Figure 7.2: Flow capacity extrapolation map at reduced rotational speed $4700\,\mathrm{rpm\,K^{-0.5}}$.
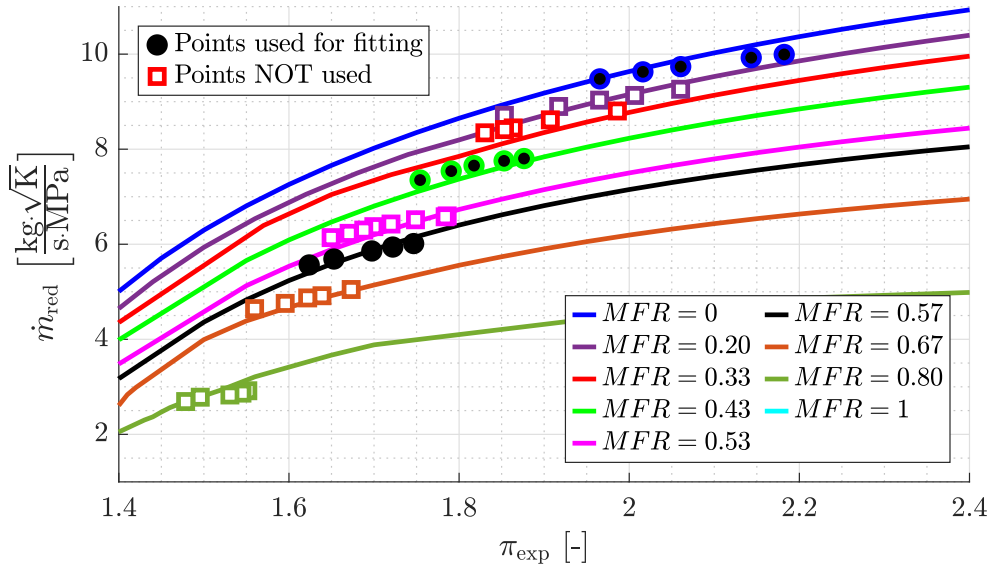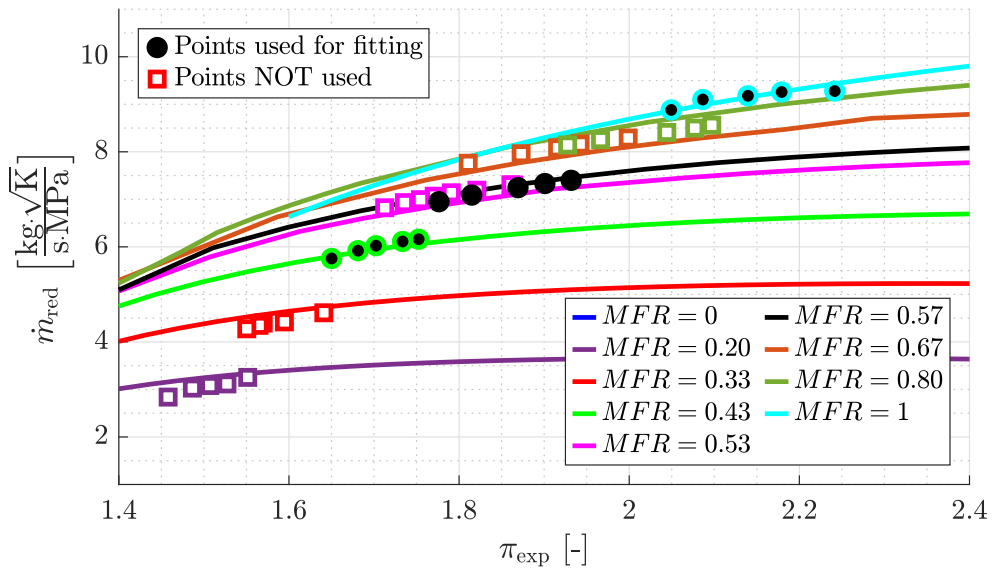
(a) Hub branch

(b) Shroud branch

Figure 7.3: Flow capacity extrapolation map at reduced rotational speed $5800\,\mathrm{rpm}\,\mathrm{K}^{-0.5}$.

(a) Hub branch
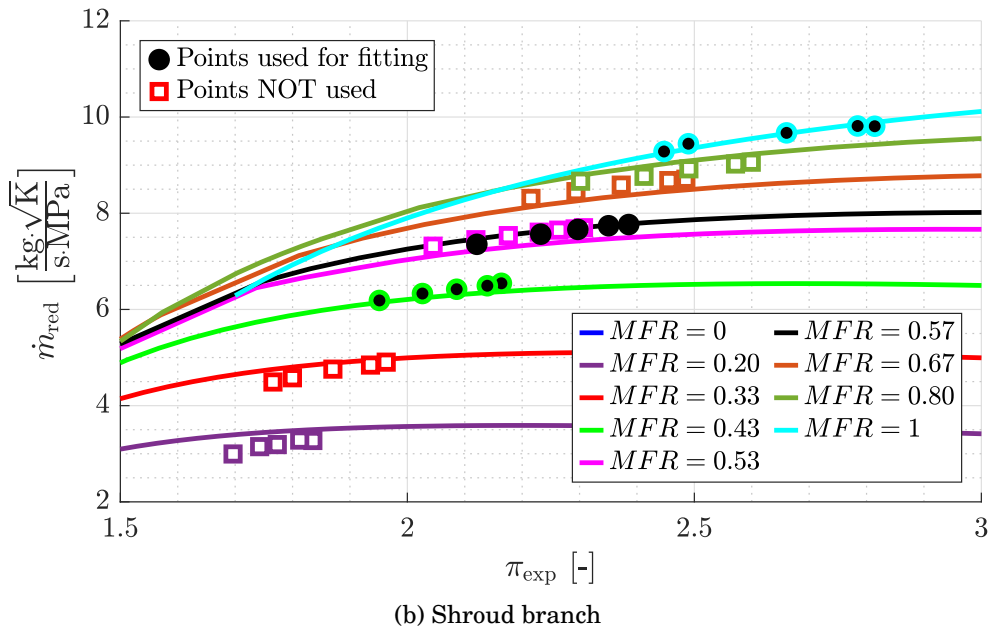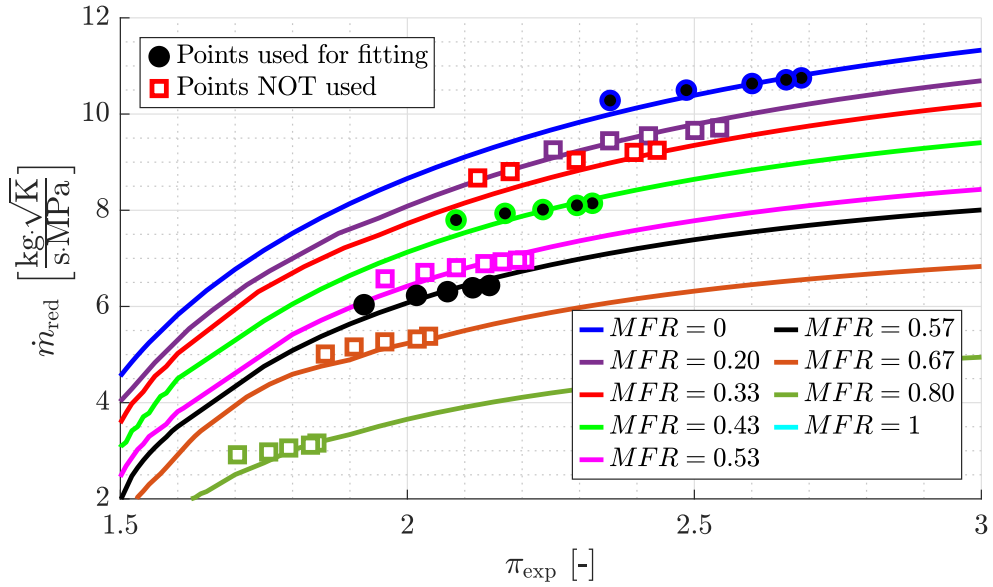
(b) Shroud branch

Figure 7.4: Flow capacity extrapolation map at reduced rotational speed $6900\,\mathrm{rpm\,K^{-0.5}}$.
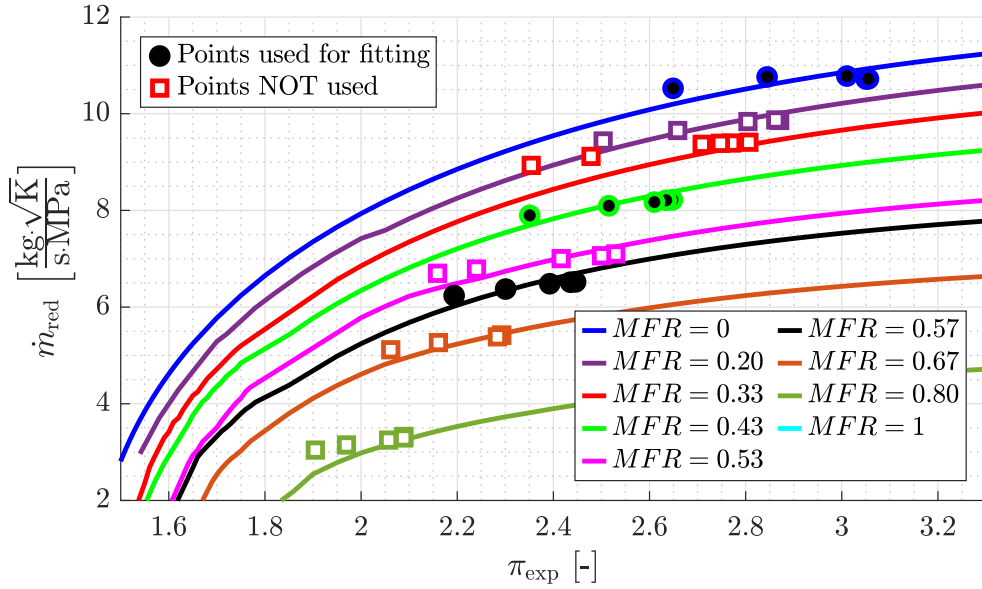
(a) Hub branch
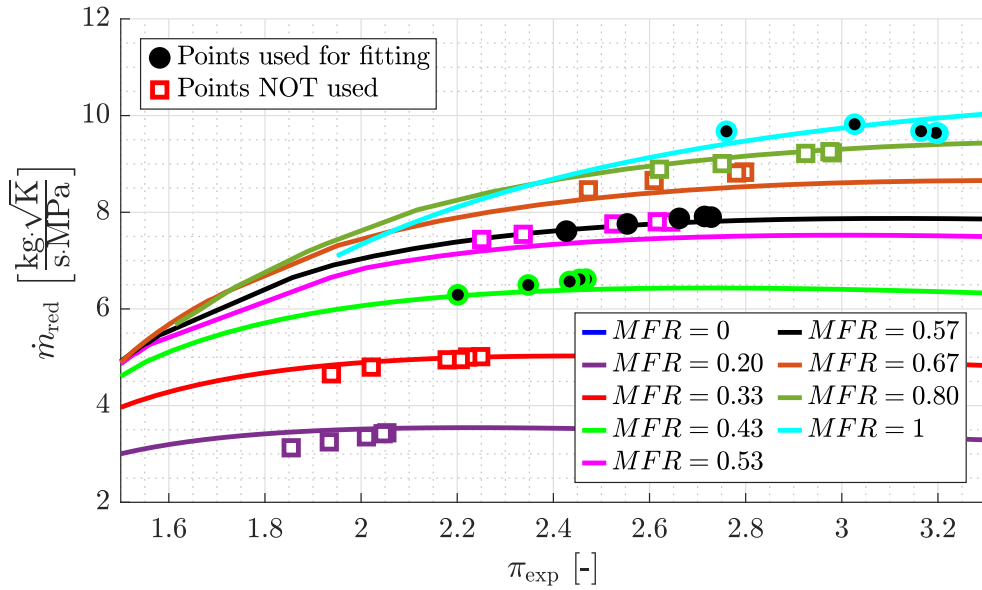
(b) Shroud branch

Figure 7.5: Flow capacity extrapolation map at reduced rotational speed $7400\,\mathrm{rpm\,K^{-0.5}}$.

The modelled reduced mass flow at *MFR* values near the ones used to fit the model is practically coincident with the measured reduced mass flow in all reduced rotational speeds and both flow branches. Since the *MFR* values employed to fit the model are 0, 0.43, 0.57 and 1, these *MFR* values and those near them are expected to be predicted appropriately.

The modelled reduced mass flow rate at *MFR* values further from the values employed for the fitting could also be considered reasonable since it is always lower than 4%, a value close to the expanded uncertainty of the experimental data. *MFR* values such as 0.2 for the shroud branch or 0.8 for the hub branch are captured adequately.

Therefore, the effective area model based on the information extracted from the mass flow CFD analysis and the experimental data measured offers appropriate estimations of the reduced mass flow in twin-entry turbines. Moreover, it can extrapolate toward other *MFR* values with a reasonable error at different reduced rotational speeds and for both flow branches.

The accuracy of these extrapolations can be assessed plotting the error committed. The reduced mass flow rate predictions given by the model can be compared to the data not used to feed the model with the same boundary conditions. The error in terms of percentage is plot against *MFR* for different reduced rotational speeds and for both branches in Fig. 7.6.

The error committed in most extrapolated points is lower than 3%, which is lower than the expanded uncertainty of the steady-state measurements and similar to the results obtained in the CFD simulations. Therefore, the reduced mass flow rate predictions provided by the model could be considered reliable.

A similar study has been carry out but using different *MFR* values to feed the model. In this case, *MFR* 0.33, 0.53 and 0.67 are used. Fig. 7.7(a) and 7.7(b) show the extrapolation at reduced rotational speed of $4700 \, \mathrm{rpm \, K^{-0.5}}$ for the hub and shroud branches, respectively.

Although maps under unequal admission conditions such as *MFR* 0.33 or 0.67 are not usually provided by the manufacturers, the extrapolation capacity towards extreme *MFR* values can be evaluated with this study.

The most noticeable discrepancy between this extrapolation and that carried out before is the model now produces higher error at partial admission conditions. These *MFR* values are the furthest from those employed to fit the model in this case, and they are expected to be the worst captured. Nevertheless, the model and experiment discrepancies could still be considered small since it is always lower than 5%.

The reduced mass flow rate extrapolations under extreme unequal admission conditions such as *MFR* 0.2 or 0.8 are captured accurately with a reasonable error in Fig. 7.7 despite the fact that partial admission conditions are not used to feed the model.

172
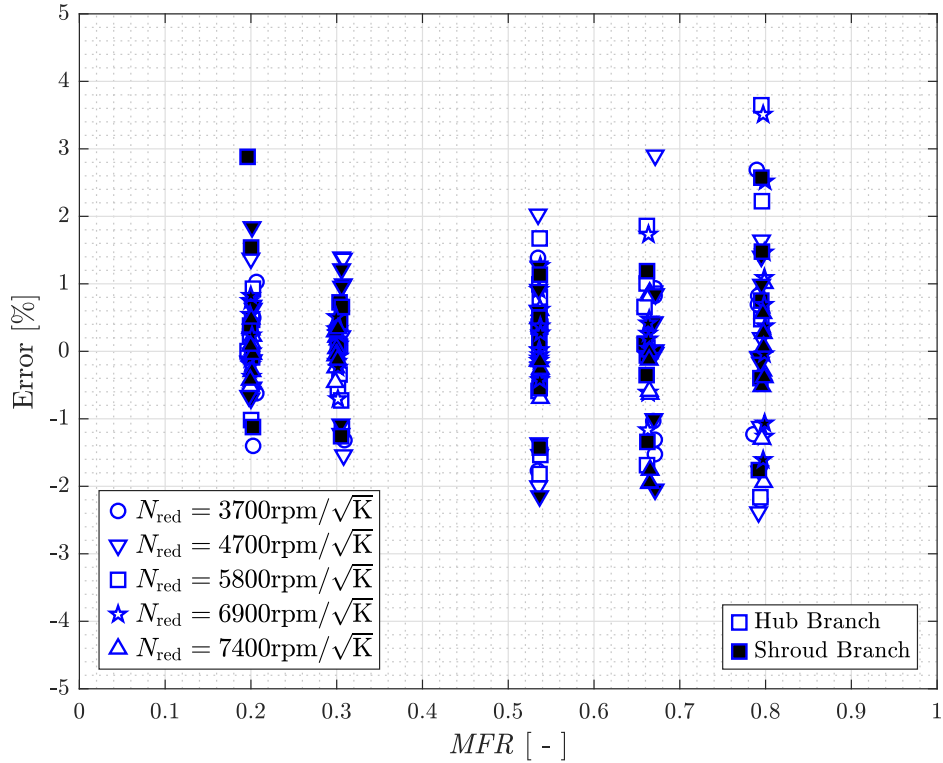
Figure 7.6: Error committed in the reduced mass flow rate extrapolations.

The modelled reduced mass flow rate using *MFR* values of 0, 0.43, 0.57 and 1 is plotted again in figures 7.8 - 7.11, but these figures show a unique *MFR* value under different reduced rotational speeds. Thus, the effect of the reduced rotational speed can be evaluated more thoroughly.

Figures 7.8 - 7.11 show that the speedlines are more separated at the hub branch than at the shroud branch for all *MFR* values. This difference is due to the effective outlet radius of each branch. The hub branch always have a smaller effective outlet radius than the shroud branch. Since the shroud branch effective outlet radius is closer to the rotor inlet radius than the hub branch effective outlet radius, the behaviour of the shroud branch is more similar to an axial turbine. Moreover, the shroud branch speedlines collapse when the *MFR* decreases. As explained in Chapter 6, the effective outlet radius changes with *MFR*, increasing the shroud branch effective outlet radius when the *MFR* decreases. Therefore, the shroud branch behaviour is expected to be more similar to an axial turbine when the *MFR* is decreased.

The hub branch speedlines have the same behaviour against the *MFR* since its effective outlet radius also increases when the *MFR* decreases. However,

173
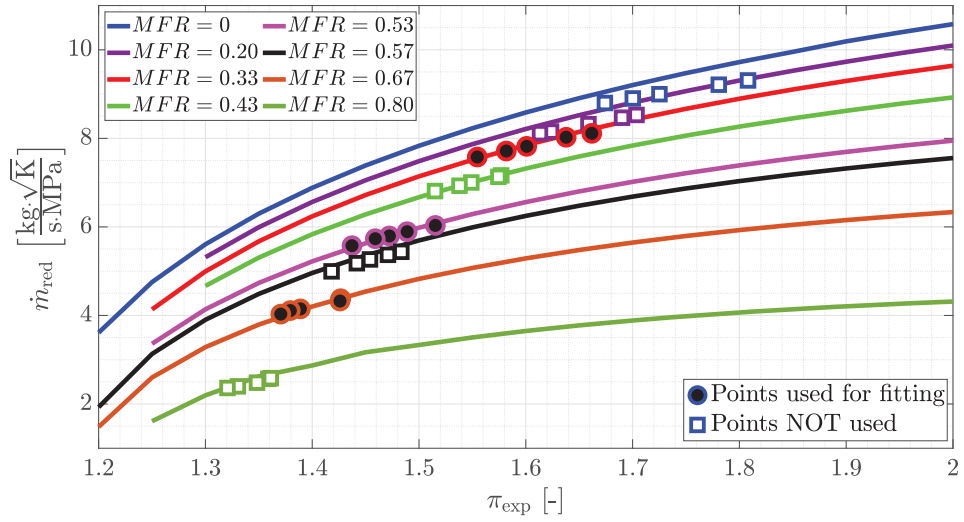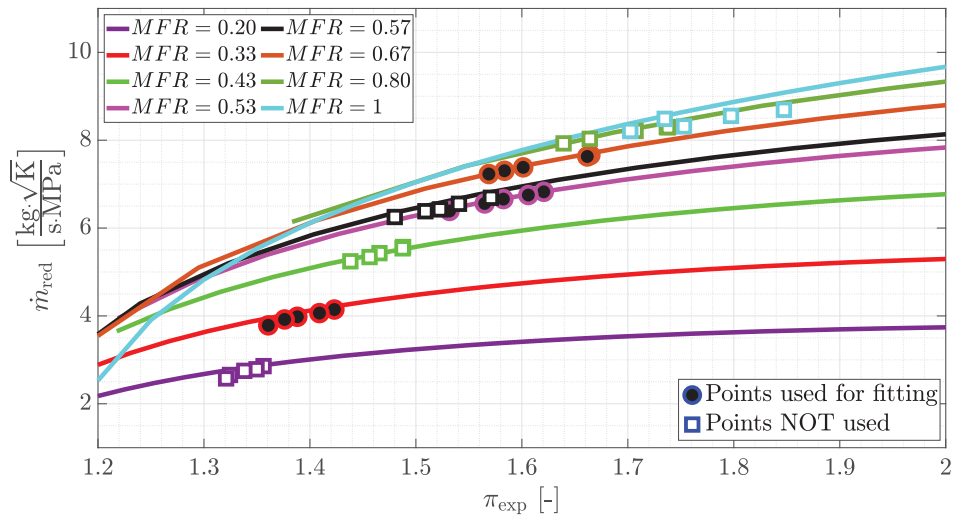
(a) Hub branch

(b) Shroud branch

Figure 7.7: Flow capacity extrapolation map using different *MFR* to feed the model.

(a) Hub branch
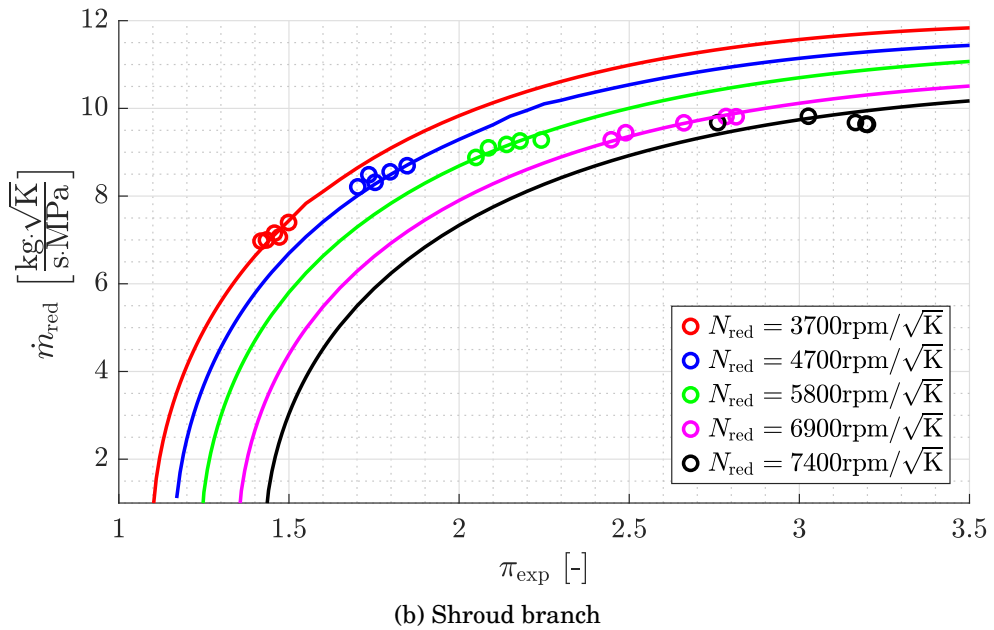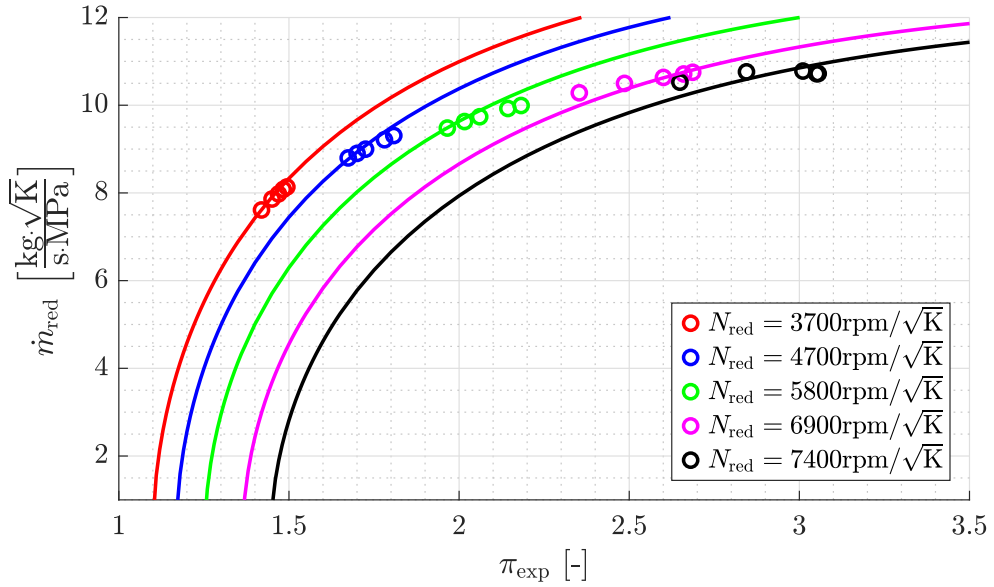
(b) Shroud branch

Figure 7.8: Reduced mass flow rate extrapolation map at *MFR* 0 for the hub branch and 1 for the shroud branch.
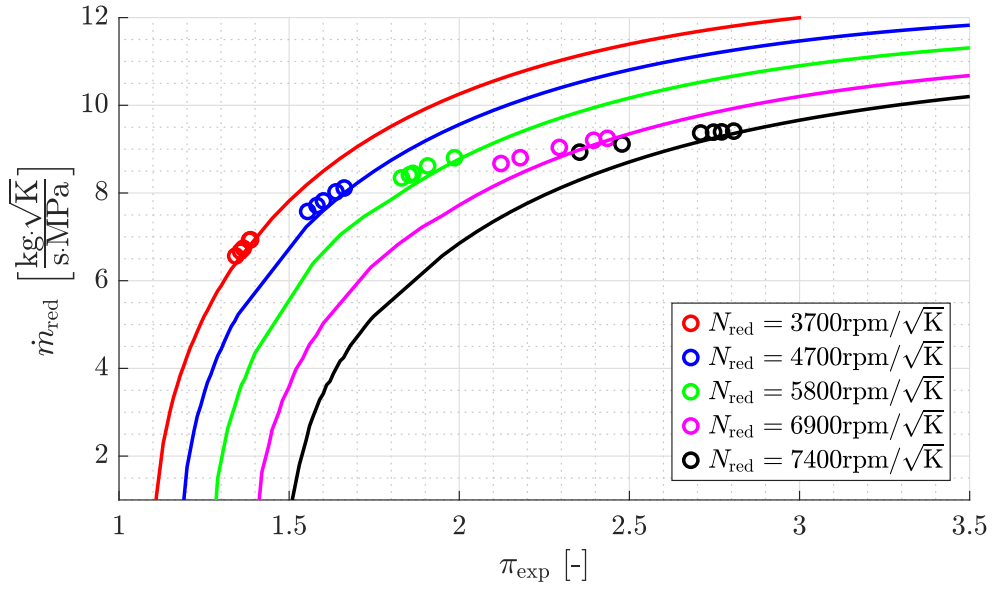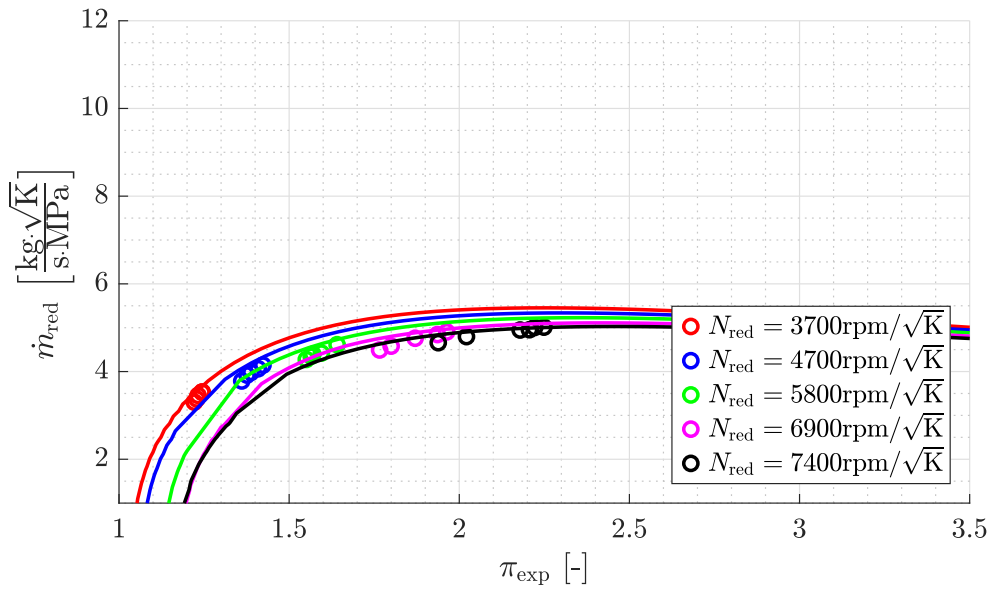
(a) Hub branch

(b) Shroud branch

Figure 7.9: Reduced mass flow rate extrapolation map at *MFR* 0.33.
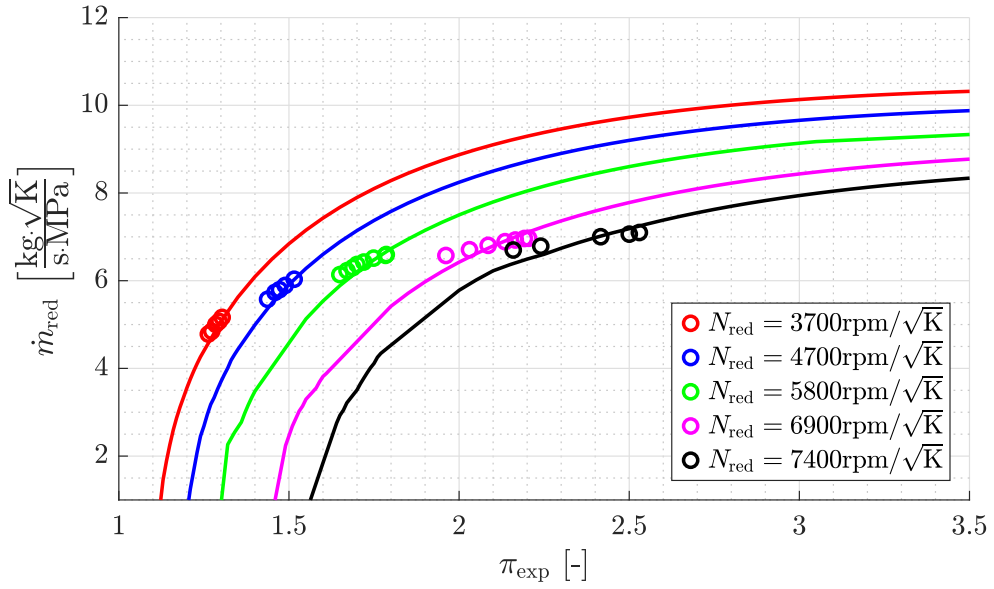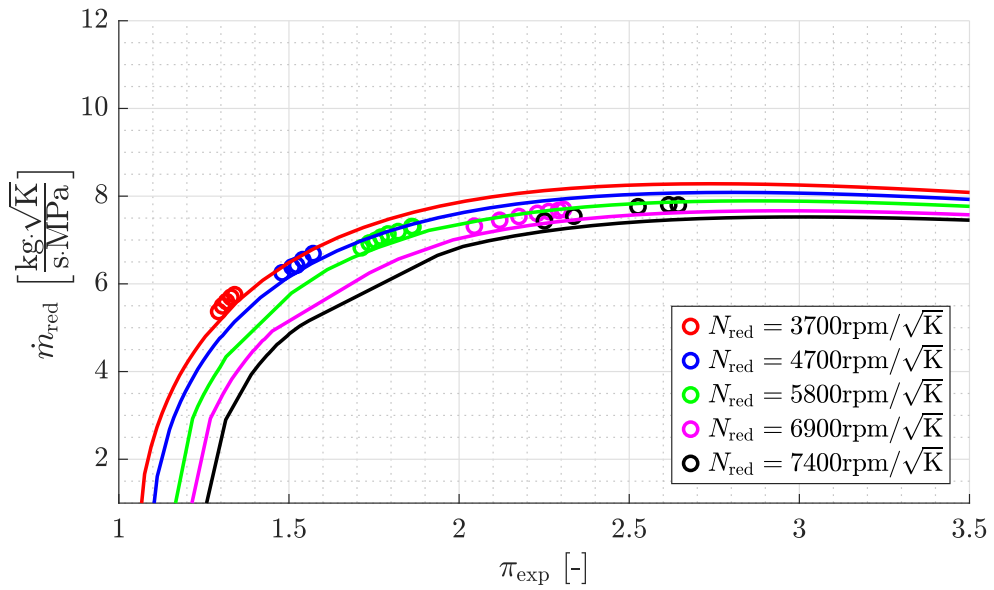
(a) Hub branch

(b) Shroud branch

Figure 7.10: Reduced mass flow rate extrapolation map at *MFR* 0.53.

(a) Hub branch
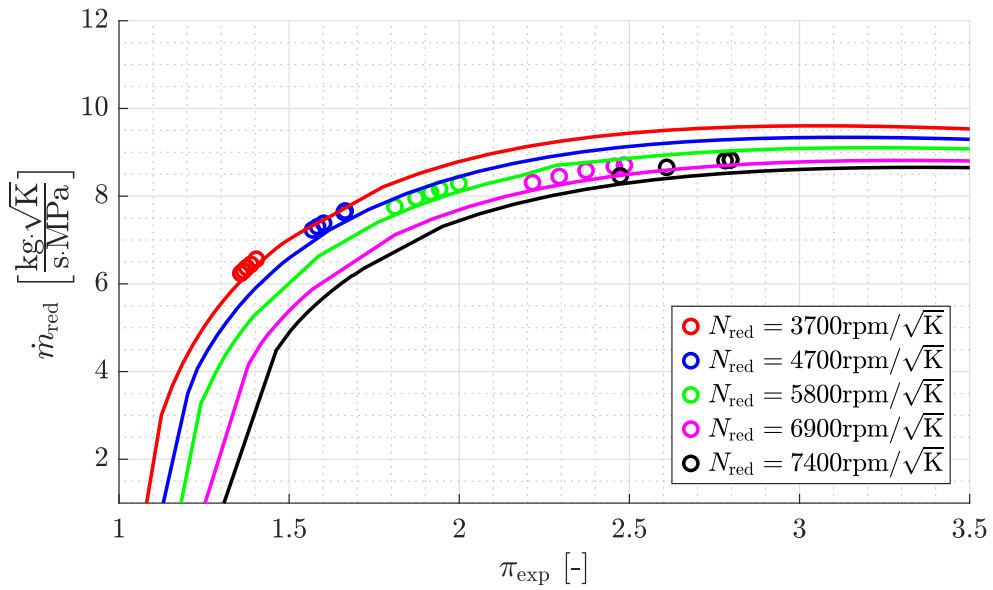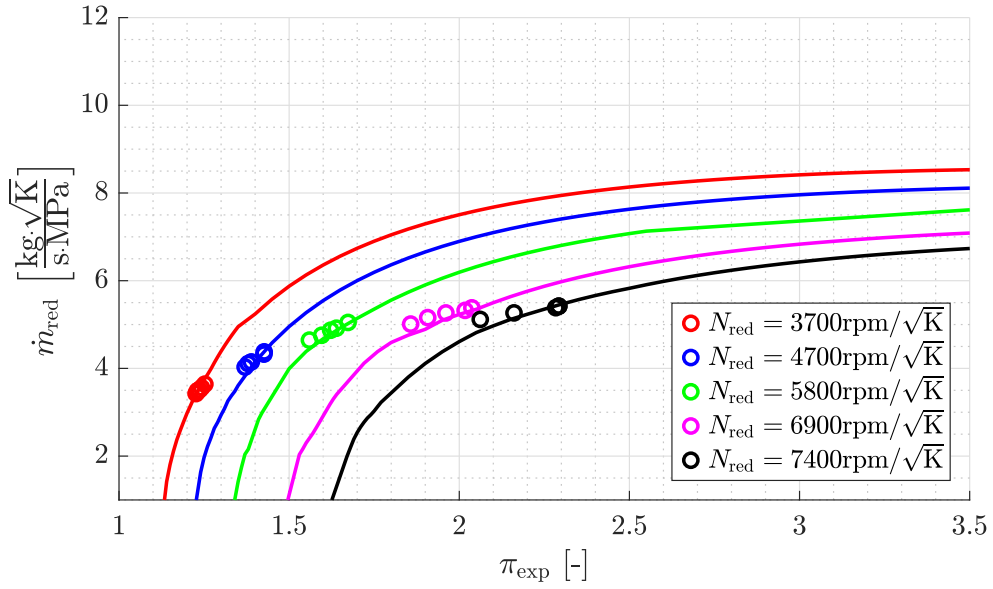
(b) Shroud branch

Figure 7.11: Reduced mass flow rate extrapolation map at *MFR* 0.67.

the maximum hub branch effective outlet radius (at *MFR* 0) is the same than the minimum shroud branch effective outlet radius (at *MFR* 1). Therefore, this effect cannot be appreciated as well as in the shroud branch.

7.3 Efficiency map extrapolation

There is available a considerable number of experimental measurements under different admission conditions. All these data have been employed to adjust the calibration coefficients and validate the model in the previous chapter. Nevertheless, the maps typically provided by the manufacturer is limited. Thus, the model could be fed with only some of this experimental measurements to examine if the model is capable of extrapolating in the efficiency map. The data not used to feed the model could be employed to check the robustness of the efficiency map extrapolation toward other *MFR* values.

The experimental data at *MFR* values of 0, 0.43, 0.57 and 1 and all the reduced rotational speeds has been utilised to feed the model. The apparent efficiency map extrapolation versus the blade speed ratio (σ) is shown in figures 7.12 - 7.15 for each measured reduced rotational speed, respectively. These figures are divided into two sub-figures showing the extrapolation for each flow branch separately. The lines represent the extrapolation provided by the model. The circles with the black face represent the measured working points employed for the fitting. The squares with the white face represent the measured working points not employed for the fitting.

The apparent efficiency increases with *MFR* for the hub branch and decreases for the shroud branch under all reduced rotational speed conditions. Thus, the apparent efficiency is inversely proportional to the mass flow rate passing through the correspondent flow branch. As pointed out in Chapter 5, the momentum exchange between flow branches helps explain this efficiency behaviour under unequal admission conditions. The flow branch with a higher mass flow rate transmits some of its momentum to the flow branch with a lower mass flow rate. Therefore, the flow branch with the higher mass flow rate will have losses due to this momentum exchange that decrease the apparent efficiency, and the flow branch with the lower mass flow rate will have gains due to this momentum exchange that increase the apparent efficiency.

The maximum apparent efficiency under the same reduced rotational speed is obtained at a higher blade speed ratio when *MFR* increases for the hub branch and when *MFR* decreases for the shroud branch.

The modelled apparent efficiency at intermediate *MFR* values is practically coincident with the measured apparent efficiency in all reduced rotational speeds and both flow branches. The modelled apparent efficiency at *MFR* values further from the values employed for the fitting could also be considered reasonable.
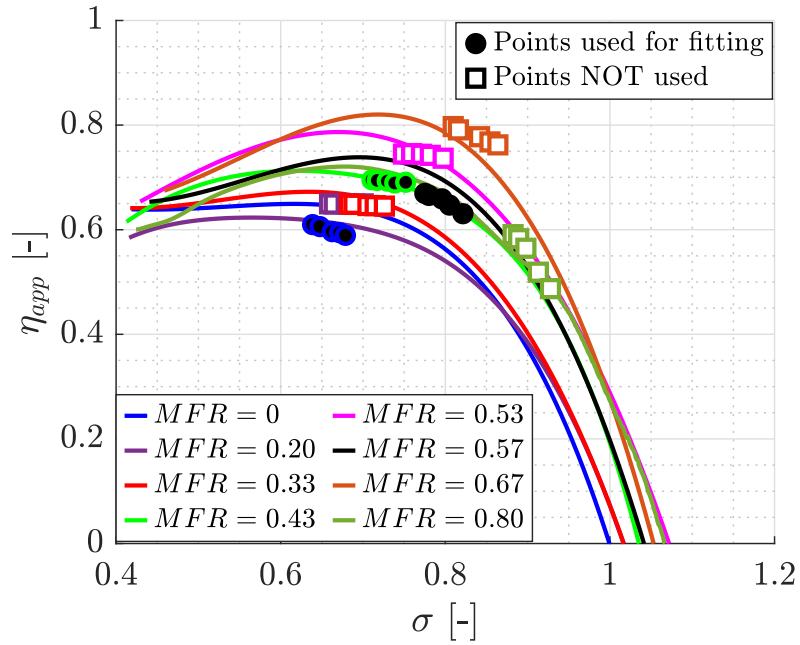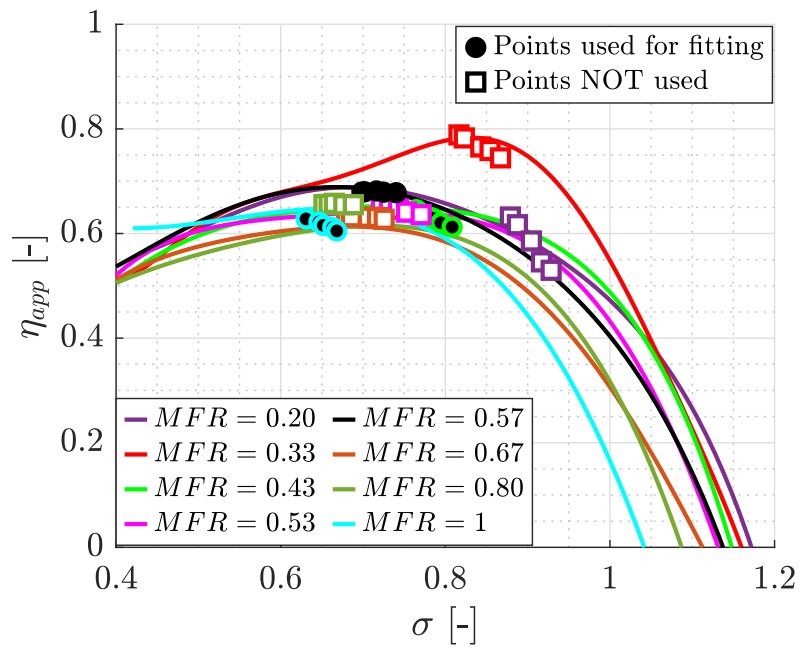
(a) Hub branch

(b) Shroud branch

Figure 7.12: Apparent efficiency extrapolation map at reduced rotational speed $4700\,\mathrm{rpm\,K^{-0.5}}$.
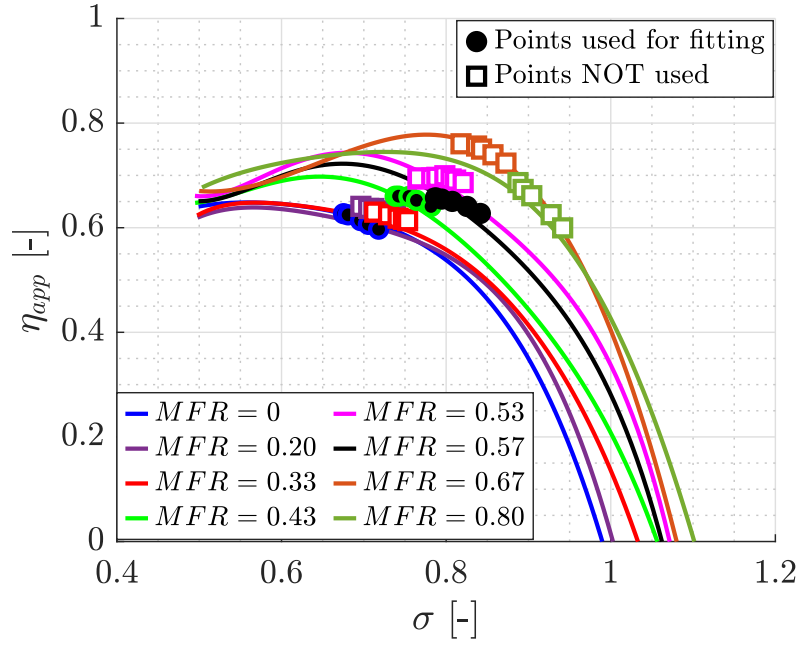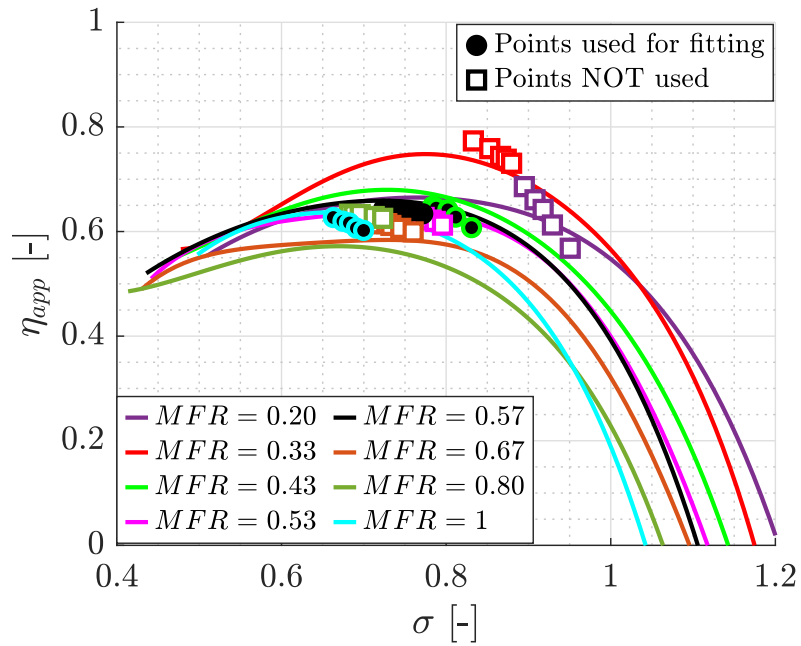
(a) Hub branch

(b) Shroud branch

Figure 7.13: Apparent efficiency extrapolation map at reduced rotational speed $5800\,\mathrm{rpm\,K^{-0.5}}$.
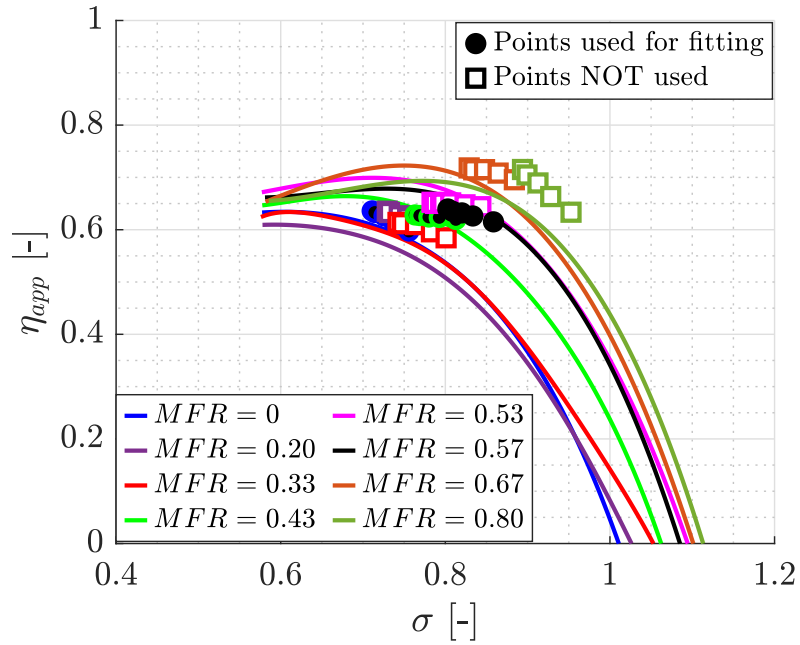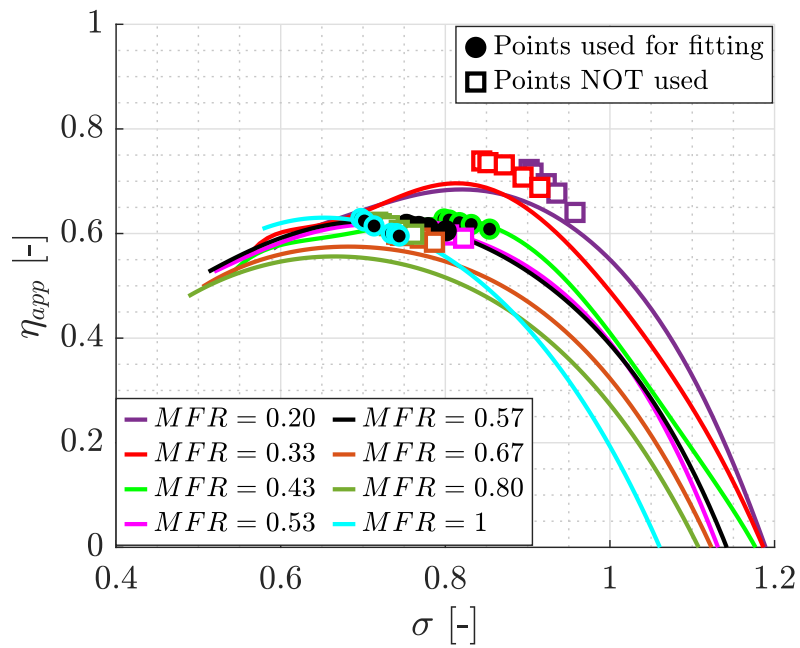
(a) Hub branch

(b) Shroud branch

Figure 7.14: Apparent efficiency extrapolation map at reduced rotational speed $6900\,\mathrm{rpm\,K^{-0.5}}$.
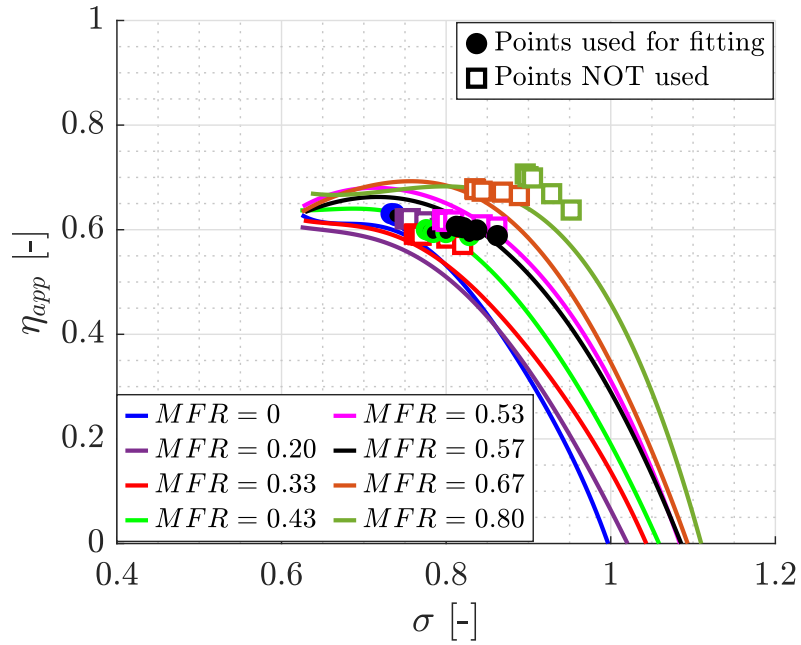
(a) Hub branch
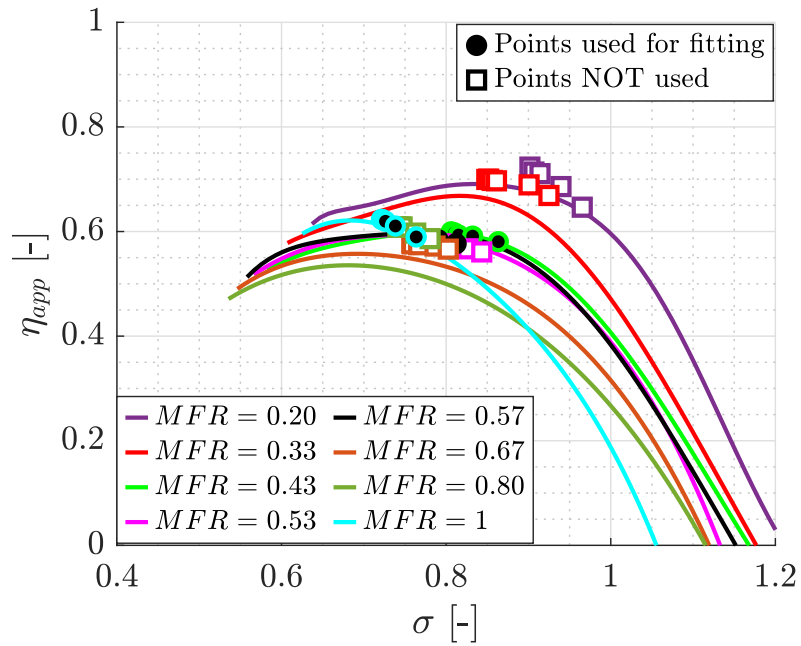
(b) Shroud branch

Figure 7.15: Apparent efficiency extrapolation map at reduced rotational speed $7400 \, \text{rpm} \, \text{K}^{-0.5}$.

The most noticeable discrepancies between the model and the experiments can be observed at extreme unequal admission conditions such as 0.2 or 0.8. These *MFR* values are the furthest from those employed for the fitting, and they are expected to be the worst captured. Nevertheless, the model and experiment discrepancies could still be considered small since it is lower than 0.05 efficiency points.

The apparent efficiency trends seem to be captured appropriately for all *MFR* values and reduced rotational speeds. Therefore, the apparent efficiency predictions provided by the model could be considered reasonable for all *MFR* and reduced rotational speed conditions, whether they are employed to fit the model or not.

The same modelled apparent efficiency is plotted in figures 7.16 - 7.19, but they show a unique *MFR* value under different reduced rotational speeds. Thus, the effect of the reduced rotational speed can be evaluated more thoroughly.

An increase of *MFR* for the hub branch and a decrease for the shroud branch lead to wider speedlines at their peak. The speedlines under partial admission conditions (Fig. 7.16) are remarkably close. The speedlines become more spread when the mass flow rate of the correspondent flow branch is decreased. Therefore, the apparent efficiency variability with the reduced rotational speed is higher when there is low mass flow through the correspondent flow branch and lower when there is higher mass flow through the correspondent flow branch.

Despite the efficiency that can be measured is the apparent efficiency, it is equally relevant to obtain the actual efficiency extrapolation maps. Figures 7.20 - 7.23 show the actual efficiency extrapolation maps employing the same data to fit the map as for the apparent efficiency extrapolation. Although there is no experimental data to compare the predictions, the trends against *MFR* and reduced rotational speed can be analysed.

The actual efficiency trends against the reduced rotational speed and *MFR* are similar to the trends of the apparent efficiency. However, there is a more noticeable difference between the actual efficiency under *MFR* values where there is more mass flow passing through the correspondent flow branch and the actual efficiency under *MFR* values where there is less mass flow passing through the correspondent flow branch. The primary contributors to these differences are the momentum exchange between flow branches and the sudden expansion produced downstream of the junction of the volutes.

The actual efficiency under unequal admission conditions can become lower than under partial admission conditions at low blade speed ratios. In these cases, the momentum difference between flow branches is high and could induce higher losses on the flow branch with higher momentum due to the momentum exchange with the other flow branch. These losses do not exist under partial admission conditions. Therefore, they have a slightly higher actual efficiency at

(a) Hub branch
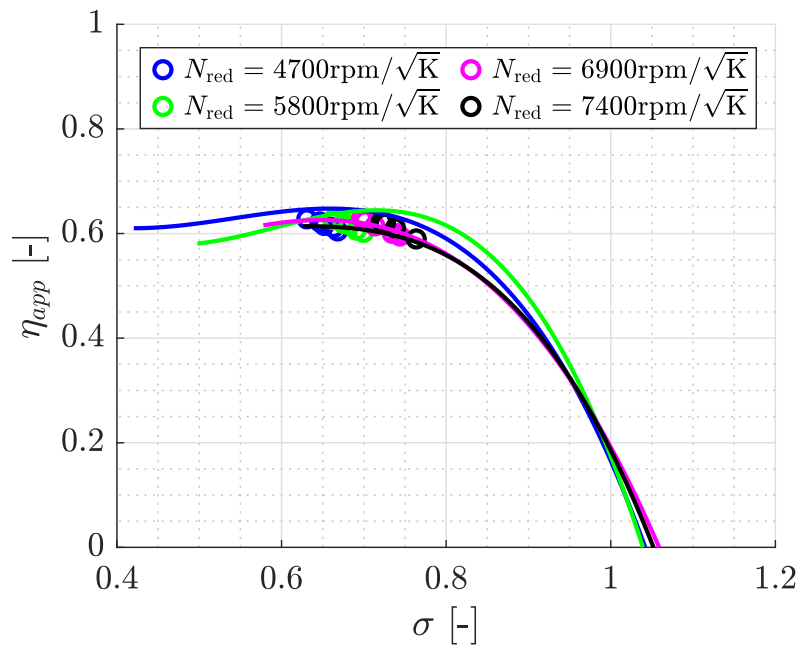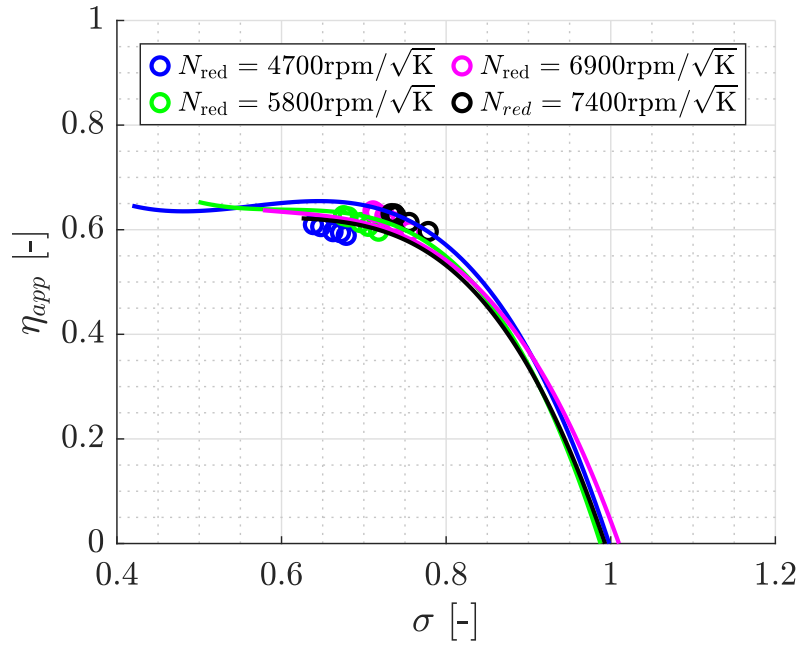
(b) Shroud branch

Figure 7.16: Apparent efficiency extrapolation map at *MFR* 0 for the hub branch and 1 for the shroud branch.
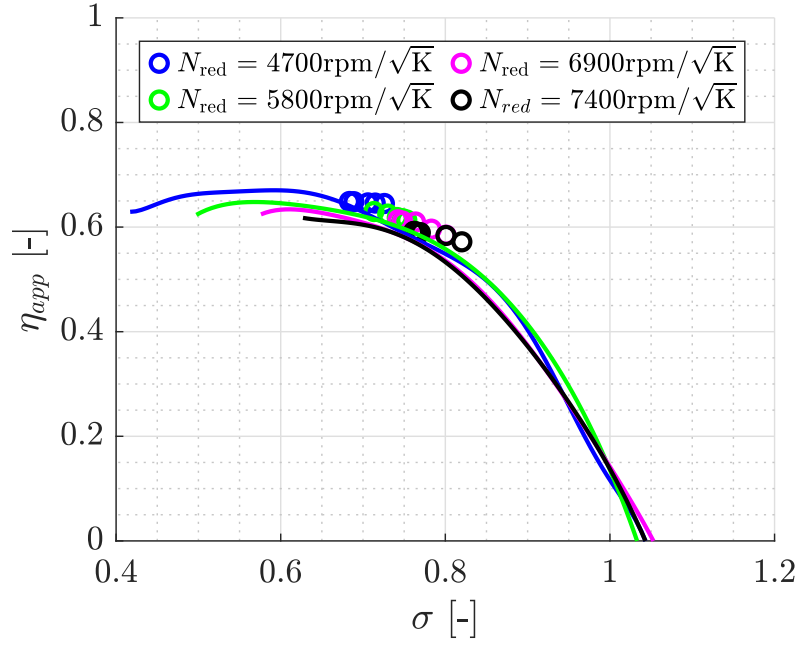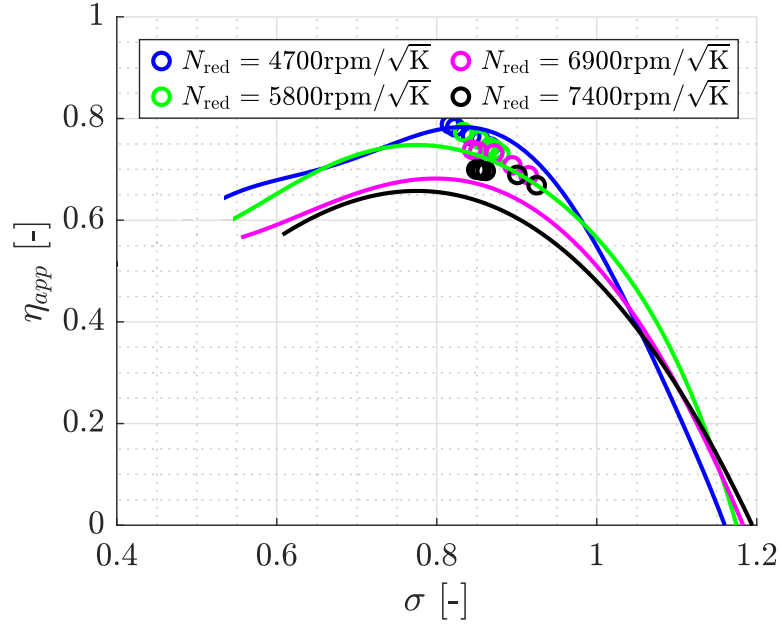
(a) Hub branch

(b) Shroud branch

Figure 7.17: Apparent efficiency extrapolation map at *MFR* 0.33.

(a) Hub branch
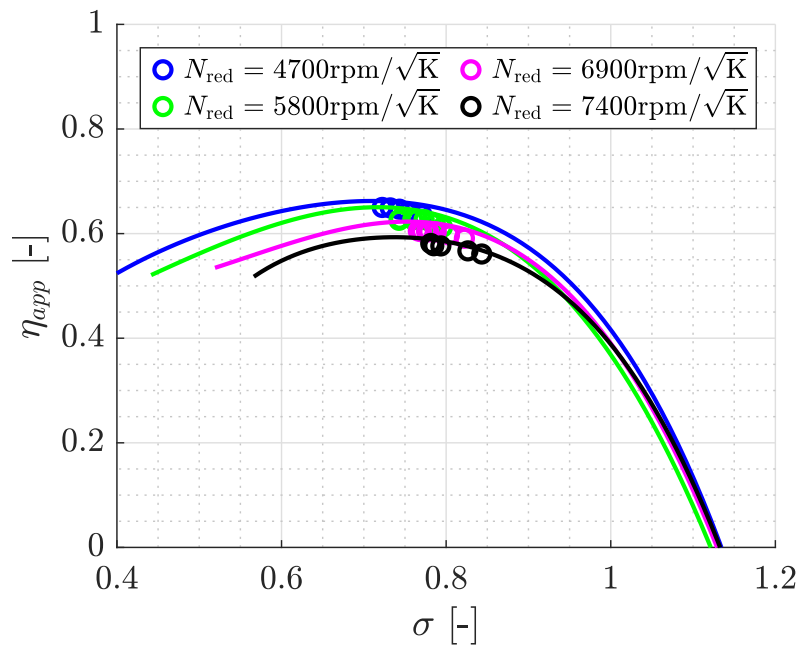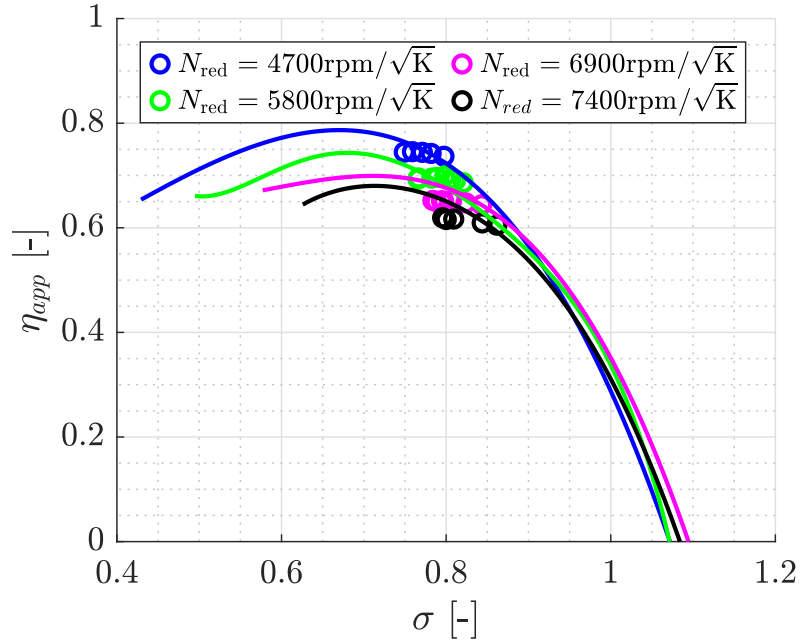
(b) Shroud branch

Figure 7.18: Apparent efficiency extrapolation map at *MFR* 0.53.
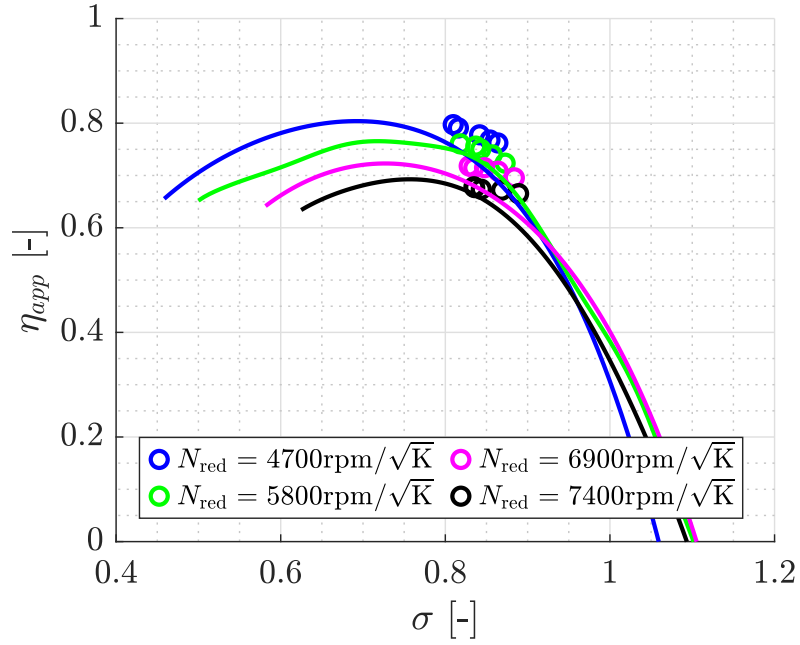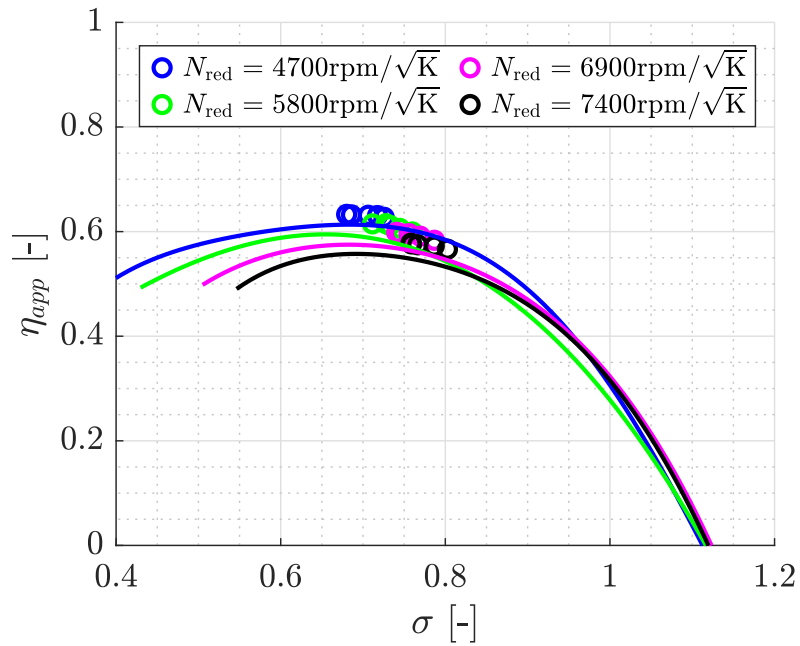
(a) Hub branch

(b) Shroud branch

Figure 7.19: Apparent efficiency extrapolation map at *MFR* 0.67.
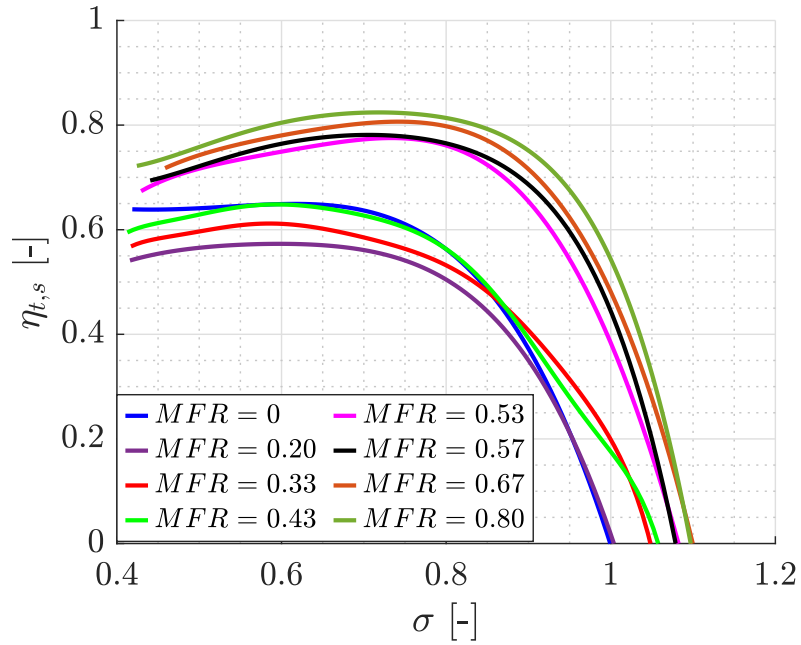
(a) Hub branch
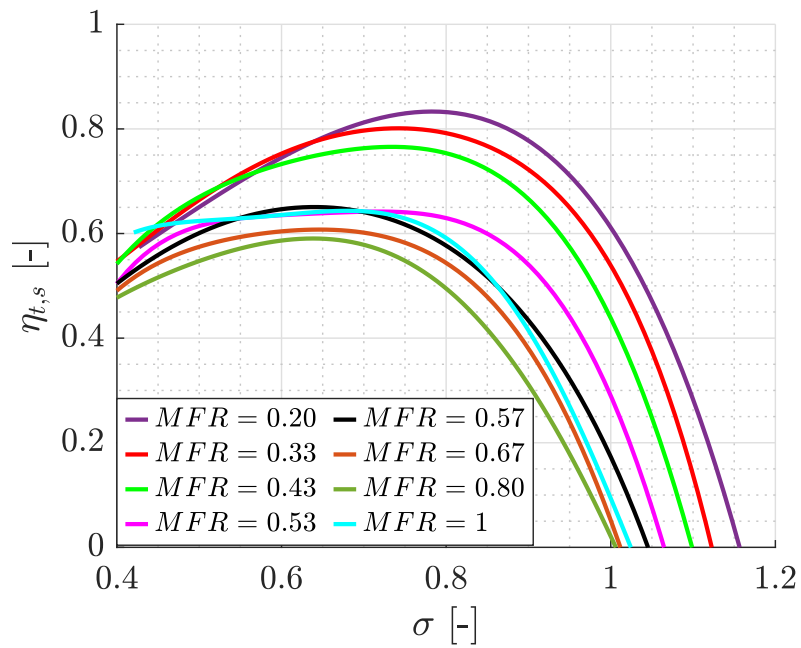
(b) Shroud branch

Figure 7.20: Actual efficiency extrapolation map at reduced rotational speed $4700\,\mathrm{rpm\,K^{-0.5}}$.
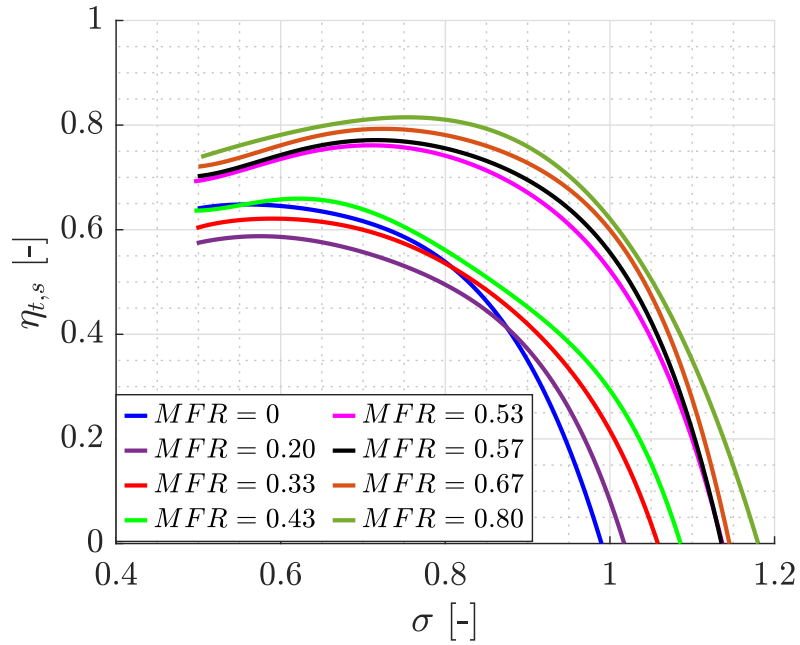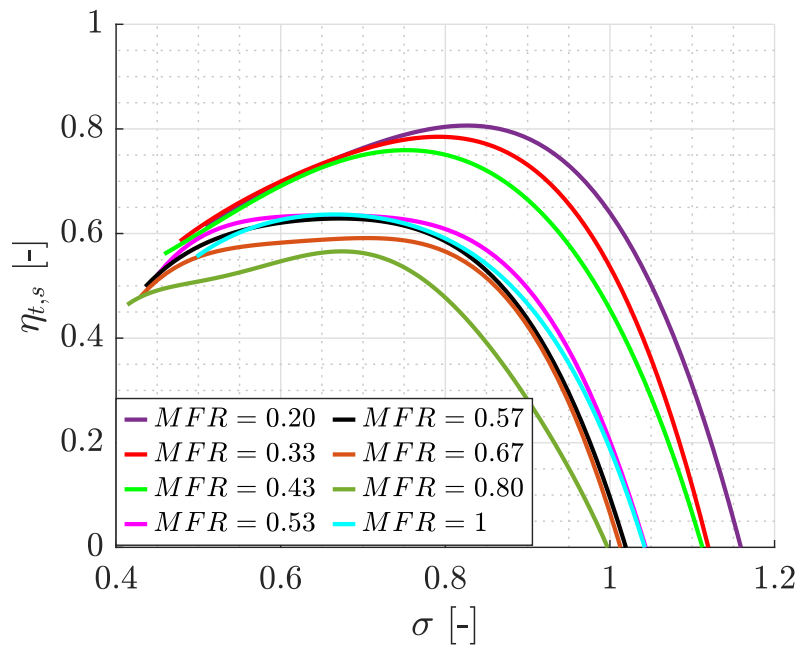
(a) Hub branch

(b) Shroud branch

Figure 7.21: Actualt efficiency extrapolation map at reduced rotational speed $5800 \, \text{rpm} \, \text{K}^{-0.5}$.
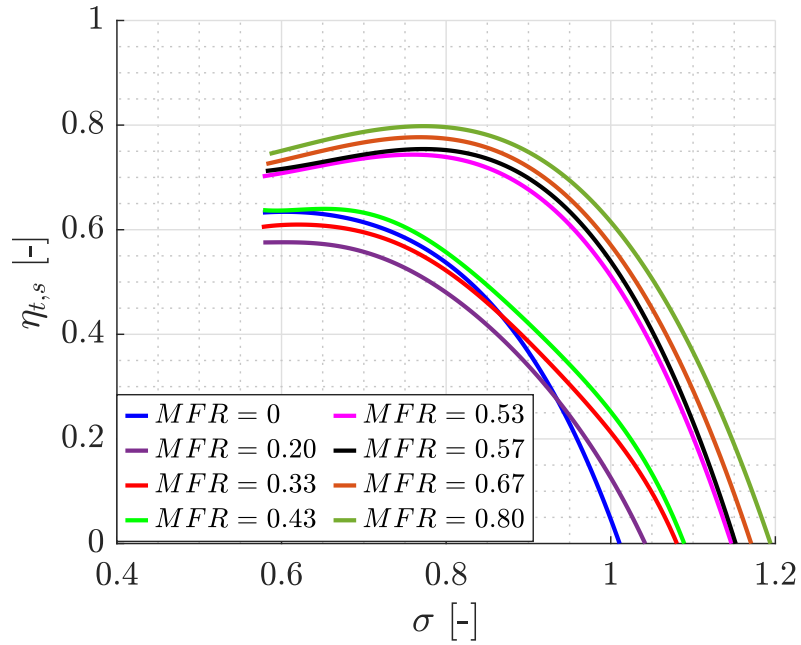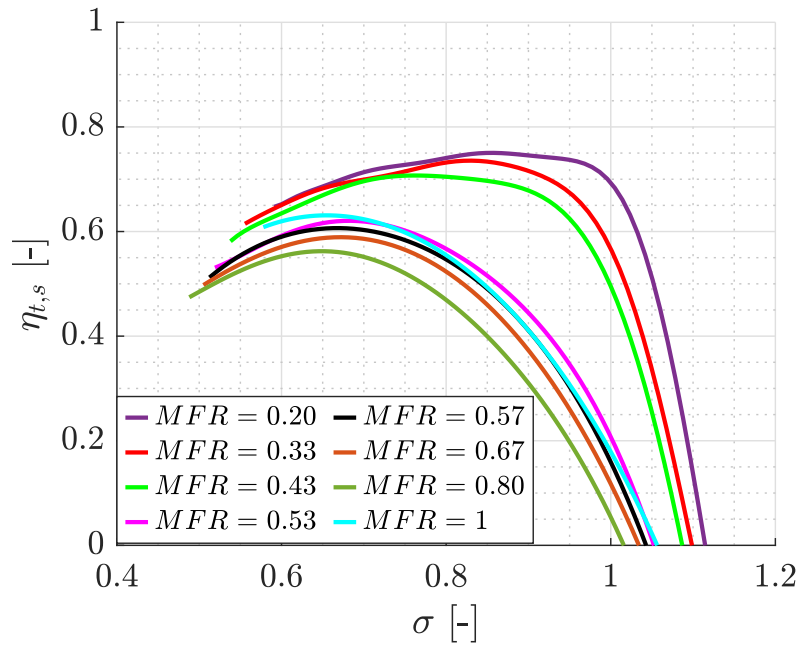
(a) Hub branch

(b) Shroud branch

Figure 7.22: Actual efficiency extrapolation map at reduced rotational speed $6900\,\mathrm{rpm\,K^{-0.5}}$.
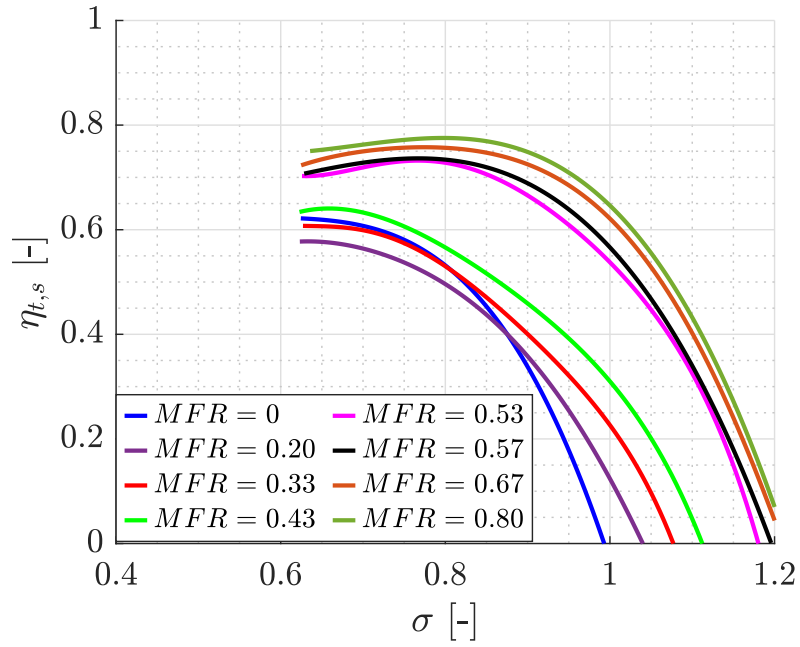
(a) Hub branch
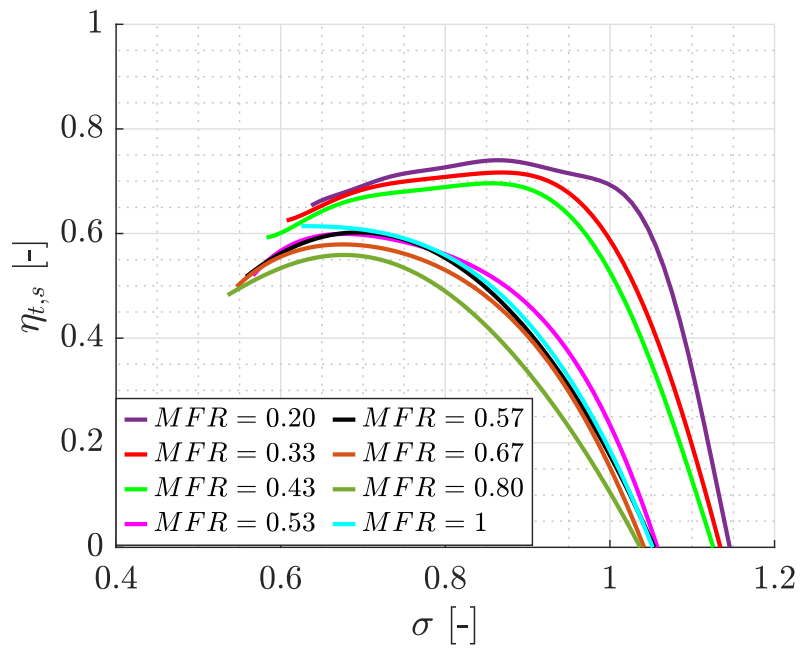
(b) Shroud branch

Figure 7.23: Actual efficiency extrapolation map at reduced rotational speed $7400 \, \mathrm{rpm \, K^{-0.5}}$.

low blade speed ratios. On the other hand, the actual efficiency under partial admission conditions is lower at high blade speed ratios. The momentum exchange between flow branches has lower effect on these cases, and the sudden expansion downstream of the junction of the volutes becomes the dominant effect.

7.3.1 Comparison of the presented efficiency model with other twin-entry turbine efficiency models

The apparent efficiency obtained with the presented efficiency model could be compared with the apparent efficiency provided by other twin-entry turbine efficiency models to check the validity and benefits of the results. The current apparent efficiency can be compared with the apparent efficiency provided by the empirical model developed by Serrano et al. [95]. It could also be compared with the apparent efficiency provided by one commercial software such as GT-POWER. GT-POWER is considered one of the most advanced engine simulation software packages. Most major engine manufacturers and vehicle OEMs are currently employing it.

The empirical and commercial efficiency models have been adjusted and calibrated with the same experimental data than the data used in the current efficiency model. Then, the same experimental measurements provided to the current model to evaluate its extrapolation capacity has been provided to both models: all reduced rotational speeds and *MFR* values of 0, 0.43, 0.57 and 1.

The apparent efficiency predicted by the three efficiency models under the *MFR* values not employed to fit the models is shown in Fig. 7.24 for both flow branches separately. The apparent efficiency obtained with the three models is plotted against the efficiency experimentally measured. Thus, the accuracy of their efficiency predictions can be assessed. The straight line represents perfect concordance between the apparent efficiency modelled and measured. The dotted lines represent a discrepancy of 0.05 efficiency points.

The GT-POWER efficiency model predictions seem to be the worst correlated with the experimental measurements. Nevertheless, the accuracy of each efficiency model could be appropriately assessed computing the error produced by each efficiency model using Eq. 7.1. The apparent efficiency error is computed with Eq. 7.1 for each efficiency model and each flow branch, as presented in Table 7.1.

$$\epsilon = \sqrt{\frac{\Sigma\left(\eta_{\mathrm{mod}} - \eta_{\mathrm{Exp}}\right)^2}{n}} \qquad (7.1)$$

As observed in Fig. 7.24, the GT-POWER model produces the highest apparent efficiency error. The apparent efficiency error produced by the empirical
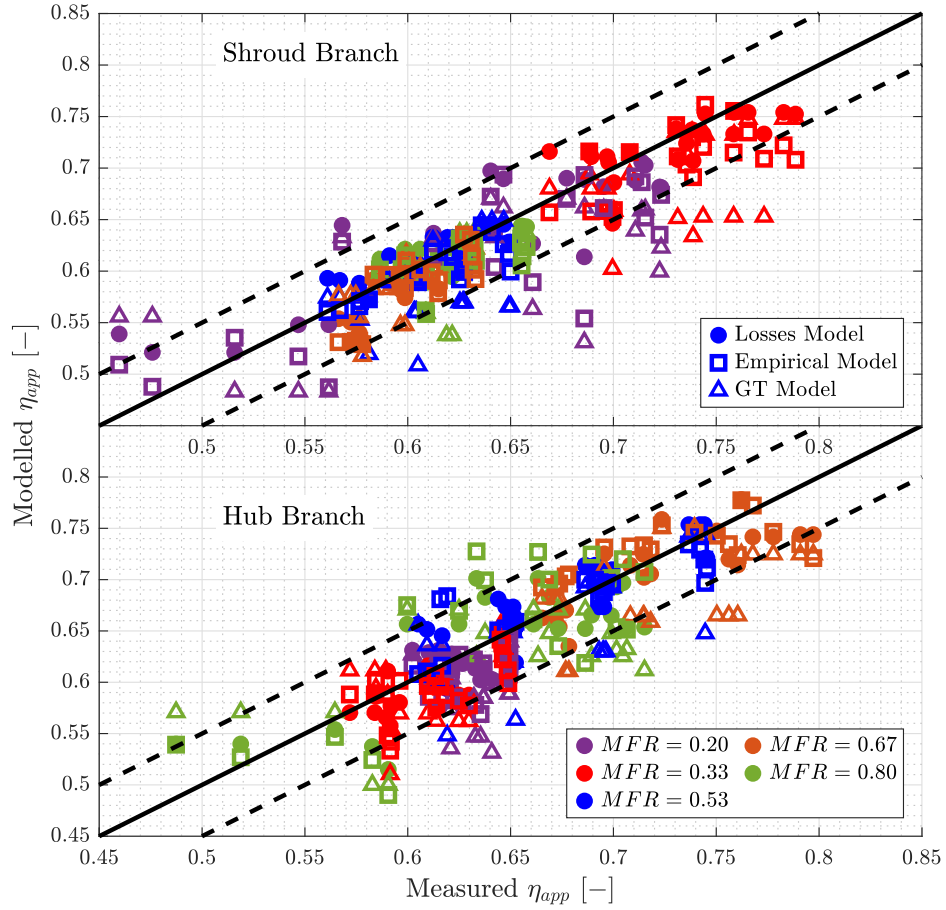
Figure 7.24: Apparent efficiency comparison of different models.

Table 7.1: Apparent efficiency error for each model and flow branch.

Model	Shroud Branch	Hub Branch
Losses	2.64%	2.98%
Empirical	3.41%	3.44%
GT-POWER	4.90%	4.94%

model is reduced. Nevertheless, the apparent efficiency produced by the new efficiency model presented here is even lower than the produced by the empirical model.

The error reduction under unequal admission conditions is noticeable. The losses-based model presented in the current work considers sources of losses that other developed models have not considered. An essential source of losses under unequal admission conditions is the momentum exchange between flow branches. Other developed efficiency models have not considered this physical phenomenon, and it has been proven that it is relevant to correctly understand the twin-entry turbines flow behaviour under unequal admission conditions.

7.4 Flow analysis and models performance with a different geometry

The models presented in the current work have been developed based on a unique twin-entry turbine geometry. It would be relevant to corroborate that they work with other geometries appropriately. A new twin-entry turbine geometry has been simulated. This new geometry is named during the dissertation as T2, and the main geometry studied is called T1 in this section. The CAD model of T2 is shown in Fig. 7.25.

Figure 7.25: T2 CAD model.

The exact geometrical parameters cannot be disclosed in the current work, but T2 is nearly twice the size of T1. All the variables are presented in a non-dimensional form. The non-dimensional mass flow rate and rotational speed are computed following Eq. 7.2 and 7.3, respectively. The subscript ND indicates they are non-dimensional variables.

195

$$\dot{m}_{\mathrm{ND}} = \dot{m} \cdot \frac{\sqrt{\gamma \cdot R \cdot T_{0t}}}{D_3^2 \cdot p_{0t}} \tag{7.2}$$

$$N_{\mathrm{ND}} = \frac{N \cdot D_3}{\sqrt{\gamma \cdot R \cdot T_{0t}}} \tag{7.3}$$

There are no available experimental measurements on this twin-entry turbine geometry. However, CFD simulations can be carried out under different admission conditions to obtain widespread maps. The CFD simulations carried out on this geometry have the same setup explained in Chapter 4: U-RANS simulations using the $k - \omega$ SST model for the turbulence with steady boundary conditions and a sliding mesh model for simulating the rotor movement. A mesh independence study has been carried out to ensure the validity of the results. The case used to carry out this mesh independence study has an *MFR* value of 0.51 and a non-dimensional rotational speed of 11.5. The efficiency and the reduced mass flow rate while increasing the number of cells are shown in Table 7.2. The optimum mesh that provides accurate results maintaining the lowest computational cost is the one with 4.72 million cells. The GOA is near 2 in both cases, and the GCI is lower than 0.2%.

Table 7.2: T2 Mesh independence study: variation of efficiency and reduced mass flow rate.

N of cells ($\cdot 10^6$)	η [-]	$\dot{m}_{\mathrm{ND}}$ [-]
1.33	0.5786	0.1286
2.32	0.5821	0.1287
3.22	0.5836	0.1288
4.72	0.5840	0.1289
5.83	0.5845	0.1289
GOA	1.647	1.757
GCI (%)	0.196	0.189

The twin-entry turbine T2 has been simulated at four different non-dimensional rotational speeds and seven different *MFR* values for a total of 28 cases simulated. The non-dimensional rotational speeds and *MFR* values selected are summarised in Table 7.3.

The flow capacity and efficiency maps obtained from the CFD simulations are shown in Fig. 7.26 and 7.27, respectively. The flow behaviour has the same trends as the previous twin-entry turbine: the reduced mass flow rate decreases with *MFR* for the hub branch and increases for the shroud branch. The apparent

Table 7.3: *MFR* and non-dimensional rotational speeds simulated for T2.

MFR [-]	N_{ND} [-]
0.20	
0.32	8.5
0.43	10.3
0.51	11.5
0.60	14.7
0.70	
0.80	

efficiency increases with *MFR* value for the hub branch and decreases for the shroud branch.
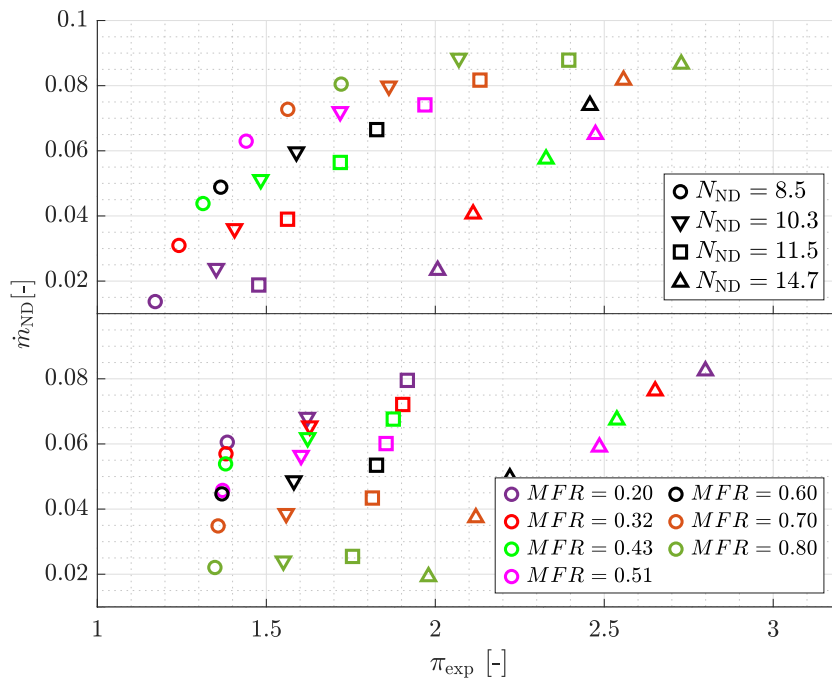
Figure 7.26: Flow capacity map T2.

7.4.1 Flow capacity map

Once there are enough data, the models proposed in the current thesis can be applied to this new geometry. Regarding the effective area model used to extrapolate in the flow capacity map, the first step is to corroborate that the
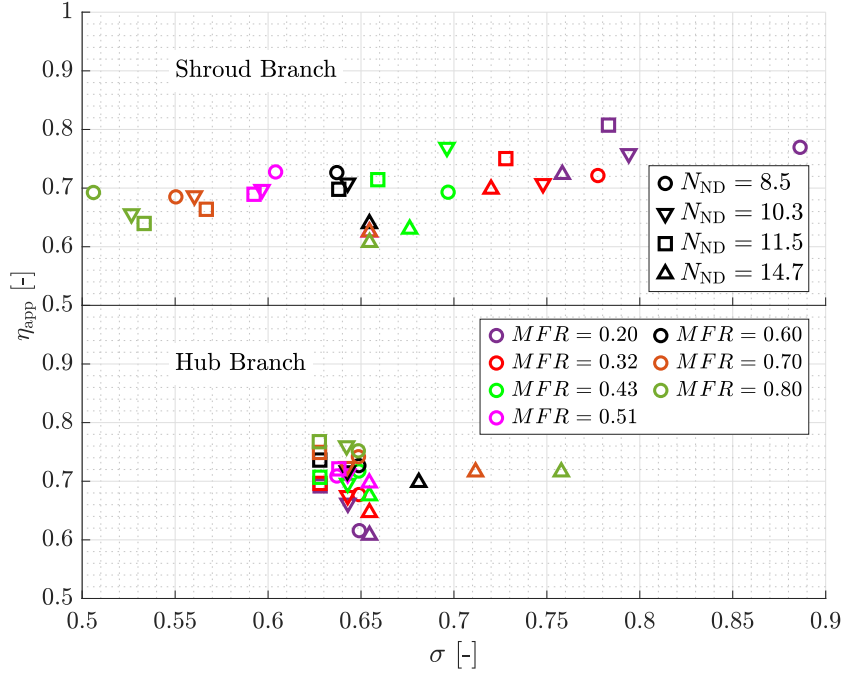
Figure 7.27: Efficiency map T2.

rotor inlet and outlet areas vary linearly with *MFR*.

The percentage of area occupied by each branch is plotted against *MFR* in Fig. 7.28. The circles represent the results obtained with the previous turbine (T1), and the triangles represent the results obtained with this new turbine (T2). Dark blue symbols are the percentage of area occupied by the hub branch, and light blue symbols are the percentage of area occupied by the shroud branch.

Both twin-entry turbines show the same behaviour against *MFR*: the percentage of rotor inlet and outlet areas occupied by the hub branch increases linearly with *MFR*, and the percentage of area occupied by the shroud branch decreases linearly with *MFR*. Since both twin-entry turbines have the same behaviour in terms of area variation, the effective area model presented could be used on this new geometry.

The geometrical parameters of this new twin-entry turbine are introduced in the model. Then, the calibration coefficients of the effective area model can be adjusted employing the data obtained from the CFD simulations. The calibration coefficients adjusted for each branch are summed up in Table 7.4.

The non-dimensional mass flow rate computed from the model with these calibration coefficients is compared to the one obtained from the CFD simulations in Fig. 7.29. The quality of the effective area model presented can be assessed if the non-dimensional mass flow rate results computed for this new
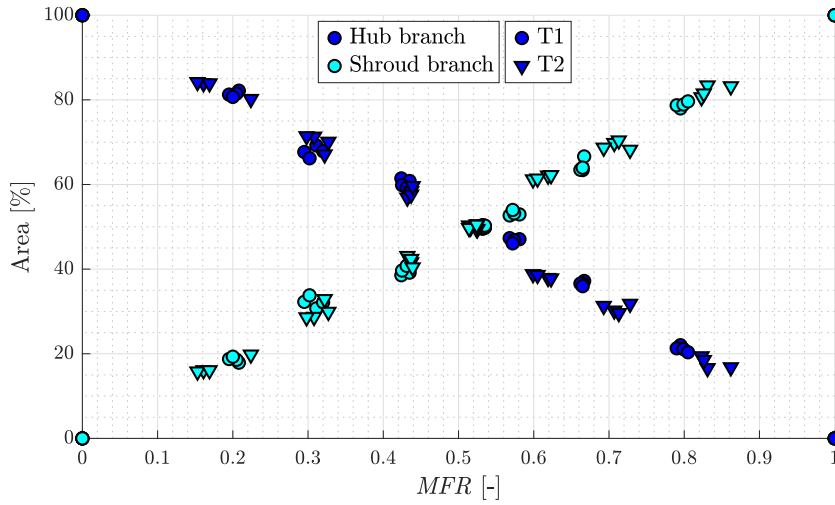
Figure 7.28: Rotor inlet and outlet areas behaviour against *MFR* of T2.

geometry are accurate.

Table 7.4: Effective area calibration coefficients for each twin-entry turbine branch of T2.

Coefficient	Hub Branch	Shroud Branch
a	0.618	0.405
b	0.191	0.391
c	0.935	0.885
d	$0 + 0.4 \cdot MFR$	$1 - 0.4 \cdot MFR$

The effective area model adequately reproduces the non-dimensional mass flow rate in both branches of T2. The R^2 value is high in both branches, which indicates a good correlation between the modelled non-dimensional mass flow rate and the one obtained with the CFD simulations. The RMSE is lower than 3.5% in both branches, which is similar to the obtained with the other geometry. Therefore, the effective area model presented in the current thesis can be applied to other geometries, giving accurate results.

7.4.2 Efficiency map

About the efficiency model employed to extrapolate in the efficiency map, the first step is to corroborate that the losses distribution is similar to the obtained with the other geometry in both branches.
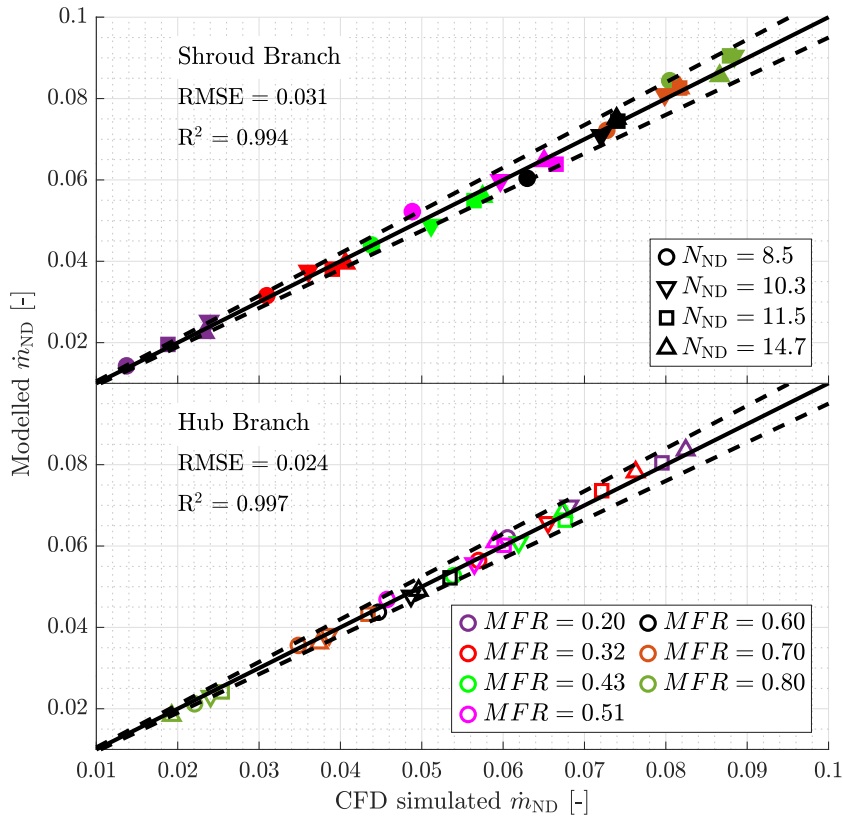
Figure 7.29: Comparison of the T2 modelled non-dimensional mass flow rate against the one obtained with the CFD simulations.

Fig. 7.30 shows the modelled total pressure losses distribution for each twin-entry turbine part and compare them with those obtained from the CFD simulations. The total pressure losses are divided by the maximum total pressure losses to make them non-dimensional (i.e. the value under *MFR* 0.2 and N_{ND} 14.7 for the hub branch and the value under *MFR* 0.8 and N_{ND} 14.7 for the shroud branch). The modelled total pressure losses are under-predicted when the yellow bars are at the top of the bar, and they are over-predicted when the yellow bars are at the bottom, under 0.

The overall total pressure losses have the same behaviour against *MFR* for T2: they decrease with *MFR* for the hub branch and increase for the shroud branch. The most relevant losses are still produced in the rotor part for both branches. The volute and interspace losses have similar trends against *MFR*, increasing when there is more mass flow passing through the correspondent branch. The outlet losses are nearly constant with *MFR*. All these trends are the same trends observed for the previous geometry. Therefore, it is reasonable
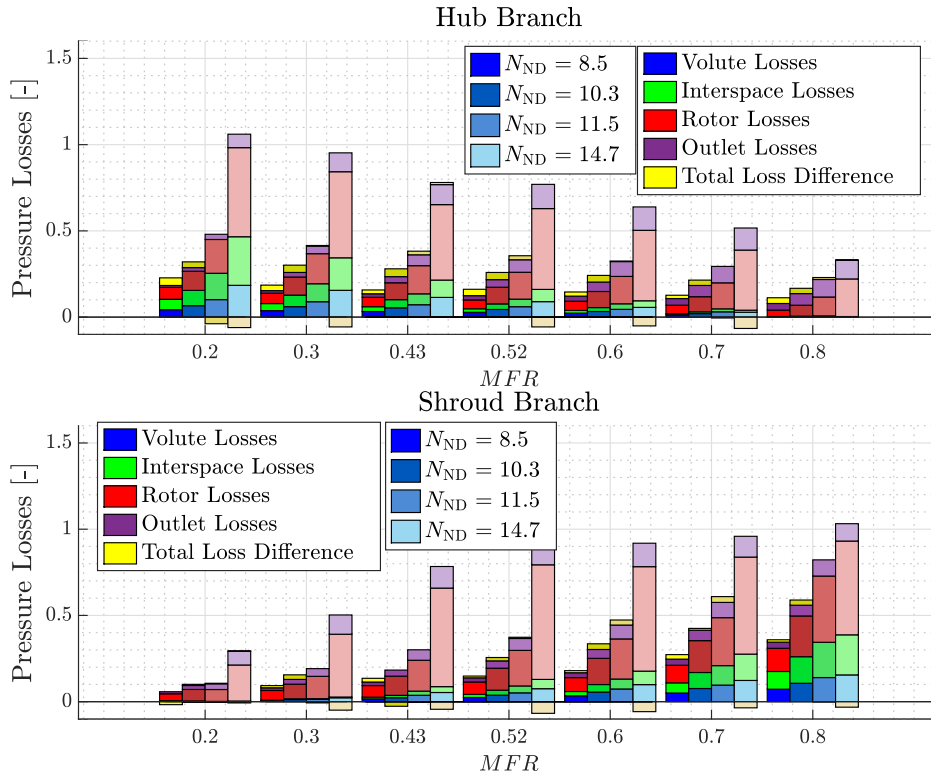
Figure 7.30: Total pressure losses distribution in T2.

to use the efficiency model presented in the current thesis on this new geometry.

The geometrical parameters required by the efficiency model have been introduced. Then, the fitting parameters of the efficiency model can be adjusted employing the data obtained from the CFD simulations. The fitting parameters adjusted for each branch are summed up in Table 7.5.

The apparent efficiency computed from the model with these fitting parameters is compared to the apparent efficiency obtained from the CFD simulations in Fig. 7.31. The quality of the efficiency model presented can be assessed if the apparent efficiency results computed for this new geometry are accurate.

The efficiency model adequately reproduces the apparent efficiency in both branches of T2. Despite not having a R^2 as high as for the non-dimensional mass flow rate, it could still be considered high in both branches, indicating a good correlation between the modelled apparent efficiency and the obtained with the CFD simulations. The RMSE computed as a unique value for both branches is 0.0854, lower than 9%. This value is a bit higher than the obtained with the previous geometry. This discrepancy could be reduced if more data were available to adjust the fitting parameters better. However, it could still be

Table 7.5: Efficiency model fitting parameters for each branch of T2.

Parameter	Hub Branch		Shroud Branch
Volute			
$Z_{\text{vol,pass}}$	0.067		0.049
Interspace			
$Z_{\text{int,pass}}$	0.097		0.057
$Z_{\text{int,SudExp}}$	0.075		0.115
Rotor			
$Z_{\text{rot,pass}}$	0.085		0.089
$Z_{\text{rot,inc}}$		0.101	
K^{+}		0.072	
K^{-}		0.170	
Outlet			
$Z_{\text{out,SudExp}}$	0.005		0.010
$Z_{\text{out,mix}}$	0.005		0.009
Common			
Z_{ME}		0.055	

considered accurate enough. Therefore, the efficiency model presented in the current thesis can be applied to other geometries, giving accurate results.
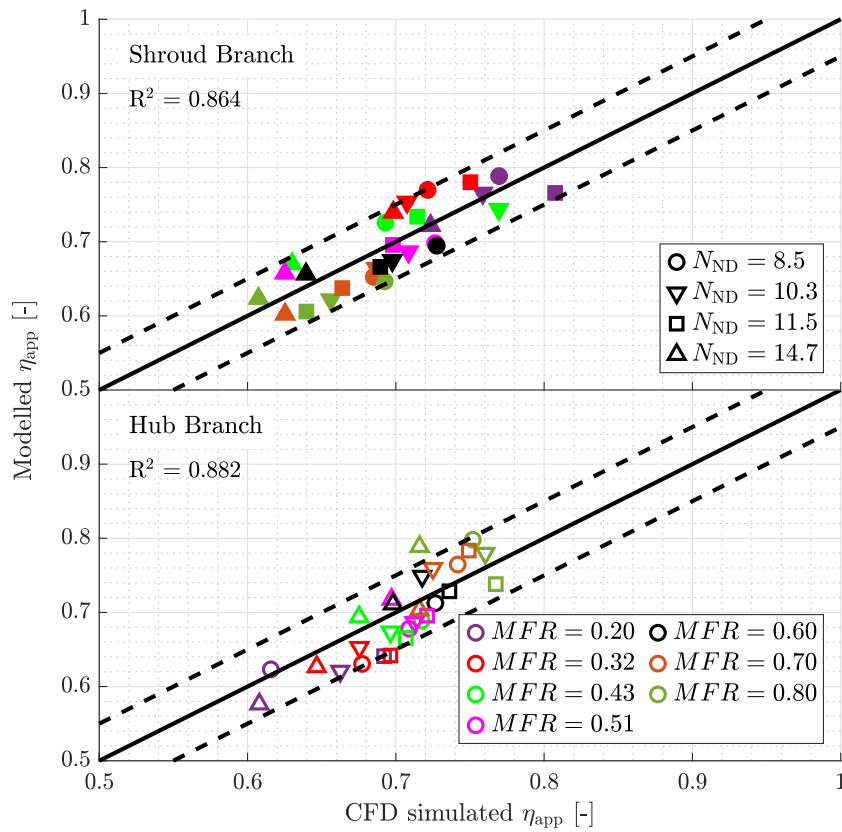
Figure 7.31: Comparison of the T2 modelled apparent efficiency against the obtained with the CFD simulations.

7.5   Summary

This chapter presents the extrapolation capacity of the models presented in Chapter 6 in the twin-entry turbine flow capacity and efficiency maps. The effective area model extrapolates in the flow capacity map, and the efficiency model extrapolates in the efficiency map. The application of all the flow analysis and the models developed on a different geometry is also presented in this chapter.

7.5.1   Flow capacity map

The extrapolation capacity of the effective area model towards other *MFR* values in the flow capacity map has been proven, using some of the experimental data to fit the model. The other experimental data have been employed to check that it adequately predicts the flow behaviour in the flow capacity map.

The model has provided reasonable predictions for all *MFR* values and reduced rotational speeds, having an error lower than 3% in most cases when *MFR* 0, 0.43, 0.57 and 1 are used. The behaviour of the reduced mass flow rate against the expansion ratio has been captured appropriately. In the case where *MFR* 0.33, 0.53, 0.67 are used to feed the model, the error in the predictions at partial admission conditions is a bit higher, but always lower than 5%. However, the error could still be considered acceptable.

Additionally, an analysis focused on the reduced rotational speed has demonstrated that the shroud branch has more similar behaviour to an axial turbine than the hub branch. This is due to the shroud branch effective outlet radius is closer to the rotor inlet radius. Moreover, this effect is more noticeable when *MFR* decreases since the effective outlet radius increases, as explained in Chapter 6.

7.5.2   Efficiency map

The extrapolation capacity of the efficiency model towards other flow admission conditions have also been proven. A limited set of data has been used to fit the model, while the other experimental data have been employed to check the precision of the predictions in the efficiency map.

The modelled apparent efficiency depends on *MFR*, increasing for the hub branch and decreasing for the shroud branch. The area variation with *MFR* described in Chapter 6 produces an increment in the passage losses when the mass flow of the corresponding branch increases. Moreover, the momentum exchange between flow branches is relevant to understand these variations. The flow branch with higher momentum will exhibit losses under unequal admission conditions. Meanwhile, the flow branch with lower momentum will experience

gains due to this momentum exchange. Additionally, the speedlines become wider at their peak when the *MFR* is increased for the hub branch and decreased for the shroud branch. This behaviour leads to a higher apparent efficiency variability with the reduced rotational speed when low flow passes through the correspondent flow branch.

The modelled actual efficiency behaviour against *MFR* is similar to the apparent efficiency. However, there are more significant differences between the extrapolations under *MFR* values where the mass flow of the correspondent branch is high and under *MFR* values where it is low. The primary contributors to these differences are the sudden expansion produced downstream of the junction of the volutes and the momentum exchange between flow branches.

The current efficiency model has been compared with an empirical and a commercial model. The extrapolations provided by the current model have an error of 2.98% for the hub branch and 2.64% for the shroud branch. The error provided by the empirical model employing the same amount of data is half a point higher, and by the commercial model is two points higher. Hence, the current losses-based efficiency model improves the accuracy of the twin-entry turbine efficiency map extrapolations.

7.5.3 Additional geometry

The flow behaviour has been first analysed to ensure that it is similar to the flow behaviour of the previous twin-entry turbine. Since the rotor inlet and outlet areas behaviour against *MFR* and the losses distribution are similar, it is reasonable to use the proposed effective area and efficiency models.

Therefore, the effective area and efficiency models presented in the current thesis have been applied to a different geometry to corroborate that they can be utilised for different twin-entry turbines sizes.

The non-dimensional mass flow rate and the apparent efficiency computed with the models and those obtained from the CFD simulations have been compared. Although the RMSE obtained in both models is slightly higher than the correspondent RMSE of T1, it still could be considered acceptable. This slightly higher RMSE could be reduced having more data available to adjust the fitting parameters of the models. Nevertheless, given the differences in geometry between T2 and T1 and the accuracy achieved by the models developed in this work, they appear to provide a good general physical description of the twin-entry turbines behaviour.

7.6 References

[95] J. R. Serrano, F. J. Arnau, L. M. García-Cuevas, and V. Samala. "A robust adiabatic model for a quasi-steady prediction of far-off non-measured performance in vaneless twin-entry or dual-volute radial turbines". In: *Applied Sciences* 10.1955 (2020). DOI: 10.3390/app10061955 (cit. on pp. 25, 193).

CHAPTER 8

Conclusions and future works

Contents

8.1 Introduction

NOWADAYS, emission regulations are becoming more restricted worldwide to reduce the effect of global warming and improve the air quality in urban areas. Moreover, there is a lack of fuel supply increasing its price. Since alternative cleaner technologies are still in development, the efficiency of ICE must be improved. One of the key components to achieve the objectives marked by the regulations is introducing a turbocharger in the engine. The turbocharger allows downsizing the engine, maintaining its overall performance since a higher inlet pressure is reached. With a smaller engine, fuel consumption and pollutant emissions are strongly reduced.

Twin-entry turbines are becoming the typical turbine configuration adopted by the manufacturers for high number of cylinder engines, as well as spark ignition engines with big overlaps between exhaust valve opening times of consecutive firing order cylinders. They have the advantage of reducing the interferences between cylinders and improving the volumetric efficiency. Therefore, twin-entry turbines must be analysed thoroughly to optimise their performance.

The current work has presented an experimental and computational analysis of the flow behaviour within twin-entry turbines, focusing on the phenomena under unequal admission conditions. Based on these analyses, an effective area and an efficiency model have been developed to adequately extrapolate in the flow capacity and efficiency maps of twin-entry turbines, respectively. Hence, the performance of twin-entry turbines under unequal admission conditions could be optimised, increasing the ICE efficiency and reducing their fuel consumption and pollutant emissions.

This chapter presents first the primary conclusions extracted from the experimental analysis, followed by the primary conclusions extracted from the computational analysis. Then, the main contributions to the twin-entry turbine modelling are exposed. Finally, the limitations of the current work and possible future works are proposed.

8.2 Experimental analysis

Two different experimental campaigns have been performed. The first campaign performs steady-state measurements within the range of *MFR* values, focusing on those under unequal admission conditions. The unequal admission conditions are not commonly provided by the manufacturers, and they are the most frequent admission conditions in real operating conditions. These measurements are performed to analyse the general trends against *MFR* and obtain wider performance maps. The reduced mass flow rate decreases with *MFR* for the hub branch and increases for the shroud branch. The apparent efficiency

increases with *MFR* for the hub branch and decreases for the shroud branch. These steady-state measurements are used to validate the CFD simulations and the developed models globally.

The second campaign performs LDA and temperature measurements at the rotor outlet section to corroborate the hypothesis made on the one-dimensional models of studying twin-entry turbines as two single-entry VGT turbines working in parallel. The axial Mach number measured increases with the radial position from hub to shroud due to a sudden expansion downstream of the rotor nut. The concentration of particles coming from the shroud branch also increases with the radial position and depends strongly on *MFR*. Additionally, the outlet temperature also varies with the radial position. All these measurements lead to the conclusion that the flow is not homogeneous at the outlet section measured. This behaviour means that the flow is not fully mixed at the outlet: the flow from the hub branch is still concentrated near the rotor hub, and the flow from the shroud branch is still concentrated near the rotor shroud. Therefore, the hypothesis made on the one-dimensional models has been corroborated.

8.3 CFD analysis

The CFD simulations have been first validated with steady-state measurements. Thus, the flow analysis inferred from these CFD simulations could be considered reliable.

The flow from each branch has been tracked within the twin-entry turbine, showing that the flow from the hub branch remains concentrated near the rotor hub and the flow from the shroud branch remains concentrated near the rotor shroud. This behaviour is the same found with the LDA measurements. It means that the flow from each branch does not fully mix within the rotor.

Moreover, the rotor inlet and outlet areas corresponding to each branch depend linearly on *MFR*. The rotor inlet and outlet areas corresponding to the hub branch decrease with *MFR*, and those corresponding to the shroud branch increase with *MFR*. The rotor inlet flow angle also depends linearly on *MFR*. The rotor outlet flow angle, although also depends on *MFR*, depends on more variables such as the reduced rotational speed.

The total pressure losses have been identified and quantified in each twin-entry turbine part separately, focusing on the phenomena under unequal admission conditions.

The volute total pressure losses have been quantified with a passage losses model. These losses decrease with *MFR* for the hub branch and increase for the shroud branch.

The interspace total pressure losses can be divided into three main sources: passage losses, sudden expansion losses and losses due to the momentum ex-

change between flow branches. The passage losses are quantified with a model similar to the one used in the volutes. The sudden expansion losses are due to the expansion found downstream of the junction of the volutes at *MFR* lower than 0.4 for the hub branch and higher than 0.6 for the shroud branch. The losses due to the momentum exchange between flow branches are produced by the contact between branches without fully mixing. The flow branch with higher momentum transmits some of it to the flow branch with lower momentum. This means that the flow branch with higher momentum has losses, but the flow branch with lower momentum has gains. This phenomenon becomes relevant under unequal admission conditions and has not been found in the literature.

The rotor total pressure losses can be divided into four main sources: passage, incidence, tip and losses due to the momentum exchange between flow branches. The passage and incidence losses have been quantified with its conventional models, and the tip losses have been quantified with the model proposed by Serrano et al. [94]. Since the flow from each branch do not fully mix within the rotor, the losses due to the momentum exchange between flow branch are also relevant in the rotor under unequal admission conditions.

The outlet total pressure losses have been quantified with a sudden expansion model, a mixing flow model and also momentum exchange between flow branches. The main sources of losses are the sudden expansions downstream of the rotor nut and to connect to the outer plenum case. Since the flow from each branch finally mixes in this part, the mixing flow model quantifies this source of losses. However, the flow from each branch is still separated just at the rotor outlet before mixing. Therefore, the losses due to the momentum exchange between flow branches have a small effect also on the outlet losses.

All these losses are relevant to assess the behaviour under unequal admission conditions. The momentum exchange between flow branches is a key phenomenon to explain this behaviour, and it has not been considered in the literature.

8.4 Twin-entry turbine modelling

The information extracted from the analyses of the experimental campaigns and the CFD simulations has been used to develop an effective area and an efficiency model for twin-entry turbines. Since the phenomena under unequal admission conditions have been adequately assessed, these models are expected to provide more accurate predictions in these cases than other empirical or commercial models that do not consider these phenomena.

The models developed in the current thesis need some geometric parameters that are usually provided by the manufacturers, or they can be easily measured such as the rotor inlet and outlet diameters or the blade height. The equations

that define the physical phenomena modelled depend on some fitting parameters that need to be adjusted. Thus, the models must be fed with experimental or CFD data to calibrate these fitting parameters. In the current thesis, the experimental data has been used to adjust the fitting parameters and validate the results. If there is no data to adjust the fitting parameters, the model uses a default set of parameters based on those obtained on both geometries studied during this work.

The hypothesis of modelling twin-entry turbines as two separated single-entry VGT turbines working in parallel funded by Serrano et al. [49] has been corroborated with a CFD flow analysis and validated with experimental measurements by means of an LDA technique. Therefore, the developed models are applied to each flow branch separately.

8.4.1 Flow capacity map

The model developed to extrapolate in the flow capacity map is an effective area model. This model considers each flow branch as a single equivalent nozzle. The effective area of this equivalent nozzle needs to be modelled. It depends on some geometrical parameters as the rotor inlet and outlet areas corresponding to each flow branch.

The CFD mass flow analysis and the LDA experimental measurements have detected that these geometrical parameters depend on the mass flow admission conditions. Therefore, these geometrical parameters change in the model depending on *MFR*. Implementing these modifications, the effective area model only needs 5 parameters to be adjusted with experimental data for each flow branch.

The effective area model has been fitted and validated with steady-state experimental data. The RMSE in both flow branches is lower than the expanded uncertainty of the experimental measurements. Therefore, the effective area model could be considered reliable.

The effective area model capability of extrapolating towards other *MFR* values in the flow capacity map has been proven. Some of the experimental data have been utilised to feed the model, and the other experimental data have been used to check that the predictions provided by the model are appropriate. The predictions of the model could be considered reasonable under all *MFR* and reduced rotational speed conditions since the extrapolation error is lower than 3% when partial and full admission conditions maps are provided to feed the model. When the model is fed with a narrower set of data, the error is slightly worse but lower than 5% in the worst cases found at partial admission conditions.

Analysing the effect of the reduced rotational speed, the shroud branch speedlines are more collapsed than the hub branch speedlines. Since the shroud

branch effective outlet radius is always closer to the rotor inlet radius than the hub branch effective outlet radius, the shroud branch has a behaviour more similar to an axial turbine. This effect is more noticeable when the *MFR* decreases since the effective outlet radius increases.

8.4.2 Efficiency map

The model developed to extrapolate in the efficiency map is a losses-based efficiency model. The primary sources of losses have been modelled separately in the volutes, the interspace between volutes and rotor, the rotor and the outlet regions. Each part is solved iteratively employing Brent's method [115] to obtain the efficiency of each flow branch.

The current efficiency model needs 6 fitting parameters for each flow branch and 4 additional fitting parameters common for both flow branches. Hence, the model needs 16 fitting parameters to be adjusted with experimental data. The efficiency model has been fitted and validated with the steady-state experimental data. To validate the model, the apparent efficiency has been compared to the experimentally measured efficiency since it is the efficiency that can be measured. The error obtained with this efficiency model is acceptable, being lower than 7% for both flow branches combined. Therefore, the efficiency model could be considered reliable.

The efficiency model capability of extrapolating towards other *MFR* in the efficiency map has been proven. Some of the experimental data have been utilised to feed the model, and the other experimental data have been utilised to check that the predictions provided by the model are appropriate. The predictions of the model could be considered reasonable under all *MFR* and reduced rotational speed conditions.

The modelled apparent efficiency varies with *MFR*, increasing for the hub branch and decreasing for the shroud branch. The area variation with the *MFR* produces an increment in the passage losses when the mass flow of the corresponding branch increases. Moreover, the momentum exchange between flow branches produces losses in the flow branch with the higher mass flow and gains in the flow branch with the lower mass flow. This phenomenon contributes to explain the apparent efficiency behaviour against *MFR*.

The modelled actual efficiency has a similar behaviour against *MFR*. Nevertheless, the differences between the extrapolations under *MFR* values lower and higher than 0.5 are more significant in the actual efficiency. The primary contributors to these differences are the momentum exchange between flow branches and the sudden expansion downstream of the junction of the volutes.

The efficiency model developed in the current thesis has been compared to an empirical model previously developed in the CMT-Motores Térmicos and to a commercial model considered as the state-of-the-art in turbine modelling. The

extrapolations provided by the current model have an error of 2.98% for the hub branch and 2.64% for the shroud branch. The error provided by the empirical model using the same data is half a point higher, and the commercial model is two points higher. Hence, the current losses-based efficiency model improves the accuracy of the twin-entry turbine efficiency map extrapolations.

8.5 General conclusions

Twin-entry turbines have been computationally and experimentally analysed, assessing the flow patterns and the main physical phenomena under unequal admission conditions. The flow from each branch does not fully mix within the rotor. Moreover, the flow distribution between branches changes with *MFR*, as observed in the LDA measurements and the CFD simulations. The main sources of losses within twin-entry turbines have been identified and quantified. One key source of losses is the momentum exchange between flow branches. It is an essential phenomenon to understand the flow behaviour under unequal admission conditions that has not been found in the literature. Moreover, other important sources of losses under unequal admission conditions have been found, as the sudden expansion downstream of the volutes outlet in the branch with higher mass flow rate or the mixing losses at the outlet section.

The information extracted from these analyses has been used to develop an effective area and an efficiency model capable of predicting the twin-entry turbine performance under unequal admission conditions better than state-of-the-art models. Additionally, a twin-entry turbine with a considerably different geometry has been analysed, founding the same flow behaviour. The models developed have been applied to this geometry, giving good results. It means that these models provide a reasonable physical description of the behaviour of twin-entry turbines under unequal admission conditions. Since these admission conditions are the most common in real operation, the performance of twin-entry turbines will be better predicted most time of the operation. This improvement in the performance prediction could lead to higher ICE efficiency, reducing fuel consumption and pollutant emissions.

8.6 Limitations and future works

The primary objectives proposed in Chapter 1 have been achieved. However, the flow analysis and the models proposed in the current thesis have some limitations to be discussed.

The main sources of losses have been identified, and most of twin-entry turbine losses have been assessed. However, other minor effects have not been considered in the current thesis, like considering the possibility of having un-

burnt fuel liquid particles inside the flow. Other sub-models could be developed to consider these minor effects, but there should be a trade-off between the improvement of including them and adding more fitting parameters to the model.

Although the unequal admission conditions have been properly assessed with the presented models and represent the most frequent admission conditions in real operation, the experimental measurements and the CFD simulations carried out are steady-state. However, some accumulation effects in real operating conditions could modify the twin-entry turbine performance. The models presented in the current thesis have been introduced in the VEMOD code, and they could be coupled with the available quasi-2D approximation to properly capture the accumulation effects in the volutes when working under pulsating flow conditions. Moreover, some CFD simulations with pulsating flow boundary conditions could be carried out to corroborate that the presented models can be appropriately coupled with this quasi-2D approximation. Then, it could be meaningful to run whole engine simulations to explore the impact of these models at engine level.

There are experimental measurements under pulsating flow conditions of the studied twin-entry turbine at CMT-Motores Térmicos. The pulsating conditions have been obtained using a rotating valve in one of the branches leaving the other branch with steady-state boundary conditions. An extension of this work could be to connect the turbocharger to a real engine in a new gas stand and instantaneously record the desired parameters. Therefore, the models presented in the current thesis could also be validated under real pulsating flow conditions.

The losses analysis carried out in twin-entry turbines through CFD simulations could also be performed in double-entry turbines. Double-entry turbines also have two volutes, but they discharge the mass flow in half the rotor in the tangential direction instead of the axial direction. These turbines have different sources of losses than the ones identified in twin-entry turbines since, for example, there is no mass flow arriving at half the rotor channels under partial admission conditions. Therefore, a new losses-based model for double-entry turbines could be developed.

References

[1] **Galindo, J., Serrano, J. R., García-Cuevas, L. M., and Medina, N.**
"Experimental and computational analysis of the flow passing through each branch of a twin-entry turbine"
in: *14th International Conference on Turbochargers and Turbocharging* (2020), pp. 278–288   (cit. on p. vii)

[2] **Galindo, J., Serrano, J. R., García-Cuevas, L. M., and Medina, N.**
"Using a CFD analysis of the flow capacity in a twin-entry turbine to develop a simplified physics-based model."
in: *Aerospace Science and Technology* 112 (2021). DOI: 10.1016/j.ast .2021.106623   (cit. on p. vii)

[3] **Galindo, J., Serrano, J. R., García-Cuevas, L. M., and Medina, N.**
"Twin-entry turbine losses: an analysis using CFD data."
in: *International Journal of Engine Research* (2021). DOI: 10.1177/1468 0874211007647   (cit. on p. vii)

[4] **Galindo, J., Tiseira, A. O., García-Cuevas, L. M., and Medina, N.**
"Experimental assessment of the rotor outlet flow in a twin-entry radial turbine by means of Laser Doppler Anemometry"
in: *International Journal of Engine Research* (2021). DOI: 10.1177/1468 0874211034411   (cit. on p. vii)

[5] **Galindo, J., Serrano, J. R., García-Cuevas, L. M., and Medina, N.**
"Assessment of a twin-entry turbine efficiency model including momentum exchange between branches"
in: *International Journal of Heat and Fluid Flow* (2022). Under Review   (cit. on p. vii)

[6] **European Comission**
Emissions in the automotive sector
2018. URL: https://ec.europa.eu/growth/sectors/automotive/en vironment-protection/emissions_en   (cit. on pp. 2, 14)

[7] **Environmental Protection Agency**
Environmental protection agency control of air pollution from motor vehicles: Tier 3 motor vehicle emission and fuel standards
2015. URL: https://www.epa.gov/regulations-emissions-vehicles-and-engines/final-rule-control-air-pollution-motor-vehicles-tier-3 (cit. on pp. 2, 14)

[8] **Gong, H., Ge, Y., Wang, J., and Yin, H.**
"Light-duty vehicle emissions control: a brief introduction to the China 6 emissions standard"
in: *Johnson Matthey Technology Review* 61 (2017), pp. 269–278. DOI: 10.1595/205651317X696199 (cit. on pp. 2, 14)

[9] **International Council On Clean Transportation**
India Bharat Stage VI emission standards
2016. URL: https://theicct.org/sites/default/files/publications/India%20BS%20VI%20Policy%20Update%20vF.pdf
(cit. on p. 2)

[10] **European Environment Agency**
EEA Report No 13/2019, EMEP/EEA air pollutant emission inventory guidebook 2019
2019. DOI: 10.2800/293657 (cit. on p. 3)

[11] **International Civil Aviation Organization**
Resolution A40-18: Consolidated statement of continuing ICAO policies and practices related to environmental protection - Climate change
(cit. on p. 3)

[12] **Garrett, T., Newton, K., and Steeds, W.**
"Turbocharging and supercharging"
in: *Motor Vehicle* (2000), pp. 556–589 (cit. on p. 3)

[13] **Payri, F.**
"Predicción de las actuaciones de los grupos de sobrealimentación para motores diesel de automoción"
PhD thesis. Universidad Politécnica de Madrid 1973 (cit. on p. 4)

[14] **Serrano Cruz, J. R.**
"Análisis y modelado de transitorios de carga en MEC turboalimentados"
PhD thesis. Universitat Politècnica de València 1999 (cit. on p. 4)

[15] **Rodríguez, A.**
"Analisis comparativo y sintesis de la respuesta transitoria en motores diesel de inyeccion directa turboalimentados"
PhD thesis. Universitat Politècnica de València 2001 (cit. on p. 4)

[16] **Reyes-Belmonte, M. Á.**
"Contribution to the experimental characterization and 1-D modelling of turbochargers for IC engines"
PhD thesis. Universitat Politècnica de València   Dec. 2013. DOI: 10.499 5/Thesis/10251/34777   (cit. on p. 4)

[17] **López Hidalgo, M. A.**
"Estudio teórico-experimental de la dinámica rotacional de un turbocompresor de MCIA. Aplicación al diagnóstico de fallos"
PhD thesis. Universitat Politècnica de València   2014. DOI: 10.4995/Thesis/10251/37746   (cit. on p. 4)

[18] **Dombrovsky, A.**
"Synthesis of the 1D modelling of turbochargers and its effects on engine performance prediction"
PhD thesis. Universitat Politècnica de València   2017. DOI: 10.4995/Thesis/10251/82307   (cit. on p. 4)

[19] **Cervelló, C.**
"Contribución a la caracterización experimental y al modelado de turbinas de geometría variable en grupos de sobrealimentación"
PhD thesis. Universitat Politècnica de València   2005. DOI: 10.4995/Thesis/10251/1902   (cit. on p. 4)

[20] **Fajardo Peña, P.**
"Methodology for the numerical characterization of a radial turbine under steady and pulsating flow"
PhD thesis. Universitat Politècnica de València   July 2012. DOI: 10.499 5/Thesis/10251/16878   (cit. on pp. 4, 73)

[21] **García-Cuevas González, L. M.**
"Experiments and modelling of automotive turbochargers under unsteady conditions"
PhD thesis. Universitat Politècnica de València   2014. DOI: 10.4995/Thesis/10251/48458   (cit. on pp. 4, 129, 159)

[22] **Inhestern, L. B.**
"Measurement, simulation, and 1D-modeling of turbocharger radial turbines at design and extreme off-design conditions"
PhD thesis. Universitat Politècnica de València   2019. DOI: 10.4995/Thesis/10251/119989   (cit. on p. 4)

[23] **Soler Blanco, P.**
"Simulation and modelling of the performance of radial turbochargers under unsteady flow"
PhD thesis. Universitat Politècnica de València   2020. DOI: 10.4995/Thesis/10251/141609   (cit. on p. 4)

217

[24] **Samala, V.**
"Experimental characterization and mean line modelling of twin-entry and dual-volute turbines working under different admission conditions with steady flow"
PhD thesis. Universitat Politècnica de València   2020. DOI: 10.4995/Thesis/10251/153475   (cit. on p. 4)

[25] **Carlucci, A. P., Ficarella, A., Laforgia, D., and Renna, A.**
"Supercharging system behavior for high altitude operation of an aircraft 2-stroke diesel engine"
in: *Energy Conversion and Management* 101 (2015), pp. 470–480. DOI: 10.1016/j.enconman.2015.06.009   (cit. on p. 14)

[26] **Luongo, A., Nuccio, P., and Vignoli, M.**
"Optimization of a light aircraft spark-ignition engine"
in: *SAE Technical Paper Series*. Vol. Paper No: 2006-01-2420. SAE International   Aug. 2006. DOI: 10.4271/2006-01-2420   (cit. on p. 14)

[27] **Keromnes, A., Delaporte, B., Schmitz, G., and Moyne, L. L.**
"Development and validation of a 5 stroke engine for range extenders application"
in: *Energy Conversion and Management* 82 (2014), pp. 259–267. DOI: 10.1016/j.enconman.2014.03.025   (cit. on p. 14)

[28] **Puma-Benavides, D. S., Izquierdo-Reyes, J., Dios Calderon-Najera, J. de, and Ramirez-Mendoza, R. A.**
"A systematic review of technologies, control methods, and optimization for extended-range electric vehicles"
in: *Applied Sciences* 11.15 (July 2021), p. 7095. DOI: 10.3390/app11157095   (cit. on p. 14)

[29] **Falcao, A., Gato, L., Henriques, J., Borges, J., Pereiras, B., and Castro, F.**
"A novel twin-rotor radial-inflow air turbine for oscillating-watercolumn wave energy converters"
in: *Energy* 93 (2015), pp. 2116–2125. DOI: 10.1016/j.energy.2015.10.046   (cit. on p. 14)

[30] **Setoguchi, T., Santhakumar, S., Takao, M., Kim, T. H., and Kaneko, K.**
"A performance study of a radial turbine for wave energy conversion"
in: *Proceedings of the Institution of Mechanical Engineers, Part A: Journal of Power and Energy* 216.1 (Feb. 2002), pp. 15–22. DOI: 10.1243/095765002760024917   (cit. on p. 14)

[31] **Malin, M., Redtenbacher, C., Lurf, G., Wermuth, N., and Wimmer, A.**
"Evaluation of strategies for highly transient operation of diesel-gas engines"
in: *Internal Combustion Engine Division Fall Technical Conference*. Vol. Volume 1: Large Bore Engines; Fuels; Advanced Combustion. Paper No: ICEF2018-9710, V001T01A010. ASME 2018. DOI: 10.1115/ICEF2018-9710   (cit. on p. 14)

[32] **Ntonas, K., Aretakis, N., Roumeliotis, I., Pariotis, E., Paraskevopoulos, Y., and Zannis, T.**
"Integrated simulation framework for assessing turbocharger fault effects on diesel-engine performance and operability"
in: *Journal of Energy Engineering* 146.4 (Aug. 2020), p. 04020023. DOI: 10.1061/(asce)ey.1943-7897.0000673   (cit. on p. 14)

[33] **Yamamoto, T., Furuhata, T., Arai, N., and Mori, K.**
"Design and testing of the Organic Rankine Cycle"
in: *Energy* 26 (2001), pp. 239–251. DOI: 10.1016/S0360-5442(00)00063-3   (cit. on p. 14)

[34] **Kang, S. H.**
"Design and experimental study of ORC (Organic Rankine Cycle) and radial turbine using R245fa working fluid"
in: *Energy* 41 (2012), pp. 514–524. DOI: 10.1016/j.energy.2012.02.035   (cit. on p. 14)

[35] **El-Khattam, W. and Salama, M.**
"Distributed generation technologies, definitions and benefits"
in: *Electric Power Systems Research* 71 (2004), pp. 119–128. DOI: 10.1016/j.epsr.2004.01.006   (cit. on p. 14)

[36] **Facchinetti, E., Favrat, D., and Marechal, F.**
"Design and optimization of an innovative solid oxide fuel cell gas turbine hybrid cycle for small scale distributed generation"
in: *Fuell Cells* 14 (2014), pp. 595–606. DOI: 10.1002/fuce.201300196   (cit. on p. 14)

[37] **Fraser, N., Blaxill, H., Lumsden, G., and Bassett, M.**
"Challenges for increased efficiency through gasoline engine downsizing"
in: *SAE International Journal of Engines* 2 (2009), pp. 991–1008. DOI: 10.4271/2009-01-1053   (cit. on p. 14)

[38] **Chiong, M. S., Rajoo, S., Martinez-Botas, R. F., and Costall, A. W.**
"Engine turbocharger performance prediction: One-dimensional modelling of a twin entry turbine"

in: *Energy Conversion and Management* 57 (2012), pp. 68–78. DOI: 10.1 016/j.enconman.2011.12.001 (cit. on pp. 16, 22)

[39] **Romagnoli, A., Copeland, C. D., Martinez-Botas, R., Seiler, M., Rajoo, S., and Costall, A.**
"Comparison between the steady performance of double-entry and twin-entry turbocharger turbines"
in: *Journal of Turbomachinery* 135.1 (Oct. 2012). DOI: 10.1115/1.4006 566 (cit. on pp. 16, 18)

[40] **Uhlmann, T., Lückmann, D., Aymanns, R., Scharf, J., Höpke, B., Scassa, M., Rütten, O., Schorn, N., and Kindl, H.**
"Development and matching of double entry turbines for the next generation of highly boosted gasoline engines"
in: *Anais do XXII Simpósio Internacional de Engenharia Automotiva*. Vol. 1. 2. Editora Edgard Blücher Aug. 2014. DOI: 10.5151/engpro-si mea2014-100 (cit. on p. 16)

[41] **SAE**
Supercharger testing standard
SAE J1723. Society of Automotive Engineers Aug. 1995
(cit. on p. 18)

[42] **SAE**
Turbocharger gas stand test code
SAE J1826. Society of Automotive Engineers Mar. 1995
(cit. on p. 18)

[43] **Luján, J. M., Bermúdez, V., Serrano, J. R., and Cervelló, C.**
Test bench for turbocharger groups characterization
SAE Technical Paper 2002-01-0163. SAE International Mar. 2002. DOI: 10.4271/2002-01-0163 (cit. on p. 18)

[44] **Serrano, J. R., Tiseira, A., García-Cuevas, L. M., Inhestern, L. B., and Tartoussi, H.**
"Radial turbine performance measurement under extreme off-design conditions"
in: *Energy* 125 (Apr. 2017), pp. 72–84. DOI: 10.1016/j.energy.2017.02 .118 (cit. on p. 18)

[45] **Aghaali, H. and Hajilouy-Benisi, A.**
"Experimental and theoretical investigation of twin-entry radial inflow gas turbine with unsymmetrical volute under full and partial admission conditions"
in: *Turbo Expo: Power for Land, Sea and Air*. Paper No: GT2007-27807. ASME Jan. 2007, pp. 1099–1107. DOI: 10.1115/GT2007-27807
(cit. on p. 18)

[46] **Brinkert, N., Sumser, S., Weber, S., Fieweger, K., Schulz, A., and Bauer, H. J.**
"Understanding the twin scroll turbine: flow similarity"
in: *Journal of Turbomachinery* 135 (2 2013), p. 021039. DOI: 10.1115/1.4006607
(cit. on p. 18)

[47] **Romagnoli, A., Martinez-Botas, R. F., and Rajoo, S.**
"Steady state performance evaluation of variable geometry twin-entry turbine"
in: *International Journal of Heat and Fluid Flow* 32.2 (2011), pp. 477–489. DOI: 10.1016/j.ijheatfluidflow.2010.12.002
(cit. on p. 18)

[48] **Usai, V. and Marelli, S.**
"Steady state experimental characterization of a twin entry turbine under different admission conditions"
in: *Energies* 14.8 (Apr. 2021), p. 2228. DOI: 10.3390/en14082228
(cit. on p. 18)

[49] **Serrano, J. R., Arnau, F. J., García-Cuevas, L. M., Samala, V., and Smith, L.**
"Experimental approach for the characterization and performance analysis of twin entry radial-inflow turbines in a gas stand and with different flow admission conditions"
in: *Applied Thermal Engineering* 159 (2019). DOI: 10.1016/j.applthermaleng.2019.113737
(cit. on pp. 19, 39, 40, 87, 129, 211)

[50] **Serrano, J. R., Arnau, F. J., García-Cuevas, L. M., Soler, P., Smith, L., Cheung, R., and Pla, B.**
"An experimental method to test twin and double entry automotive turbines in realistic engine pulse conditions"
in: *SAE Technical Papers* (2019). DOI: doi:10.4271/2019-01-0319
(cit. on p. 19)

[51] **Serrano, J. R., Arnau, F. J., García-Cuevas, L. M., and Soler, P.**
"Experimental validation of a one-dimensional twin-entry radial turbine model under non-linear pulse conditions"
in: *International Journal of Engine Research* (2019). DOI: 10.1177/1468087419869157
(cit. on p. 19)

[52] **Morrison, R., Stuart, C., Kim, S. I., Spence, S., Starke, A., and Leonard, T.**
"Investigation of a novel turbine housing to produce a non-uniform spanwise flow field at the inlet to a mixed flow turbine and provide variable geometry capabilities"
in: *Proceedings of the ASME Turbo Expo 2021: Turbomachinery Technical Conference and Exposition*. Vol. Volume 2D: Turbomachinery -

Multidisciplinary Design Approaches, Optimization, and Uncertainty Quantification; Radial Turbomachinery Aerodynamics; Unsteady Flows in Turbomachinery. American Society of Mechanical Engineers   June 2021. DOI: 10.1115/gt2021-59382   (cit. on p. 19)

[53]   **Jin, J., Pan, J., Lu, Z., Wu, Q., and Xu, L.**
"Effect of balance valve on an asymmetric twin-scroll turbine for heavy-duty diesel engine."
in: *International Journal of Engine Research* (2020). DOI: 10.1177/1468 087420930162   (cit. on p. 19)

[54]   **Yeo, J. H. and Baines, N. C.**
"Laser velocity measurements in a twin-entry vaneless radial turbocharger turbine."
in: *JSME International Journal Series B* 37.4 (1994), pp. 861–870. DOI: 10.1299/jsmeb.37.861   (cit. on p. 19)

[55]   **Aghaei, R., Tousi, A. M., and Tourani, A.**
"Comparison of turbulence methods in CFD analysis of compressible flows in radial turbomachines"
in: *Aircraft Engineering and Aerospace Technology: An International Journal* (2008), pp. 657–665. ISSN: 0002-2667. DOI: 10.1108/000226608 10911608   (cit. on p. 20)

[56]   **Menter, F. R.**
"Two-equation eddy-viscosity turbulence models for engineering applications"
in: *AIAA journal* 32.8 (1994), pp. 1598–1605. DOI: 10.2514/3.12149
(cit. on p. 20)

[57]   **Menter, F. R., Langtry, R., and Hansen, T.**
"CFD simulation of turbomachinery flows - verification, validation and modelling"
in: *European Congress on Computational Methods in Applied Sciences and Engineering*. Ed. by ECCOMAS2004   2004   (cit. on p. 20)

[58]   **Galindo, J., Hoyas, S., Fajardo, P., and Navarro, R.**
"Set-up analysis and optimization of CFD simulations for radial turbines"
in: *Engineering Applications of Computational Fluid Mechanics* 7 (2013), pp. 441–460. DOI: 10.1080/19942060.2013.11015484
(cit. on pp. 20, 73)

[59]   **Cerdoun, M. and Ghenaiet, A.**
"Characterization of a twin-entry radial turbine under pulsatile flow condition"
in: *International Journal of Rotating Machinery* (2016), pp. 1–15. DOI: 0.1155/2016/4618298   (cit. on p. 20)

222

[60] **Galindo, J., Fajardo, P., Navarro, R., and García-Cuevas, L. M.**
"Characterization of a radial turbocharger turbine in pulsating flow by means of CFD and its application to engine modelling"
in: *Applied Energy* 103 (2013), pp. 116–127. DOI: 10.1016/j.apenergy.2012.09.013   (cit. on p. 20)

[61] **Fürst, J. and Žák, Z.**
"CFD analysis of a twin scroll radial turbine"
in: *EPJ Web of Conferences*. Vol. 180 2018. DOI: 10.1051/epjconf/201818002028   (cit. on p. 20)

[62] **Palfreyman, D. and Martinez-Botas, R. F.**
"The pulsating flow field in a mixed flow turbocharger turbine: An experimental and computational study"
in: *Journal of turbomachinery* 127 (1 2005), pp. 144–155. DOI: 10.1115/1.1812322   (cit. on p. 20)

[63] **Jasak, H. and Beaudoin, M.**
"OpenFOAM Turbo tools: from general purpose CFD to turbomachinery simulations"
in: *ASME-JSME-KSME 2011 Joint Fluids Engineering Conference*. Vol. Volume 1, Symposia - Parts A, B, C, and D. ASMEDC Jan. 2011. DOI: 10.1115/ajk2011-05015   (cit. on p. 20)

[64] **Yokoyama, T., Hoshi, T., Yoshida, T., and Wakashima, K.**
"Development of twin-entry scroll radial turbine for automotive turbochargers using unsteady numerical simulation"
in: *11th International Conference on Turbochargers and Turbocharging* (2014), pp. 471–478. DOI: 10.1533/978081000342.471   (cit. on p. 20)

[65] **Wang, A. and Zheng, X.**
"Design criterion for asymmetric twin-entry radial turbine for efficiency under steady and pulsating inlet conditions"
in: *Proceedings of the Institution of Mechanical Engineers, Part D: Journal of Automobile Engineering* 233.8 (Mar. 2018), pp. 2246–2256. DOI: 10.1177/0954407018757926   (cit. on p. 20)

[66] **Menaouar, B. M., Mohamed, H., Mohamed, B., Ahmed, G., and Kamel, H. M.**
"The separation wall effect of a volute twin entry cross section area on the mixed inflow turbine performance."
in: *Engineering Review* 41 (2020), pp. 11–20. DOI: 10.30765/er.1383
(cit. on p. 20)

[67] **Fan, H., Ni, J., Shi, X., Qu, D., Zheng, Y., and Zheng, Y.**
"Simulation optimization of a new twin-entry turbocharger turbine with double incidence angles"
in: *Journal of Engineering for Gas Turbines and Power* 141.5 (Mar. 2019).
DOI: 10.1115/1.4041315 (cit. on p. 20)

[68] **Chebli, E., Casey, M., Martinez-Botas, R., Sumser, S., Müller, M., Künzel, S., Leweux, J., Gorbach, A., and Schmidt, W.**
"The variable outlet turbine concept for turbochargers"
in: *Journal of Turbomachinery* 136.12 (Aug. 2014). DOI: 10.1115/1.4028231 (cit. on p. 20)

[69] **Bencherif, M. M., Hamidou, M. K., Hamel, M., and Abidat, M.**
"Study of unsteady performance of a twin-entry mixed flow turbine"
in: *Journal of Applied Mechanics and Technical Physics* 57.2 (Mar. 2016), pp. 300–307. DOI: 10.1134/s0021894416020139 (cit. on p. 21)

[70] **Cravero, C., Domenico, D. D., and Ottonello, A.**
"Numerical simulation of the performance of a twin scroll radial turbine at different operating conditions"
in: *International Journal of Rotating Machinery* 2019 (June 2019), pp. 1–13. DOI: 10.1155/2019/5302145 (cit. on p. 21)

[71] **Ghenaiet, A. and Cerdoun, M.**
"Simulations of steady and unsteady flows through a twin-entry radial turbine"
in: *Turbo Expo: Power for Land, Sea and Air*. Vol. Paper No: GT2014-25764. ASME 2014. DOI: 10.1115/GT2014-25764 (cit. on p. 21)

[72] **Müller, M., Streule, T., Sumser, S., Hertweck, G., Nolte, A., and Schmid, W.**
"The asymmetric twin scroll turbine for exhaust gas turbochargers"
in: *Proceedings of ASME Turbo Expo 2008: Power for Land, Sea and Air*. Vol. Volume 6: Turbomachinery, Parts A, B, and C. ASMEDC Jan. 2008.
DOI: 10.1115/gt2008-50614 (cit. on p. 21)

[73] **Cravero, A. and Ottonello, A.**
"Uncertainty quantification methodologies applied to the rotor tip clearance effect in a twin scroll radial turbine."
in: *Fluids* 5 (2020). DOI: 10.3390/fluids5030114 (cit. on p. 21)

[74] **Hajilouy-Benisi, A., Rad, M., and Shahhosseini, M. R.**
"Flow and performance characteristics of twin-entry radial turbine under full and extreme partial admission conditions"
in: *Archive of Applied Mechanics* 79.12 (Jan. 2009), pp. 1127–1143. DOI: 10.1007/s00419-008-0295-5 (cit. on p. 21)

[75] **Xue, Y., Yang, M., Martinez-Botas, R. F., Yang, B., and Deng, K.**
"Unsteady performance of a mixed-flow turbine with nozzled twin-entry volute confronted by pulsating incoming flow"
in: *Aerospace Science and Technology* 95 (2019). DOI: 10.1016/j.ast.2019.105485
(cit. on p. 21)

[76] **Cerdoun, M. and Ghenaiet, A.**
"Unsteady behaviour of a twin entry radial turbine under engine like inlet flow conditions"
in: *Applied Thermal Engineering* 130 (2018), pp. 93–111. DOI: 10.1016/j.applthermaleng.2017.11.001
(cit. on pp. 21, 96)

[77] **Palenschat, T., Newton, P., Martinez-Botas, R. F., Müller, M., and Leweux, J.**
"3-D Computational loss analysis of an asymmetric volute twin-scroll turbocharger"
in: *Proceedings of ASME Turbo Expo 2017: Turbomachinery Technical Conference and Exposition*. Vol. Volume 8: Microturbines, Turbochargers and Small Turbomachines; Steam Turbines. American Society of Mechanical Engineers June 2017. DOI: 10.1115/gt2017-64190
(cit. on p. 21)

[78] **Baines, N.**
"Turbocharger turbine pulse flow performance and modelling - 25 years on"
in: *9th International conference on turbochargers and turbocharging* 2010, pp. 347–362
(cit. on p. 21)

[79] **Payri, F., Serrano, J. R., Fajardo, P., Reyes-Belmonte, M. A., and Gozalbo-Belles, R.**
"A physically based methodology to extrapolate performance maps of radial turbines"
in: *Energy Conversion and Management* 55 (Mar. 2012), pp. 149–163. DOI: 10.1016/j.enconman.2011.11.003
(cit. on pp. 21, 23, 131)

[80] **Romagnoli, A. and Martinez-Botas, R.**
"Performance prediction of a nozzled and nozzleless mixed-flow turbine in steady conditions"
in: *International Journal of Mechanical Sciences* 53.8 (2011), pp. 557–574. ISSN: 0020-7403. DOI: 10.1016/j.ijmecsci.2011.05.003
(cit. on p. 22)

[81] **Costall, A. W., McDavid, R. M., Martinez-Botas, R. F., and Baines, N. C.**
"Pulse performance modeling of a twin entry turbocharger turbine under full and unequal admission"

in: *Journal of Turbomachinery* 133.2 (Oct. 2010). DOI: 10.1115/1.4000566 (cit. on p. 22)

[82] **Chiong, M. S., Rajoo, S., Romagnoli, A., Costall, A. W., and Martinez-Botas, R. F.**
"Assessment of partial-admission characteristics in twin-entry turbine pulse performance modelling"
in: *Proceedings of ASME Turbo Expo 2015*. Vol. Volume 2C: Turbomachinery. American Society of Mechanical Engineers   June 2015. DOI: 10.1115/gt2015-42687 (cit. on p. 22)

[83] **Chiong, M. S., Rajoo, S., Romagnoli, A., Costall, A. W., and Martinez-Botas, R. F.**
"One-dimensional pulse-flow modeling of a twin-scroll turbine"
in: *Energy* 115 (Nov. 2016), pp. 1291–1304. DOI: 10.1016/j.energy.2016.09.041 (cit. on pp. 22, 142)

[84] **Fredriksson, C. F., Qiu, X., Baines, N. C., Müller, M., Brinkert, N., and Gutmann, C.**
"Meanline modeling of radial inflow turbine with twin-entry scroll"
in: *Proceedings of ASME Turbo Expo 2012*. Vol. Volume 5: Manufacturing Materials and Metallurgy; Marine; Microturbines and Small Turbomachinery; Supercritical CO2 Power Cycles. American Society of Mechanical Engineers   June 2012. DOI: 10.1115/gt2012-69018 (cit. on p. 22)

[85] **Hajilouy-Benisi, A., Rad, M., and Shahhosseini, M. R.**
"Modeling of twin-entry radial turbine performance characteristics based on experimental investigation under full and partial admission conditions"
in: *Scientia Iranica* (2009), pp. 281–290. URL: http://scientiairanica.sharif.edu/article_3231.html (cit. on pp. 22, 108)

[86] **Xue, Y., Yang, M., Martinez-Botas, R. F., Romagnoli, A., and Deng, K.**
"Loss analysis of a mix-flow turbine with nozzled twin-entry volute at different admissions"
in: *Energy* 166 (Jan. 2019), pp. 775–788. DOI: 10.1016/j.energy.2018.10.075 (cit. on p. 23)

[87] **Palenschat, T., Mueller, M., Rajoo, S., Chiong, M. S., Newton, P., Martinez-Botas, R., and Tan, F. X.**
"Steady-state experimental and meanline study of an asymmetric twin-scroll turbine at full and unequal and partial admission conditions"
in: *SAE Technical Paper* (2018). DOI: 10.4271/2018-01-0971 (cit. on pp. 23, 108, 116)

[88] **Wei, J., Xue, Y., Deng, K., Yang, M., and Liu, Y.**
"A direct comparison of unsteady influence of turbine with twin-entry and single-entry scroll on performance of internal combustion engine."
in: *Energy* 212 (2020), pp. 93–111. DOI: 10.1016/j.energy.2020.1186 38
(cit. on p. 23)

[89] **Wei, J., Xue, Y., Yang, M., Deng, K., Wang, C., and Wu, X.**
"A reduced-order model of twin-entry nozzleless radial turbine based on flow characteristics"
in: *Energy* 214 (Jan. 2021), p. 118890. DOI: 10.1016/j.energy.2020.1 18890
(cit. on p. 23)

[90] **Serrano, J. R., Arnau, F. J., Dolz, V., Tiseira, A., and Cervelló, C.**
"A model of turbocharger radial turbines appropriate to be used in zero- and one-dimensional gas dynamics codes for internal combustion engines modelling"
in: *Energy Conversion and Management* 49.12 (Dec. 2008), pp. 3729–3745. DOI: 10.1016/j.enconman.2008.06.031
(cit. on p. 23)

[91] **Serrano, J. R., Arnau, F. J., García-Cuevas, L. M., Dombrovsky, A., and Tartoussi, H.**
"Development and validation of a radial turbine efficiency and mass flow model at design and off-design conditions"
in: *Energy Conversion and Management* 128 (2016), pp. 281–293. DOI: 10.1016/j.enconman.2016.09.032
(cit. on pp. 23, 131)

[92] **Galindo, J., Tiseira, A., Fajardo, P., and García-Cuevas, L. M.**
"Development and validation of a radial variable geometry turbine model for transient pulsating flow applications"
in: *Energy Conversion and Management* 85 (2014), pp. 190–203. DOI: 10.1016/j.enconman.2014.05.072
(cit. on pp. 24, 92)

[93] **Torregrosa, A., García-Cuevas, L. M., Inhestern, L., and Soler, P.**
"Radial turbine sound and noise characterisation with acoustic transfer matrices by means of fast one-dimensional models"
in: *International Journal of Engine Research* (2019). DOI: 10.1177/1468 087419889429
(cit. on p. 24)

[94] **Serrano, J. R., Arnau, F. J., García-Cuevas, L. M., and Inhestern, L. B.**
"An innovative losses model for efficiency map fitting of vaneless and variable vaned radial turbines extrapolating towards extreme off-design conditions"
in: *Energy* 180 (2019), pp. 626–639. DOI: 10.1016/j.energy.2019.05 .062
(cit. on pp. 24, 27, 139, 210)

[95] **Serrano, J. R., Arnau, F. J., García-Cuevas, L. M., and Samala, V.**
"A robust adiabatic model for a quasi-steady prediction of far-off non-measured performance in vaneless twin-entry or dual-volute radial turbines"
in: *Applied Sciences* 10.1955 (2020). DOI: 10.3390/app10061955
(cit. on pp. 25, 193)

[96] **Olmeda, P., Tiseira, A., Dolz, V., and García-Cuevas, L. M.**
"Uncertainties in power computations in a turbocharger test bench"
in: *Measurement* 59 (2015), pp. 363–371. DOI: 10.1016/j.measurement.2014.09.055
(cit. on pp. 43, 44)

[97] **Serrano, J. R., Olmeda, P., Arnau, F. J., and Samala, V.**
"A holistic methodology to correct heat transfer and bearing friction losses from hot turbocharger maps in order to obtain adiabatic efficiency of the turbomachinery"
in: *International Journal of Engine Research* 21.8 (Mar. 2019), pp. 1314–1335. DOI: 10.1177/1468087419834194
(cit. on p. 47)

[98] **Fan, Q., Liu, X., Xu, L., Subash, A. A., Brackmann, C., Aldén, M., Bai, X.-S., and Li, Z.**
"Flame structure and burning velocity of ammonia/air turbulent premixed flames at high Karlovitz number conditions"
in: *Combustion and Flame* 238 (Apr. 2022), p. 111943. DOI: 10.1016/j.combustflame.2021.111943
(cit. on p. 47)

[99] **Adouni, H., Chouari, Y., Bournot, H., Kriaa, W., and Mhiri, H.**
"A novel ventilation method to prevent obstruction phenomenon within sewer networks"
in: *International Journal of Heat and Mass Transfer* 184 (Mar. 2022), p. 122335. DOI: 10.1016/j.ijheatmasstransfer.2021.122335
(cit. on p. 47)

[100] **Lehmann, J., Agel, M. R., Engelhardt, K. H., Pinnapireddy, S. R., Agel, S., Duse, L., Preis, E., Wojcik, M., and Bakowsky, U.**
"Improvement of pulmonary photodynamic therapy: Nebulisation of curcumin-loaded tetraether liposomes"
in: *Pharmaceutics* 13.8 (Aug. 2021), p. 1243. DOI: 10.3390/pharmaceutics13081243
(cit. on p. 47)

[101] **Fischer, A.**
"Fundamental flow measurement capabilities of optical Doppler and time-of-flight principles."
in: *Experiments in Fluids* 62 (2021). DOI: 10.1007/s00348-020-03127-x
(cit. on p. 47)

[102] **Grosjean, N., Graftieaux, L., Michard, M., Hübner, W., Tropea, C., and Volkert, J.**
"Combining LDA and PIV for turbulence measurements in unsteady swirling flows."
in: *Measurement Science and Technology* 8.12 (1997). DOI: `10.1088/0957-0233/8/12/015` (cit. on p. 47)

[103] **Pedersen, N., Larsen, P. S., and Jacobsen, C. B.**
"Flow in a centrifugal pump impeller at design and off-design conditions - Part I: Particle Image Velocimetry (PIV) and Laser Doppler Velocimetry (LDV) measurements."
in: *Journal of Fluids Engineering* 125 (2003), pp. 61–72. DOI: `10.1115/1.1524585` (cit. on p. 48)

[104] **Zhang, N., Zheng, F., Liu, X., Gao, B., and Li, G.**
"Unsteady flow fluctuations in a centrifugal pump measured by laser Doppler anemometry and pressure pulsation."
in: *Physics of Fluids* 32 (2020). DOI: `10.1063/5.0029124` (cit. on p. 48)

[105] **Theis, A., Reviol, T., and Böhle, M.**
"Analysis of the losses in an axial fan with small blade aspect ratios using CFD-technique and laser Doppler anemometry."
in: *Proceedings of the ASME Turbo Expo 2020: Turbomachinery Technical Conference and Exposition. Volume 2A: Turbomachinery* (2020). DOI: `10.1115/GT2020-14283` (cit. on p. 48)

[106] *Simcenter STAR-CCM+ Documentation*
Siemens   2019 (cit. on p. 73)

[107] **Roache, P. J.**
"Perspective: A method for uniform reporting of grid refinement studies"
in: *Journal of Fluids Engineering* 116.3 (Sept. 1994), pp. 405–413. ISSN: 0098-2202. DOI: `10.1115/1.2910291` (cit. on p. 74)

[108] **Chiong, M. S., Rajoo, S., Romagnoli, A., Costall, A. W., and Martinez-Botas, R. F.**
"Integration of meanline and one-dimensional methods for prediction of pulsating performance of a turbocharger turbine"
in: *Energy Conversion and Management* 81 (May 2014), pp. 270–281. DOI: `10.1016/j.enconman.2014.01.043` (cit. on p. 92)

[109] **Futral, S., Wasserbauer, C., USN, A., and Administration, S.**
Off-design performance prediction with experimental verification for a radial-inflow turbine
tech. rep. NASA TN D-2621   1965. URL: `http://books.google.es/books?id=N1kzLAHfK-IC` (cit. on pp. 96, 100, 109, 142)

[110] **Chen, H. and Baines, N. C.**
"The aerodynamic loading of radial and mixed-flow turbines"
in: *International Journal of Mechanical Sciences* 36 (1994), pp. 63–79.
DOI: 10.1016/0020-7403(94)90007-8   (cit. on pp. 109, 110, 147)

[111] **Serrano, J. R., Navarro, R., García-Cuevas, L. M., and Inhestern, L. B.**
"Turbocharger turbine rotor tip leakage loss and mass flow model valid up to extreme off-design conditions with high blade to jet speed ratio"
in: *Energy* 147 (Mar. 2018), pp. 1299–1310. DOI: 10.1016/j.energy.2018.01.083   (cit. on pp. 111, 147, 148)

[112] **Serrano, J. R., Navarro, R., García-Cuevas, L. M., and Inhestern, L. B.**
"Contribution to tip leakage loss modeling in radial turbines based on 3D flow analysis and 1D characterization"
in: *International Journal of Heat and Fluid Flow* 78 (2019). DOI: 10.1016/j.ijheatfluidflow.2019.108423   (cit. on pp. 111, 147)

[113] **Winterbone, D. E. and Pearson, R. J.**
Theory of engine manifold design: wave action methods for IC engines
ed. by Pub., P. E. Professional Engineering Pub.   2000. ISBN: 978-1-86058-209-7   (cit. on pp. 119, 152)

[114] **Kanzow, C., Yamashita, N., and Fukushima, M.**
"Levenberg–Marquardt methods with strong local convergence properties for solving nonlinear equations with convex constraints"
in: *Journal of Computational and Applied Mathematics* 172.2 (Dec. 2004), pp. 375–397. DOI: 10.1016/j.cam.2004.02.013
(cit. on pp. 137, 155)

[115] **Brent, R. P.**
"An algorithm with guaranteed convergence for finding a zero of a function"
in: *The Computer Journal* 14.4 (Apr. 1971), pp. 422–425. DOI: 10.1093/comjnl/14.4.422   (cit. on pp. 143, 145, 151, 153, 212)